SANDIA REPORT

SAND87—0098 Volume I • UC—80
Unlimited Release
Printed February 1987

Proceedings of the Fast Burst Reactor Workshop Held in Albuquerque, NM, April 8 – 10, 1986

T. F. Luera, Conference Coordinator

Prepared by
Sandia National Laboratories
Albuquerque, New Mexico 87185 and Livermore, California 94550
for the United States Department of Energy
under Contract DE-AC04-76DP00789

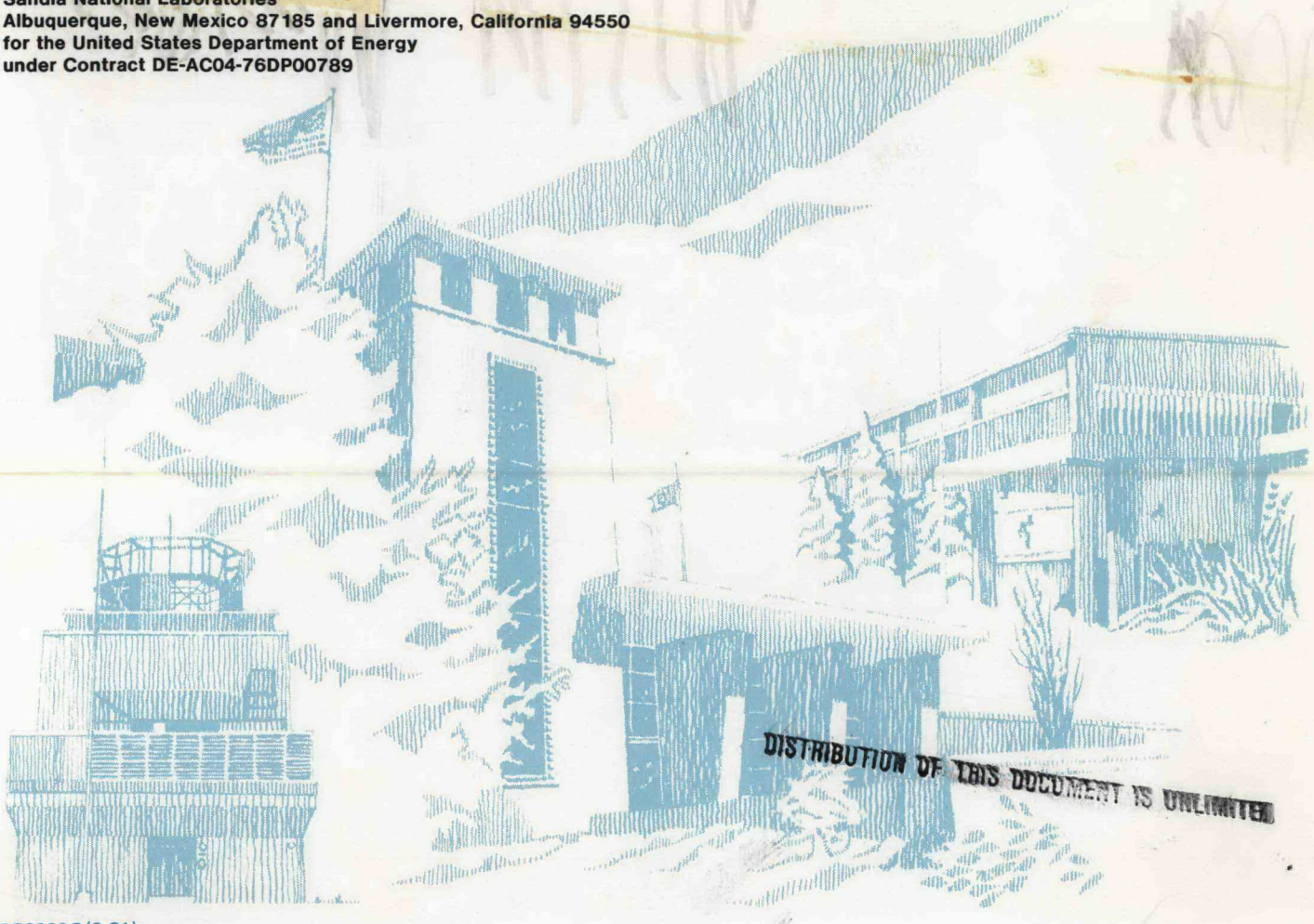

SF2900Q(8-81)

DISCLAIMER

Issued by Sandia National Laboratories, operated for the United States Department of Energy by Sandia Corporation.

Printed in the United States of America
Available from
National Technical Information Service
U.S. Department of Commerce
5285 Port Royal Road
Springfield, VA 22161

NTIS price codes
Printed copy: A11
Microfiche copy: A01

SAND--87-0098-Vol.1

DE87 009239

WORKSHOP ON FAST BURST REACTOR TECHNOLOGY

The Fast Burst Reactor Workshop was held at Sandia National Laboratories, Albuquerque, on April 8-10, 1986. Papers presented at the meeting are reproduced here without further editing. If full papers were not available, summaries furnished by the authors are substituted. These proceedings are published in two volumes. Volume I is Unlimited Release, and Volume II is Specified External Distribution Only.

VOLUME I

MASTER

CONF-860420

FOREWORD

This Fast Burst Reactor Workshop was sponsored by Sandia National Laboratories in cooperation with the Trinity Section of the American Nuclear Society and the University of New Mexico. The technical sessions were held at the Sandia National Laboratories' Technology Transfer Center in Albuquerque, New Mexico. Approximately 70 persons participated in the Workshop.

This Workshop was the second major meeting of scientists and technologists devoted entirely to this rather specialized topic. The first was a National Topical Meeting sponsored by the University of New Mexico and the American Nuclear Society in January 1969. A third meeting, the Army Material Command Research Reactor Symposium held at White Sands Missile Range in February 1973, had a slightly broader scope but was largely devoted to fast burst reactor technology.

The Workshop, which marked the 25th anniversary of the Trinity Section, was highlighted by two historic events. First, through the efforts of J. A. Grundl and others, the original natural uranium fuel model of Lady Godiva, which had stood on display at the Smithsonian Institution, found a permanent home at the National Atomic Museum in Albuquerque. Second, Lady Godiva was designated as an ANS Nuclear Historic Landmark. A plaque authorized by the ANS was presented to T. F. Wimett, who accepted it for Los Alamos at the Workshop banquet. The plaque is inscribed with these words:

LADY GODIVA

> Lady Godiva, the world's first fast-neutron assembly to be operated in the burst-excursion mode, was used in the definitive determination of delayed neutron parameters in 1955.

The Workshop ended in a special session on security, safeguards, and safety as they relate to fast burst reactor facilities. This session included formal papers and culminated a lively panel discussion involving Department of the Army and Department of Energy security, safety, and reactor operations personnel.

The success of the Workshop was due in large measure to the enthusiastic efforts of the authors and the session chairmen. Special thanks are also extended to the members of the organizing committee.

T. F. Luera
Sandia National Laboratories

TABLE OF CONTENTS
VOLUME I

TABLE OF CONTENTS (Cont'd)
VOLUME I

TABLE OF CONTENTS (Cont'd)
VOLUME I

TABLE OF CONTENTS
VOLUME II

PARADISE LOST

KEYNOTE SPEECH
APRIL 8, 1986

R. M. Jefferson

I am honored to be asked to be your keynote speaker. Particularly since I am neither older nor wiser than you. Perhaps being older than most of you is enough. I am honored for another reason and that is the fact that I gave up neutron transport in 1973 and am now engaged in garbage transport.[1] But perhaps as one now detached, I can offer some observations based upon the fact at one time I was part of your community. Many times I tickled the dragon's tail and then watched the dragon breathe on me and in a sense that's what I want to talk about today.

I think I can best explain where I want to go by a story that I heard from a professor at the University of Texas named Margaret Maxey. She tells a story about her oldest daughter who went away to school for her freshman year. The whole semester went by and they didn't receive one single letter from her. Well, finally they got a letter and they were very excited. They opened it up and it said, "Dear Mom and Dad, I haven't written because I broke my arm." She went on to say, "I'm sure you are curious to know how I did that. It all started when the girl across the hall was cooking in her room. We knew that was against the rules in the dormitory but everybody does it, and we'd done it before but on this particular night the little stove caught fire, and before we knew it, the room was on fire. We tried to put it out with the fire extinguisher, but it didn't work and by the time we decided that the fire was way out of control, it truly was out of control. There wasn't any way to get down out of our third story room except to jump out of the window. So I jumped out of the window, and in the fall I broke my arm, and I also fractured my skull. The whole dormitory burned down, and as a result, there were a lot of injuries. The ambulances were busy but I was on the back side of the dormitory, and no one could even see me till this nice young man who works in the filling station across the way came over and found me. He took me and put me in his car and took me to the hospital. They patched me up and then released me. There wasn't any place for me to stay since the dormitory burned down so I moved in with him. I'm sure you'll like him, and as soon as he learns English well enough he's going to get his GED and maybe start college some day himself. When the three of us come home this summer I hope you'll welcome us with open arms."

---

1 Mr. Jefferson is now a consultant on nuclear waste transportation and disposal.

Then the next paragraph said, "Now there's just one other thing I want to say and that is there was no fire in the dormitory, and I did not jump out the window, and I did not break my arm, and I'm not living with any young man, and I'm not pregnant, but I am flunking freshman algebra, and I wanted you to see it in perspective."

What I'd like to do is talk about some of the perspectives I see now as an outsider in your industry, and I guess one of the best ways to develop perspective is to start back with the history. Some of you lived it and some of you didn't so I apologize to those who have heard it before and maybe even recited it; but nonetheless, it all started, as Bill Snyder said a few minutes ago, back in 1945, January 8, 1945, as a matter of fact, when Otto Frish and a group of (I think it was) 11 men at Los Alamos put together the Dragon experiment. It was an experiment designed to validate the calculations and measurements that had previously been made concerning the prompt critical region. It was an experiment which they thought needed to be done in order to further define some of the technology in the prompt critical region for use in weapon design. And it was a very, very exotic setup. I went back and read about it this past week. It's the kind of thing that you absolutely could not do today. It started off with a rig that looked like a oil derrick, about 18 feet tall, held together with "C" clamps. The fuel system consisted of little bricks made out of uranium hydride (10 hydrogen to 1 uranium roughly). These little blocks (1" x 1/2" x 1/2") were all stacked up with a hole in the middle. Then they made a slug out of these little blocks. The intent was to drop the slug through the hole in the middle of the assembly. They were very careful since they had included an extremely exotic safety system. The slug was coupled to an electromagnet which was in turn held on top of the derrick by a rope over a pulley. When the time came to drop the slug, the current to the electromagnet was cut, and this slug fell down a track that was slightly inclined so that it would always stay on one side. Thus, the slug would pass through the assembly in a repeatable geometry. It's interesting that they conducted 537 pulses in 25 days and the experiment was disassembled. It is now 41 years later, and we're a mature activity or I should say you are. You don't do things like that anymore; you don't do the simple things and the crude things. Everything is very, very sophisticated; you are no longer checking out the theoreticians in quite the same manner. Now you're checking out the refinements and nuances and things like that. But one thing remains the same. It is just like Dick Feynman said when the experiment was proposed: "This is just like tickling the tail of a sleeping dragon."

Well that's what I'd like to talk about: This tickling the dragon's tail that you're involved in. It's incredible that in three weeks from the arrival of a fuel until the experiment was over, the reactor was built and disassembled. In three weeks today, after you get your funding, you can't even begin to put together a team. Nonetheless, it's interesting that had it not been for an accident, evidently pulse reactors would have gone away when they disassembled Dragon.

But it turns out that in 1952 there was an unplanned excursion in Jemima (a critical assembly at the Pajarito facility) that produced 1×10^{16} fissions. You compare that to Dragon, which produced on the order 2×10^{11} fissions, and you get some concept of how different these two were. The interesting thing in the Jemima accident was that it didn't cause any damage; it didn't contaminate the building; it didn't do anything. So it was sort of one of those "eurekas" that, if you are smart enough to see as they come by, can offer something new. Some studies were done, and it was found that the pulse was self-terminating; that it, in fact, did not depend upon mechanical disassembly but on thermal expansion.

As a result of that event in 1953, another machine, "Godiva" was modified from a critical assembly into an assembly that made it possible to make pulses. It's interesting what happens from there. In 1957 Godiva II came along. In 1958 or 1962 (I can't figure out which because the Russians are pretty inexact), the Russians put together a pulse reactor at Dubna. In 1961 there was Kukla, and also in 1961 there was the SPR, in 1962 there was FRAN, and in 1963, there was White Sands, which was originally called the Molly-G. I happen to like the names rather than acronyms. In 1964 it was Super Kukla, and now it's several generations later.

I'm reminded, when you talk about those kind of things, of the 1969 meeting[2] and an experience we had there. The Russians sent two people to that meeting. Originally one of them spoke very broken English and the other no English at all. The one who spoke the broken English was identified to us as the professor. The one who spoke no English was identified simply as the KGB. They managed to maintain this aura through most of the meeting until a group of us took them out to an Indian reservation. They wanted to see two things -- they'd heard about them and they really wanted to see them. They wanted to see the Rio Grande and an Indian reservation. Well, the Rio Grande was an enormous disappointment to them. It's like Mark Twain said "You never realize how much beauty water adds to a river till you see the Rio Grande." But nonetheless we took them out to an Indian reservation and Bob Long was with us and his son, who was at that time about 8 years old. It turned out that the Russian who didn't speak any English and Bob Long's son got lost, got separated from us and we were looking frantically for them fearing for this Russian's life, since he spoke only Russian, and he was alone on an Indian reservation. I didn't find them but the person who did said they rounded the corner of this particular house there on the reservation, and here was this Russian and Bob Long's son talking to each other in perfectly clear midwe tern English. Well at that point the pretense was up, and it turned out the KGB man was the

---

2 The ANS Topical meeting on Fast Burst Reactors held at the University of New Mexico.

one who spoke poor English and the professor was the one who spoke the very good English. We got a lot of communication going following that. Later we were driving up Central Avenue somewhere about the University area. As I remember there were five of us in the car -- the two Russians, Bob Long, somebody else and myself. Somebody had the temerity to ask the Russians what they used their pulse reactor for, and there was this long, painful silence that lasted about four blocks. Finally, the professor said we use ours for exactly the same thing you use yours. That was the end of the conversation.

But the reason I went back into this history is to get some perspective on what's going on now. I'd like to look at three aspects that I think beg comparison. One of the big factors in your business today has turned out to be safeguards or security. When I go out and visit the facility here and I see all the fences, and the guards, and the TVs, and the weapons, and all these sorts of things, I'm somewhat fondly reminded of days gone by. I can remember an experiment we conducted one time where security did become a problem. We had a beam port through the side of the building and we had an experiment outside the building that had some enriched uranium in it, and so we decided that something had to be done security wise. So what we did was put a television camera up and trained it on the uranium and put a monitor in the guard shack a couple hundred yards away, and that satisfied everybody. Well it satisfied them until 2:00 one morning when my phone rang and they said the television just quit. Well you know how those things happen; it never happens when its convenient and all that. It was, as I said, 2:00 a.m. It was 20 below zero and the wind was blowing 40 miles an hour. No wonder the television quit. So a couple of us came out here and worked on the thing for about an hour and got it working and nobody seemed to think it was a big deal. I remember another example of how tied up we were with safeguards in those days. We ordered a replacement core for SPR-II one time. It was made in Oak Ridge and it was delivered here. 106 kg of 93% enriched uranium metal by Railway Express. Well that wasn't the half of it, it was in seven boxes (there were six plates and then the rods). Each plate weighed 17 kilos and we only got six of the seven boxes. There was one plate missing. As I look back, it's absolutely amazing we did not put the US military services on a full alert, did not mobilize the National Guard. We just simply notified the Railway Express Agency that we were missing one of the packages and about a week later they found it and it got here and nobody though the worst of it. It's also interesting that it was just shortly after that that I left the pulsed reactor business, and one of the first tasks I took on was a safeguards task, a study done for the AEC under Dixie Lee Ray. Dixie and I are still close friends as a result of that study, but at the conclusion of that study someone in jest sent me a letter offering me money for plutonium and then signed it Colonel Gaddafi. It's been a long time.

But it concerns me with all due respect to the Colonel, that we've overdone security and safeguards in some ways to the point now where the security becomes more important than the safety; where it interferes with the operation to the point where "those people who

are running the system" are the guards instead of the operators; the security people instead of the technical people; people who really don't know the reactor and really don't care about the safety of those people operating it.

Another perspective that comes back to me is the technical one. In 41 years, surely this has gotten to be a mature technology. It's like someone once told me when I complained that everything was so much work, it was so hard to do anything. Somebody said all the simple things have already been done, and I think that's the case in fast burst reactors. The yields have been pushed up to the mechanical limits, the fuel materials have been improved, and what you're doing now is more and more exotic and esoteric sorts of things -- manipulating the designs to boost performance by small margins and things like that. I think what that does is it produces a next generation which is very, very complex, and that concerns me because at the same time it becomes less personal. I said in the beginning that I liked reactors that had names instead of acronyms. I look at that as part of the bureaucratization of your job where it's important now to state things with the cold hard facts of life. So in the true FDR style everything has an acronym now. It's disturbing to look back at Dragon and Godiva and Jemima and Kukla and to think that I'm part of the group that named one SPR as an acronym. It kind of bothers me now. The other thing that bothers me in this area is we become more and more dependent upon computers. I'm reminded of an experiment I performed one time at the University of New Mexico. I was teaching in the graduate school there and I had a student come to me and say, "Can I use a calculator on a test?" You've got to understand that I grew up with a slide rule. If you didn't know how to make a slide rule function, you weren't an engineer, and here I was teaching people who were using slide rules, and this upstart had the temerity to come and ask me if he could use a calculator. Well I thought about it and I finally decided that I would let him use the calculator and announced to the class that they could use calculators if they wanted to. the only thing they had to do was put a "C" after their name. I assured them it would make no difference in their grade at all. I just wanted to see if the people with calculators did any better than those people with slide rules. They didn't. They did worse, and it bothers me that we become so dependent on the computer today that we quit thinking about what we're doing. We're so dependent upon the computer that if the computer says it then it's got to be true. I think that when the time comes that we quit depending upon the rational mind that is when we get in trouble.

That leads me into another area -- operations. Early on, the operation of these machines was a marriage between man and machine. I remember when I first came into this business, learning from people who could look at the machine and do some mental calculations to determine or predict its behavior. Tom Wimett is one of those who simply understood that machine in such an intimate way that he know what the machine was going to do when he did certain things to the

machine. Then over the period that I was involved with pulsed reactors I saw things become more and more institutionalized. The bureaucratic desire to reduce everything to writing. It's gotten to the point now where we've written a manual for this marriage between man and machine, and I want to tell you how successful I think that will be. Next time you go to your local bookstore see how many marriage manuals there are and how many divorces are taking place. That is how successful I think those kinds of instruction books really are. One example I can think of that is when Tech Specs became "the idea". The idea was that we would write a set of things that were absolutely necessary for the operator to know in order to operate the reactor. It would sit right there on the console and in a few pages he could flip through and find out anything he wanted to know. Thus he could stay within the Tech Specs. Now the Tech Specs are thicker than the SARs were in those days. There's no way for the operator to know where to find anything in the Tech Specs any more. Its become just simply another bureaucratic document that's lying on the console ready to separate the operator from reality. It somehow reminds me of that scene in "Around the World in 80 Days" where this Prussian aviator is flying over the English Channel. His aircraft is slowly losing altitude and he's there thumbing through the manual trying to find out what to do next. I think we're sinking slowly into the sea when we depend upon the procedure and scrap our mental abilities. It's like most technical fields though in that it is people that are truly important in what you do. But there's been a change. In the first generation of these machines the people were in fact totally in control. They had a thorough understanding. I've seen Tom Wimett stand at a blackboard and think like a neutron. I don't see that happening any more. I came along in sort of the second generation with an intimate recall of the history involved and a familiarity with the technology, not only the mathematical but the practical as well, and I see a third generation that becomes one who's strong on theory and weak on history; people who have lost both the "feel" for what's happening and the intuitive understanding of what's taking place. I see down the road a fourth generation coming who's strong on instructions and forgotten everything else.

Now why do I tell all these things to you? Well, I want to remind you of something I think you already know. I want to tell you something you have probably already concluded. That is that no matter what you call your machine, how you name it, how you operate it, you're still tickling the dragon's tail. The only difference is that in the beginning you were tickling the tip of the tail and now you've moved a great deal farther up the anatomy. There's a lot of tail behind you now and because the dragon has remained asleep for the most part of all these years there is a tendency to become complacent; a tendency to assume, that it's all routine; a tendency to think that the dragon is a very sound sleeper. I'm concerned that not only is the dragon not a sound sleeper but he's awake and waiting. I'm concerned that the opportune moment will come along and you'll find out that euphemism that you see on the walls is true; that is "sometimes the dragon wins". Suddenly you become entangled in the maze of too many procedures and too much security and too little thinking, and the result is a mistake. Now let me tell you

I've been on lots of boards looking at mistakes and I've never found one that wasn't a stupid mistake. They are easy to see when you look back at them. They are easy for a review board to say "Gee you should have done this instead of that." You are in a situation today where that's exactly what will happen. People will be much more interested in fixing the blame than fixing the problem. And I think its important not to become dependent upon the things in your business but to retain dependence upon your ability to outthink the dragon. Because if you don't, the letter won't begin with "Dear Mom and Dad" and it won't have to do with "flunking freshman algebra".

Thank you.

SESSION I

PHYSICS

E. J. Dowdy, Chairman
Los Alamos National Laboratory

DYNAMICS OF ANNULAR FUEL IN FAST BURST REACTORS

T. F. Wimett
Los Alamos National Laboratory, Los Alamos, New Mexico 87545

INTRODUCTION

For generation of short-duration fission pulses, the performance of fast burst reactors is always limited by stress failure as a result of rapid heating in the fuel components. Typically, dynamic stresses increase far more than linearly with inverse pulse duration. The major cause of this large stress increase is fuel metal inertia, i.e., the rapid heating or thermal shock gives rise to stress waves.

Some analyses of shock effects in burst reactors have been reported starting with G. E. Hansen[1] of Los Alamos National Laboratory who predicted the fuel failure threshold for Lady Godiva using a first order approximation in spherical geometry. D. Burgreen[2] provided some approximate solutions to the thermoelastic differential equations of fuel motion in rods, spheres and thin shells. J. A. Reuscher[3,4] produced solutions for hollow right circular cylinders and rods by using numerical analysis and the digital computer.

The problem of predicting a stress failure threshold had not yet been solved with useful certainty, as stated in a concluding remark by J. A. Reuscher.[3]

The purpose of this report is to identify failure modes and their parametric dependencies and provide more certainty in the prediction of damage thresholds. Certain approximations will be made that generate differential equations which are amenable to analytic solutions. These then will be compared with some SPRII displacement data which were kindly provided by J. A. Reuscher (SNL).

Analysis

The dynamic thermoelastic displacement equation in cylindrical geometry with angular symmetry written in terms of elastic moduli E, ν, is

$$\frac{E(1-\nu)}{(1-2\nu)(1+\nu)} D^2(u) + \frac{E}{2(1+\nu)} \frac{\partial^2 u}{\partial z^2} + \frac{E}{(2(1-2\nu)(1+\nu)} \frac{\partial^2 v}{\partial r \partial z}$$

$$- \frac{E\beta}{(1-2\nu)} \frac{\partial T}{\partial r} = \rho \frac{\partial^2 u}{\partial t^2} \qquad (1)$$

where $$D^2(u) = \frac{\partial^2 u}{\partial r^2} + \frac{1}{r} \frac{\partial u}{\partial r} - \frac{u}{r^2} \qquad (2)$$

u = radial displacement
v = axial displacement

The stress components are

$$\text{radial, } \frac{\tau_r}{E} = \frac{(1-\nu)}{(1-2\nu)(1+\nu)}\frac{\partial u}{\partial r} + \frac{\nu}{(1-2\nu)(1+\nu)}\left[\frac{u}{r} + \frac{\partial v}{\partial z}\right] - \frac{\beta T}{(1-2\nu)}$$

$$\text{tangential, } \frac{\tau_\theta}{E} = \frac{(1-\nu)}{(1-2\nu)(1+\nu)}\frac{u}{r} + \frac{\nu}{(1-2\nu)(1+\nu)}\left[\frac{\partial u}{\partial r} + \frac{\partial v}{\partial z}\right] - \frac{\beta T}{(1-2\nu)}$$

$$\text{axial, } \frac{\tau_z}{E} = \frac{(1-\nu)}{(1-2\nu)(1+\nu)}\frac{\partial v}{\partial z} + \frac{\nu}{(1-2\nu)(1+\nu)}\left[\frac{\partial u}{\partial r} + \frac{u}{r}\right] - \frac{\beta T}{(1-2\nu)}$$

$$\text{shear, } \frac{\tau_{rz}}{E} = \frac{1}{2(1+\nu)}\left(\frac{\partial u}{\partial z} + \frac{\partial v}{\partial r}\right)$$

Infinite cylinder approximation.

In all approximations, we assume no axial (z) dependence in T.

Assume axial strain, $\frac{\partial v}{\partial z} = \beta T_o$ where T_o is plate averaged temperature, and

$$\frac{\partial^2 u}{\partial z^2} = 0 \qquad \left(\frac{\partial u}{\partial z} \text{ independent of } z\right)$$

Equation (1) yields

$$D^2(u) = \frac{(1+\nu)}{(1-\nu)}\beta\frac{\partial T}{\partial r} + \frac{(1-2\nu)(1+\nu)\rho}{(1-\nu)E}\frac{\partial^2 u}{\partial t^2} \tag{3}$$

Disc or thin annular plate approximation.

Assume $\tau_z = 0$
$\tau_{rz} = 0$

Using stress component definitions

$$\text{If } \tau_{rz} = 0, \ \frac{\partial u}{\partial z} = -\frac{\partial v}{\partial r} \text{ or } \frac{\partial^2 v}{\partial r \partial z} = -\frac{\partial^2 u}{\partial z^2}$$

$$\text{if } \tau_z = 0, \ \frac{\partial v}{\partial z} = -\frac{\nu}{1-\nu}\left[\frac{\partial u}{\partial r} + \frac{u}{r}\right] + \frac{1+\nu}{1-\nu}\beta T$$

$$\text{and } \frac{\partial^2 v}{\partial r \partial z} = -\frac{\nu}{1-\nu}D^2(u) + \frac{1+\nu}{1-\nu}\beta\frac{\partial T}{\partial r} = -\frac{\partial^2 u}{\partial z^2}$$

Putting this into equation (1) yields

$$D^2(u) = (1+\nu)\beta\frac{\partial T}{\partial r} + \frac{(1-\nu^2)\rho}{E}\frac{\partial^2 u}{\partial t^2} \tag{4}$$

To solve Eqs. (3) and (4), we let $u = u_1 + u_2$ where u_1 is the static displacement and u_2 is dynamic. Since these equations are alike except for constant coefficients, their solutions are similar except for term coefficients.

The static displacement equations are:

$$D^2(u_1) = \frac{(1+\nu)}{(1-\nu)} \beta \frac{\partial T}{\partial r} \quad , \text{ (inf. cyl.)}$$

$$D^2(u_1) = (1+\nu) \beta \frac{\partial T}{\partial r} \quad . \text{ (disc.)}$$

And the wave equation for u_2 is:

$$D^2(u_2) = \frac{1}{c^2} \frac{\partial^2 u_1}{\partial t^2} + \frac{1}{c^2} \frac{\partial^2 u_2}{\partial t^2} \tag{5}$$

where the wave velocity, $c = \sqrt{\frac{(1-\nu)\ E}{(1-2\nu)(1+\nu)\rho}}$ (inf. cyl.)

and $$c = \sqrt{\frac{E}{(1-\nu)^2\ \rho}} \qquad \text{(disc)}$$

<u>Static solutions</u> With boundary conditions, $\tau_r(a) = \tau_r(b) = 0$,

$$u_1(r) = \frac{(1+\nu)}{(1-\nu)} \frac{\beta}{r} \int_a^r Trdr + \frac{(1-3\nu)\beta T_o r}{2(1-\nu)} + \frac{(1+\nu)\beta T_o a^2}{2(1-\nu)\ r} \qquad \text{(inf. cyl.)}$$

$$u_1(r) = (1+\nu) \frac{\beta}{r} \int_a^r Trdr + \frac{(1-\nu)\beta T_o r}{2} + \frac{(1+\nu)\beta T_o a^2}{2r} \qquad \text{(disc)}$$

For both approximations, $u_1(a) = a\beta T_o$

$$u_1(b) = b\beta T_o \quad .$$

where $T_o = \frac{2}{(b^2-a^2)} \int_a^b Trdr$.

Solution of basic wave equation:

$$D^2(u) = \frac{\partial^2 u}{\partial r^2} + \frac{1}{r} \frac{\partial u}{\partial r} - \frac{u}{r^2} = \frac{1}{c^2} \frac{\partial^2 u}{\partial t^2} \quad .$$

Assume separability or let $u = y(r) \cdot B(t)$

Then $$\frac{d^2y}{dr^2} + \frac{1}{r}\frac{dy}{dr} - \frac{y}{r^2} = \frac{y}{B}\frac{1}{c^2}\frac{d^2B}{dt^2} \tag{6}$$

Now assume sinusoidal oscillation,

Then $$\frac{d^2B}{dt^2} = -\omega^2 B$$

And Eq. (6) becomes

$$\frac{d^2y}{dr^2} + \frac{1}{r}\frac{dy}{dr} - \frac{y}{r^2} = -\frac{\omega^2 y}{c^2} = -k^2 y \text{ where } k = \frac{\omega}{c} \tag{7}$$

the solution is $$y = C_1^m J_1(z) + C_2^m N_1(z) \tag{8}$$

where $z = kr$
$J_1(z)$ = Bessel function of first order and first kind
$N_1(z)$ = Bessel function of first order and second kind.

Again, the boundary condition is $\tau_r(a) = \tau_r(b) = 0$, and forgetting static components βT_o and $\beta T(r)$

$$\tau_r = \frac{E}{(1-2\nu)(1+\nu)}\left[(1-\nu)\frac{\partial u_2}{\partial r} + \frac{\nu u_2}{r}\right] \qquad \text{(inf. cyl.)}$$

or $$\frac{\partial u_2}{\partial r} = -\frac{\nu}{1-\nu}\frac{u_2}{r}, \quad r = a,b \qquad \text{(inf. cyl.)} \tag{9}$$

and $$\tau_r = \frac{E}{(1-\nu^2)}\left[\frac{\partial u_2}{\partial r} + \frac{\nu u_2}{r}\right] \qquad \text{(disc)}$$

or $$\frac{\partial u_2}{\partial r} = -\frac{\nu u_2}{r}, \quad r = a,b \qquad \text{(disc)} \tag{10}$$

Introducing boundary conditions, Eq. (8) yields

$$z_a\, c_1 J_1'(z_a) + c_2 N_1'(z_a) = G\, c_1 J_1(z_a) + c_2 N_1(z_a)$$

and $z_b\, c_1 J_1'(z_b) + c_2 N_1'(z_b) = G\, c_1 J_1(z_b) + c_2 N_1(z_b)$ where primes denote d/dz and $z_a = ka$, $z_b = kb$, and $G = \frac{\nu}{1-\nu}$ (inf. cyl.), $G = \nu$ (disc)

Introducing Bessel relations and combining boundary conditions yields with P = 1-G

$$\frac{c_1}{c_2} = \frac{P\,N_1(z_a) - z_a N_0(z_a)}{z_a J_0(z_a) - P\,J_1(z_a)} = \frac{P\,N_1(z_a) - z_b N_0(z_a)}{z_b J_0(a_b) - P\,J_1(a_b)} \tag{11}$$

Eq. (11) can readily be solved for z_a, since $z_b = \frac{bz_a}{a} = Rz_a$.

(A digital computer will find z_a to any desired accuracy.)

and $y(a) = C_1 J_1(z_a) + c_1 N_1(z_a)$

$y(b) = c_1 J_1(z_b) + c_2 N_1(z_b)$

Since the ratio, c_1/c_2, is provided by Eq. (11), we may without loss of generality, let y(b) = 1 to solve for c_1 and c_2

$$\text{or} \quad c_2 = \frac{1}{N_1(z_b) + \left(\frac{c_1}{c_2}\right) J_1(z_b)}$$

Actually, there are an indefinite number of z_a solutions, one for each harmonic. Thus, we define orthogonal functions associated with these harmonics

$$\psi_m(r) = C_1 J_1(k_m r) + c_2 N_1(k_m r) \tag{12}$$

$$\text{and} \quad k_m = \frac{\omega_m}{c}$$

These functions may now be used to obtain complete solutions to Eq. (5) by expanding the displacements in infinite series, thus

$$u_1 = \sum_m A_m(t)\, \psi_m(r) \tag{13}$$

$$u_2 = \sum_m B_m(t)\, \psi_m(r) \tag{14}$$

Eq. (7) can be rewritten with $\psi_m(r)$ for y and k_m for k or

$$D^2\left[\psi_m(r)\right] = -\, k_m^{\,2}\, \psi_m(r)$$

$$\text{and with (14),} \quad D^2(u_2) = -\sum_m k_m^{\,2} B_m(t)\, \psi_m(r) \tag{15}$$

To evaluate $B_m(t)$ we must use Eq. (5) or

$$\frac{1}{c^2}\left(\frac{\partial^2 u_1}{\partial t^2} + \frac{\partial^2 u_2}{\partial t^2}\right) = -\sum_m k_m^{\,2} B_m(t)\, \psi_m(r)$$

and for term m we can write using Eq. (14) for u_2

$$\frac{d^2 B_m}{dt^2} + \omega_m^2 B_m = - \frac{d^2 A_m}{dt^2} \tag{16}$$

We obtain A_m by multiplying both sides of Eq. (13) by $r\psi_m(r)$ and integrating over r. Using the orthogonality of ψ_m we find

$$A_m = \frac{\int_a^b u_1 \psi_m(r)\, r dr}{\int_a^b \psi_m^2(r)\, r dr} \tag{17}$$

These integrals can be readily evaluated by use of Eq. (17) which we can rewrite as

$$\frac{d}{dr}\left[\frac{1}{r}\frac{d(r\psi_m)}{dr}\right] = - k_m^2 \psi_m$$

As an example, we will assume a flat temperature distribution over r so that

$$u_1 = r\beta T_o(t)$$

and we readily find

$$A_m = \frac{2(1+\nu)\,[R - \psi_m(a)]\, a\beta T_o(t)}{R^2 z_a^2 - 1+\nu^2 - (z_a^2 - 1+\nu^2)\,\psi_m^2(a)} \qquad \text{(disc)}$$

and for the infinite cylinder, one simply replaces ν by $\frac{\nu}{1-\nu}$.

Finally, the most difficult integral is found in the solution of Eq. (16) for B_m

Letting $A_m = A_m^* \frac{T_o(t)}{T_o}$

And assuming a burst function for $T_o(t)$,

$$\frac{T_o(t)}{T_o} = \frac{e^{\alpha t}}{1+e^{\alpha t}} \quad \text{where } t = 0 \text{ at burst peak.}$$

$$f = \frac{e^{\alpha t}}{(1+e^{\alpha t})^2} \quad \text{which is a normalized burst function divided by } \alpha.$$

Integration of Eq. (16) yields

$$B_m(t) = \frac{-A_m^*}{2i\omega_m} \left\{ e^{i\omega_m t} \int_{-\infty}^{t} e^{-iw_m t}\, dt\, \alpha^2\, f'(\alpha,t) \right.$$

$$\left. -e^{-i\omega_m t} \int_{-\infty}^{t} e^{i\omega_m t}\, dt\, \alpha^2\, f'(\alpha,t) \right\} ,$$

where the primes denote time derivatives. Now we introduce a variable which controls vibration excitation as

$q_m = \frac{\omega_m}{\alpha} = \frac{\tau_o}{\tau_m}$ where τ_o is the burst period and τ_m is mth harmonic time constant.

With fuel inertia effects, $\alpha = \frac{3.52}{\Delta t}$

Performance of the integration in $B_m(t)$ yields

$$B_m(t) = -A_m^* \sum_n \frac{n!\, e^{n\alpha t}\, \mathrm{Re} \prod_1^n (n+iq_m)}{(1+e^{\alpha t})^{n+1} \prod_1^n (n^2+q_m^2)} \quad \text{for } t < 0$$

$$= -A_m^*\, S_o(q_m) \cos \omega_m t + A_m^* \sum_n \frac{e^{-n\alpha t}\, \mathrm{Re} \prod_1^n (n+iq_m)}{(1+e^{-\alpha t})^{n+1} \prod_1^n (n^2+q_m^2)} \quad t > 0$$

where $S_o(q) = \frac{1}{2} \sum_{n=1}^{\infty} \frac{n!\, \mathrm{Re} \prod_1^n (n+iq)}{2^n \prod_1^n (n^2+q^2)}$ (excitation function)

Note: For approximate calculations ($\pm$ 1% error) one can use

$$S_o(q) = \frac{4\, e^{\frac{8q}{\pi}}}{(1+e^{\frac{8q}{\pi}})^2} \quad \text{for } 0 < q < 1.8 \quad .$$

We now can write the complete expressions for u(r). For convenience we will write them in normalized form.

$$\frac{u(r)}{\alpha\beta T_o} = \frac{f_1(r)e^{\alpha t}}{(1+e^{\alpha t})} - \sum_m N_m\psi_m(r) \sum_{n=1}^{\infty} \frac{n!\, e^{-n\alpha|t|}\ \mathrm{Re}\prod_1^n (n+iq_m)}{(1+e^{-\alpha|t|})^{n+1}\ \prod_1^n (n^2+q_m^2)} \qquad t \le 0$$

$$= \frac{f_1(r)e^{\alpha t}}{(1+e^{\alpha t})} + \sum_m N_m\psi_m(r) \sum_{n=1}^{\infty} \frac{n!\, e^{-n\alpha|t|}\ \mathrm{Re}\prod_1^n (n+iq_m)}{(1+e^{-\alpha|t|})^{n+1}\ \prod_1^n (n^2+q_m^2)} \qquad (18)$$

$$- \sum_m N_m\psi_m(r)\, S_o(q_m) \cos\omega_m t \quad . \qquad t > 0$$

where $f_1(r) = \dfrac{u_1(r)}{a\beta T_o}$

$$N_m = \frac{A_m^*}{a\beta T_o}$$

With the foregoing definitions and equations, it is possible to describe completely such characteristics as

(a) fundamental frequency $f_1 = \dfrac{\omega_1}{2\pi} = \dfrac{k_1 c}{2\pi} = \dfrac{z_a^1 c}{2\pi a}$

(b) Ratio of inside-to-outside vibration amplitude

$$= \frac{\psi_m(a)}{\psi_m(b)} = \psi_m(a), \text{ since } \psi_m(b) \equiv 1$$

(c) Ratio of mth-to-first harmonic frequency = $\dfrac{k_m}{k_1}$

(d) An expression for time variation of hoop stress, $\tau_\theta(r,t)$ to yield a function which is essentially the same as Eq. (18) except for $f_1(r)$ and a constant factor in the other terms.

Following is a table of some of the solutions for flat temperature distribution over the SPRII fuel annulus with a = 0.825 in., b = 4.039 in., ν = 0.38, E = 12.3 x 10^6 (kpsi), ρ = 17.1.

TABLE I

m	Disc Approximation $z_{a(m)}$	$\psi_m(a)$	N_m	Infinite Cylinder Approximation $z_{a(m)}$	$\psi_m(a)$	N_m
1	0.3666	1.052	3.353	0.3483	1.657	2.8509
2	0.9547	-2.311	0.9612	0.9003	-2.496	1.3514
3	1.6830	2.304	0.1265	1.6523	2.328	0.1551

Notice that $\psi_2(a)$ is negative in all harmonics above. Remembering that $\psi_m(b) = 1$, this means [see Eq. (18)] that inside dynamic displacement is 180° out of phase with outside; for the other harmonics, they are in phase. Therefore, the second harmonic involves oscillating radial thickness of the fuel annulus while the first and third describe radial oscillation of the entire annulus.

Analysis of SPRII

Let us now examine displacement data taken on SPRII to see how they support the above theory. These data are 117 selected samplings of Bentley displacement output taken 20 μs apart for eleven different bursts. One detector was placed near the inside surface and two were placed at diametric opposed positions on the outer radial surface of a fuel annulus which is shown in Fig. 1. The outside radius is 4.039 inches while the inside hole is 0.825 inches in radius. The stacking of six rings in the assembly is drawn as a cross section in Fig. 2. The fuel annulus with detectors was apparently the third one from the top.

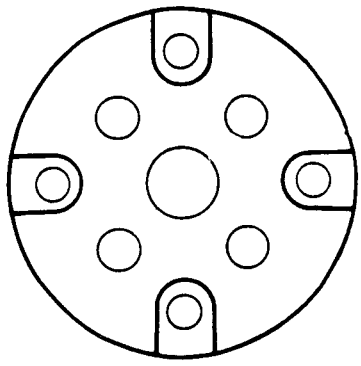

Fig. 1.
Plan view of SPRII fuel plate.

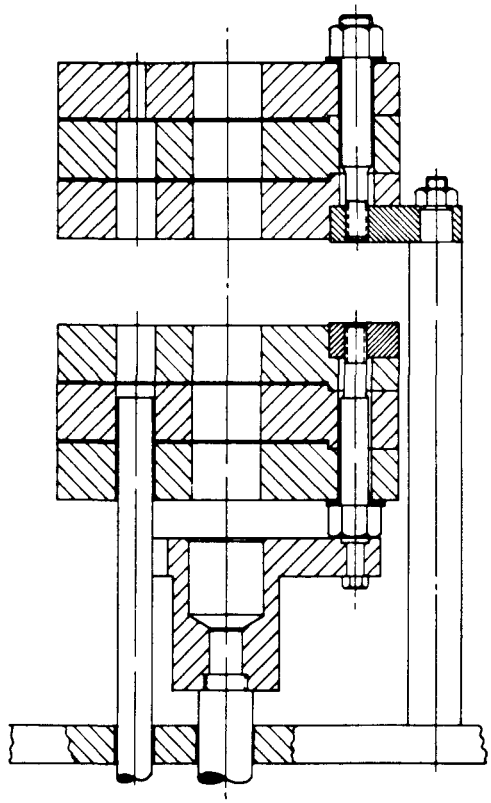

Fig. 2.
Cross section view of SPRII burst assembly.

Figure 3 shows the raw data from four different bursts as plots of displacement versus time. Points for the upper curve were obtained by averaging data from the outside detectors. The lower curve includes data from the single inside detector. Chain dotted horizontal lines are drawn at $a\beta T_o$ and $b\beta T_o$ which theory says should respresent the average displacements. One can see that most of the plots tend to agree with this for, at least, the first few cycles. However, there appears to be some low frequency vibration which we attribute to oscillation of supports for detectors and/or the burst assembly. For the largest (damaging) burst, T_o = 415 C, this oscillation is clearly evident.

In order to compare the displacement solutions with these data, a more complete description of displacement was required along with a means to correct the data for unwanted equipment vibration.

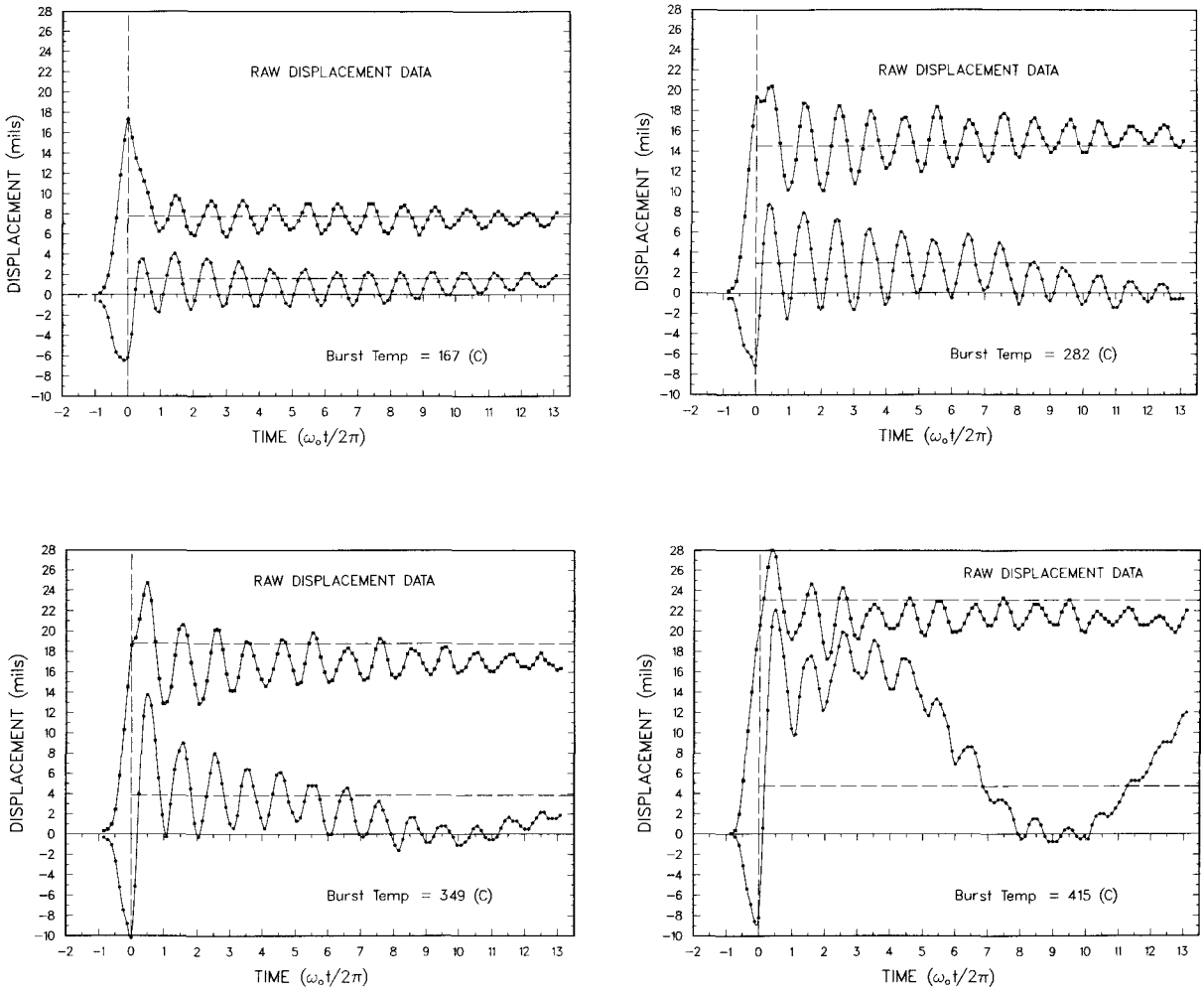

Fig. 3.
Raw displacement data from four typical bursts on SPRII. The outside data is an average of the response of two diametrically opposed Bently detectors. The time scale is arbitrarily normalized to a fundamental frequency of 6000 Hz.

First, the actual temperature distribution T(r), as given in Ref. 3 was included as a power series in the expression for A_m. Next, to account for the well-known burst narrowing from fuel inertia, the effect of which is to increase excitation over that expected from the simple burst function employed in the foregoing solutions, q_m is redefined as $q_m = \omega_m \Delta t/3.52$. The q_1 used for these calculations were obtained from limited data. Data were available for the three highest-yield bursts in the form of burst duration and α. For the other eight bursts, only α was available. Accordingly, Δt was found for the weak bursts by using q_1 as a fit parameter ($\Delta t = 3.52\ q_1/\omega_1$ and q_m are multiples of q_1).

By plotting these Δt versus α for the weak bursts (136, 144, and 167) and the known values for the three large bursts it was possible to extrapolate between these two sets to estimate Δt for the five remaining bursts which gave reasonable values for $\alpha\Delta t$ in all cases. Further, an asymmetric burst function was employed in solving for B_m. For a given q_m, the asymmetry was then controlled by one parameter, B. The decay of vibrations visible in the raw data was introduced as exponential with one decay constant which was included in the harmonics by dividing it by the harmonic frequency ratio.

Least-squares fitting of the theory with data was accomplished by introducing the vibration decay variable as a fit parameter and q_1, $a\beta T_o$, and B were input parameters. A time shift had to be used to line up the data with the burst peak at t = 0. A fit parameter was used for initial vibration frequency and another was found necessary because the hoop frequency evidentally increases with time. To these were added four fit parameters needed to subtract unwanted low frequency oscillation from the data. The fitting included only the last 96 data points.

After applying such least-squares fitting to all the burst data, it was determined that a discontinuity existed in excitation. For bursts greater than 167 C, excitation did not increase as expected. To better fit the data, a program was written which used the predicted q_1 up to the burst peak (t=0) but required q_1 to change linearly with time from t=0 to $\omega_1 t/2 = 0.5$ where it attained the value of a fit parameter for q_1 where it remained. This provided a measure of observed vibration amplitude after burst time.

Some typical results from this least-squares fitting are presented in Fig. 4. The goodness of fit is shown as χ^2. We note that a good fit was obtained for the low temperature burst, 167(C), with a residual that looks like the expected electromagnetic pickup of burst radiation. For the larger bursts, there is increasing distortion which, for the moment, we'll call reflected tractions. Also, we note that the vibration amplitudes do not increase as we might expect.

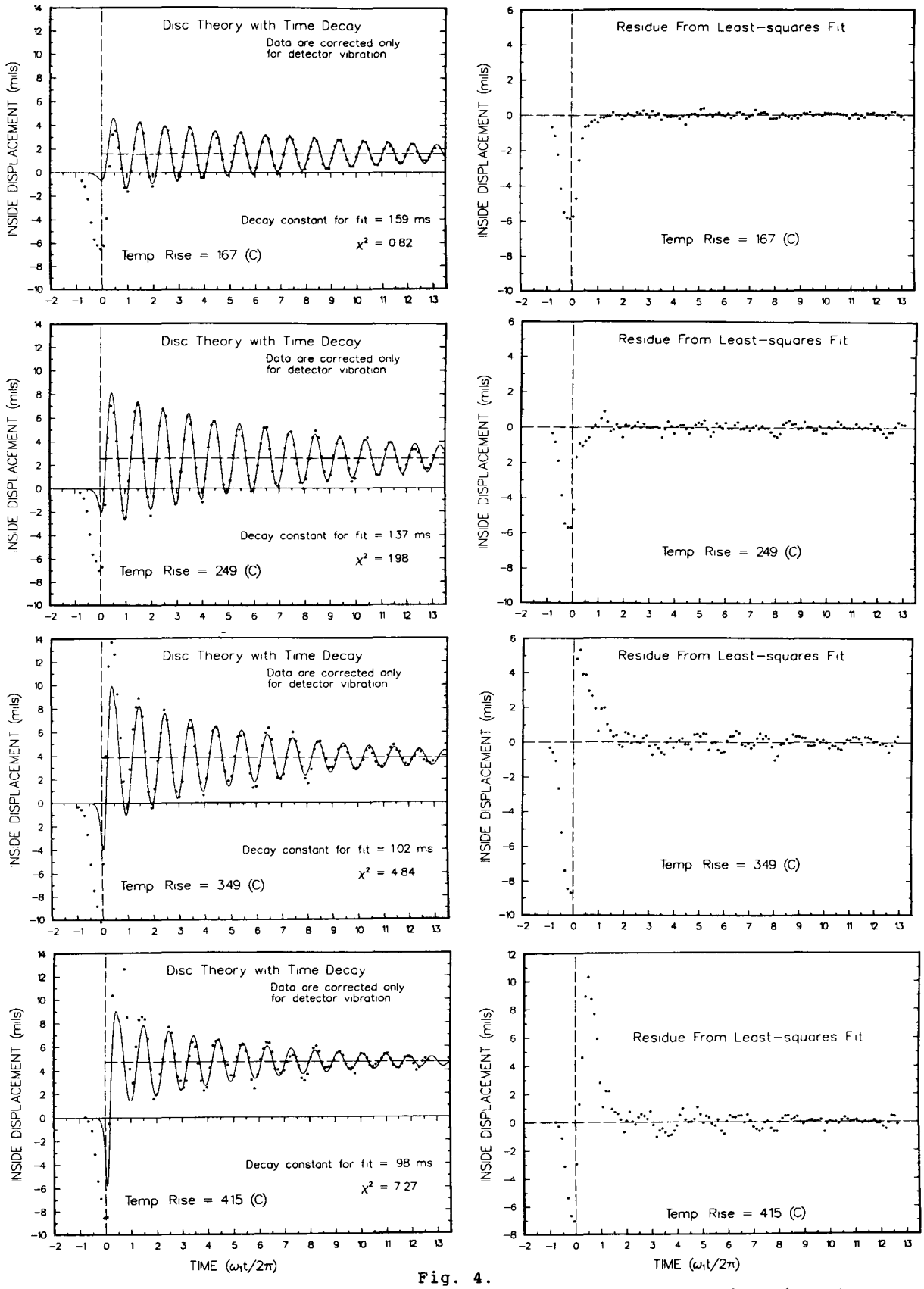

Fig. 4.
The results of least-squares fitting of inside displacement data with disc theory.

A plot of initial vibration amplitude for the inside taken from fits as in Fig. 4 is presented in Fig. 5 along with the expected amplitude (solid curve). The first harmonic excitation so calculated (solid line in Fig. 5) appears to be as expected. However, all data points are clearly low above T_o = 167 C. This suggests plastic deformation which, as shown by J. A. Reuscher[4], reduces vibration peaks where yield strength is exceeded. This may not produce fuel cracks but certainly absorbs energy and results in dislocations in the deformed metal.

For three typical bursts, the behavior of inside stress with time,as computed using T = T(r) and asymmetric bursts, is illustrated in Fig. 6. The burst shapes employed are also shown with arbitrary amplitude but the correct time scale.

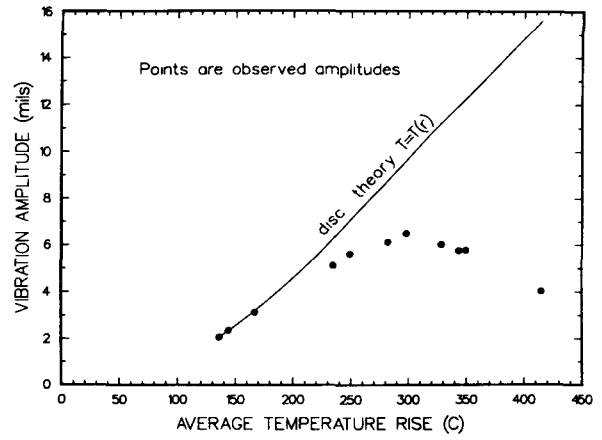

Fig. 5.
Fundamental (hoop) vibration amplitude, extrapolated to burst time (t=0) as obtained in least-squares fitting, plotted against plate-averaged burst temperature rise. The solid curve is drawn through the computed results for eleven data sets.

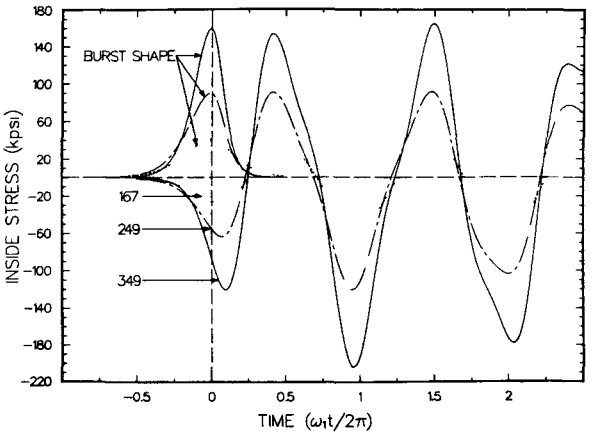

Fig. 6.
Computed inside stress versus time for three bursts. Associated burst shapes (arbitrary amplitude) employed in the computations are identified by the same line-type as sed for the stress curves. Bursts are identified by plate-average temperature rise.

Finally, we calculated peak tangential (hoop) stresses using the different approximations. These are displayed in Fig. 7 along with curves of yield strength for the fuel. Again, we have evidence of fuel failure above T_o ~ 190 C (inside temperature ~ 280 C) as inside compression clearly exceeds yield strength in that region.

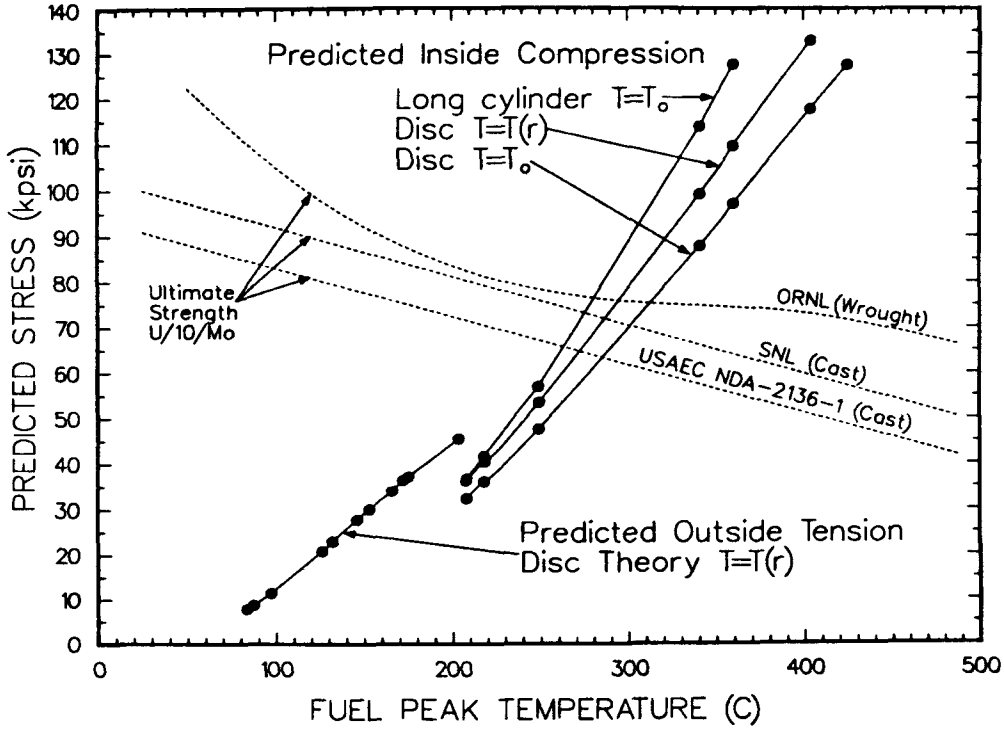

Fig. 7.
Maximum stress calculated from fundamental vibration mode plotted versus the peak temperature (outside or inside surface) attained in the burst excursion.

CONCLUSIONS

The two approximations employed should be considered extreme limits in predicting inside displacements for a fuel plate such as that for SPRII, where the ratio of outside diameter to plate thickness is ~ 6. Yet the crucial inside stresses predicted using those approximations are in general agreement. Of course, the outside stress is overpredicted by the infinite cylinder model but is of no importance since it never approaches yield.

The predicted vibration frequency for the overriding fundamental (first harmonic) is ~ 6680 Hz for the disc model and ~ 8030 Hz for the infinite cylinder. Vibration frequency of data extrapolated to room temperature is ~ 6100 Hz depending on where in the 2-ms data interval it is observed. On this basis alone, the disc model is more attractive, and the 9% error could derive from coupling with mounting bolts, fuel penetrations, and/or the use of incorrect elastic moduli.

As a tool to be used in reactor design, the disc model is easy to use, particularly with the flat temperature assumption. No machine computation is necessary to evaluate peak stresses, only a knowledge of q_1 and the first harmonic terms for excitation amplitude (along with inside temperature rise).

DEFINITIONS

α = Reciprocal burst period
ρ = Fuel density (U/10/Mo)
ν = Poisson's ratio
β = Thermal expansion coefficient
T = $T(r,t)$ = Fuel temperature rise
T_o = Average temperature rise in fuel section
E = Young's Modulus
a = inside radius of fuel annulus
b = outside radius of fuel annulus
R = b/a
u = $u(r,t)$ = radial displacement component
u_1 = $u_1(r,t)$ = static displacement
u_2 = $u_2(r,t)$ = dynamic displacement
$J_1(z)$ = Bessel function of fist kind, first order
$J_o(a)$ = Bessel function of first kind, zero order
$N_1(z)$ = Bessel function of second kind, first order
$N_o(z)$ = Bessel function of second kind, zero order
ω_m = Angular vibration frequency of harmonic m
q_m = $\omega_m/\alpha \rightarrow \omega_m \Delta t/3.52$
z_a = $k_m a$
z_b = Rz_a
Δt = burst duration at half-maximum

REFERENCES

1. G. E. Hansen, "Burst Characteristics Associated with the Slow Assembly of Fissionable Materials," Los Alamos National Laboratory report LA-1441, July (1952).

2. D. Burgreen, "Thermoelastic Dynamics of Rods, Thin Shells, and Solid Spheres," Nucl. Sci. Eng., 12, 203-217 (1962).

3. J. A. Reuscher, "Thermomechanical Analysis of Fast Burst Reactors," Fast Burst Reactors, CONF-690102 (1969), pp. 51-74.

4. J. A. Reuscher, "Analysis of Internal Heating Shock Effects in Reactor Fuel Components," Nucl. Eng. and Design, 18, 213-251 (1972).

Monte Carlo Determination of the Energy-Dependent Neutron-Gamma Flux Behind Cadmium Loaded Polyethylene Slabs Irradiated by the Sandia Pulse Reactor III

R. F. Sartor, R. T. Perry, and T. A. Parish

The Sandia Pulse Reactor III is the third generation of a series of bare fast reactors that are designed, constructed and operated by Sandia National Laboratories. Figure 1 illustrates the cutaway view of the SPR-III. One of the uses of the Sandia Pulse Reactor III is the production of a neutron-gamma irradiation field for testing of the resistance of electronic components to radiation damage. Although there is a reactor cavity for radiation effect tests on small items, this study is concerned with larger items that do not fit within the cavity and instead are tested in the SPR-III leakage field. Some component tests require a lower neutron to gamma dose ratio than directly available from the reactor. In these cases, there is a need to (1) shield the test components from the neutron flux of the reactor and (2) increase the incident gamma-ray flux. Presently, cadmium loaded polyethylene slabs are used as shields to modify the neutron to gamma dose ratio. Figure 2 illustrates a typical experimental configuration. The primary goal of this research is to develop a calculational model for predicting the energy-dependent neutron-gamma flux behind a cadmium loaded polyethylene shield when subjected to irradiation by the Sandia Pulse Reactor III. The secondary goal is to develop calculated results that can be used to predict energy-dependent neutron-gamma flux behind shields with different thicknesses, different cadmium loadings within the polyethylene, and various detector locations.

The cadmium loaded polyethylene slabs used to tailor the neutron-gamma dose ratio consist of cadmium oxide homogeneously mixed in polyethylene. Cadmium has a large radiative capture cross section for thermal neutrons making cadmium a gamma source when in a thermal neutron flux. Since the Sandia Pulse Reactor III emits a fast neutron spectrum, the polyethylene is useful as a moderating material to slow the fast neutrons down to thermal energies.

Prior to the calculational methodology presented here, the neutron spectrum and gamma dose behind the shields could only be experimentally measured. Shield configurations would be experimentally tested and adjusted in an iterative fashion until the particular test requirements were fulfilled. A calculational method was needed to allow an experimenter to accurately test and select a shield configuration without excessive experimental determination of the neutron-gamma flux behind the shield.

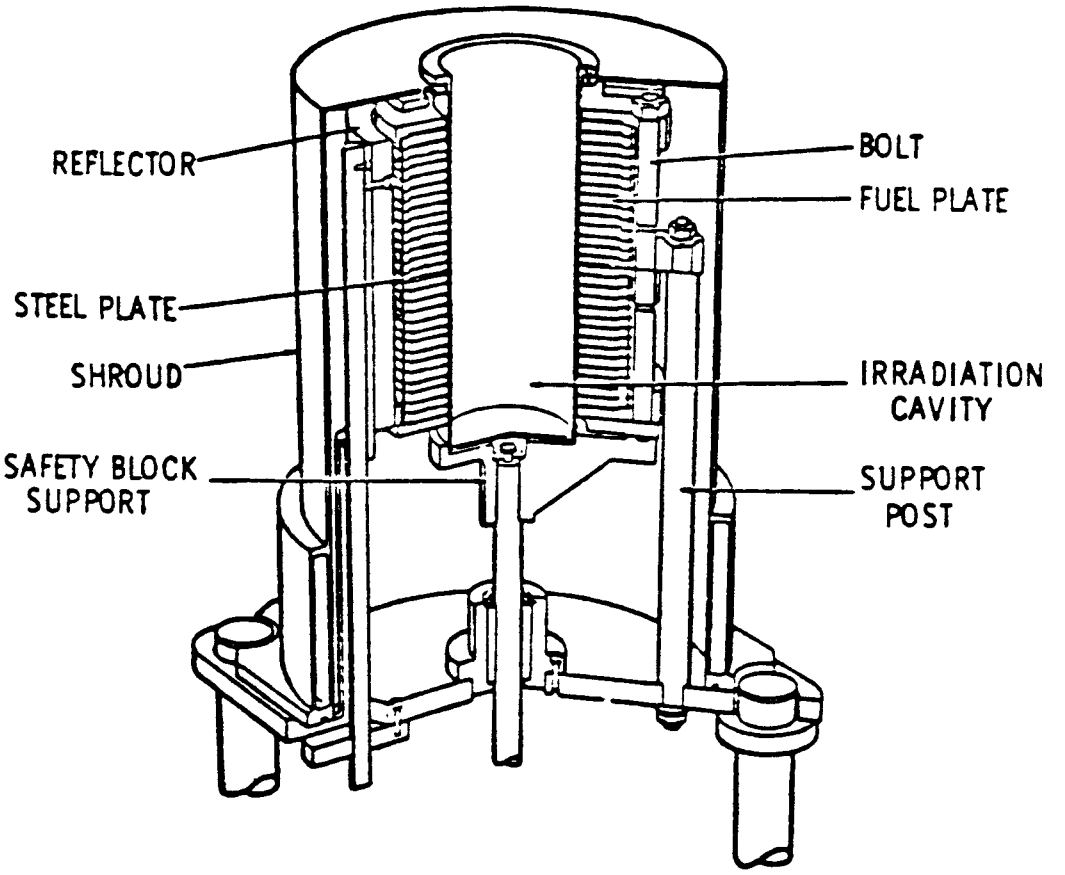

From Berry F. Estes & Jon A. Reuscher, Results of the Initial Test Program for the Sandia Pulsed Reactor III (SPR III), Sandia Laboratories, 1976

Figure 1. Cutaway View of the Sandia Pulse Reactor III

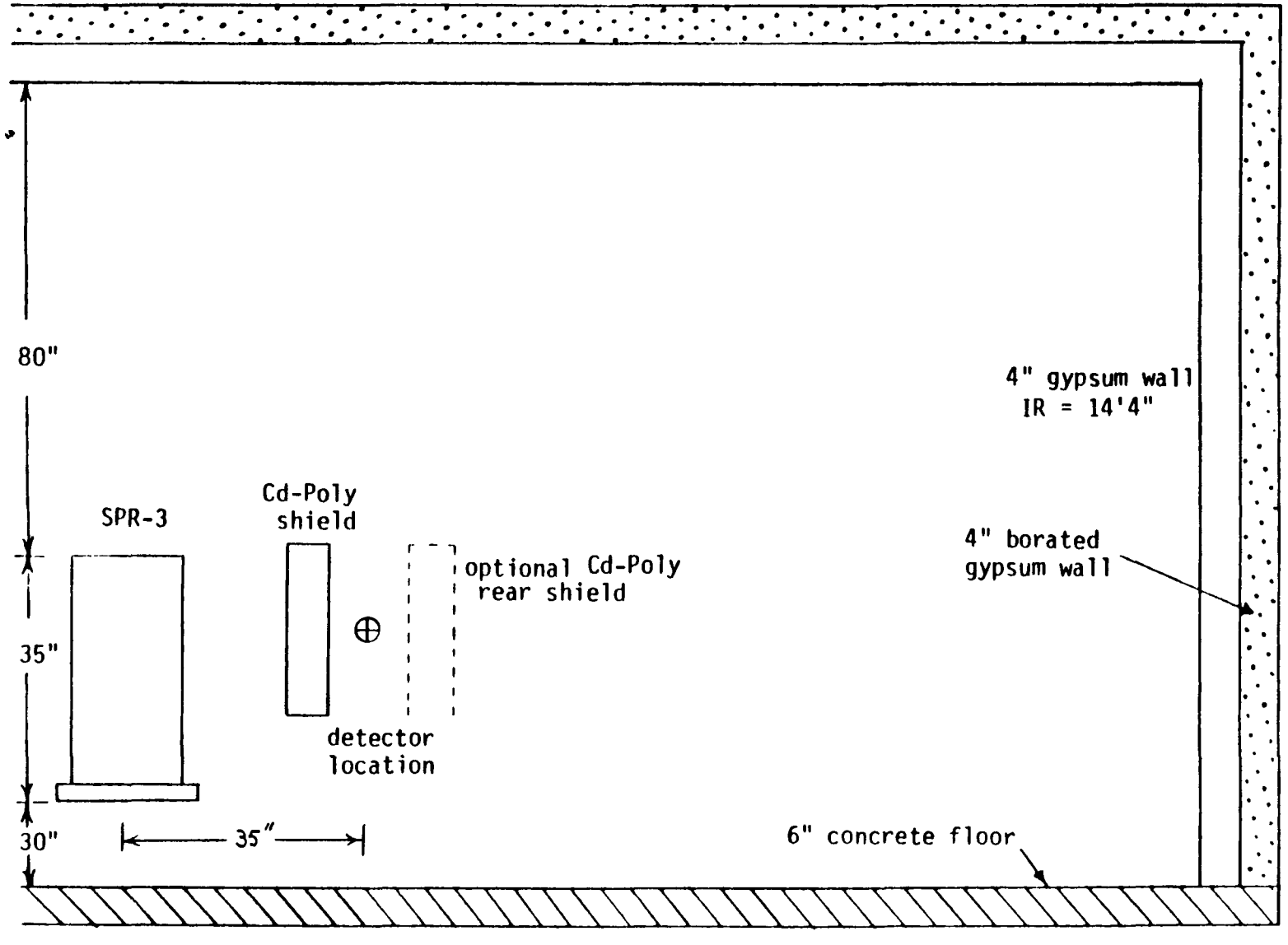

Figure 2. Sandia Pulse Reactor III and Cd-Poly Slab Geometry

In order to develop a calculational model, the Monte Carlo method was selected for determining the neutron-gamma spectrum behind the cadmium loaded polyethylene slabs. The Monte Carlo method was chosen because of the difficulty of the problem, including (1) the complex geometry of the reactor and test area, (2) the presence of both neutrons and gamma rays, (3) particle scatterings from the room wall, and (4) neutron thermalization and gamma production within the cadmium loaded polyethylene. To implement the Monte Carlo analysis of this problem, the MORSE-SGC (Multigroup Oak Ridge Stochastic Experiment--Super Grouped Constants) computer code was employed. MORSE-SGC is appropriate for this problem because it can (1) be used to model complex and arbitrary geometries in three dimensions and (2) calculate the energy-dependent neutron-gamma flux at a detector location. MORSE-SGC also has the advantage of using standard AMPX format multigroup cross section libraries.

Calculational results had not been previously obtained behind the cadmium loaded polyethylene shields because the gamma production cross sections for cadmium were not available in a coupled multigroup neutron-gamma cross section library. A library of cross sections for the materials used in the experimental configuration, including a cadmium cross section set, was prepared for this study at Los Alamos National Laboratory. This library was called RTP35. The RTP35 library was prepared from the MATXS6 library at LANL using the TRANSX-CTR code. The MATXS6 library is an 80 neutron and 24 gamma group library developed for fast reactor analysis from ENDF/B-V. The gamma production cross sections for cadmium were developed from the Livermore Library for inclusion in RTP35.

Two benchmark cases were computed to compare calculational results against experimental results. The first benchmark was a free field measurement, that is only the reactor and experimental area was described in the input geometry, and there was no shield present in this problem (see Figure 2). The detector was placed 17 inches from the reactor centerline. The calculational and experimental results for this case are presented in Table 1.

Table 1

Comparison of Calculated and Measured Parameters of SPR-3 Leakage Field at 17" From Centerline

	Calculated	Measured
Total Neutron Fluence	2.41E+12	2.55E+12
Neutron Fluence above 10 keV	2.34E+12	2.51E+12
Neutron Fluence above 3 MeV	3.02E+11	3.31E+11
Gamma Dose (rads Si)	408	524

The agreement between the experiment and the MORSE calculation is reasonable and generally supportive of the cross section library for the reactor and room materials and the geometrical model employed.

The second benchmark problem includes a representative cadmium-polyethylene shield as illustrated in Figure 3. Figures 4 and 5 show the multigroup neutron and gamma flux as calculated using MORSE-SGC. Since the fluxes are dependent on the reactor energy release, the flux units are normalized to per megajoule of reactor energy. The calculated and experimental results, as presented in Table 2, show some discrepancies. The calculated total neutron fluence is 69 percent larger than the measured value while the calculated neutron fluences above neutron energies of 10 keV and 3 MeV are both approximately 20 percent lower than the measured values. The calculated gamma dose is 56 percent lower than the experimentally measured value. The gamma dose is based on silicon at the detector location. This indicates the necessity of further evaluation and refinement of the computer model and the cadmium cross section set used in this study.

Table 2

Comparison of Calculated and Measured Parameters of A Representative Cd-Poly Shield Configuration

	Calculated	Measured
Total Neutron Fluence	9.74E+11	5.77E+11
Neutron Fluence above 10 keV	2.98E+11	3.60E+11
Neutron Fluence above 3 MeV	3.28E+10	4.23E+10
Gamma Dose (rads Si)	147	337

Calculations were also performed for several shield configurations for which experimental results were not available for comparison. These calculations included variations as follows: (1) the thickness of a five weight percent cadmium loaded polyethylene shield was varied; (2) rear shields were added in some cases; (3) the cadmium loading was changed in a four-inch-thick shield; (4) the spectra and doses behind inhomogeneous polyethylene and cadmium shields were studied; and (5) the distance between the detector and shield was varied. From these results several items of interest were determined. As would be expected, increasing the shield thickness increases the neutron shielding. It was found that the gamma dose reaches a maximum level for five weight percent cadmium loaded polyethylene shields at a thickness of six inches. The second item is that the use of rear shields, at test locations near the reactor, did not significantly affect the neutron-gamma spectrum. This indicates the amount of radiation reflected from the

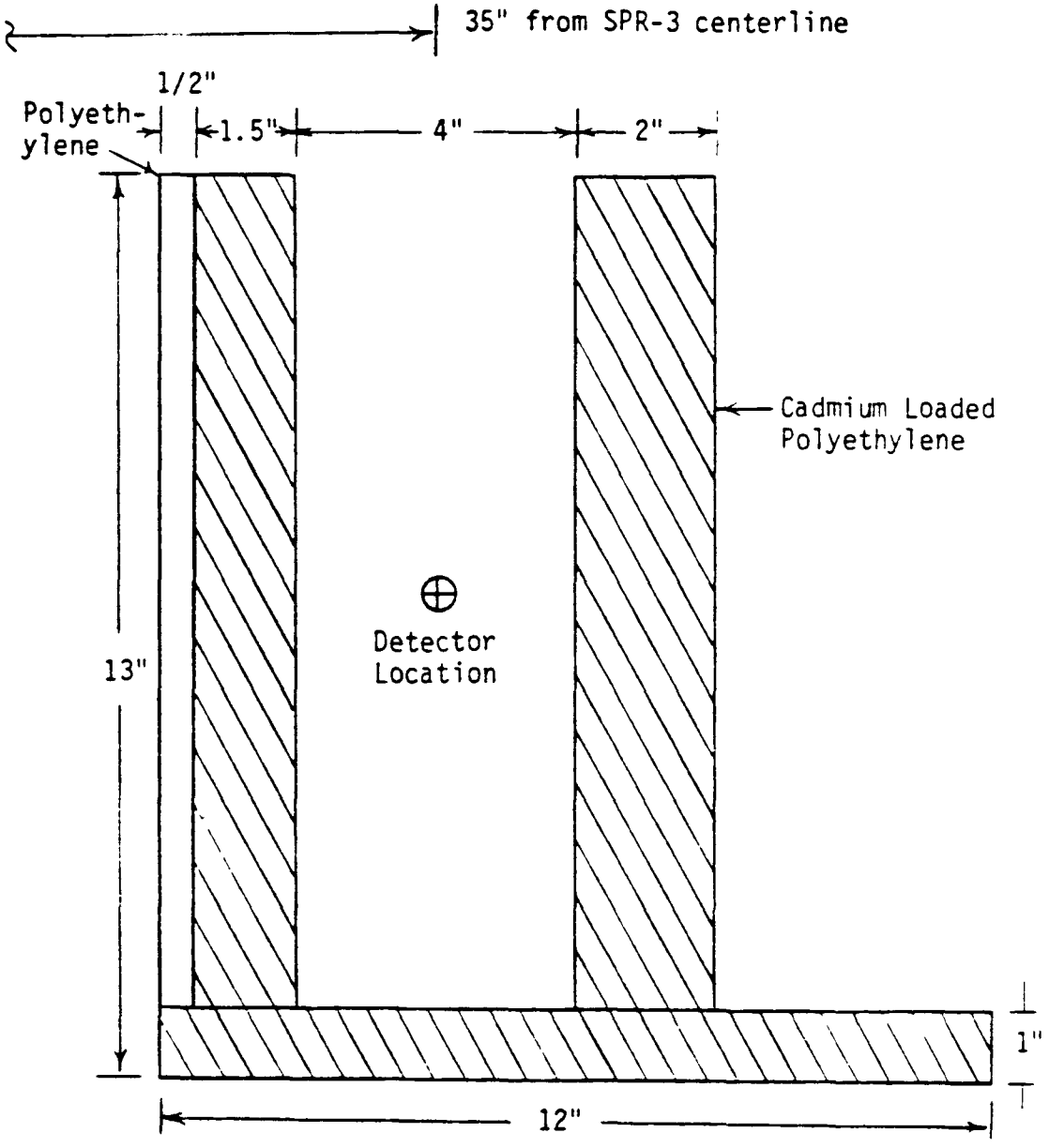

Figure 3. Shield Configuration for Benchmark Case Two

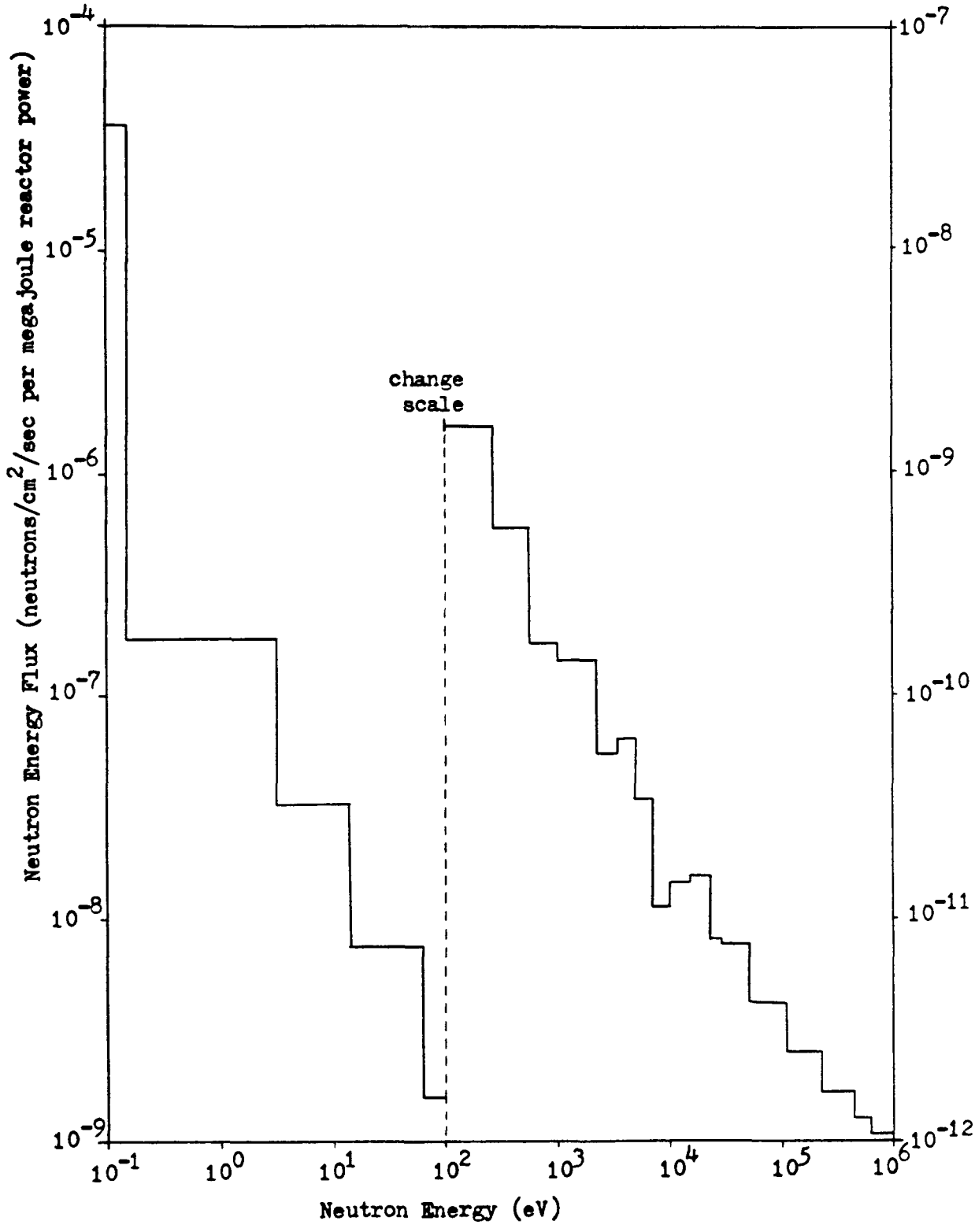

Figure 4. Neutron Flux Behind A Representative Cd-Poly Shield

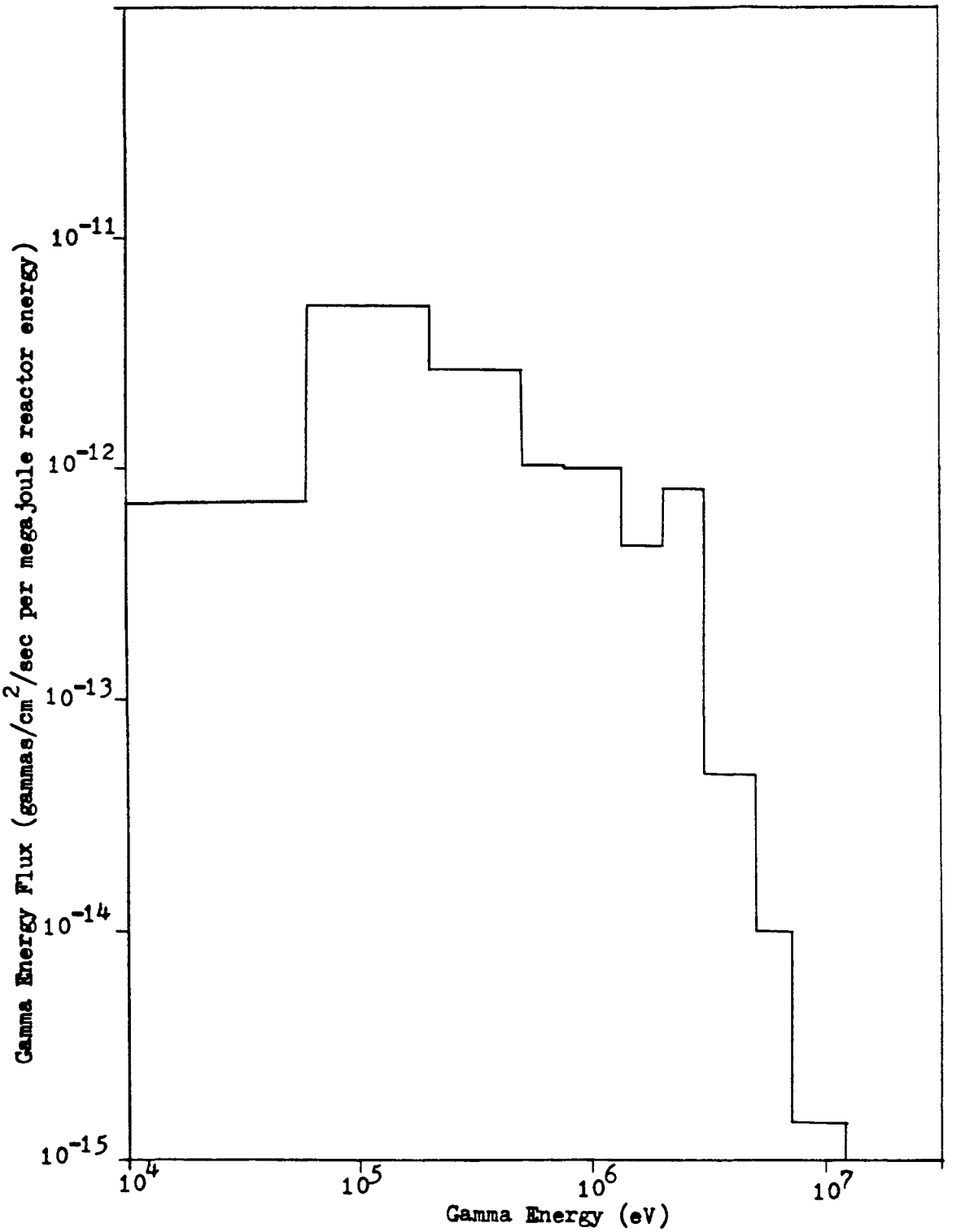

Figure 5. Gamma Flux Behind A Representative Cd-Poly Shield

room structure is insignificant in comparison to the "direct shine" from the reactor. The third item of interest is that, for a fixed geometry, variation of the loading of cadmium in the polyethylene shows a general trend of more neutron shielding and neutron-to-gamma conversion with increases of cadmium loading below five weight percent cadmium. It was also seen that the performance of layered polyethylene and cadmium slabs (with the cadmium side facing the test or detector location) did not greatly differ from the homogeneous cadmium-polyethylene shields. This indicates that for the homogeneous cadmium-polyethylene shields currently being used there is probably a corresponding inhomogeneous shield that will provide the same radiation field. Furthermore, for the layered shields there was no significant difference in the neutron-to-gamma ratio for shields using 1/32 inches of cadmium or shields with 1/64 inches of cadmium. The last point is that variation of the detector location between one-half inch and four inches behind the shield showed little variation in the neutron fluences and kerma, but the gamma dose decreased significantly with increasing distance from the shield.

Further research must be done to eliminate the discrepancies that exist in the second benchmark case. Although the computer model includes radiative capture, the predicted amount of gamma radiation released is probably too low. Also the calculational method for determining the total neutron fluence must be improved to better predict the value that was measured. Unfortunately, there is the possibility that errors exist within the cross section library, RTP35, which was specifically made for and first used in this research. Of significance to further research, is the recently released VITAMIN-E library, which also contains a coupled neutron-gamma cross section set for cadmium. The VITAMIN-E library should be used to repeat the calculations of the benchmark problems and compare these results with the previously calculated and measured results.

References

Raymond F. Sartor, Monte Carlo Determination of the Neutron-Gamma Spectrum Behind Cadmium Loaded Polyethylene Slabs Irradiated by the Sandia Pulse Reactor III, Thesis, Texas A&M Univ., College Sta., TX, May, 1986.

Berry F. Estes & Jon A. Reuscher, Results of the Initial Test Program for the Sandia Pulsed Reactor III (SPR III), Sandia Laboratories, 1976.

R. E. MacFarlene, TRANSX-CTR: A Code for Interfacing MATXS Cross-Section Libraries to Nuclear Transport Codes for Fusion Systems Analysis, LA-9863-MS, 1984.

CURRENT STATUS OF THE SKUA BURST ASSEMBLY MACHINE

E. A. Plassmann and T. F. Wimett
Los Alamos National Laboratory, MS J562,
Los Alamos, NM 87545

ABSTRACT

The design philosophy for the SKUA Burst Assembly Machine, being developed at Los Alamos, is reviewed along with results of supporting calculations. Several novel applications are also discussed to show the unique capabilities available.

HISTORY

The original concept for the SKUA assembly was proposed more than ten years ago. The earliest reference to it in the Los Alamos Critical Experiments Facility (LACEF) progress reports is September 1975, where the design of the assembly is already fairly well established. SKUA is the sixth fast burst assembly (Table I) to be developed at Los Alamos.

TABLE I
LACEF BURST ASSEMBLIES

1951	Lady Godiva (spherical)	World's first burst assembly
June 1957	Godiva II (cylindrical)	
Dec. 1959	Godiva III	Converted to SPR-II at Sandia
Nov. 1963	Moly G (10% Mo-alloy)	To White Sands-WSFBR
Feb. 1967	Godiva IV (1.5% Mo-alloy)	Shortest burst and highest peak power
May 1978	SKUA	Flux enhancement

The SKUA assembly was intended to vaporize a thin U(93) foil for study of the resulting infra-red spectrum. This

program was terminated before the design was completed, but construction continued because there was sufficient interest in possible future experiments.

Delayed critical was first achieved with the SKUA assembly in May 1978. Experiments relating to basic design considerations, control element reactivity calibrations, and central flux trap worth evaluations continued until March 1980 at which time further work on the assembly was postponed while the Safety Analysis Report (SAR) supplement for burst operation was in the approval process. Although final approval of the SAR was obtained, the mechanical and control modification necessary for burst operation have not yet been made. After these few past years of inactivity we are now again proceeding toward SKUA burst operation.

DESIGN CONSIDERATIONS AND MEASUREMENTS

Schematic diagrams of SKUA design show a top view (Fig. 1) and a cross-sectional side view (Fig. 2) of the assembly. The fuel is enriched uranium, U(93), alloyed with 1.5% molybdenum in the form of a hollow right circular cylinder

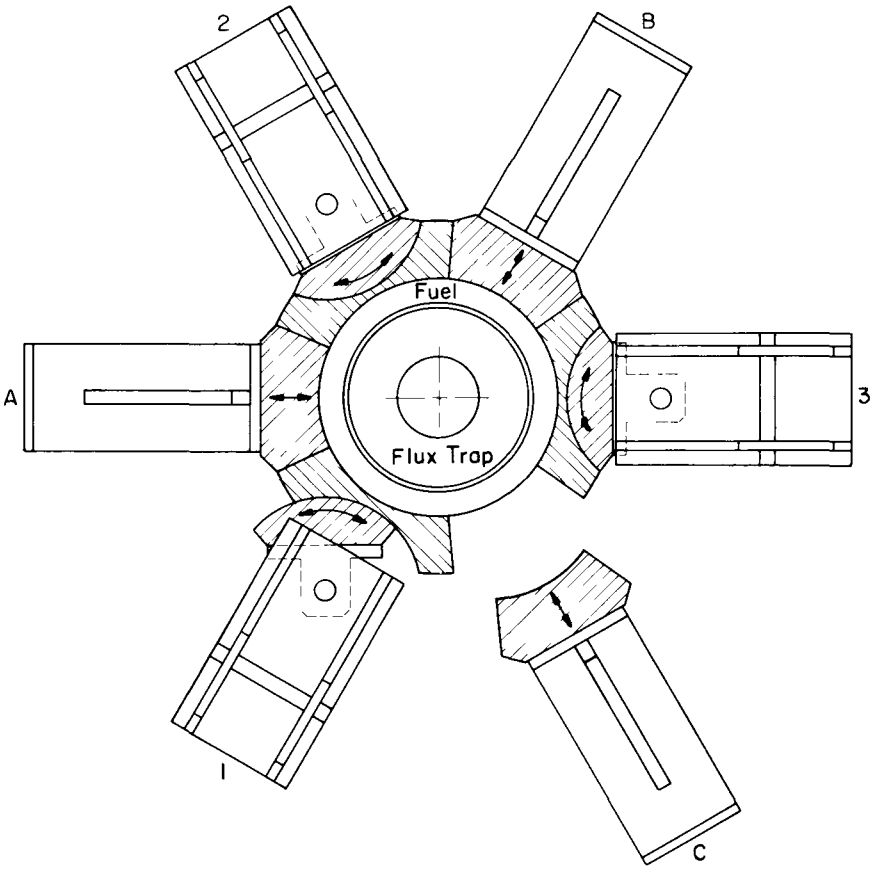

Fig. 1. Top schematic view of the SKUA assembly.

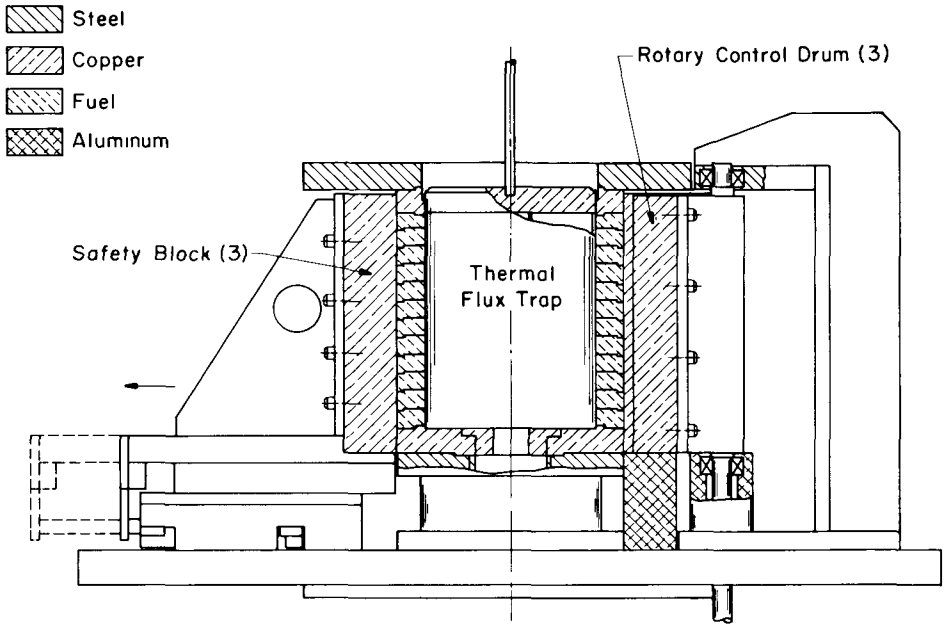

Fig. 2. Cross sectional schematic view of the SKUA assembly.

made up of a stack of twelve annular rings. This fuel stack is 30.5-cm (12-in.) high, with nominal 24.1 cm (9.5 in.) and 31.8 cm (12.5 in.) inside and outside diameters, and weighs 188 kg. All the fuel rings are clad with aluminum by an intermetallic ion-plating process to minimize UO_2 contamination during burst operation.

Reactivity control is achieved with copper reflectors. This eliminates penetration holes in the fuel rings which would structurally weaken them. Three copper segments that move by hydraulic actuators in the radial direction provide the independent major shutdown or SCRAM mechanisms. Total shutdown provided by these three safety blocks is measured as 9.9$. There are also three rotary control drums. Two of these are vernier control elements electrically driven with stepping motors to give precise positional readouts. The reactivity worth curve for each of these copper drums (Fig. 3) was obtained in a stepwise manner by adding reactivity with the drum being measured and then subsequently removing reactivity with the other identical drum. Thus, the resulting curve is influenced by interaction between the drums. There is remarkable linearity in the region from 10° to 60° where the differential worth is approximately 0.039$/degree.

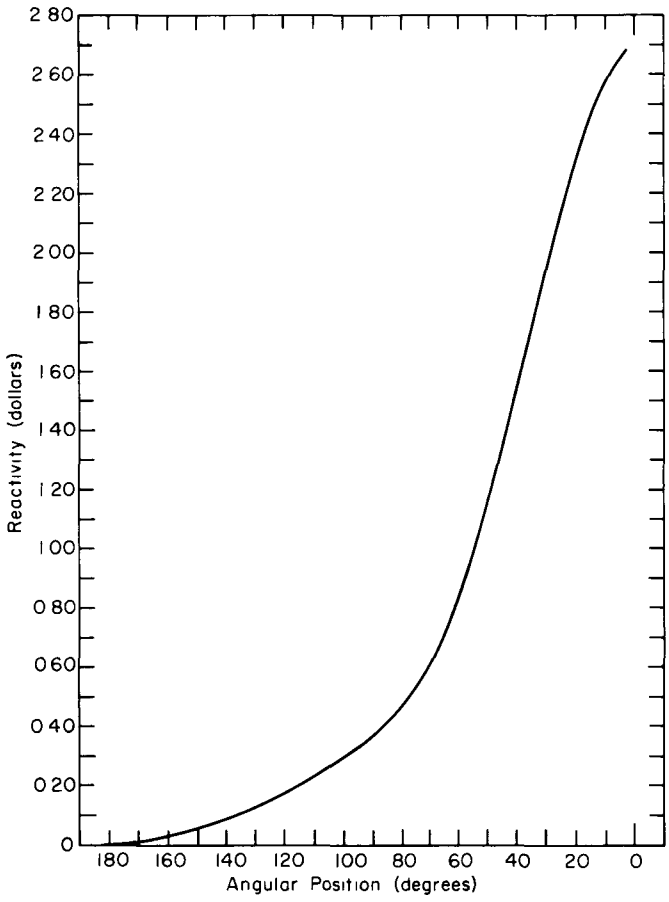

Fig. 3. Measured SKUA copper control drum curve.

The third rotary control element is the burst drum driven with a hydraulic system that rotates this heavy element into position within 0.15 s. This massive copper drum and associated steel support weighs 49 kg, so a special shock absorber system (Fig. 4) had to be designed. Optimum adjustment of these absorbers results in a burst drum insertion time of 0.10 s to within about three degrees of closure and another 0.05 s deceleration time to rotate that last three degrees. Because this final three degrees is worth only about two cents in reactivity, if a burst were initiated at any time during the deceleration, the yield would be reduced by less than five percent. The probability of preinitiation during the earlier part of the burst drum stroke is computed as less than 1.4% which is quite acceptable. The reactivity insertion rate for this element is nearly 15 $/sec, almost as fast as that for the Godiva-IV burst rod.

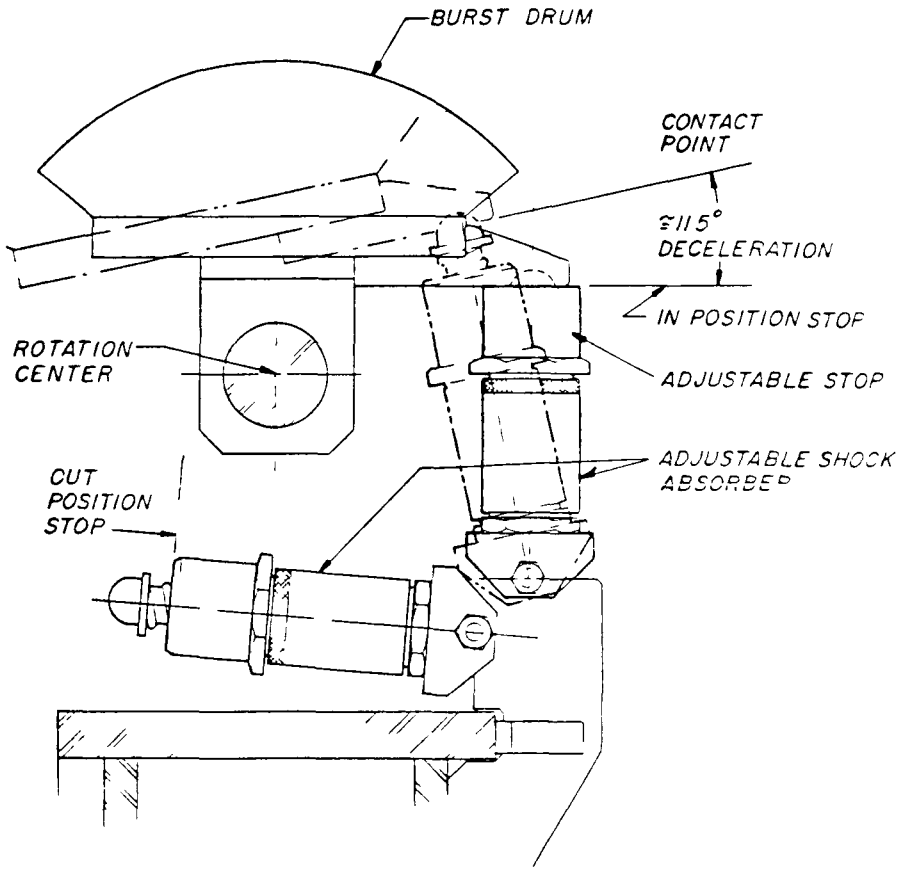

Fig. 4. Shock absorber system for SKUA burst drum.

The central flux trap (Fig. 5) is intended to be essentially neutral in reactivity contribution when it is inserted into the SKUA core. This is true when using $ZrH_{1.8}$ in the system; it actually adds 0.3$ in reactivity. When substituting an equal volume of polyethylene, the flux trap acts as a poison of about 6.4$. The use of zirconium hydride as a moderator has the advantage of higher temperature stability compared with polyethylene which is commonly used for this purpose. However, fabrication difficulties make it impossible to approach the theoretical hydrogen density which would be competitive with polyethylene. With the present dimensions, zirconium hydride is only about 50% as effective as polyethylene in producing uranium fission inside the flux trap. Using neutron transport calculations, we intend to optimize materials to achieve the design objective of zero reactivity worth for the flux trap as a whole. The central graphite liner thermally protects the moderating material from temperatures generated when uranium is melted or vaporized in the central cavity. The outer boral and cadmium sleeves prevent thermal neutrons from reflecting back into the enriched uranium fuel stack. The final uranium carbide sleeve is intended to act as a buffer

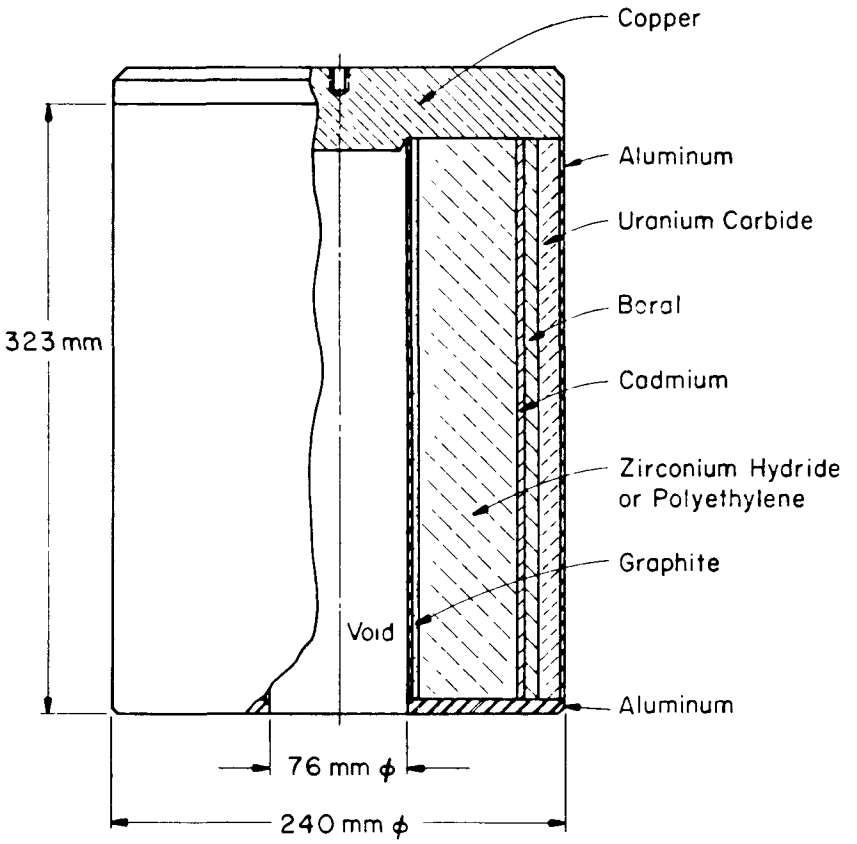

Fig. 5. SKUA central flux trap design.

to prevent fission peaking on the inside fuel surface. This carbide buffer may not be needed in the final design, thus allowing for more zirconium hydride or polyethylene moderating volume.

The high worth of 2.7$ for a rotary copper control drum and the large magnitude of flux or power tilting produced by the action of reflector controls are unexpected results. The cause of this tilting is a combination of high reflector worth and the decoupling effect of the large neutron moderator and poison in the flux trap. A direct measurement of the flux tilt by activating uranium-loaded aluminum wires wrapped around the inner and outer surfaces of a fuel ring shows an azimuthal maximum power ratio of almost 2.5 when a 70° segment of the copper reflector is removed. Flux tilt by the copper control drums alone results in a 17% increase in reactivity worth of one drum when another drum is withdrawn, and an additional 17% when the third drum is withdrawn. The total measured reactivity control for the three copper drums is 7.8$. We found that by substituting aluminum for copper in these drums, this total worth is reduced to 5.0$ which would still provide adequate control. This substitution has the added advantage of reducing the moment of inertia, and hence the required driving torque, for the

burst drum by a factor of three. Moreover, the azimuthal flux tilting effect would be minimized because with proper adjustment of the total excess available reactivity all the drums are essentially "in" or near maximum reactivity when a burst is generated.

APPLICATIONS

A comparison of SKUA and Godiva-IV burst characteristics (Table II) shows the estimated SKUA burst width more than an order of magnitude longer than that for Godiva IV. This assumes that the flux trap is inserted in the SKUA core. Without the flux trap, the burst width should be less than half this long. The 300°C temperature rise is close to the maximum for Godiva-IV; we have driven it to a 365°C rise but generally stay below 300°C. However, the temperature rise allowable for SKUA should be subject only to the phase change limitation that occurs at about 600°C.

TABLE II

COMPARISON OF BURST CHARACTERISTICS (ΔT = 300°C)

	Godiva IV	SKUA (estimated)
Burst Width (μs)	30	400
Joules/burst	1.8×10^{6}	5.4×10^{6}
Leakage Neutrons	8.9×10^{16}	2.67×10^{17}
Flux at 1 m (n/cm^2-s)	2.35×10^{16}	5.3×10^{15}
Central fluence (n/cm^2)	3.3×10^{14}	3.3×10^{14}
Central flux (n/cm^2-s)		
average	1.1×10^{19}	8×10^{17}
peak	2×10^{19}	1.5×10^{18}

SKUA can effectively be employed to vaporize various compounds which are enriched in ^{235}U. With a 100 g foil of U(93) at the center of the flux trap, possible energy depositions for a rather intense burst have been computed (Fig. 6) along with the resulting temperatures throughout the assembly. The 110°C temperature increase shown for Boral will be considerably reduced in the present design which employs a cadmium barrier inside the Boral. The thickness of central U(93) to be vaporized is 0.3 mm. Temperatures shown apply to the horizontal midplane of SKUA with a burst yield of 10 MJ and duration of 2 ms.

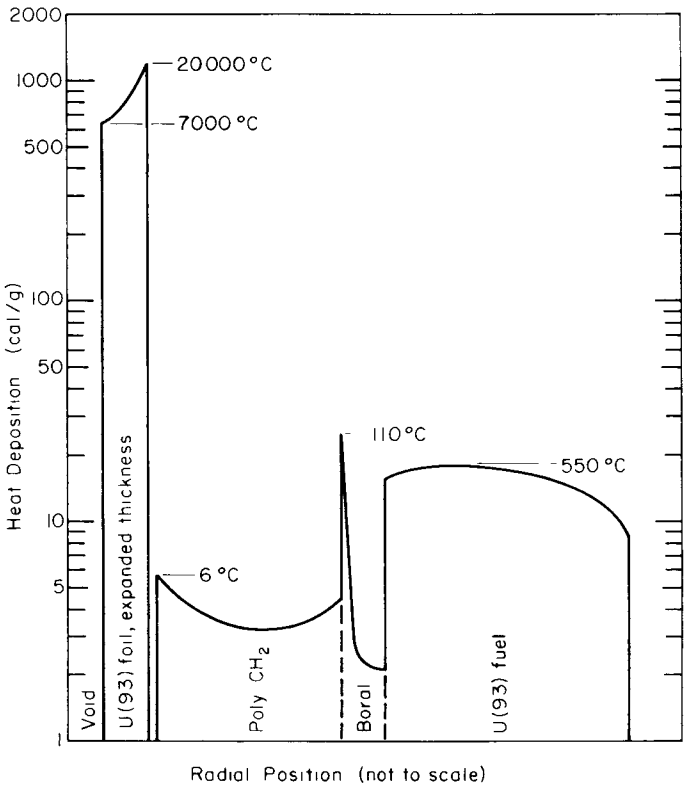

Fig. 6. Computer temperature profile at SKUA midplane for U(93) sample vaporization.

Results of burst kinetic analyses indicate that fissile samples placed inside the flux trap will significantly alter the burst behavior. For a given burst yield, or fuel temperature increase, the samples may effectively increase burst duration by an order of magnitude. For example, a moderate burst yield, which exhibits a duration of 313 μs measured at half maximum power with no sample, would be modified to a duration of at least 2.4 ms when a 0.011 mm thick U(93) foil weighing 15 g is placed inside the flux trap. Figure 7 illustrates the enormous sample perturbations of the period-reactivity relation. We have plotted the reciprocal reactor period, α, versus excess reactivity measured from "apparent" prompt critical which is defined as one dollar excess reactivity above delayed critical, where the dollar unit corresponds to the natural delayed neutron fraction for the uranium fuel. Because of an additional effective delayed neutron group associated with thermal fission in the sample, true prompt criticality actually occurs at higher values of excess reactivity. The thin foil sample, which adds about 1$ reactivity, also increases the

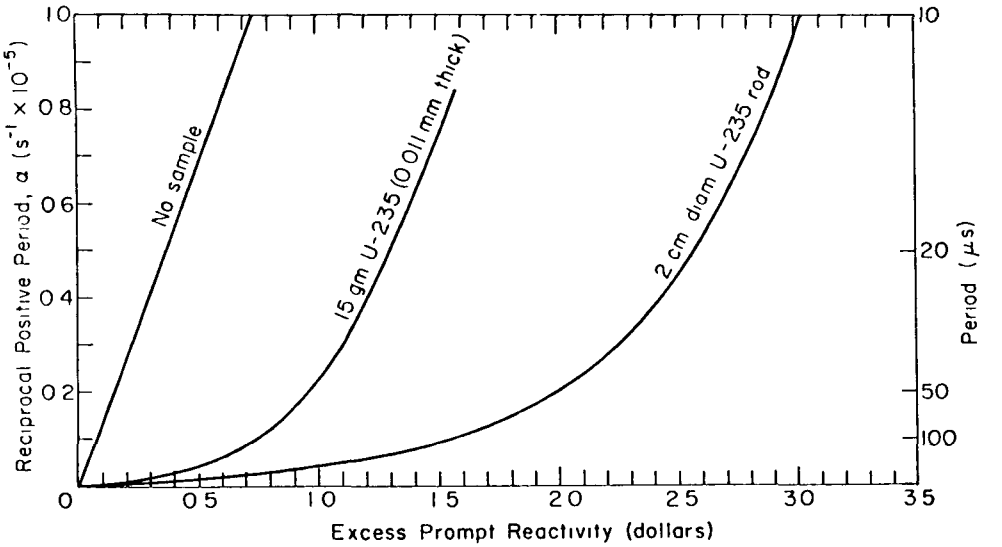

Fig. 7. Sample reactivity perturbations calculated for SKUA.

excess prompt reactivity needed to attain a 50 μs period by 0.8$. On the graph, we have also included a central uranium rod which adds 3$ reactivity at delayed critical and requires an 1.85$ increase in excess prompt reactivity for the same period. However, it will not be possible to attain periods this short with such a sample, because of excessive fuel temperature rise associated with the resulting bursts.

We also have the option of supplying intense bursts of fast neutrons in the large 9.5" diameter by 12" high cavity when the flux trap is removed. Operation under these conditions requires additional reactivity control. To better estimate assembly parameters with all or part of the flux trap removed, we made some neutron transport calculations that had the Boral, cadmium, and uranium carbide liners in place but added various thicknesses of the moderator annulus. Because of these thermal neutron absorbers, any neutron moderator inside the cavity was expected to behave as a reactivity poison. However, results of the calculations (Fig. 8) indicate that this isn't always the case. Clearly, the first 5 mm of polyethylene increases reactivity owing to simple scattering of fast neutrons. The 14$ increase in reactivity predicted for removal of the standard 46-mm thick moderator cannot be accommodated by the existing control rods. Our early critical experiments have shown that such reactivity adjustment is readily accomplished by merely replacing a selected fuel disk by one of normal uranium. The calculations also show (Fig. 9) the effect of polyethylene moderator in thermalizing the central neutron flux. The abundance of neutrons in the "thermal" group (below 0.1 eV) is plotted on a logarithhmic scale as a function of polyethylene thickness.

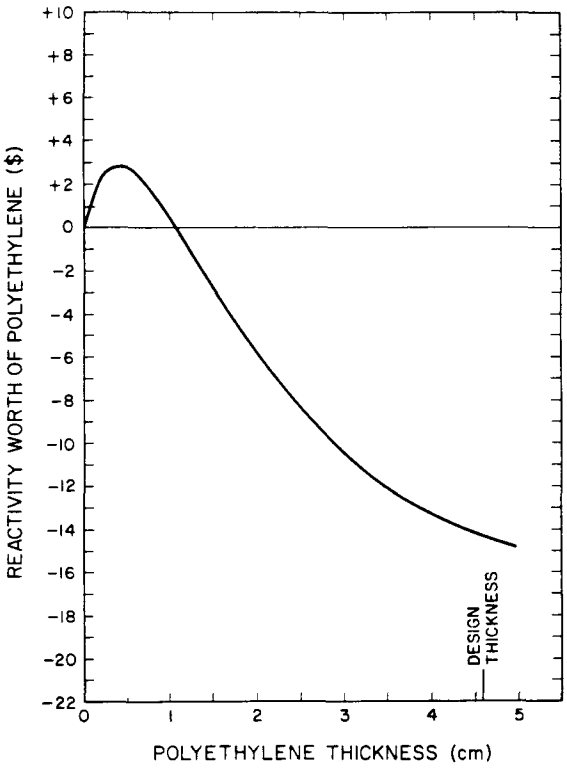

Fig. 8. Polyethylene effectiveness in SKUA flux trap.

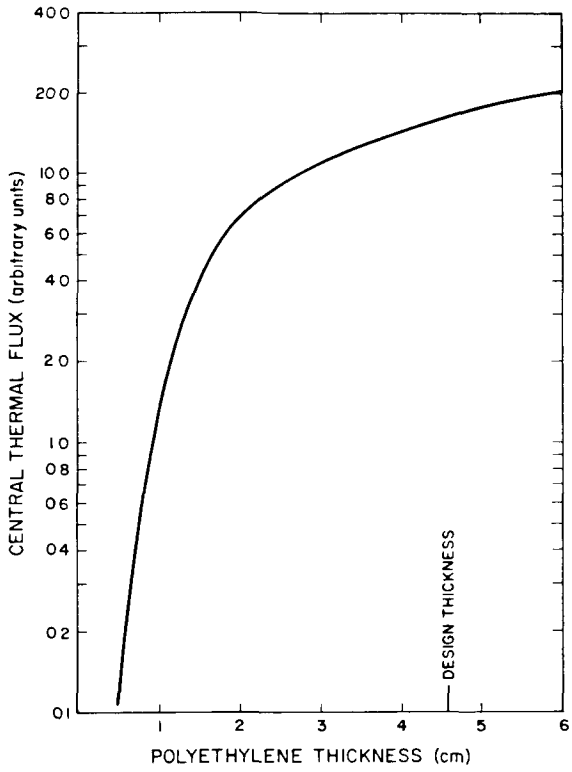

Fig. 9. Thermal neutron flux in SKUA cavity.

Another application of SKUA in a simulated core meltdown experiment was examined in support of a reactor safety study. The object is to melt several hundred grams of uranium carbide (UC) which would then drop into liquid sodium. We selected a thin (1-mm-thick) annular sample, 160 mm long and 110 mm in diameter with a mass of approximately 600 g. TWOTRAN calculations were used to optimize neutron moderation both in the (external) SKUA flux trap and inside the sample annulus. Zirconium was used to isolate the sample from the moderators. The calculated radial fission power distributions (Fig. 10) through different horizontal planes show some peaking at the ends of the sample. This is because the sample does not extend the full vertical length of the flux trap and implies that even longer samples could be considered. By comparing the radially averaged fission power at the coldest region in the sample to the maximum in SKUA central fuel plate, we find a factor of 20 gain in sample energy deposition per gram over that in the fuel hot spot. Radial temperature equilibrium in the sample will occur in approximately 0.1 s. Assuming 880 J/g to melt UC (at greater than 2800°C), we calculate a hot spot temperature rise of approximately 300°C in SKUA to melt the coldest part of the sample under burst conditions.

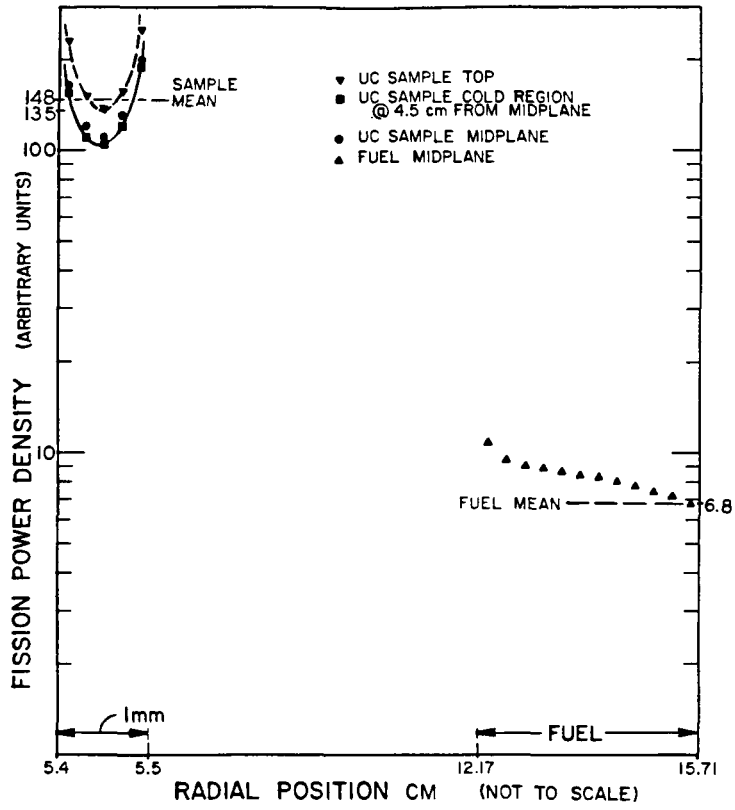

Fig. 10. Calculated radial fission power for SKUA with central UC sample.

Because thermal radiation will result in heat loss from the sample while it is dropping, we calculate that the yield must be increased by about 25%, to a burst of approximately 380°C temperature rise, to maintain sample melt during the experiment. This corresponds to approximately 2.5 x 10^{17} total fissions which is well within the capability of SKUA.

THE REACTOR-PUMPED LASER: KINETICS EFFECTS ON THE SPR III REACTOR*

Douglas M. Minnema
Reactor Applications Division
and
David A. McArthur
Reactor-Laser Systems Division
Sandia National Laboratories

ABSTRACT

The Sandia Pulsed Reactor III (SPR III) is being used as the pumping source for evaluation of energy deposition and laser physics in gas mixtures for reactor-pumped lasers. The test apparatus includes moderating and reflecting materials both near and in the glory hole, and occasionally, small quantities of uranium deposited on ceramic tubes in the glory hole. These materials significantly affect reactor behavior.

The most prominent change that occurs with moderating material in the glory hole is an increase in the effective neutron lifetime of the reactor, and a factor of 2 to 3 has been observed in these tests. This affects several aspects of the reactor's behavior: initial reactor period, pulse width, and yield versus initial reactivity insertion. The most significant effect occurs when small quantities of uranium (ranging from 0.4 grams to 6 grams U_3O_8) are included in the package. There is an apparent increase in lifetime up to a factor of 7 over the normal value, and a large change in the pulse symmetry. Investigation suggests that the moderating material and uranium behave as a pseudo delayed-neutron precursor with a delay time of about 1.6 milliseconds, and an apparent yield of 0.00017. This paper provides a detailed discussion of these observations.

1.0 INTRODUCTION

The Sandia Pulsed Reactor III (SPR III) is being used as a pumping source for evaluation of energy deposition and laser physics in gas mixtures for reactor-pumped lasers. This paper discusses the significant variations that this experiment

---

* This work performed at Sandia National Laboratories, which is operated for the U.S. Department of Energy under Contract number DE-AC04-76DP00789.

introduces in the reactor's neutron kinetics compared to its standard configuration.

This series is unique compared to experiments normally performed at the SPR Facility due to its complexity and the amount of reflecting and moderating material in and near the reactor core. The experiment includes large amounts of aluminum material surrounding the reactor, a thick aluminum plate just above the shroud, and large amounts of polyethylene in the glory hole (in some cases as much as 1.3 kilograms). In past studies, moderators and reflectors were usually placed external to the reactor, resulting in positive reactivity worths (Reference 1). In this experiment, the configurations tend to be strongly negative in worth, with minor exceptions. Measured worths ranged from $+0.58 to $-5.80 for various configurations.

The laser cell consists of a stainless steel pressure cell surrounded by cylinders of polyethylene and wrapped on the outside with boron loaded silastic. The polyethylene thickness can be varied in order to optimize the total energy deposition and deposition rate in the cell. The boron loaded silastic was intended to enhance the shroud's decoupler in reducing the thermal neutron scatter back into the reactor fuel region.

Two methods were used for converting the thermal neutrons into energy deposition in the cell. The first method uses a ceramic cylinder coated with fully enriched U_3O_8 within the cell. The high energy fission fragments deposit their energy locally within the gas. Early tests used U_3O_8 quantities of about 6 grams, but it was found that this amount created large kinetics problems for the reactor. Later it was determined that due to the thickness of the coating, self absorption of the fission products in the coating was significant, and the total U_3O_8 mass could be reduced by a factor of 2 without significant loss of energy deposition in the gas. The U_3O_8 mass can be reduced by another factor of 5 by pumping a smaller volume of laser gas. The second method is to mix Helium-3 gas with the laser gas being studied. The ^3He captures neutrons yielding protons and tritons that deposit their energy locally in the gas. In the later tests the ceramic cylinders became the main method for energy deposition, with quantities of about 0.4 grams of U_3O_8 for coatings.

2.0 INSTRUMENTATION

This report utilizes parameters that are routinely measured during a reactor pulse operation. The reactor periods are measured using fission chambers with Racal-Dana timer/counters. The timer/counters are programmed to measure the time interval for one exponential folding time of the reactor power level, providing a direct measure of the period. Trigger levels are set for the power range of about 50 to 200 watts, so there is negligible temperature feedback. The experiment's reactivity worth is based on a delayed critical run at 1 watt, and comparison of control rod positions with a standard free field value.

The pulse parameters are measured using 5.25" diameter Pilot B scintillators with photodiodes, feeding into the SPR Pulse

Analysis System. This computer controlled system records the pulse shape, fuel temperatures, and reactor assembly, generating a pulse data sheet for the experimenters and plotting the reactor assembly on the operations log sheet. A typical pulse data sheet is illustrated in Figure 1. The computer calculates several parameters of the pulse, primarily the trigger-to-peak time and Full Width at Half Maximum (FWHM), and performs a log-linear curve fit of the data between the 5% and 15% of peak levels to determine a reactor period. The program also calculates several values that monitor the pulse symmetry for comparison with theoretical and empirical standards. The integral of the Energy-to-Peak is ratioed with the total energy, the fall time from peak to 50% power is ratioed with the rise time from 50% to peak power, and the FWHM is ratioed with the reactor period. These ratios yield information as to the effect of experiments on the pulse compared with free field data.

3.0 EXPERIMENTAL CONFIGURATION

Since the start of the Falcon reactor-pumped laser program in August, 1984, over 200 pulse operations have been performed on 9 configurations. These configurations mainly involve changes in laser cell dimensions, polyethylene thicknesses, and neutron converters. Changes in gas mixtures and pressures were found to have negligible effects upon reactor kinetics except for the ^3He, which will be considered separately. Table 1 lists the 9 laser configurations that have been evaluated to the present time.

Table 1
Reactor-Pumped Laser Experiment Configurations

Data Set	Laser Cell OD(cm)	Laser Cell Content	Polyethylene Thickness(cm)	Polyethylene Mass(gm)
1	7.00	6gm U_3O_8	2.10	1921
2	7.00	6gm U_3O_8	1.04	840
3	7.00	6gm U_3O_8+50psia ^3He	1.04	840
4	7.00	50psia ^3He	2.10	1921
5	7.00	50psia ^3He	1.04-2.54	840-2436
6	3.60	50psia ^3He	1.60-3.30	869-2051
7	2.54	30-50psia ^3He	2.70-3.40	1422-2030
8	2.54	0.4gm U_3O_8	2.70-3.40	1422-2030
9	2.54	0.4gm U_3O_8	3.40	2030

Polyethylene length is 32 cm in all data sets.

4.0 EXPERIMENTAL RESULTS

The 9 configurations can be grouped into 3 categories for data evaluations: (1) variations in polyethylene thickness; (2) use of the ^3He gas; and (3) use of the U_3O_8 ceramic cylinders. This

SANDIA PULSED REACTOR PULSE ANALYSIS PROGRAM

Figure 1: Typical Standard Reactor Configuration Pulse Data Sheet.

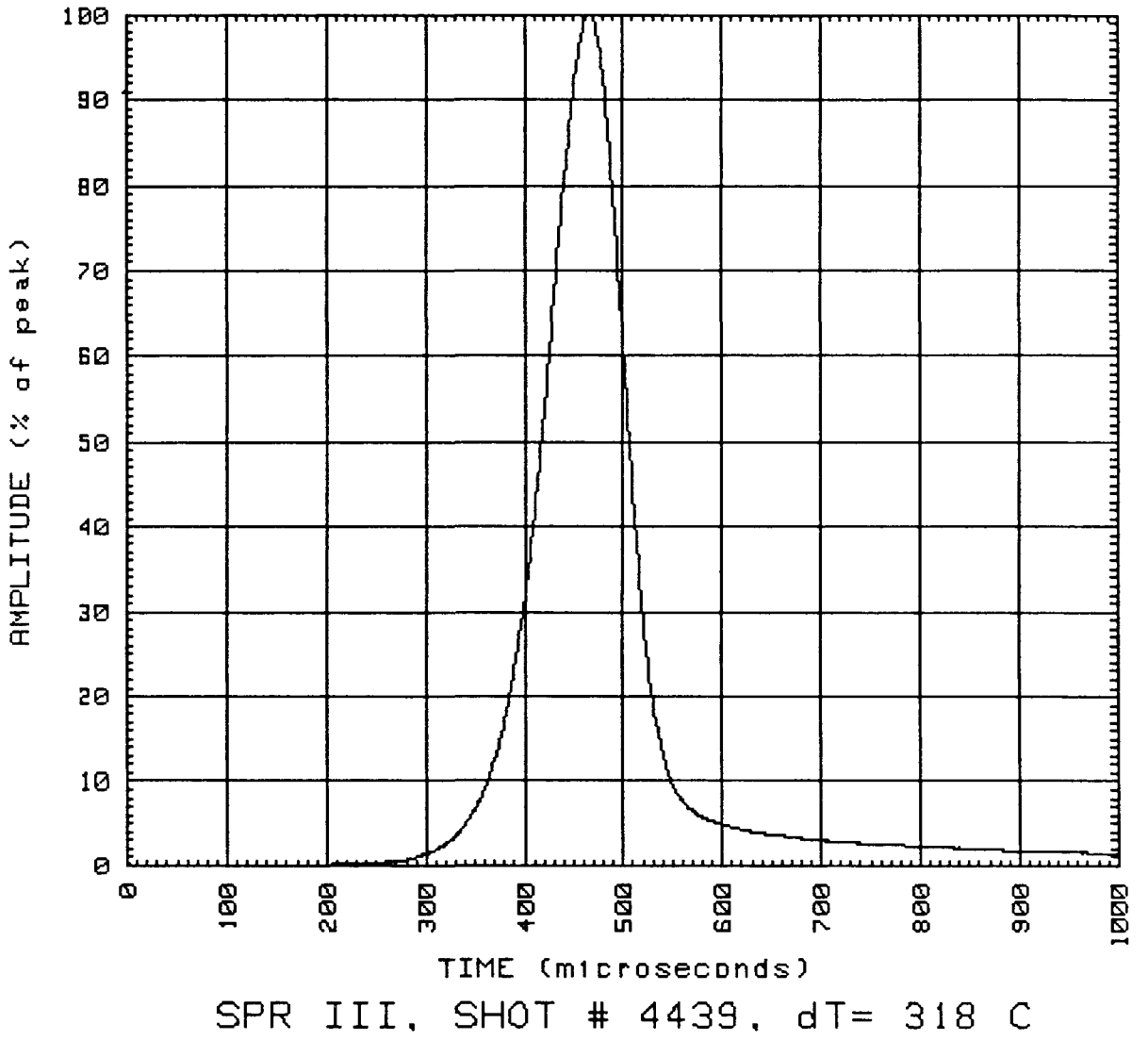

Shot time was 16:07:04 on April 2 1986
Upper Block midcore dT= 269 C

The source was the photodiode #3 detector.
Peak voltage = 12.3300 volts
Peak area = 1575.0 volt-microseconds
Ratio of Energy-to-Peak to Total Energy = .437

Trigger to peak time = 465.5 microseconds
Full width half maximum = 89.0 microseconds
Fall to Rise time ratio at FWHM = .854

Initial Period = 31.4 uS. +/- .3% (1 sigma)
FWHM to Period ratio = 2.84

evaluation is complicated by the fact that these categories can not be completely isolated from each other, since they occurred in conjunction with each other in the tests. However, contributions from each category can be evaluated by comparing results for different combinations.

In two cases the main kinetics change is the neutron lifetime of the reactor. This change reveals itself in several of the parameters: initial reactor period, trigger-to-peak time, FWHM, and reactor yield as a function of reactivity insertion. Since these all relate to each other through the lifetime, this is expected. The U_3O_8 ceramic cylinders create an additional variation that is more unexpected, a broadening of the reactor pulse that causes all of the symmetry parameters to deviate from their normal response.

4.1 Standard Reactor Parameters

Before discussing the experimental data, it is important to review the parameters of the SPR III reactor in a normal configuration. Figure 2 shows the yield, in temperature change, as a function of reactivity insertion. Nominally it requires a reactivity insertion of \$1.08 to reach a yield of about 300° C. When the reactivity insertion is plotted as a function of inverse reactor period, the slope yields a neutron lifetime of 15.7 nanoseconds (Figure 3).

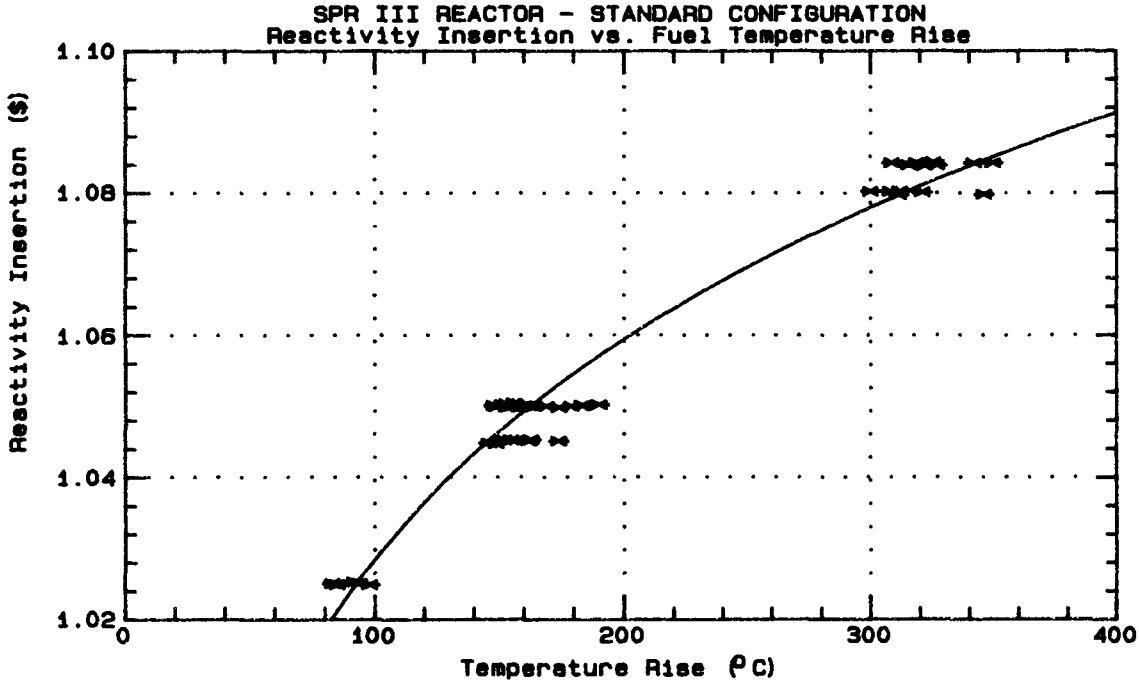

Figure 2: Reactor Yield in temperature rise as a function of Reactivity Insertion for the standard SPR III configuration.

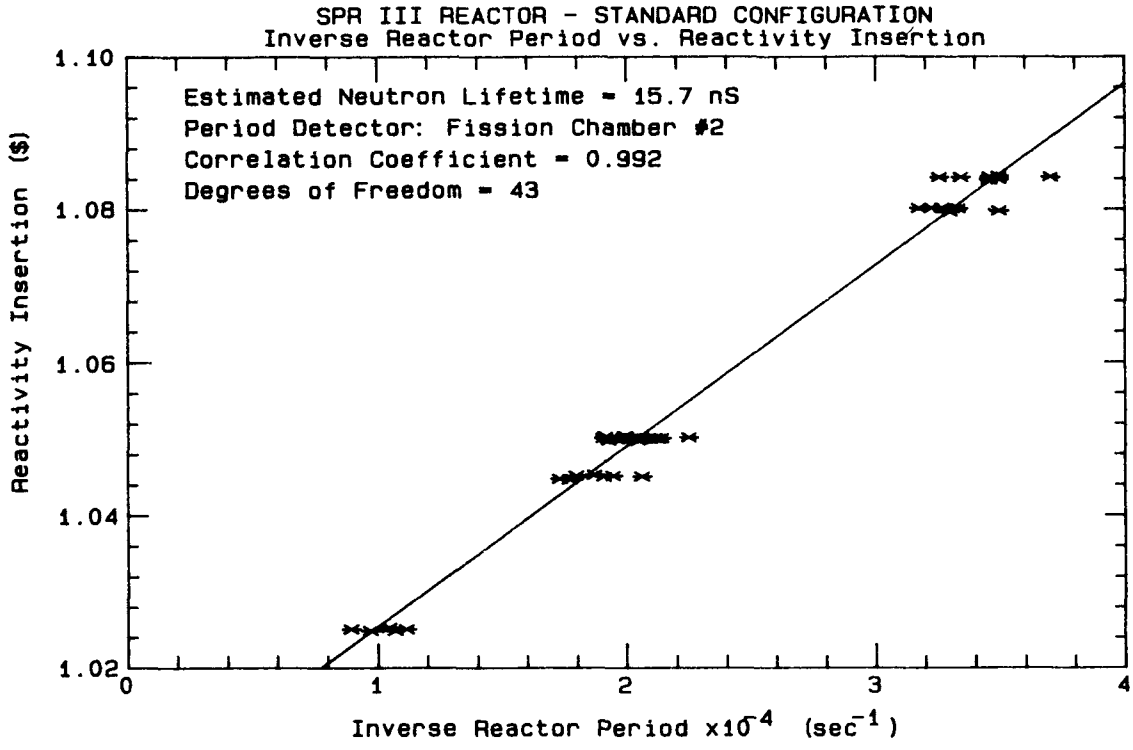

Figure 3: Reactivity Insertion as a function of Inverse Reactor Period for the standard SPR III configuration. The slope of the line yields the neutron lifetime.

4.2 Polyethylene Thickness

Polyethylene thicknesses were varied throughout the test series in attempts to maximize energy deposition in the cell while minimizing lifetime changes that reduce the energy deposition rate. Also, the cell diameter was varied in order to reduce the total mass of polyethylene while maintaining the thickness. The polyethylene length was 32 cm, totally within the glory hole. The fuel was 40.64 cm long, so the polyethylene did not extend the full length of the core; however, at the ends of the cell stainless steel flanges acted as axial reflectors.

In one series of tests, sealed cans were used for measuring pressure rise during the shots, rather than the full laser configuration. These cans contained either a 7.00 cm or a 3.8 cm diameter laser cell pressurized to about 48 psia of ^{3}He, and polyethylene sleaves ranging in thickness from 1.0 cm to 3.3 cm. These cans could be placed directly into the experiment tube and did not require the supporting structure of the other tests. These cells contained ^{3}He, but the gas pressure was constant, so the effects of the polyethylene changes could be evaluated directly for each cell diameter.

The reactivity worth of these sealed cans was a strong function of the polyethylene thickness. Figure 4 shows the experiment reactivity worth as a function of polyethylene thickness for both cell diameters. This suggests that the ^{3}He has negligible effects on the worth of the experiment.

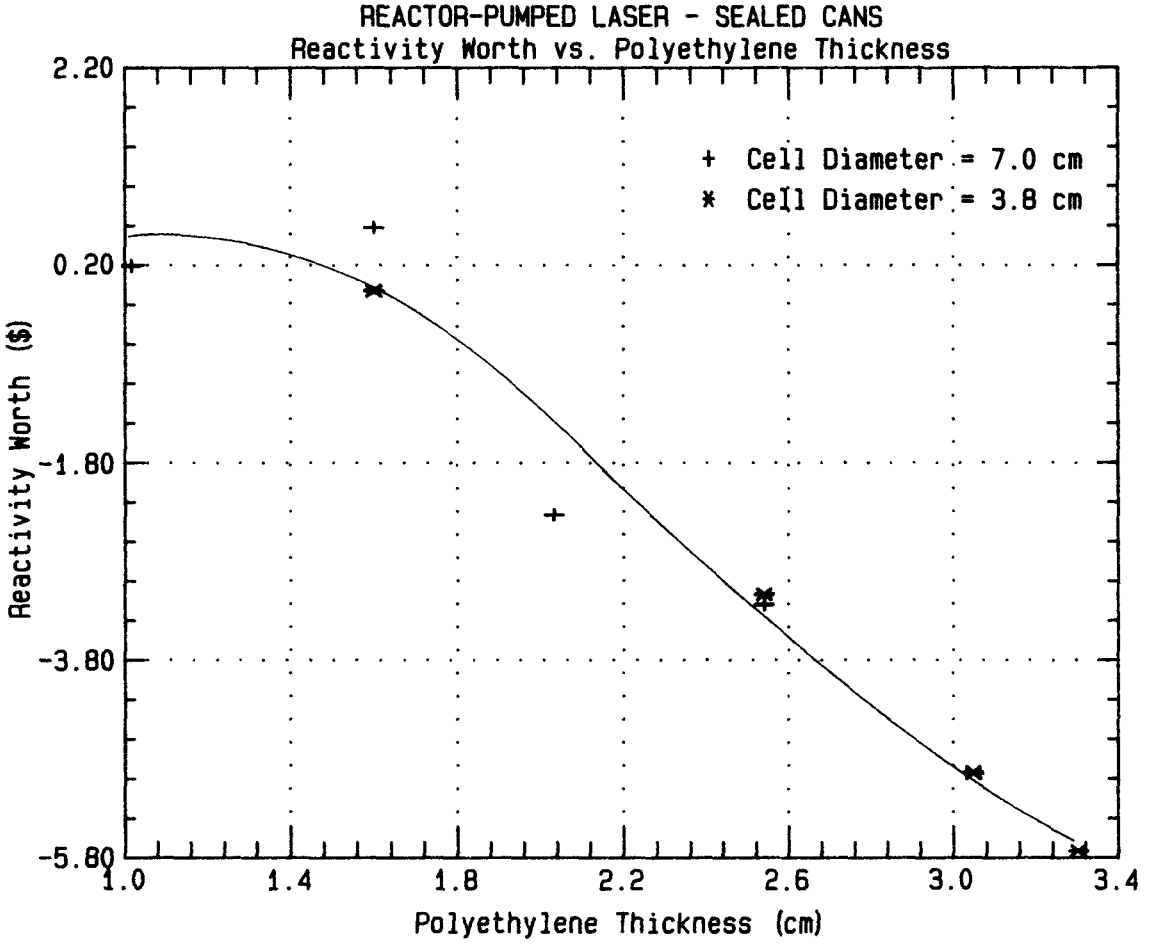

Figure 4: Experiment Reactivity Worth at delayed critical as a function of Polyethylene Thickness for two cell diameters.

Figure 5 shows the estimated neutron lifetime as a function of the polyethylene thickness for both cell diameters. This figure shows that both configurations have increased lifetimes from free field, however neither show any real dependence upon the thickness. This suggests an asymptotic effect on the lifetime, where the effect may occur with a small amount of polyethylene, and then after that no further increase is observed. The difference between the two cell diameters is probably due to geometrical considerations rather than the polyethylene thickness.

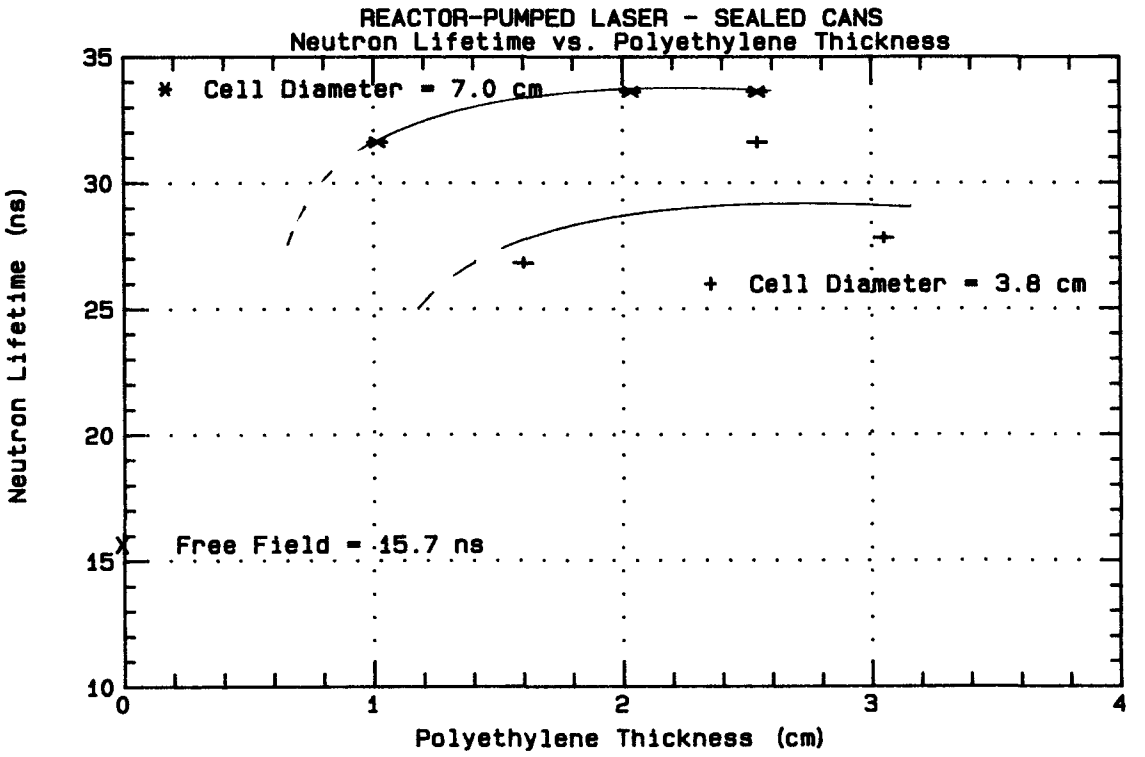

Figure 5: Estimated Neutron Lifetime as a function of Polyethylene Thickness for two cell diameters.

4.3 Helium-3 Neutron Converter

Helium-3 has a very high cross-section for thermal neutrons of about 5330 barns. Therefore, the gas could have a significant effect upon the neutron lifetime in the reactor. A review of the data shows that there appears to be an inverse dependence between the ^3He pressure and the reactor lifetime, however there are insufficient data to quantify this relationship. Comparison between a few comparable reactivity insertions with different pressures suggests that lifetime decreases with increasing ^3He pressures. This agrees with the theoretical definition of lifetime as inversely proportional to the macroscopic absorption cross-section (Reference 2).

The pressure of the ^3He has a minor effect upon the total worth of the package, as shown in figure 6. However, this function is significant in terms of reactivity insertion for a pulse, and so the reactor operators are required to monitor the pressure to insure that it does not change between the minipulse and the design pulse. Another example also illustrates the effect of ^3He on lifetime. In moving from data set 2 to 3 of table 1, the only difference is the addition of the ^3He. The next section discusses the results with U_3O_8 in detail, but it is notable that the addition of the ^3He forced the lifetime to change from 40 ns down to 30 ns, a very significant drop.

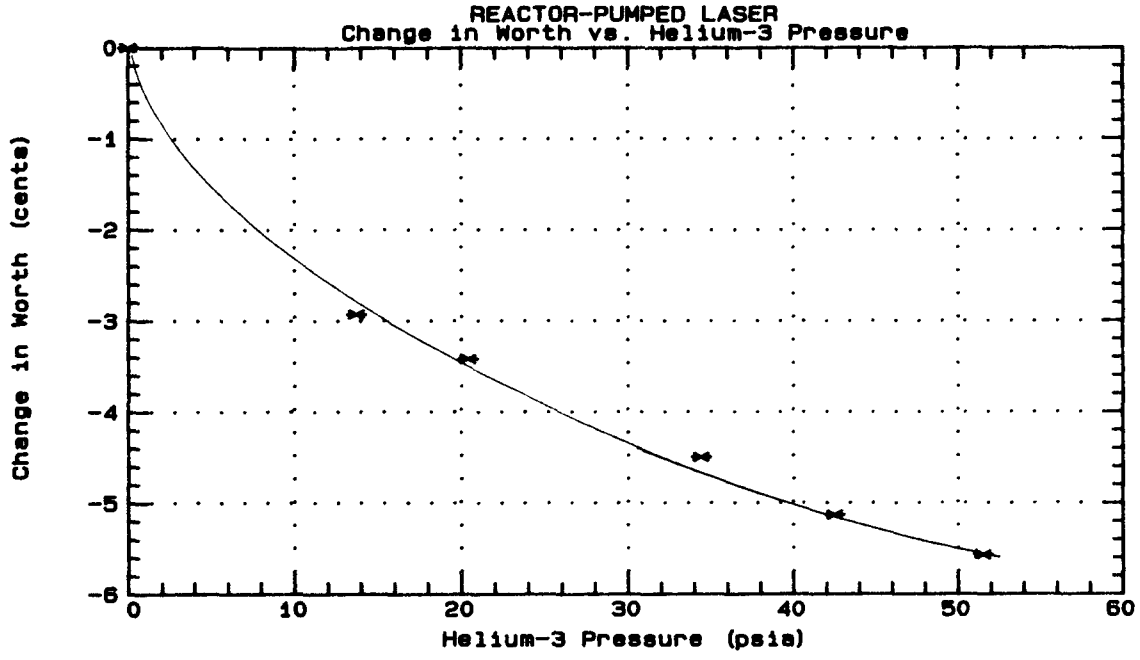

Figure 6: Change in Experiment Reactivity Worth as a function of the ^3He Pressure in the 7.0 cm diameter cell.

4.4 Uranium Oxide Neutron Converters

The first series of laser experiments included ceramic alumina cylinders coated with 6 gm of U_3O_8 for converting neutrons into energy deposition in the laser cell. This series provided the most confusion initially, since almost all of the pulse parameters varied drastically from expected values. Figure 7 shows the pulse data sheet for the highest yield delivered on the 6 gm cylinder. Note the broad pulse and the large tail contribution, especially compared to a standard pulse (Figure 1). The large tail causes all of the symmetry parameters to deviate from the expected values, as can be seen in figure 8. This figure shows the ratio of the FWHM to initial reactor period for six data sets. The Nordheim-Fuchs model predicts this ratio to be a constant value of 3.524 (Reference 3), however, at higher yields the thermal expansion of the fuel lags the temperature rise due to the inertia of the fuel mass. This retarding of expansion results in a greater yield for the pulse and the ratio of FWHM to initial reactor period is reduced to 2.8.

The FWHM to period ratio for the 6 gm cylinder increased with pulse yield rather than decreased, along with the other parameters. Also, the initial reactor period and FWHM both suggested an extremely large change in the neutron lifetime of the reactor (Figure 9). Initial estimates of yield data showed an effective lifetime of about 115 ns, more than 7 times the free field value. KENO code runs confirmed the effect of the U_3O_8 quantities on the neutron lifetime (Figure 10).

SANDIA PULSED REACTOR PULSE ANALYSIS PROGRAM

Figure 7: Pulse Data Sheet for Laser Cell with 2.1 cm Poly and 6 gm U_3O_8 convertor.

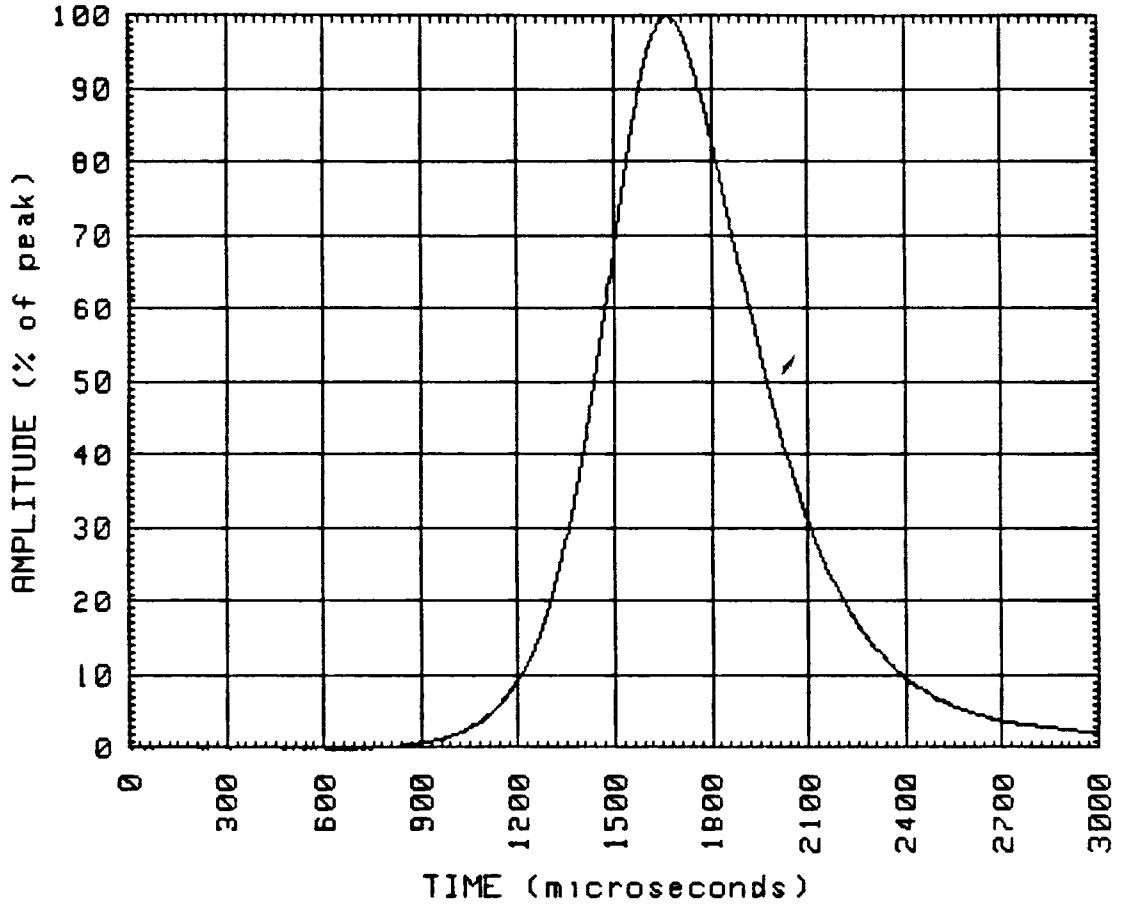

SPR III, SHOT # 3273-H, delta T= 310 deg C

Shot time was 18:39:05 on August 8 1994

Detector used for this pulse was the photodiode #2 detector

Peak voltage = 1.0630 volts,
Peak area = 6.407 E-04 volt-sec.,

Trigger to peak time = 1662.0 microseconds
Full width half maximum = 534.0 microseconds
Ratio of fall time to rise time based on FWHM = 1.373

Maximum heating rate was 17.00 degrees C per second
Maximum temperature was measured at 18.24 seconds after the shot.

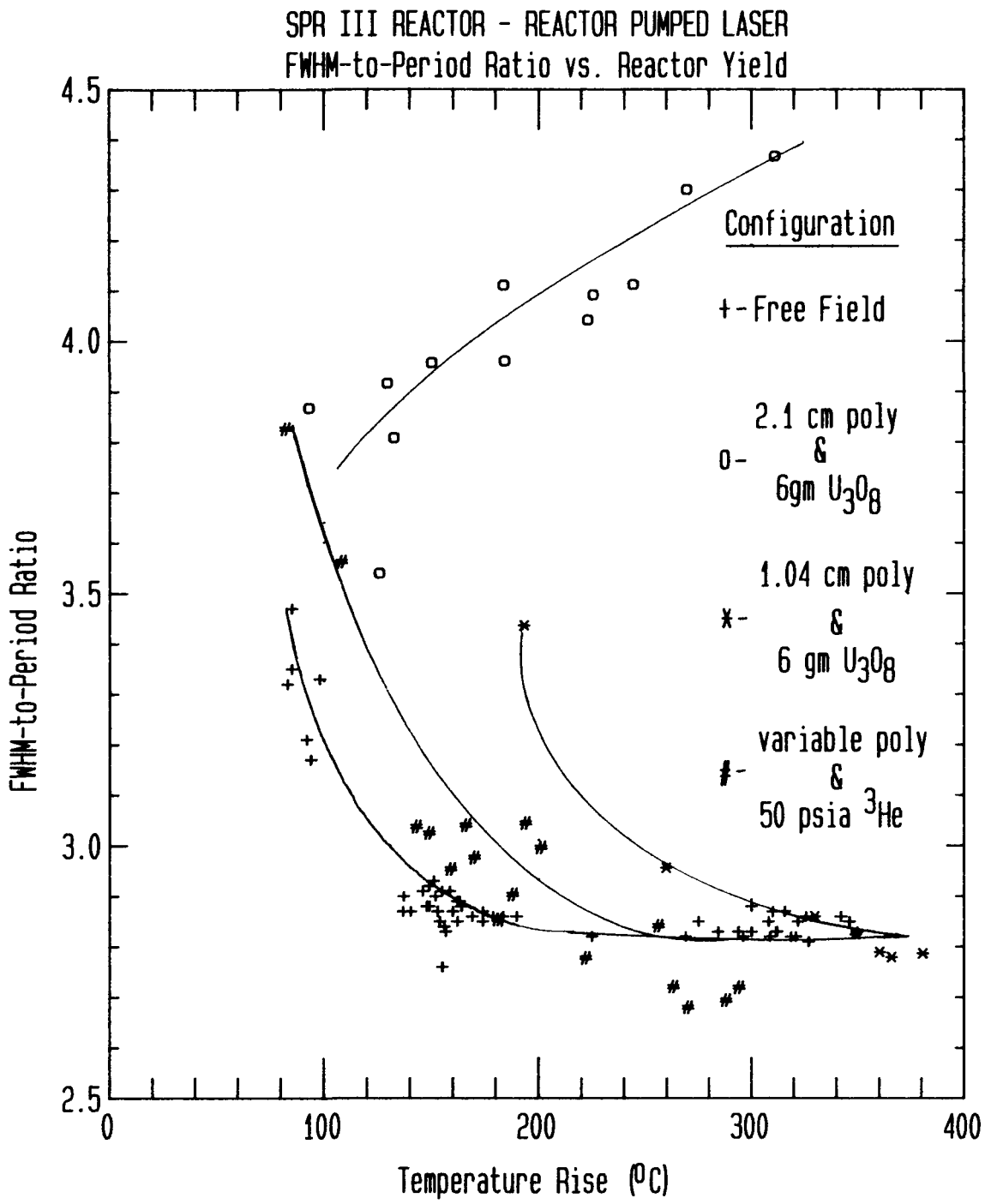

Figure 8: Full Width at Half Maximum to Period Ratio as a function of the reactor yield in temperature rise for free field and three experiment configurations. Note the deviation in the 2.1 cm poly & 6 gm U_3O_8 from the other curves.

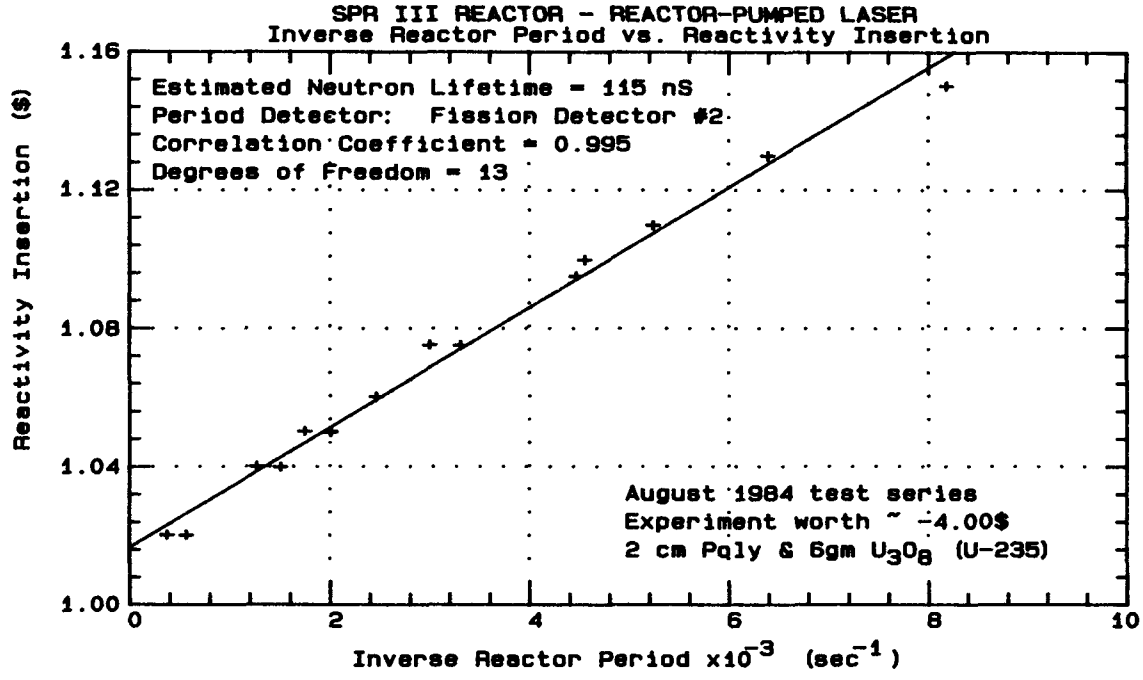

Figure 9: Reactivity Insertion as a function of Inverse Reactor Period for the laser cell with the 6 gm U_3O_8 cylinder. The slope yields the neutron lifetime.

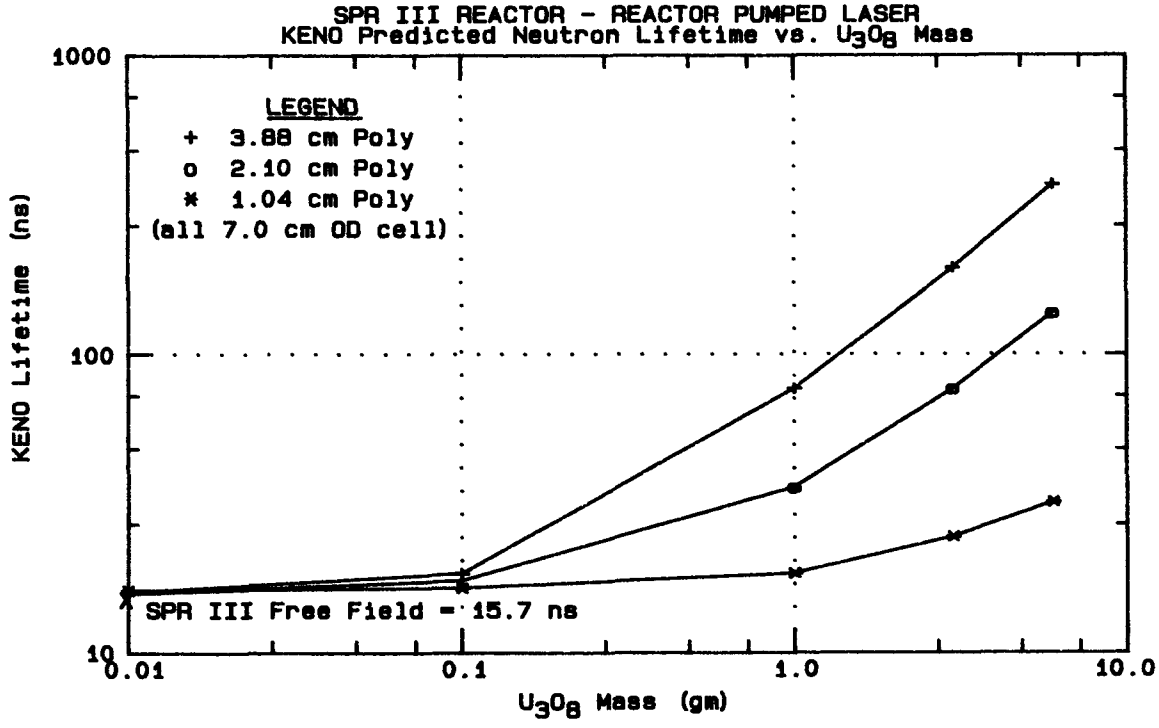

Figure 10: Neutron Lifetime as predicted by the KENO code as a function of the U_3O_8 mass for three polyethylene thicknesses and the 7.0 cm diameter cell.

The longer lifetime explains the initial reactor period; however, the pulse symmetry parameters are normally independent of lifetime. Therefore, it was postulated that fissions in the U_3O_8 coating were creating a neutron source that acted as a delayed neutron precursor group. The delay would be due to the thermalization and diffusion of the reactor's neutrons through the polyethylene before causing fissions in the cylinder. The fast neutrons from the cylinder that penetrate back into the fuel would be delayed in time from the initial reactor pulse. If this group were fast enough the reactor would deviate from the Nordheim-Fuchs model in the manner described. A multiple linear regression was performed to fit the pulse data to a two group inhour equation. One of the groups would represent the normal six-group average delayed precursors, and the second group would represent the pseudo-delayed group described here. The fit yielded a neutron lifetime of 106.6 ns, a group fractional yield of 0.00017, and a group half-life of 1.63 milliseconds. The correlation coefficient for the fit was 0.99999 with 15 degrees of freedom.

Note that when the polyethylene thickness was reduced by half in data set 2 of table 1, the lifetime was reduced to 40.7 ns, and the symmetry parameters all returned to the normal behavior. This is due to the fact that the reduced moderation probably reduced the fission yield in the U_3O_8, reducing the fractional yield, and the half-life probably was shortened due to reduced delay time in the polyethylene. These two conditions would both contribute to a return to more normal kinetics. When the quantity of U_3O_8 was reduced to 0.4 gm in later tests, the lifetime dropped further to about 31 ns. Both of these observations are also supported by figure 10.

5.0 CONCLUSIONS

The reactor-pumped laser experiments provide a unique opportunity to evaluate the kinetics effects of large moderating experiments in the glory hole of SPR III. Extensive neutron lifetime changes can be introduced even when the experiment's reactivity worth may not indicate any significant variation from free field conditions. The conditions that generate a lifetime change may not always be obvious in a complex experiment, and separating the contributors is difficult at best.

The most significant result is the effect of the U_3O_8 upon the reactor. The addition of enriched uranium in a moderating experiment creates a pseudo delayed-neutron group which has a strong kinetic effect on the system. The large effect that such a small quantity of material can have on the reactor illustrates how sensitive the relationship is between reactor and experiment. This serves as a reminder of the care with which an experiment must be examined when considering its kinetics effect upon the reactor.

Bibliography

1. Coats, R. L.; Neutron Kinetics of a Reflected Burst Reactor; Ph.D. Thesis, University of Oklahoma Graduate College, 1966.

2. Hetrick, D. L.; Dynamics of Nuclear Reactors; University of Chicago Press; 1971. Chapter 1.

3. Hetrick, D. L.; Dynamics of Nuclear Reactors; University of Chicago Press; 1971. Chapter 5, section 5-5.

SESSION II

SIMULATION FIDELITY AND SILICON DAMAGE

D. M. Woodall, Chairman
University of New Mexico

Editor's Note: This paper was unavailable for publication. A summary is included.

USE OF NPN BIPOLAR TRANSISTORS

FOR

SILICON EQUIVALENT NEUTRON DAMAGE

Boyce Ahlport
Don Garrison
Northrop Electronics Division
Hawthorne, CA 90250

With the closing of the Northrop Triga Reactor, Northrop shifted its neutron irradiations to the several government Fast Burst Reactors. As a control, an inexpensive NPN bipolar transistor was chosen to monitor the silicon equivalent damage created by the differing neutron spectra. Noticeable biases occurred between the comparisons with 1 Mev silicon equivalent dosimetry reported by the several facilities and the damage observed in the monitor transistors and other semiconductors being irradiated.

A special effort was committed to automate the measurement of the monitor transistors. Their behavior was then studied and quantified so that a more precise determination of the neutron fluence could be obtained. The techniques needed for accurate read-out of fluences from monitor transistors, with supporting data, is presented. The variabilities are mostly related to the choice of monitor transistor, test conditions, ambient and self-heating, and timing/annealing of the measurements. The occurrence of reverse annealing, varying with measurement current, is detailed. Also the monitoring of V_{BE} as a thermometer to correct the damage factor to a standard temperature is noted. The electrical measurement errors have been made negligible.

Some preliminary comparisons are given for the several facilities, using their historic 1 Mev(Si)/sulfur conversions. These comparisons do not include any adjustments for the biases developed by experiment positioning or recent changes in the silicon 1 Mev damage equivalence curve.

Hardness Parameter Studies at the White Sands Missile Range Fast Burst Reactor

T.M. Flanders
M.H. Sparks

Nuclear Effects Laboratory, White Sands Missile Range, N.M.

Abstract

This is a progress report on a continuing investigation of the 1 MeV equivalence concept. The Silicon displacement damage cross section published in ASTM Standard E722 has been re-examined. The original data used to produce the damage cross section was obtained in order to verify the average value for the damage cross section around 1 MeV. The Standard damage cross section was also compared to a damage cross section sometimes used in transport calculations for 1 MeV dose.

The report also presents an early analysis of a comparison of silicon displacement damage by fission neutrons and by fusion neutrons. Thirty 2N2222A transistors were exposed to fission spectrum, 14 MeV, and 3 MeV neutrons. This is the first in a series of planned experiments to monitor the 1 MeV equivalence of various neutron sources.

A) Introduction

Many system designs have neutron hardness requirements for semiconductors using spectra that cannot be conveniently synthesized in a laboratory environment. Nearly all specifications for neutron survivability are in units of 1 MeV fluences, whether the spectrum can be reproduced by existing neutron sources or not. Also, data which has been obtained with different neutron spectra already exist for semiconductors, and there can be a significant cost savings resulting from not having to retest the semiconductors to new spectrum requirements. Various methods have evolved for handling this problem.

One method measures the relative damage produced by the test and reference spectra by experimentally determining the degradation of the devices. The parameter commonly measured is gain. The relative damage between the two spectra is then used to establish a neutron fluence damage ratio. A fission spectrum is commonly used as the standard for damage equivalence between two experimentally different spectra.

A second method is completely analytical. A neutron transport analysis is made to determine the number of displaced silicon atoms for the specified neutron spectrum. The 1 MeV neutron

fluence that will produce the identical number of displacements is also determined analytically. The ratio of the specified spectrum fluence to the 1 MeV fluence determines the damage equivalency of the two spectra. The analytical approach is necessary for cases where the specified spectrum cannot be reproduced in the laboratory.

The approach generally used is a combination of the two methods. The energy spectrum of the source of neutrons is determined experimentally and a response function is folded with the spectrum to determine the equivalent 1 MeV fluence. ASTM Standard E722-80 (1) documents this procedure. The standard has currently been revised by the ASTM sub-committee on the effects of ionizing radiation on materials. This method has been in use since the mid-seventies.

B) Shape of the Damage Function

A fundamental issue in this problem is the silicon displacement damage cross section. This cross section curve has not been characterized adequately by experimental means. However, there are several theoretical tabulations of this data. The theoretical calculations do not all agree in detail on the shape of the cross section curve. This has a severe impact on trying to establish the equivalent damage of neutrons of one energy relative to another energy.

It is also generally assumed, for a Godiva-type spectrum, the useful threshold for damage for Silicon displacement is 10 keV. Neutrons with energies below that threshold cause an insignificant amount of damage (2). This assumption is dependent on the actual shape of the silicon damage function as well as the degree of moderation of the test spectrum.

As an example, admittedly extreme, we have made a one dimensional calculation of a FBR spectrum in a spherical cell. The Discrete Ordinates Code ANISN (3) was used to calculate the change in spectral shape as the source to detector distance increases from 16 inches to nearly 25 feet. The source spectrum was a calculated leakage spectrum for a bare assembly (4). Spherical geometry was used for the ANISN calculation and a concrete wall was modeled at about 27 feet from the source. The concrete wall was covered by 8 inches of wallboard. the inner 4 inches of wallboard were loaded with Boron. The configuration represents a simple one dimensional mockup of a typical exposure cell. The cross sections were from the DNA Few Group Coupled Neutron-Gamma Cross Section Library (5).

The resulting spectra for a few source to detector distances are shown in Figure 1. The calculated spectra clearly show that the environment in the spherical cell is composed of two components.

Component 1 is the slightly degraded fission spectrum, characteristic of a FBR. Component 2 is represented by a "background spectrum" which is constant regardless of the source to detector distance. The background component is represented by the flat line on the neutron lethargy plot. As the distance between the source and detector increases, the relative contribution of the fission portion of the spectrum decreases.

The results of this calculation are given in Table 1. The Silicon damage cross section for this exercise is the function distributed with the DNA Cross Section Library. The heritage of this curve is rumored to be from someone at TRW (6). The DNA Silicon damage cross section is shown in Figure 2 with the damage cross section recommended by the E722 standard. A significant point which is observed in the DNA damage cross section is that the damage curve is given all the way down to thermal energy. For the energies below that shown in Figure 2, the damage is the same as for 10 keV. The damage curve recommended by ASTM Standard E722 has no data below 10 keV.

As the source to detector distance increases, the spectrum gets progressively softer, as is expected. There are two columns shown in Table 1 for the calculated hardness parameter. The first column is the calculated hardness parameter when the full damage function down to thermal energies is used. The second column was calculated using the method analogous to that specified in Standard E722. The lower energy limit for damage is taken to be 10 keV. There is a significant difference in the two hardness parameters at the detector positions most remote from the source position. The difference is dependent on the inclusion of the damage predicted by the DNA response function for neutrons with energies less than 10 keV.

Table 1

Distance (inches)	SI	Fluence> 10 keV N/Source-cm^2	Total Fluence N/Source-cm^2	HP1	HP2
16	8.39	4.80 E-5	4.89 E-5	.987	.992
24	8.45	2.22 -5	2.31 -5	.978	.989
52	8.80	4.99 -6	5.92 -6	.922	.969
121	10.4	1.18 -6	2.12 -6	.737	.891
204	13.3	6.17 -7	1.56 -6	.573	.796
290	16.2	4.93 -7	1.45 -6	.495	.736

C) Impact of the Change of D(1 MeV)

An important region of the damage curve is around 1 MeV. In this region, there are significant neutron resonances. These resonances cause difficulty in determining a suitable average for the damage curve around 1 MeV. We have obtained the original data (6) used to produce the currently accepted damage function tabulated in ASTM Standard E722. We have also regrouped the data to match the energy structure of the spectrum unfolding code SAND-II. After processing the raw damage data, we calculated a new average energy and obtained a value for the damage at 1 MeV which is 94. This average is very similar to one which was proposed by Namenson et. al. (7) and was subsequently incorporated into the ASTM Standard.

It has been recognized for some time that the neutron leakage spectrum from a typical fast burst reactor is very near to that of the so-called 1 MeV equivalence. This fact arises because there is a significant population of neutrons which do appreciable displacement damage to silicon devices in the energy region around 1 MeV. In the past, the White Sands Fast Burst Reactor has been quoted as having a hardness parameter of 1.12. That is to say that it would take 1.12 neutrons of energy 1 MeV to produce the same amount of displacement damage as a typical reactor neutron. Using the newly recommended displacement cross section, the hardness parameter for the FBR is effectively 1.0. Appendix A is currently being delivered to the contractors who use the FBR.

D) Ratio of Damage of 14 MeV Neutrons to FBR Spectrum Neutrons

It has been noted by others that the observed damage ratio, caused by 14 MeV neutrons and fission spectrum neutrons, does not always agree with the ratio that can be calculated by theoretical means. It has been observed by several different groups that 14 MeV neutrons produce about 2.7 to 3 times as much damage as do neutrons having an energy distribution typical of that produced by a Fast Burst Reactor (8). The calculated damage ratio, using the E722 damage cross section tabulation, indicates that this damage ratio should be about 2.2 to 2.3.

We have exposed 2N2222A transistors at the White Sands Missile Range FBR and to fusion neutrons produced by the Lawrence Livermore Laboratories Rotating Target Neutron Source (RTNS-1). RTNS-1 is capable of producing fusion neutrons near 14 MeV and 3 MeV, depending on the target materials. All devices were exposed to all three environments. The transistors were initially irradiated at the FBR. These same transistors were then exposed to 14 MeV neutrons and subsequently to 3 MeV neutrons. All transistors were then returned to the WSMR FBR and exposed again.

After each exposure, the gain of each device was measured using a curve tracer. The inverse beta of each transistor was plotted

versus neutron fluence. Figure 3 shows the gain degradation for one such device. Damage ratios for D-T and D-D fusion environments were calculated relative to the FBR exposures for each transistor. Early analysis of the first set of transistor data indicates the average damage ratio of D-T spectrum neutrons to FBR spectrum neutrons is 2.29+-0.11. The expected damage ratio, based on the damage cross section curve was about 2.3.

We are continuing to evaluate the data from the exposures from the Livermore Deuterium-Deuterium source. The initial data shows a higher 3 MeV to FBR damage ratio than is expected. The experiment will be be repeated before any conclusions are drawn for this ratio.

E) REFERENCES

1) ASTM Standard E722-85, Annual book of ASTM Standards.

2) Verbinski, V.V., Lurie, N.A., and Rogers, V.C., "Threshold-foil Measurements of Reactor Neutron Spectra for Radiation Damage Applications, "Nuclear Science and Engineering, Vol 65, 1978, pp. 316-330.

3) Engle, W. W. Jr., A Users Manual for ANISN, A One-Dimensional Discrete Ordinates Transport Code with Anisotropic Scattering, USAEC Report K-1693, Union Carbide Corporation, (1967).

4) Flanders, T. M., Unpublished Data.

5) Bartine, D. E., J. R. Knight, J. V. Pace III, and R. W. Roussin, Production and Testing of the DNA Few-Group Coupled Neutron-Gamma Cross-Section Library, ORNL/TM-4840 (1977).

6) Private Communication from J. Humphreys.

7) Namenson, A.I.,Wolicki, E.A. and Messenger, G.C., Average Silicon Neutron Displacement KERMA Factor at 1 MeV, IEEE Transactions on Nuclear Science, NS-29, No. 1, 1982, pp.1018-1020.

8) Coppage, F. N., The Influence of Dosimetry on Earlier Damage Equivalence Ratios, IEEE Transactions on Nuclear Science, Vol. NS-22, No. 6, (1975).

Appendix A

TECHNICAL NOTE: 1 MeV FLUENCE EQUIVALENCY of the White Sands Missile Range Fast Burst Reactor.

The Dosimetry Section, Nuclear Effects Laboratory will report the Hardness Parameter(HP) for the WSMR Fast Burst Reactor as 1.0. The previous value reported for HP was 1.12.

DISCUSSION:

The ASTM standard which defines the method for determining the Hardness Parameter has been revised (Ref. 1). This revision results in a re-evaluation of the average damage cross section function around 1 MeV (Ref. 2). The previously recommended displacement KERMA cross-section for a 1 MeV neutron was either 84 or 78 MeV-mb. The new value recommended by the standard is 95 +- 4 MeV-mb. The new HP does not reflect a change in the displacement KERMA per unit fluence produced by the FBR. This represents a redefinition of the amount of damage a hypothetical 1 MeV monoenergetic neutron source would produce.

IMPACT:

HP is used to calculate neutron fluence when exposure requirements are given in terms of 1 MeV equivalence (Ref. 3). The exposure parameter measurable for the FBR is fluence greater than 3 MeV. The 1 MeV equivalence is calculated by multiplying the reported Sulfur fluence by a factor which contains the HP. The factor for converting Sulfur fluence to 1 MeV equivalence is 6.7. All 1 Mev fluences obtained prior to 1 February, 1986 may be normalized to the current value by multiplying by the ratio 6.7/7.5.

LIMITATIONS:

This calculated HP is valid only for free field conditions at a distance of 24 inches from core centerline. However, it will remain at least approximately valid for most conditions when there is no significant scattering, absorbing or neutron sources (other than the FBR) in the vicinity of the point of interest.

REFERENCES:

1. ASTM Standard E722-85, Annual book of ASTM Standards.

2. Namenson, A.I.,Wolicki, E.A. and Messenger, G.C., "Average Silicon Neutron Displacement KERMA Factor at 1 MeV," IEEE Transactions on Nuclear Science, NS-29, No. 1, 1982, pp.1018-1020.

3. Verbinski, V.V., Lurie, N.A., and Rogers, V.C., "Threshold-foil Measurements of Reactor Neutron Spectra for Radiation Damage Applications, "Nuclear Science and Engineering, Vol 65, 1978, pp. 316-330.

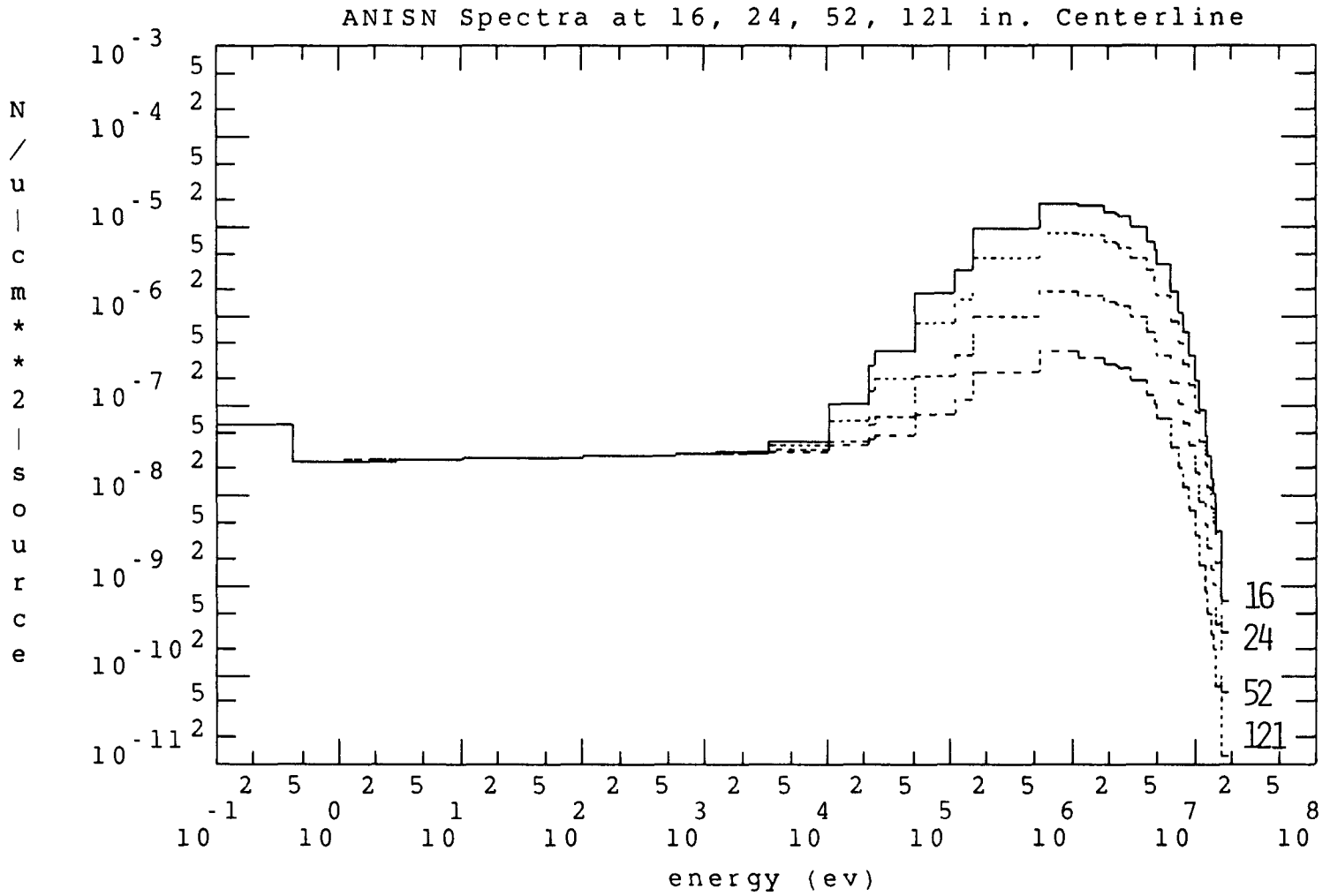
ANISN Spectra at 16, 24, 52, 121 in. Centerline
N/u-cm**2-source
10-3
10-4
10-5
10-6
10-7
10-8
10-9
10-10
10-11
5
2
10-1
100
101
102
103
104
105
106
107
108
energy (ev)
16
24
52
121

FIGURE 1

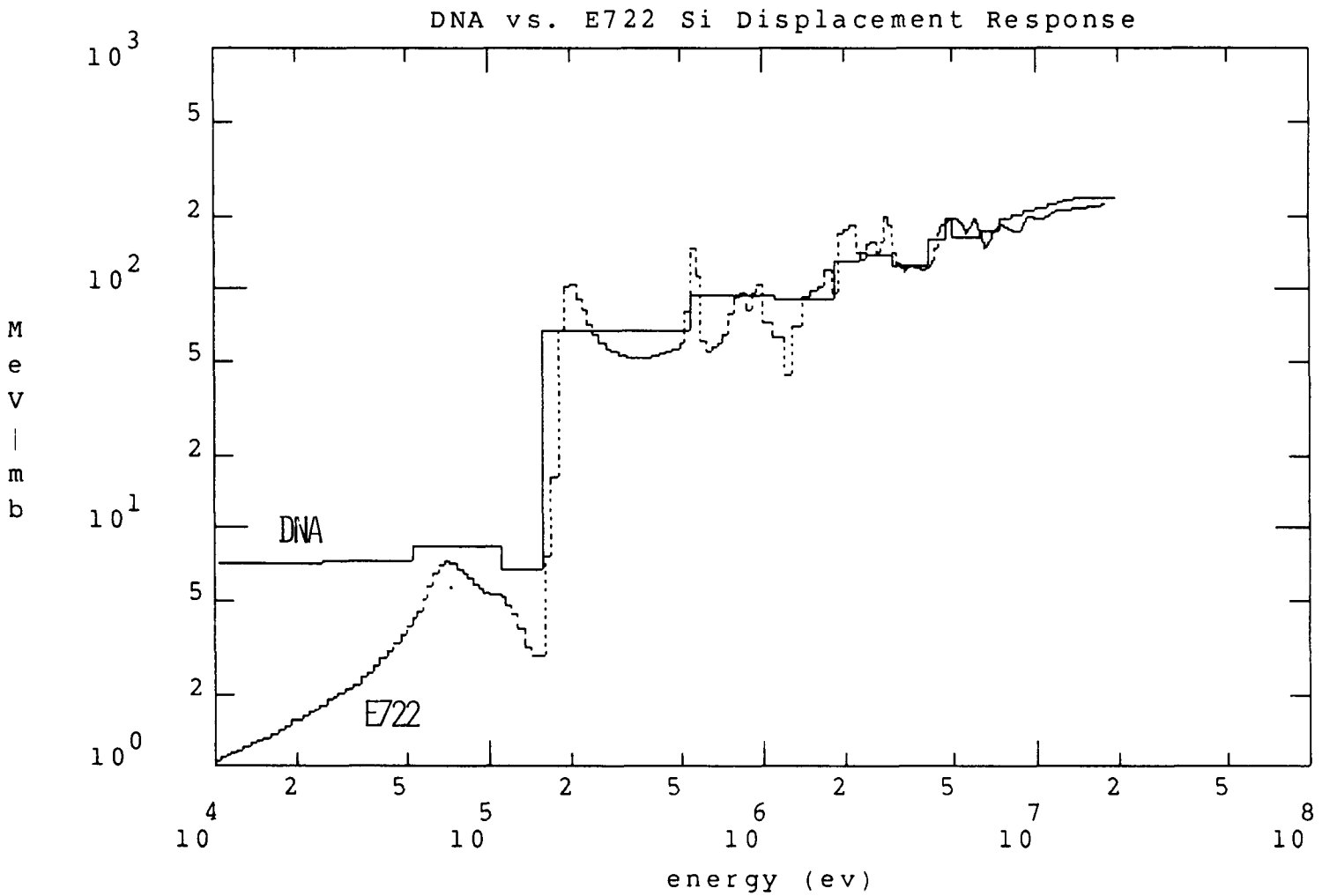
DNA vs. E722 Si Displacement Response
MeV-mb
10^3
5
2
10^2
5
2
10^1
5
2
10^0
DNA
E722
2
5
2
5
2
5
2
5
10^4
10^5
10^6
10^7
10^8
energy (ev)

FIGURE 2

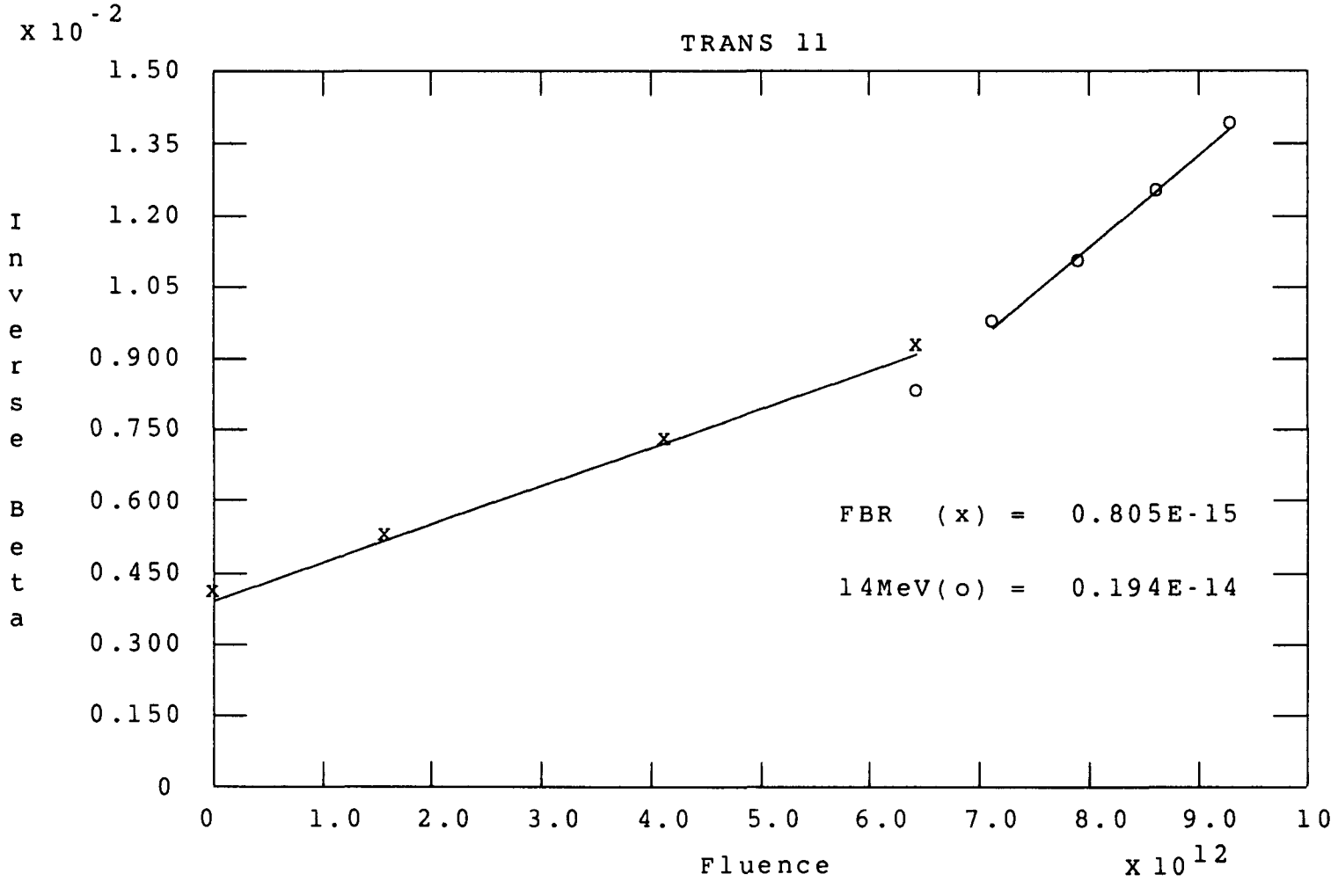
TRANS 11
X 10 -2
Inverse Beta
1.50
1.35
1.20
1.05
0.900
0.750
0.600
0.450
0.300
0.150
0
0
1.0
2.0
3.0
4.0
5.0
6.0
7.0
8.0
9.0
10
Fluence
X 10 12
FBR (x) = 0.805E-15
14MeV(o) = 0.194E-14

FIGURE 3

SILICON AND SILICON DIOXIDE NEUTRON DAMAGE FUNCTIONS

Maximo S. Lazo and David M. Woodall
The University of New Mexico
Department of Chemical and Nuclear Engineering
Albuquerque, NM 87131

Patrick J. McDaniel
Sandia National Laboratories
Organization 6433
Albuquerque, NM 87185

ABSTRACT

Radiation hardness testing of semiconductor devices has used fast burst reactor sources, for example Godiva, Triga or the Sandia Pulsed Reactor (SPR). Measurements have been made both in the burst and the steady modes of operation. Damage has traditionally been correlated with observed effects such as modification of minority and majority carrier lifetimes and mobilities. The usual damage analysis assumes an infinite medium of silicon irradiated by a neutron beam represented by an equivalent monoenergetic beam at 1.0 MeV. This assumption is of questionable validity for a number of reasons. The energy dependence of the distribution of ionization and displacement damage may not be properly included. The effect of feature size on the component response is ignored. Finally, the effect of primary knock-on atom in a molecular material such as silicon dioxide is ignored. In order to improve the state-of-the-art in silicon and silicon dioxide damage functions, we have made improved calculations to address some of these problems. Using the NJOY nuclear data processing code, we predict the neutron radiation damage response function of silicon and silicon dioxide. The methodology used includes using the Lindhard electronic screening theory to compute the distribution of damage between ionization and displacement. The variation of those results with primary kock-on atom (PKA) is of significance for a molecule such as SiO_2. The methodology of doing such molecular damage calculations is also presented in this paper. We have found significant differences between the 1.0 MeV damage response functions computed by our method and those values widely in use for both silicon and for silicon dioxide.

1.0 INTRODUCTION

This work investigates and reviews the radiation damage effects of fast neutrons in silicon and silicon dioxide. Radiation-hardness testing of semiconductor devices has used fast burst reactor sources such as Godiva, Triga and the Sandia Pulsed Reactor (SPR). Measurements have been made both in the burst and the steady modes of operation. Neutron spectra are usually determined by threshold activation of foils. A microelectronic component is observed to have a different characteristic behavior following irradiation. Such changes can be correlated with modifications in material properties, such as minority or majority carrier lifetimes or mobilities.

The assumptions of classical radiation damage analyses and the correlation of integrated circuit radiation damage effects with displacement damage in silicon may not be an adequate approximation. Traditional neutron radiation damage analysis (ASTM 1985) assumes that the damage in silicon irradiated by a flux of neutrons can be represented by infinite medium silicon damage due to a 1.0 MeV equivalent neutron beam. The damage produced by this beam then can be correlated with effects observed in reactor irradiation of components (Gover 1985), such as modifications in minority carrier lifetime, majority carrier concentration or carrier mobilities. The conversion to a 1.0-MeV equivalent basis allows for the intercomparison of damage due to different neutron sources. We question the validity of this approach. While the relationship probably holds for large discrete components based on conventional bipolar technology, it is of questionable validity for state-of-the-art microelectronic components with micrometer features. Furthermore, the approach does not address the effect of damage in molecular systems, such as SiO_2.

For the purpose of radiation effect analysis, a microelectronic system is a mixture of metallic and nonmetallic monoatomic and polyatomic solids such as Si, Ge, Au, Al, SiO_2, GaAs, and GaP. The physical dimension of the features of a typical microelectronic device are approximately 1 μm to 3 μm in width and only 10 nm to 100 nm in depth.

Neutron radiation damage in solids results from nuclear collisions and reactions that produce energetic recoil atoms. The recoiling atoms generate electronic excitation, or ionization, in the host material and elastic and inelastic collisions that may result in displacing additional host atoms from their lattices sites. Thus, the two features of such damage are residual ionization and atomic displacement damage. The structure of displacement cascades in solids can be studied via a Monte Carlo simulation (Robinson 1974 and 1985 and Mueller 1980) or via a transport calculation.

Nuclear collisions and reactions are characterized by neutron cross sections, or interaction probabilities. These parameters are measured experimentally in the range of neutron energies from a few

eV to several MeV for most elements in the periodic table and for some compound materials. Due to limitations in time and techniques, there are regions for which the cross sections are not available (MacFarlane 1984 and L. Greenwood 1985). Therefore, theoretical analysis of nuclear reactions is an important tool, both for evaluating the present measured values and for the interpolation and extrapolation of new values. The reactions between the neutron and heavy nuclei can be modeled successfully using a phenomenological model based on experimental information about the nuclear structure and an average potential, the "local optical potential" (Young 1977 and 1985).

The cross section for the interaction between a neutron and a nuclei in a solid structure is usually of the order of 10^{-8} A^2 and, thus, much smaller than the area of the elementary unit lattice cell, which is about 5 A^2. The mean free path of neutrons is large, typically many centimeters, and primary knock-on atoms (PKAs) are created uniformly in the solid. The development of a cascade started by a PKA is not modified by the presence of other cascades until it reaches very high neutron fluences. The probability of multiple neutron interactions in silicon integrated circuits has recently been measured and modeled (Srour et al., 1985).

In this paper the neutron radiation damage is calculated via the NJOY computer code (MacFarlane 1977). All nuclear reaction data are obtained from ENDF/B-V, distributed by Brookhaven National Laboratory (Kinsey 1979), and from the theoretical models included in the NJOY code. The NJOY code used the Lindhard model to calculate the partition of recoil energy between nuclear and electronic effects for the recoiling atoms.

2.0 THEORY

The probability of displacing atoms from their lattice sites depends on the incident neutron energy (E) and cross section ($\sigma(E)$), the primary recoil atom energy (E_R), and the partition of recoil energy between electronic excitation and atomic displacement ($P(E_R)$). The damage function is given by

$$D(E) = \sum_{\kappa} \sigma_{\kappa}(E) \int dE_R \; f_{\kappa}(E,E_R) P(E_R) \quad , \tag{1}$$

where the sum is over all reactions, and $f_{\kappa}(E_R)$ is the probability that a neutron with energy E in a reaction k produces a recoil with energy E_R:

E = Incident neutron energy (laboratory system).
E_R = Recoil nucleus energy (laboratory system).
$\sigma_{\kappa}(E)$ = Nuclear cross section for reaction at energy E.

The partition function or "damage efficiency" ($P(E_R)$) is given by the relation derived by Robinson (1976), based on the electronic screening theory of Lindhard (1963).

2.1 Partition of the Recoil Energy: LSS Theory

Neutron radiation damage in solids results from nuclear collisions and reactions that produce energetic recoil atoms. The recoiling atoms generate electronic excitation, or ionization, in the host material and elastic and inelastic collisions that may result in displacing additional host atoms from their lattices sites. A treatment of these atomic interactions has been developed by Lindhard (1963) based on Thomas-Fermi model of the atoms. This description of the atomic collisions is known as the LSS theory. From the LSS theory the energy damage partition function is:

$$P(E_R) = \frac{E_R}{1 + F_L(3.4008\varepsilon^{1/6} + 0.40244\varepsilon^{3/4})} \quad , \tag{2}$$

if $E_R \geq 25$ eV, and $P(E_R) = 0$ otherwise, where $\varepsilon = E_R/E_L$, and

$$E_L = 30.724\ Z_R\ Z_L(Z_R^{2/3} + Z_L^{2/3})^{1/2}(A_R + A_L)/A_L \quad , \tag{3}$$

and

$$F_L = \frac{0.0793\ Z_R^{2/3}\ Z_L^{1/2}(A_R + A_L)^{3/2}}{(Z_R^{2/3} + Z_L^{2/3})^{3/4}\ A_R^{3/2}\ A_L^{1/2}} \quad , \tag{4}$$

And Z_i and A_i refer to the charge and atomic number of the lattice nuclei (L) and the recoil nucleus (R).

Note that the original paper by Lindhard (1963) treated the derivation of the partition function for the case $Z_R = Z_L$ thoroughly, but presented only an outline for the case $Z_R = Z_L$. It is important to point out that in a series of papers by D. Parkin (1977 and 1979) and C. A. Coulter (1980), the corresponding Integral Equations for the Radiation Effects derived by Lindhard have been numerically solved for monoatomic, diatomic and polyatomic systems. These equations are treated considering the univeral scattering cross section and electronic stopping power formula of Lindhard. In this way the damage, partition functions or "damage efficiency" functions are generated. These functions then are fitted to analytic expressions of the Robinson type, which can be used in the NJOY program replacing the Lindhard's damage efficiency proposed by Robinson.

The relationship between neutron energy and recoil energy can be described by one general equation derived from conservation of energy and momentum in the center of mass system:

$$E_R(E, E_\chi, \theta) = U_3E_\chi + U_1U_4E - 2[EE_\chi U_1U_3U_4]^{1/2}\cos\theta \quad , \tag{5}$$

where:

$E_\chi = U_2 E + Q$ = total energy.
Q = Energy-mass conversion in the nuclear reaction.
θ = Angle between the incident neutron direction and the recoil atom direction,

$U_i = \frac{m_i}{m_1 + m_2}$, m = mass, and i = 1, 2, 3 or 4 for the neutron, target atom, emitted particle, and recoil atom, respectively.

The evaluation of the damage cross section for binary materials requires knowledge of the damage efficiency for each pair of elements (Dell 1980):

$$D_{i,j}(E) = \sum_\kappa \sigma_\kappa^i(E) J dE_R \; f_\kappa^i(E, E_R) \; P_{i,j}(E_R) \quad . \tag{6}$$

An average over all possible pairs weighted by atomic fraction (fr) gives an approximation to the damage cross section for the compound:

$$< D > = \sum_{i,j} fr_i fr_j D_{i,j}(E) \tag{7}$$

As an example, for SiO_2, it is necessary to determine the number of oxygen atoms displaced by silicon PKAs, which is proportional to D(Si,O), as well as by oxygen PKAs, which is proportional to D(O,O). The results are then combined according to the atomic fraction of each species of PKA. In this case

$$fr_{Si} = 1/3, \text{ and} \tag{8}$$

$$fr_O = 2/3 \quad .$$

This methodology is applied to the results generated within the NJOY calculation to obtain the corrected values for the molecule.

3.0 CALCULATIONAL RESULTS

The results of our NJOY calculations are presented here for both pure silicon and silicon dioxide. The multigroup cross-sectional set chosen for these results is the 37 group DNA set, which has been extensively used in the radiation damage literature. We also have performed this analysis for a much finer (30C group) cross-sectional set, but for the sake of comparison with published results, the results from the 37 group calculation are emphasized here.

Figure 1 displays the displacement damage in silicon as a function of neutron energy on a linear plot. The elastic scattering and total cross sections are displayed in two curves. Note that the components other than elastic scattering are dominant above 2.0 MeV. The same data are plotted over a much larger energy range in a

log-log plot in Figure 2. At high energy, both inelastic scattering and particle-producing reactions play a significant role in the displacement damage cross section.

The displacement damage cross sections for the components of SiO_2 are shown in Figure 3. Note that the oxygen PKA produces lower damage than the silicon PKA. Only values for the oxygen-on-oxygen (O-O) and silicon-on-silicon (Si-Si) damage are shown in that figure. As is apparent from Figure 3, the high energy limit is only about 75 MeV-mb, for the O-O damage and about 200 MeV-mb for the Si-Si damage. The net effect is that there is substantially less displacement damage in SiO_2 than in pure silicon. The difference between the Si-Si and the silicon-on-oxygen (Si-O) damage, as well as the difference between the O-O and the oxygen-on-silicon (O-Si) damage, is shown in Figure 4.

The ionization damage cross sections for SiO_2 and its components are shown in Figure 5. A comparison of the displacement damage cross section and the ionization damage cross section for SiO_2 is plotted in Figure 6. On this linear scale, the displacement damage is shown to be an order of magnitude smaller at high energy than the ionization damage. Figure 6 also includes the Si-Si and O-O values, from which one can determine the ratio of Si damage to SiO_2 damage at a given energy.

The summary comparison of the 1 MeV equivalent displacement damage response function for silicon is shown in Table 1, in which the results obtained using NJOY are compared with results from other authors. A caution is in order with respect to using these results. The silicon cross section has a resonance in the vicinity of 1.0 MeV. Thus, the values obtained from this type of analysis are sensitive to the group structure and group averaging scheme used. Values obtained from the fine (300 group) calculation are given in Table 2. It is noteworthy that the 14-MeV to 1-MeV ratio obtained from NJOY with this fine group structure agrees with the best experimental values obtained for such damage. Figure 7 displays a plot of those fine group values of displacement damage for silicon, indicating the resonant structure which makes group averaging such a tenuous endeavor.

4.0 CONCLUSIONS

The NJOY system provides a consistent and convenient method to compute damage cross sections for both single species materials, such as Si, and compound materials such as SiO_2. The computational results presented in this report are the most complete available for these materials. They indicate that currently used values may be in error by approximately 10 to 20 percent for Si and substantially more for SiO_2. Note that the current results are the first effort to use the most up-to-date (ENDF/B-V) cross-sectional information consistently to compute the ionization and displacement damage for Si and SiO_2. These results should be used in place of previous calculations, which were generated with various

cross-sectional sets and various model "fix-ups" for the molecular effects. Results obtained using the NJOY system also assure consistency between damage and heating crosss sections for these materials.

The key feature of the application outlined in this report is the availability of the most up-to-date cross sections through the ENDF/B-V library. This methodology can be applied to other molecular materials of interest for radiation damage in microelectronic materials. Further work is suggested for materials such as GaAs; however, additional effort may be required because the cross sections in the ENDF/B-V library might be inadequate. Cross sections generated by this method may be used in transport calculations or Monte Carlo calculations to determine the actual damage effects in the various components of a typical microelectronic device.

5.0 ACKNOWLEDGMENTS

This research has been sponsored by Sandia National Laboratories under Contract No. SNL-21-6559 to the University of New Mexico. Conversations with R. M. MacFarlane (LANL) are gratefully acknowledged.

REFERENCES

"Characterizing Neutron Energy Fluence Spectrum in Terms of an Equivalent Monoenergetic Neutron Fluence for Radiation-Hardness Testing of Electronics," ASTM Standard E-722-85, February, 1985.

Coulter, C. A. and D. M. Parkin, "Damage Energy Functions for Polyatomic Materials," Journal of Nuclear Materials 88 (1980) 249-260.

Dell, G. F., et al., "Damage Parameters for Nonmetals in a High Energy Neutron Environment," Symposium on Neutron Cross Sections From 10 to 50 MeV, BNL-NCS-51245, Vol. II, (July 1980).

Kinsey, R., Ed., ENDF/B Summary Documentation, BNL-NCS-17541 (ENDF-201), 3rd ed., Brookhaven National Laboratory, 1979.

Gover, J. E., "Basic Radiation Effects in Electronics Technology," Course Notes for INTEC SP712, Sandia National Laboratories, October 1983.

Greenwood, L. R., Argonne National Laboratory, private communication (1985).

Greenwood, L. R., "Specter: Neutron Damage Calculations for Materials Irradiations," Argonne National Laboratory, ANL/FPP/TM-197, January (1985).

Lindhard, J., V. Nielsen, M. Scharff, and P. V. Thomsen, "Integral Equations Governing Radiation Effects," Kgl. Danske Videnskab. Selskab, Mat.-fys. Medd. 33, No. 10, 2-42 (1963).

MacFarlane, R. E., "NJOY A Code System For Producing Pointwise and Multigroup Neutron and Photon Cross Sections from ENDF/B- IV and -V Evaluated Nuclear Data," RSIC PSR-118, Los Alamos National Laboratory, March 1979.

MacFarlane, R. E. and D. Graham Foster, Jr., "Advanced Nuclear Data for Radiation Damage Calculations," J. Nucl. Mat. 122, 1047 (1984).

MacFarlane, R. E., Los Alamos National Laboratory, private communication (1985).

Messenger, G. C., "Radiation Effects on Microcircuits," IEEE Transactions on Nuclear Science, Vol. NS-13, No. 6, December 1968.

Mueller, G. P., "Simulations of Cascades Damage in Silicon," IEEE Transactions on Nuclear Science, Vol. NS-27, No. 6, December 1980.

Parkin, D. M. and C. Alton Coulter, "Damage Energy Functions for Compounds and Alloys," Trans. Am. Nuc. Soc. 27 (1977).

Parkin, Don M. and C. Alton Coulter, "Displacement Functions for Diatomic Materials," Journal of Nuclear Materials 85 and 86 (1979) 611-615.

Robinson, M. T. and I. M. Torrens, Phys. Rev. B9 (1974) 5008.

Robinson, M. T., "The Theory of Radiation Induced Defect Production," in Radiation Damage in Metals, edited by N. L. Peterson and S. D. Harkness, American Society for Metals publication 1976, pp. 1-27.

Robinson, M. T., Oak Ridge National Laboratory, private communication (1985).

Rogers, V. C., L. Harris, D. K. Steinman, and D. E. Bryan, "Silicon Ionization and Displacement Kerma for Neutron from Thermal to 20 MeV," IEEE Trans. Nucl. Sci. Vol. NS-22, No. 6, December 1975.

Srour, J. R., et al., "Permanent Damage Introduced by Single Particles Incident on Silicon Devices," IEEE Trans. Nucl. Sci, 26, 4784 (1985).

Young, P. G. and E. D. Arthur, "GNASH: A Pre-Equilibrium Statistical Model Code for Calculation of Cross Sections and Emission Spectra," Los Alamos National Laboratory, LA-6947 (1977).

Young, P. G., Los Alamos National Laboratory, private communication (1985).

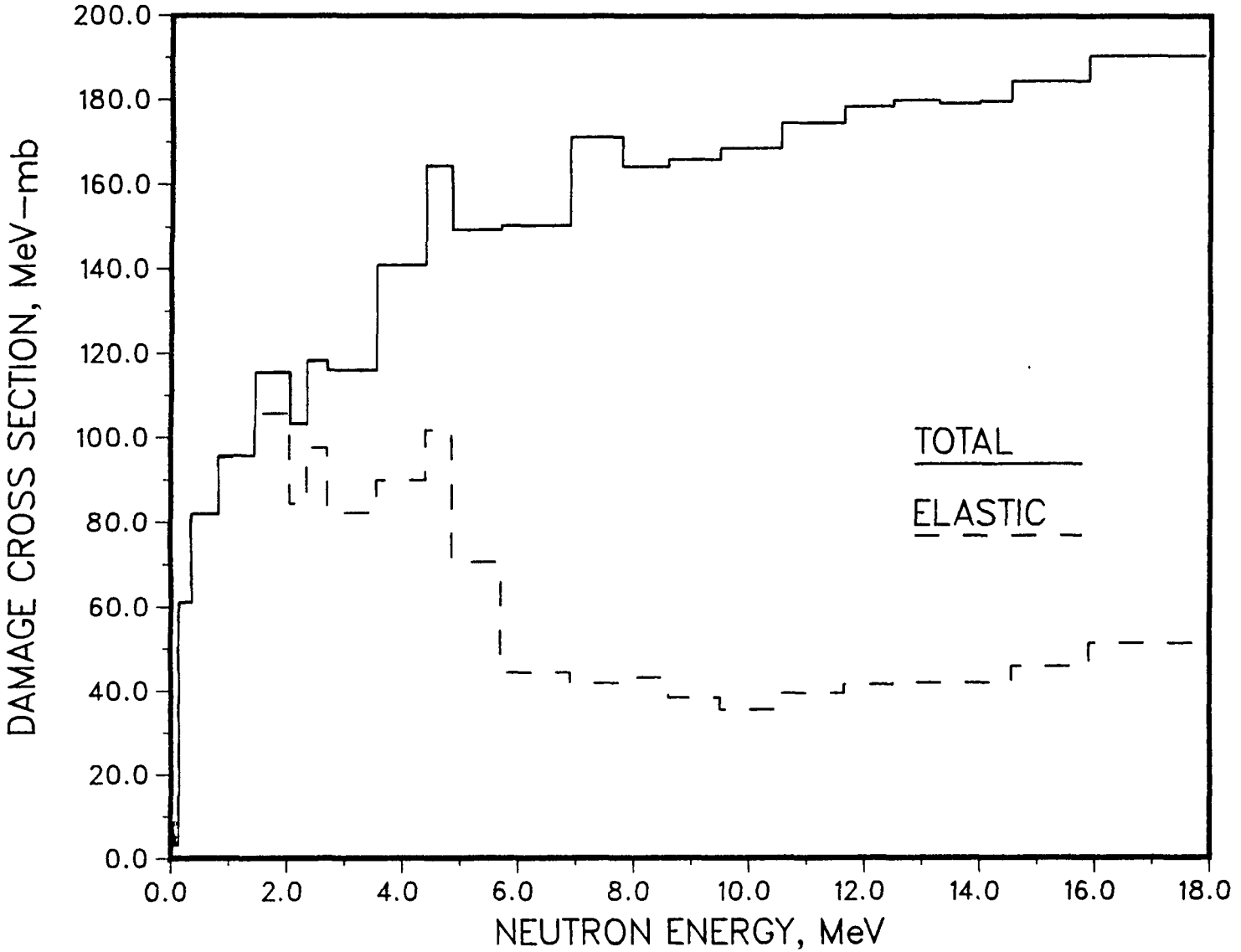

Figure 1. Silicon Displacement Damage-Energy Cross Section DNA 37-Group Calculation

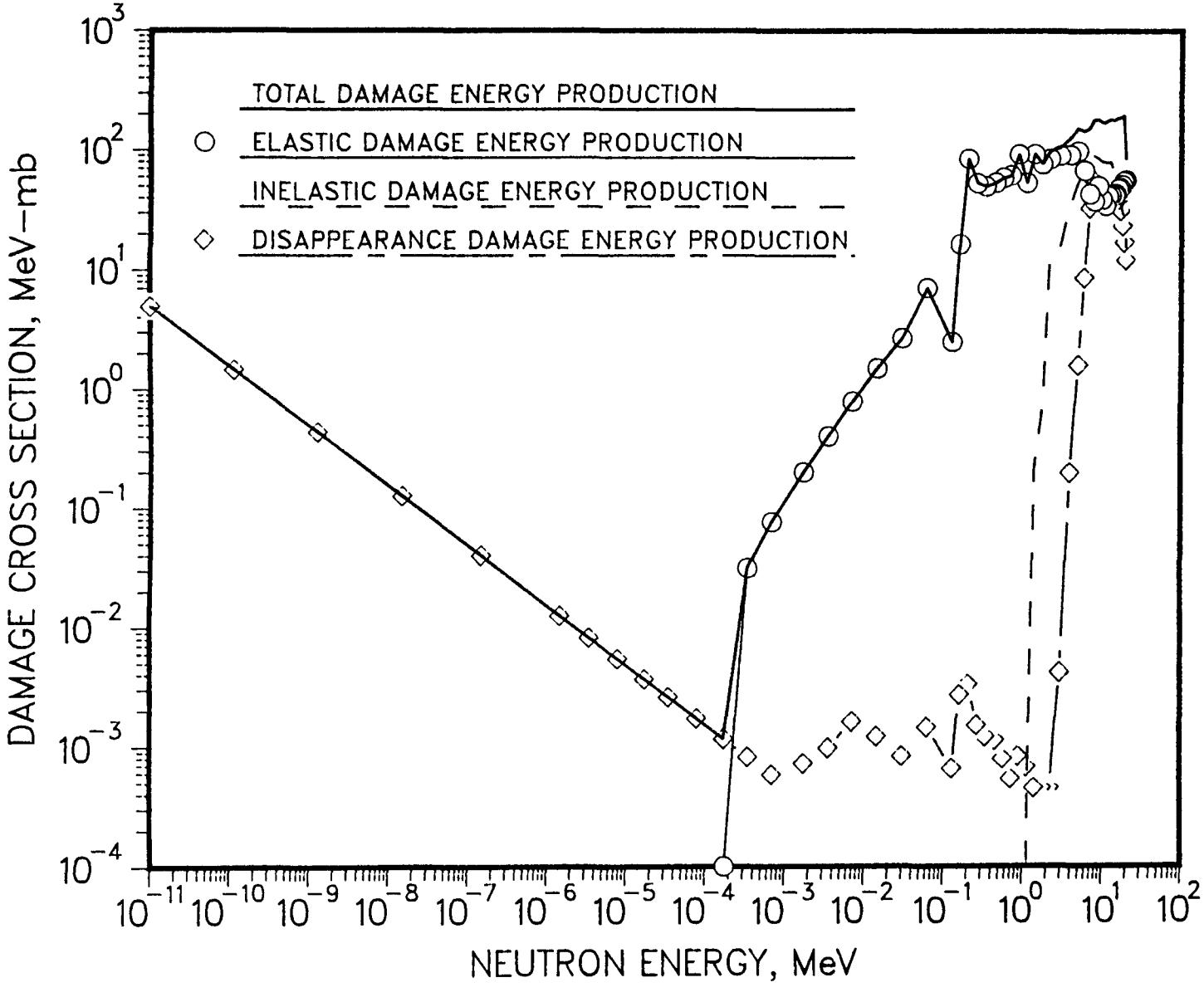

Figure 2. Components of Radiation Damage-Energy Production for Silicon

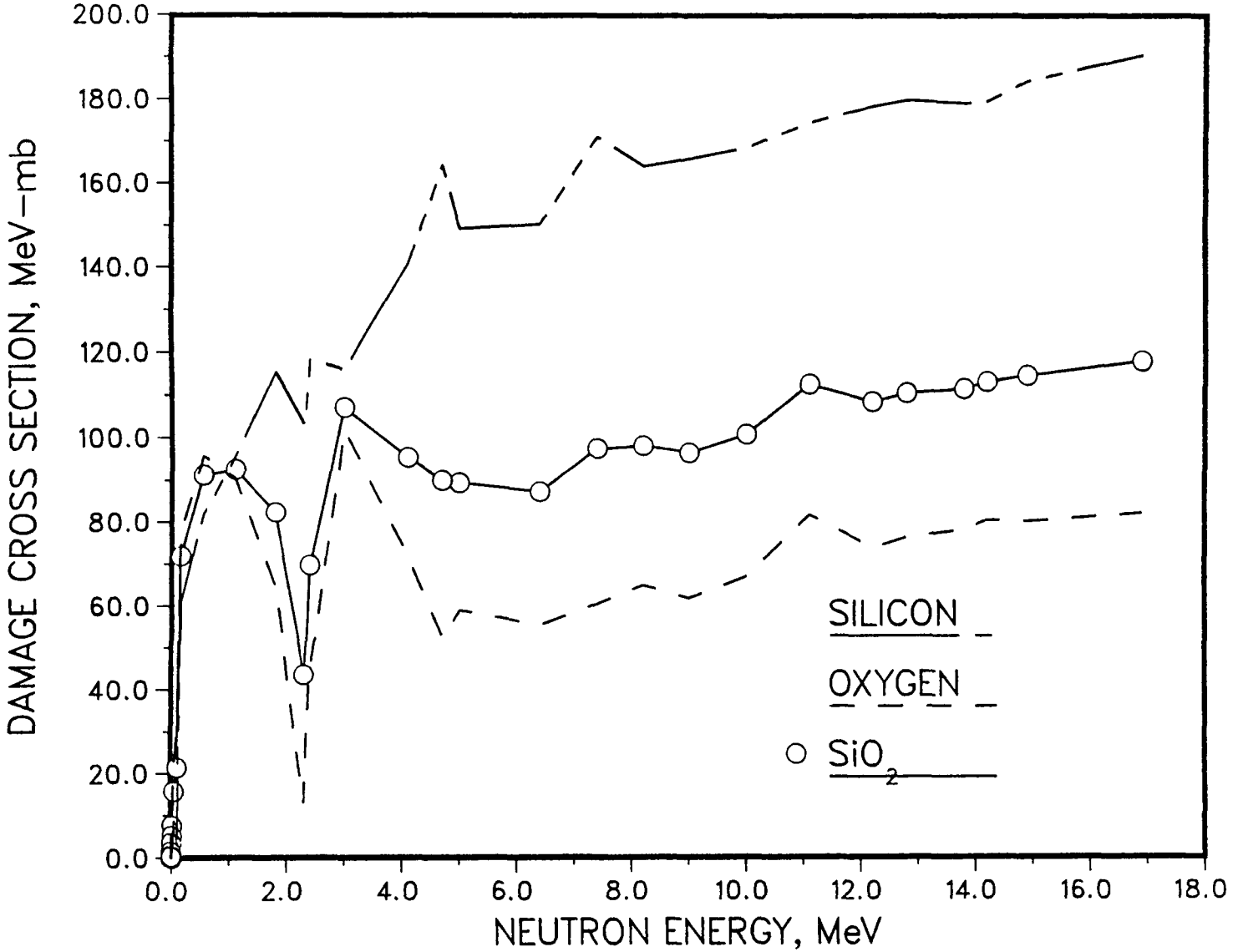

Figure 3. Displacement Cross Section for SiO_2 and its Components

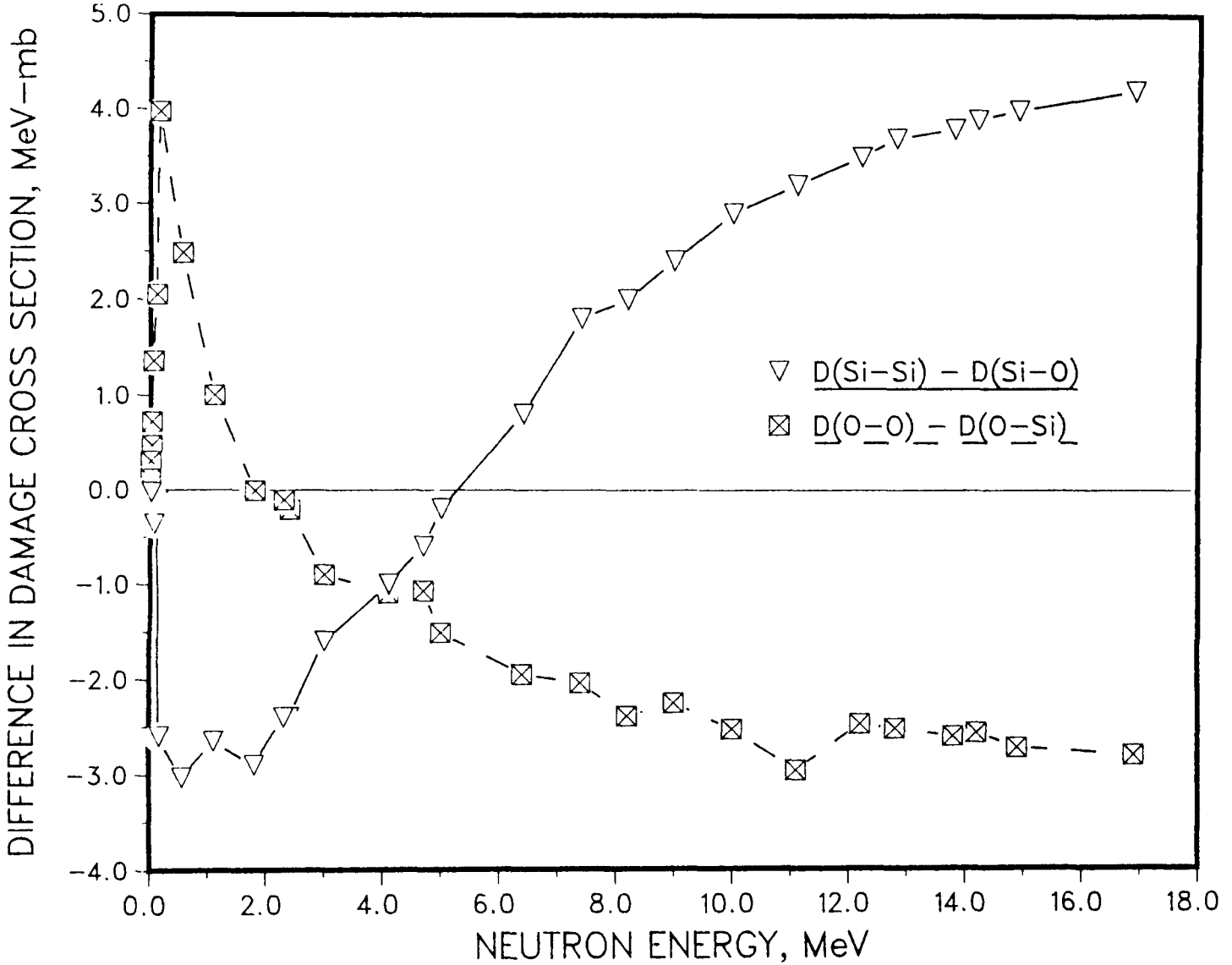

Figure 4. Difference in Damage Energy Cross Section for Components of SiO_2

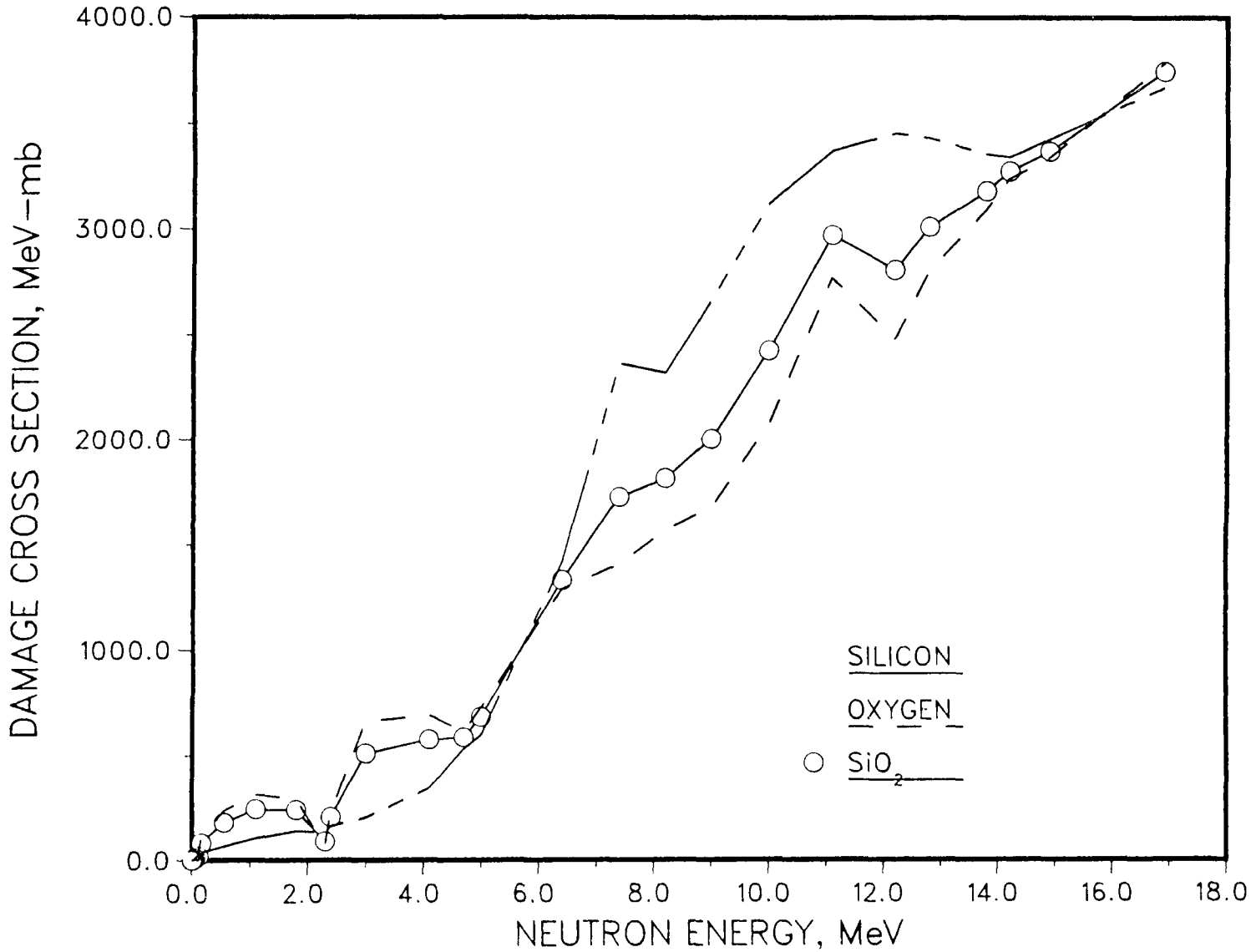

Figure 5. Ionization Cross Section for SiO_2 and its Components

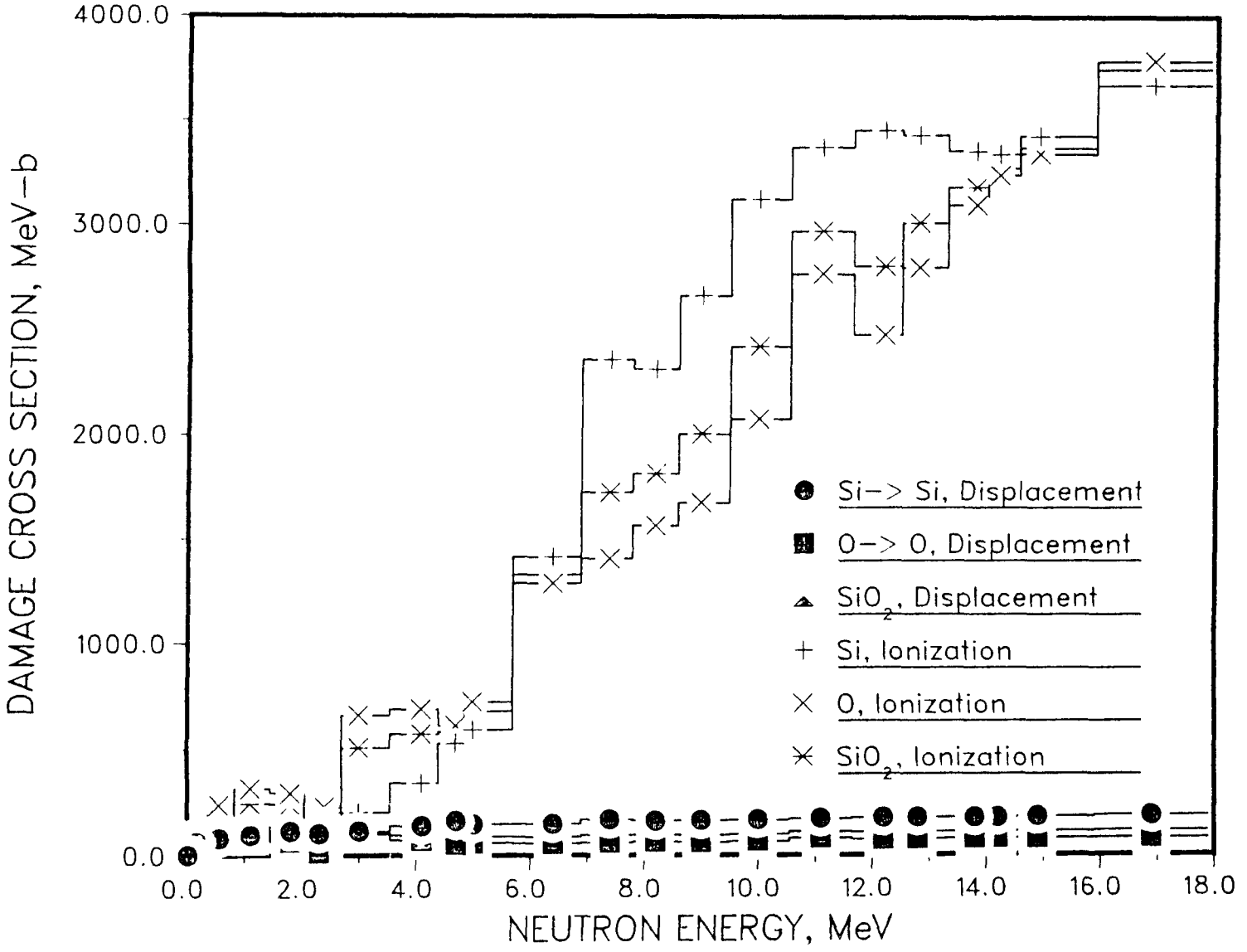

Figure 6. Displacement and Ionization Cross Section for SiO_2 and its Components

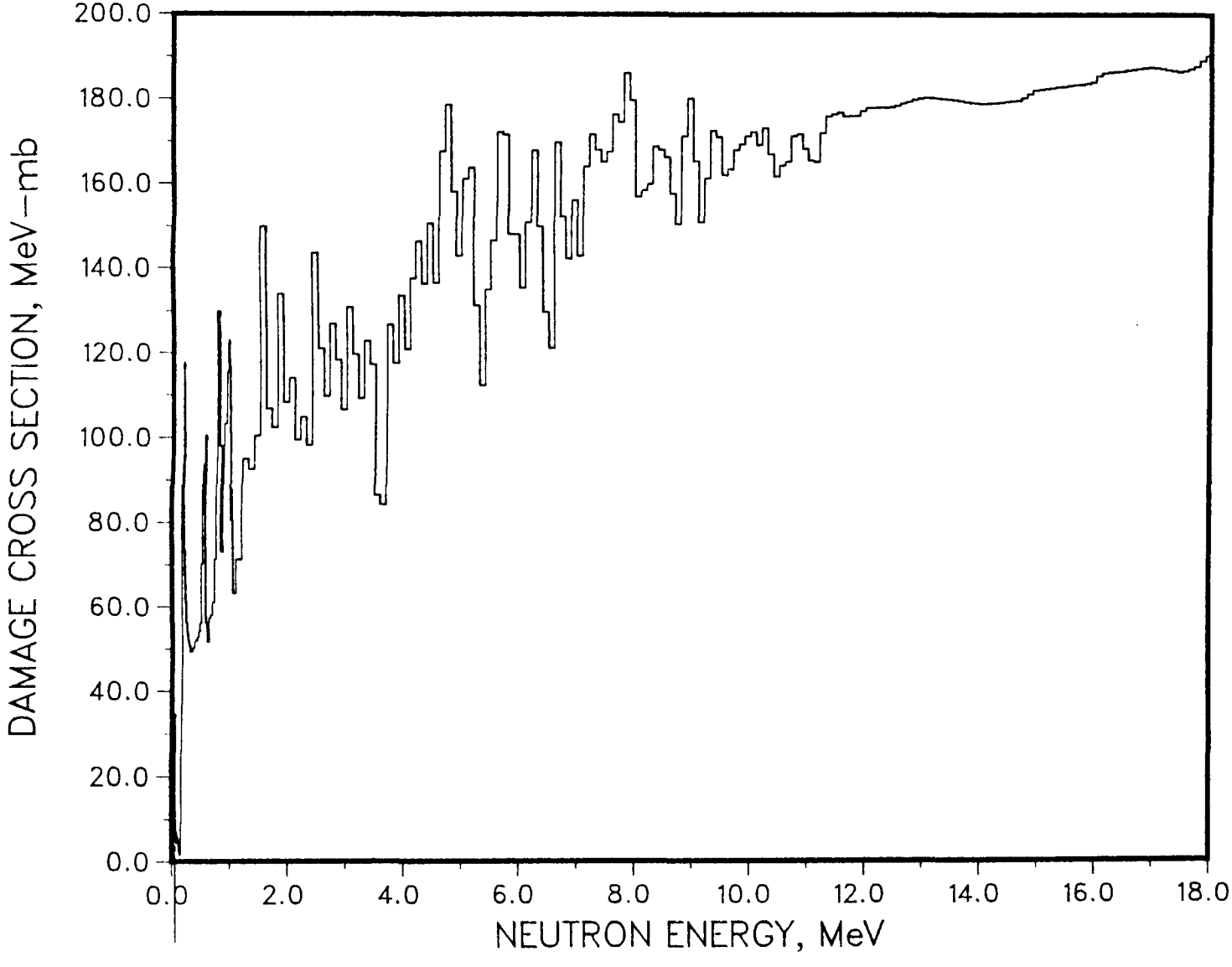

Figure 7. Silicon Displacement Damage-Energy Cross Section 300-Group Calculation

TABLE 1 . COMPARISON OF 1-MeV SILICON DISPLACEMENT DAMAGE FUNCTIONS

E Range (MeV)	*NJOY*	*ASTM*[a]	*ROGERS*[b]	*MESSENGER*[c]
19.6 - 16.9	2.13	2.37	2.25	2.28
16.9 - 14.9	2.06	2.31	2.25	2.26
14.9 - 14.2	2.01	2.26	2.25	2.25
14.2 - 13.8	2.00	2.26	2.25	2.24
13.8 - 12.8	2.01	2.25	2.25	2.23
12.8 - 12.2	1.99	2.23	2.25	2.22
12.2 - 11.1	1.95	2.17	2.12	2.21
11.1 - 10.0	1.88	2.07	2.12	2.18
10.0 - 9.05	1.85	2.06	1.96	2.16
9.05 - 8.19	1.83	1.84	1.96	2.14
8.19 - 7.41	1.91	1.89	1.82	2.11
7.41 - 6.38	1.68	1.74	1.82	2.07
6.38 - 4.97	1.66	1.93	1.93	2.00
4.97 - 4.72	1.83	2.03	1.79	1.94
4.72 - 4.07	1.57	1.69	1.79	1.90
4.07 - 3.01	1.29	1.30	1.30	1.80
3.01 - 2.39	1.32	1.73	1.70	1.65
2.39 - 2.31	1.15	1.51	1.61	1.57
2.31 - 1.83	1.29	1.69	1.63	1.49
1.83 - 1.11	1.07	0.926	0.913	1.25
1.11 - 0.550	0.914	0.866	0.873	0.838
0.550 - 0.158	0.682	0.656	0.576	0.387
0.158 - 0.111	3.45E-2	0.041	0.576	0.148
0.111 - 5.25E-2	9.64E-2	0.062	0.0529	0.0899
5.25E-2 - 2.48E-2	3.09E-2	0.030	0.0438	0.0425
2.48E-2 - 2.19E-2	2.42E-2	0.019	0.0438	0.0257
2.19E-2 - 1.03E-2	1.70E-2	0.015	0.0438	0.0777
1.03E-2 - 3.35E-3	7.51E-3	0.011	0.0428	7.51E-3
3.35E-3 - 1.23E-3	2.69E-3	0.011	2.50E-3	2.52E-3
1.23E-3 - 5.83E-4	1.08E-3	0.0	2.50E-3	9.97E-4
5.83E-4 - 1.01E-4	2.17E-4	0.0	4.72E-5	3.76E-4
1.01E-4 - 2.90E-5	2.42E-5	0.0	1.28E-4	7.15E-5
2.90E-5 - 1.07E-5	4.18E-5	0.0	9.75E-5	2.18E-5
1.07E-5 - 3.06E-6	7.32E-5	0.0	1.29E-4	7.57E-6
3.06E-6 - 1.13E-6	1.30E-4	0.0	2.17E-4	2.29E-6
1.13E-6 - 4.14E-7	2.16E-4	0.0	3.51E-4	8.31E-7
4.14E-7 - 1.00E-11	1.03E-2	0.0	9.28E-4	2.26E-7

a From ASTM 1985.

b From Rogers 1975.

c From Messenger 1968.

TABLE 2. DISPLACEMENT DAMAGE CROSS-SECTIONS FOR SILICON WITH THE FINE GROUP STRUCTURE (300-GROUP)

(MeV)	(MeV-mb)	(MeV)	(MeV-mb)	(MeV)	(MeV mb)
2 250E-05	3 005E-03	1 850E-02	1 852E+00	1 025E-01	5 047E+00
3 300E-05	2 415E-03	1 950E-02	1 928E+00	1 075E-01	4 649E+00
5 350E-05	1 924E-03	2 050E-02	2 001E+00	1 125E-01	4 256E+00
8 250E-05	1 581E-03	2 150E-02	2 077E+00	1 163E-01	3 732E+00
1 175E-04	1 367E-03	2 250E-02	2 134E+00	1 238E-01	2 948E+00
1 450E-04	1 467E-03	2 325E-02	2 206E+00	1 312E-01	2 189E+00
1 900E-04	7 350E-03	2 475E-02	2 312E+00	1 388E-01	1 619E+00
2 400E-04	1 888E-02	2 650E-02	2 392E+00	1 450E 01	1 928E+00
3 150E-04	3 152E-02	2 700E-02	2 480E+00	1 550E-01	9 248E+00
3 875E-04	4 261E-02	2 900E-02	2 617E+00	1 650E 01	3 680E+01
4 825E-04	6 227E-02	3 100E-02	2 747E+00	1 750E-01	9 361E+01
6 600E-04	8 190E-02	3 300E-02	2 878E+00	1 850E 01	1 176E+02
8 025E-04	1 080E 01	3 500E-02	2 996E+00	1 950E-01	1 013E+02
1 112E-03	1 437E-01	3 700E-02	3 068E+00	2 050E-01	8 439E+01
1 400E-03	1 752E 01	3 875E-02	3 628E+00	2 150E 01	7 362E+01
1 650E-03	2 270E-01	4 125E-02	3 127E+00	2 250E 01	6 741E+01
2 350E-03	2 954E-01	4 375E-02	2 918E+00	2 325E-01	6 143E+01
2 850E-03	3 812E 01	4 625E-02	2 673E+00	2 475E-01	5 615E+01
4 000E-03	4 805E-01	4 875E-02	2 203E+00	2 650E-01	5 374E+01
4 650E-03	6 152E-01	5 125E-02	1 267E+00	2 700E-01	5 203E+01
6 200E-03	8 079E-01	5 375E-02	3 461E+01	2 900E-01	5 088E+01
8 800E-03	9 832E-01	5 625E-02	2 120E+01	3 100E-01	4 931E+01
9 750E-03	1 050E+00	5 850E-02	9 212E+00	3 300E-01	4 934E+01
1 025E-02	1 095E+00	6 150E-02	7 397E+00	3 500E-01	5 014E+01
1 075E-02	1 140E+00	6 450E-02	6 731E+00	3 700E 01	5 050E+01
1 125E-02	1 179E+00	6 750E-02	7 326E+00	3 875E-01	5 182E+01
1 163E-02	1 230E+00	7 000E-02	6 718E+00	4 125E-01	5 213E+01
1 237E-02	1 302E+00	7 400E-02	6 438E+00	4 375E 01	5 286E+01
1 312E-02	1 374E+00	7 800E-02	6 203E+00	4 625E-01	5 424E+01
1 388E-02	1 439E+00	8 200E-02	6 119E+00	4 875E 01	5 612E+01
1 450E-02	1 514E+00	8 600E-02	5 925E+00	5 125E-01	7 022E+01
1 550E-02	1 606E+00	9 000E-02	5 713E+00	5 375E-01	9 353E+01
1 650E-02	1 690E+00	9 400E-02	5 505E+00	5 625E-01	1 005E+02
1.750E-02	1 774E+00	9 750E-02	5 310E+00	5 850E-01	5 612E+01

TABLE 2. - Continued

(MeV)	(MeV-mb)	(MeV)	(MeV-mb)	(MeV)	(MeV mb)
6 150E-01	5 158E+01	2 350E+00	9 813E+01	5 750E+00	1 715E+02
6 450E-01	5 727E+01	2 450E+00	1 434E+02	5 850E+00	1 480E+02
6 700E-01	5 808E+01	2 550E+00	1 209E+02	5 950E+00	1 479E+02
7 150E-01	6 108E+01	2 650E+00	1 096E+02	6 050E+00	1 353E+02
7 400E-01	7 133E+01	2 750E+00	1 269E+02	6 150E+00	1 509E+02
7 800E 01	1 299E+02	2 850E+00	1 182E+02	6 250E+00	1 679E+02
8 200E-01	9 796E+01	2 950E+00	1 064E+02	6 350E+00	1 498E+02
8 600E-01	7 302E+01	3 050E+00	1 308E+02	6 450E+00	1 297E+02
9 000E-01	1 032E+02	3 150E+00	1 195E+02	6 550E+00	1 211E+02
9 400E-01	1 154E+02	3 250E+00	1 091E+02	6 650E+00	1 698E+02
9 500E 01	1 223E+02	3 350E+00	1 228E+02	6 750E+00	1 522E+02
9 600E 01	1 230E+02	3 450E+00	1 171E+02	6 850E+00	1 421E+02
9 700E-01	1 168E+02	3 550E+00	8 643E+01	6 950E+00	1 561E+02
9 800E-01	1 075E+02	3 650E+00	8 422E+01	7 050E+00	1 427E+02
9 900E-01	1 010E+02	3 750E+00	1 267E+02	7 150E+00	1 641E+02
9 950E-01	9 386E+01	3 850E+00	1 174E+02	7 250E+00	1 717E+02
1 005E+00	8 836E+01	3 950E+00	1 336E+02	7 350E+00	1 680E+02
1 010E+00	8 526E+01	4 050E+00	1 208E+02	7 450E+00	1 651F+02
1 020E+00	8 047E+01	4 150E+00	1 376E+02	7 550E+00	1 676E+02
1 030E+00	8 777E+01	4 250E+00	1 462E+02	7 650E+00	1 764E+02
1 040E+00	8 053E+01	4 350E+00	1 363E+02	7 750E+00	1 745E+02
1 050E+00	6 323E+01	4 450E+00	1 506E+02	7 850E+00	1 862E+02
1 150E+00	7 131E+01	4 550E+00	1 365E+02	7 950E+00	1 796E+02
1 250E+00	9 500E+01	4 650E+00	1 677E+02	8 050E+00	1 569E+02
1 350E+00	9 244E+01	4 750E+00	1 786E+02	8 150E+00	1 584E+02
1 450E+00	1 004E+02	4 850E+00	1 580E+02	8 250E+00	1 599E+02
1 550E+00	1 498E+02	4 950E+00	1 427E+02	8 350E+00	1 688E+02
1 650E+00	1 066E+02	5 050E+00	1 611E+02	8 450E+00	1 680E+02
1 750E+00	1 023E+02	5 150E+00	1 638E+02	8 550E+00	1 662E+02
1 850E+00	1 339E+02	5 250E+00	1 312E+02	8 650E+00	1 576E+02
1 950E+00	1 081E+02	5 350E+00	1 122E+02	8 750E+00	1 505E+02
2 050E+00	1 140E+02	5 450E+00	1 350E+02	8 850E+00	1 713E+02
2 150E+00	9 944E+01	5 550E+00	1 465E+02	8 950E+00	1 802E+02
2 250E+00	1 048E+02	5 650E+00	1 722E+02	9 050E+00	1 653E+02

TABLE 2. - Continued

(MeV)	(MeV-mb)	(MeV)	(MeV-mb)	(MeV)	(MeV-mb)
9 150E+00	1 509E+02	1 235E+01	1 781E+02	1 485E+01	1 813E+02
9 250E+00	1 613E+02	1 245E+01	1 782E+02	1 495E+01	1 822E+02
9 350E+00	1 725E+02	1 255E+01	1 786E+02	1 505E+01	1 824E+02
9 450E+00	1 710E+02	1 265E+01	1 791E+02	1 515E+01	1 826E+02
9 550E+00	1 620E+02	1 275E+01	1 795E+02	1 525E+01	1 828E+02
9 650E+00	1 635E+02	1 285E+01	1 800E+02	1 535E+01	1 830E+02
9 750E+00	1 681E+02	1 295E+01	1 803E+02	1 545E+01	1 831E+02
9 850E+00	1 694E+02	1 305E+01	1 804E+02	1 555E+01	1 833E+02
9 950E+00	1 713E+02	1 315E+01	1 803E+02	1 565E+01	1 835E+02
1 005E+01	1 723E+02	1 325E+01	1 802E+02	1 575E+01	1 836E+02
1 015E+01	1 692E+02	1 335E+01	1 801E+02	1 585E+01	1 838E+02
1 025E+01	1 732E+02	1 345E+01	1 800E+02	1 595E+01	1 841E+02
1 035E+01	1 670E+02	1 355E+01	1 798E+02	1 605E+01	1 856E+02
1 045E+01	1 617E+02	1 365E+01	1 796E+02	1 615E+01	1 863E+02
1 055E+01	1 644E+02	1 375E+01	1 793E+02	1 625E+01	1 865E+02
1 065E+01	1 653E+02	1 385E+01	1 791E+02	1 635E+01	1 866E+02
1 075E+01	1 714E+02	1 395E+01	1 790E+02	1 645E+01	1 867E+02
1 085E+01	1 718E+02	1 396E+01	1 790E+02	1 655E+01	1 869E+02
1 095E+01	1 683E+02	1 397E+01	1 789E+02	1 665E+01	1 871E+02
1 105E+01	1 655E+02	1 398E+01	1 789E+02	1 675E+01	1 873E+02
1 115E+01	1 652E+02	1 399E+01	1 789E+02	1 685E+01	1 875E+02
1 125E+01	1 721E+02	1 399E+01	1 789E+02	1 695E+01	1 876E+02
1 135E+01	1 760E+02	1 401E+01	1 789E+02	1 705E+01	1 874E+02
1 145E+01	1 765E+02	1 401E+01	1 789E+02	1 715E+01	1 872E+02
1 155E+01	1 769E+02	1 405E+01	1 790E+02	1 725E+01	1 869E+02
1 165E+01	1 759E+02	1 415E+01	1 791E+02	1 735E+01	1 867E+02
1 175E+01	1 761E+02	1 425E+01	1 792E+02	1 745E+01	1 865E+02
1 185E+01	1 762E+02	1 435E+01	1 793E+02	1 755E+01	1 868E+02
1 195E+01	1 773E+02	1 445E+01	1 795E+02	1 765E+01	1 872E+02
1 205E+01	1 780E+02	1 455E+01	1 796E+02	1 775E+01	1 878E+02
1 215E+01	1 781E+02	1 465E+01	1 798E+02	1 785E+01	1 891E+02
1 225E+01	1 781E+02	1 475E+01	1 804E+02	1 795E+01	1 904E+02

DAMAGE EQUIVALENCE IN THE IRRADIATION OF SILICON

By

C. E. Lee
Technadyne Engineering Consultants, Inc.
P. O. Box 13928, Albuquerque, NM 87192

and

T. F. Luera
Sandia National Laboratories
P. O. Box 5800, Albuquerque, NM 87185

ABSTRACT

Displacement damage in silicon is evaluated for 13 displacement kerma models and 12 incident neutron energy-fluence spectral distributions. The integrals are performed interactively using an adaptive recursive Simpson integration technique in Turbo-Pascal which allows for any mixture of analytic and/or multigroup displacement kerma factors and spectral distributions. The radiation hardness parameter determined from the recent NJOY evaluation is compared with other known evaluations. The simulation fidelity, which depends on the ratio of the hardness parameter for the operational environment to that for the simulation environment, is evaluated and compared for these spectra and models. If NJOY is assumed to provide the correct neutron fluence ratio for the simulation, then the error introduced by using other kerma models is less than 10 percent except for the 14 MeV spectra.

INTRODUCTION

Fast burst reactors produce radiation environments which are used to evaluate the damage to specimens in comparable operational radiation environments (e.g., a nuclear weapon threat environment). For a proper simulation, the relationship between radiation damage produced in the reactor and that produced in the threat environment must be established accurately. The damage produced by neutrons can generally be characterized by a kerma factor, $K_D(E)$, which is proportional to the damage in the material of interest per unit fluence as a function of incident neutron energy. For neutron irradiation of silicon bipolar devices, the damage is proportional to the number of atomic displacements in silicon. In this instance $K_D(E)$ is that portion of the energy, deposited by recoil atoms in silicon, which goes into atomic collisions (as opposed to ionization and electronic excitation). In order to have equivalence between simulation and threat, the displacement dose due to simulation, $D_{simulation}$, at the reactor facility must be equal to (or equal some known multiple of, say, a) the threat displacement dose, D_{threat}:

$$D_{threat} = a \bullet D_{simulation}$$

$$D_{threat} = \int \phi_{threat}(E)\ K_D(E)\ dE \qquad (1)$$

$$D_{simulation} = \int \phi_{simulation}(E)\ K_D(E)\ dE$$

where $\phi(E)$ is the incident neutron spectrum.

A useful parameterization for comparison purposes can be made in terms of the radiation hardness parameter, HP. Assuming a knowledge of the neutron displacement kerma factor, $K_D(E)$, and the incident neutron spectrum, the neutron energy spectrum hardness parameter is given by[1,2,3]

$$HP = \phi_{eq}(E_o)/\phi = \frac{\int_{E_{min}}^{E_{max}} \phi(E)\ K_D(E)\ dE}{K_D(E_o) \int_{E_{min}}^{E_{max}} \phi(E)\ dE} \qquad (2)$$

where ASTM[3] recommends using $K_D(E_o) = 95$ MeV-mb at $E_o = 1$ MeV for 1 MeV equivalent (Si) fluence, $\phi_{eq}(1)$. The denominator terms in Equation 2 normalize the neutron spectrum hardness to the reference displacement kerma, $K_D(E_o)$, and the spectral integral. It is important not only to quote the value used for $K_D(E_o)$, and to

assure that the same $K_D(E)$ is used for the threat and simulation environments, but also to assure that the spectral normalization integral is performed and included in any analysis.

If the displacement doses (the 1 MeV fluences) are equal in both the threat and simulation environments, then the simulation fluence used by the experimentalist can be related to the threat fluence in terms of the radiation hardness parameter by

$$\phi_{simulation} = \phi_{threat} \, (HP_{threat}/HP_{simulation}) \qquad (3)$$

Because $K_D(E)$ is used to determine the threat dose as well as the simulation facility dose, the validity of the simulation depends on the ratio of the respective hardness parameters. Given that the threat and simulation neutron environments are well known, the simulation will be valid if the shape of $K_D(E)$ and the normalization of $K_D(E_o)$ used in establishing the threat and facility equivalent fluences are the same. A number of different 1-MeV normalization constants (e.g., $K_D(E_o)$ = 78, 84, and 95 MeV-mb) and different silicon $K_D(E)$ functions having somewhat different shapes have been in use. Additionally, small errors may also occur because of computational considerations, such as group structure and binning.

ANALYSIS

Several authors have previously addressed the determination of neutron spectrum hardness in silicon.[4-9] In 1984, Griffin, Zombola, and Grange[4] reported a review evaluation of the neutron displacement kerma in silicon. The review inclued the $K_D(E)$ used for a previous Kaman Sciences Corp. (KSC) PKSC[4] evaluation, ASTM,[1] New and Old Messenger,[4,7,8] Wicklund,[8] RSIC,[4,10] Bendel,[5] Rogers,[6] and Smith.[4,11] These $K_D(E)$ were given in a 37 group format in Table 2 of Reference 4. In 1985, Greenwood and Smither[9] reported a new analysis with the SPECTER code of a number of materials including silicon. Also in 1985, Lazo[12] performed an evaluation of the silicon displacement kerma using the NJOY code, which we compare with other analyses.

Messenger suggested an analytic approximation to $K_D(E)$ in the form

$$K_D(E) = A*E*(1.0-e^{-B/E}) \qquad (4)$$

where the parameters A and B were determined by a least squares fitting process. For the New and Old Messenger models, these parameters have the values[4,7,8] (A,B)=(1.10, 2.2) and (1.02, 3.6), respectively.

The K_D values supplied in Table 2 of Reference 4 for Old Messenger and New Messenger 37 group structure correspond to these analytic fits evaluated at the midpoint of each (37 group) neutron energy interval. Additionally, $K_D(E)$ is available from ASTM[2,3] in a 258 point group format, from an NJOY calculation by Lazo[12] in 283 group format, and from a SPECTER 100 group calculation.[9]

The neutron spectra for 14 MeV[4,10], RSIC Thermonuclear,[4,10] RSIC Fission (^{238}U),[4,10] and ENDF/B-V Delayed neutron source number fractions were given in 37 group format in Table 3 of Reference 4. The Annular Core Research Reactor (ACRR) bare cavity, the Sandia Pulsed Reactor (SPR-III) cavity, SPR-III leakage, and White Sands Missile Range Fast Burst Reactor (WSMR-FBR) leakage spectra used in this analysis were supplied in 621 group format from SAND-II calculations by Kelly.[15]

An analytic Maxwellian fission plus Gaussian 14 MeV spectra is available in NJOY[13] in the form (note that in Equation 5 only, E has units of eV, not MeV)

$$X(E) = 2.32472E\text{-}12\ E^{1/2}\ \exp(-E/1.4E6) + 2.51697E\text{-}11\ \exp(-5.0\ [(E/2.5E4)^{1/2}-(1.407E7/2.5E4)^{1/2}]^2) \quad (5)$$

The neutron spectra for ^{235}U fission and ^{252}Cf spontaneous fission have been given by Grundl and Eisenhaver[14] in the analytic form

$$X(E) = M(E)f(E) \quad (6)$$

where the Maxwellian is defined by

$$M(E) = A\ (E)^{1/2}\ e^{-BE/C} \quad (7)$$

with the parameters A, B, and C given in Table 1.

Table 1

MAXWELLIAN SPECTRAL PARAMETERS[14]

	A	B	C
^{235}U	0.7501	1.5	1.97
^{252}Cf	0.6672	1.5	2.13

The spectral correction factors, f(E), as determined by least squares fitting, are listed in Table 2.

Table 2

SPECTRAL CORRECTION FACTORS f(E)[14]

Energy Range E_{min}	E_{max}	$f\text{-}^{235}U$	$f\text{-}^{252}Cf$
0.0	0.25	1 + 0.8E - 0.153	1.0 + 1.2E - 0.37
0.25	0.8	1 - 0.14E + 0.082	1.0 - 0.14E + 0.098
0.8	1.5	1 + 0.04E - 0.062	1.0 + 0.024E - 0.0332
1.5	6.0	1 + 0.01E - 0.017	1.0 - 0.00064E + 0.0037
6.0	∞	1.043 exp(-0.06(E-6.0)/1.043)	1.0 exp(-0.03(E-6.0)/1.0)

For the parameter values quoted in Equation 5 and in Tables 1 and 2, the X(E) definition requires renormalization in order to ensure that $\int_0^\infty X(E) = dE = 1$. This spectral renormalization is equivalent to including the integral in the denominator of Equation 2 if $[E_{min}, E_{max}] = [0, \infty]$. For a different $[E_{min}, E_{max}]$ range the normalization would be modified. Thus, one may redefine the $\emptyset(E)$ by such a renormalization, omitting the integral in the denominator, or include it. However, it would be incorrect to omit the renormalization and also to omit the integral in the denominator of Equation 2.

If the required integrations only involved the 37 group structure, as in Reference 4, then the radiation hardness parameter would be given by

$$\emptyset_{eq}(E_o)/\emptyset = \sum_{i=1}^{37} K_{Di}\,\emptyset_i \;/\; K_D(E_o) \sum_{i=1}^{37} \emptyset_i \qquad (8)$$

However, the data treated here also involves other group structures (37, 100, 258, 283, and 621 groups) as well as analytic expressions for the Messenger models of $K_D(E)$ and the neutron spectra for 14 MeV, NJOY Fission, ^{235}U, and ^{252}Cf. Thus, a more general approach is required.

The radiation hardness parameter integrals were determined using a recursive adaptive Simpson rule integration technique recently developed in Turbo-Pascal 3.0 with 8087 math coprocessor support (16 digits, exponent range $\pm$ 308) on an AT&T 6300 and IBM-AT. Typical total CPU times for a specific integral evaluation in this analysis were the order of 0.3 to 3.0 min.

This integration technique includes options for the Hewlett-Packard transformation, error indicators on computational significance loss, and additional automatic spectrum subdivision to sense functions defined on a narrow subinterval of the total range. Extensive validation

1. Correctly reproduced a large number of known functions (including Bessel functions of the 1st and 2nd kind, exponential integrals of order n, incomplete gamma functions, error functions, airy integrals, Sievert and Dawson integrals, and Elliptic integrals of the 1st, 2nd, and 3rd kind) from their kernels; and,

2. Correctly reproduced multigroup integral results of product functions in multigroup or analytic form, defined over different group structures.

Using this Integrator program, the results for the 37 group $K_D(E)$ representations were compared with the group sum method and yielded excellent agreement. The situation of both K_D and $\emptyset(E)$ being analytic functions was validated. The case of either overlapping different group structure products or products of an analytic and group structure form was validated. Automatic submesh refinements were implemented to assure that the Integrator program could successfully deal with a product function, $K_D\emptyset$, vanishing at both end points and being nonzero at only a few selected interior points, a characteristic exhibited by some products.

In Table 3 we compare the radiation hardness parameters given in Reference 4 with the values obtained by integral evaluation of $\emptyset_{eq}(E_o)/\emptyset$, which correctly includes the spectral normalization term on the energy range $[0, \infty]$. These results agree exactly with the corresponding group summed results. We were only able to exactly reproduce group sums of Reference 4 or Integrator values if the denominator spectral normalization integral in Equation 2 was omitted, which is incorrect, of course. However, the variations are only 0.1 percent, 0.04 percent, 0.3 percent and 1.2 percent, respectively, for the 14 MeV, ^{238}U, Thermonuclear, and Delayed neutron spectra. These small differences would translate directly into additional uncertainties in $\emptyset_{eq}(E_o)/\emptyset$.

Table 3

$\phi_{eq}(E_o)/\phi$

COMPARISON OF KSC 37 GROUP SUM RESULTS AND NORMALIZED SPECTRAL INTEGRATOR

Damage Model	Neutron Spectrum			
	14 MeV	U-238 Fission	Thermo-nuclear	Delayed
ASTM81	2.260	0.833	0.675	0.578
with norm	2.257	0.833	0.675	0.578
RSIC DLC-31	2.486	0.846	0.733	0.653
with norm	2.486	0.846	0.731	0.646
Bendel	1.622	0.756	0.573	0.557
with norm	1.620	0.756	0.580	0.551
Rogers	2.256	0.827	0.682	0.590
with norm	2.250	0.827	0.679	0.584
DNA Smith	2.498	0.854	0.690	0.542
with norm	2.496	0.854	0.687	0.536
New Messenger	2.240	0.855	0.694	0.455
with norm	2.240	0.855	0.687	0.450
Old Messenger	3.237	0.969	0.874	0.440
with norm	3.237	0.969	0.871	0.435
X(E) norm factor	0.9987	0.9996	0.9966	0.9880

RESULTS AND COMPARISONS

In Table 4 we summarize the radiation hardness parameter results on the energy range [0.01, 18.0] MeV using the Integrator for 13 damage models. These models include those of Table 3, and, as well, the analytic New Messenger and Old Messenger, and the multi-group ASTM83, SPECTER, and NJOY models. Several analytic spectra are also included: ^{235}U fission and ^{252}Cf spontaneous, the NJOY fission and 14 MeV spectra. The 621 group ACRR bare cavity, SPR-III leakage and cavity, and WSMR-FBR leakage spectra were derived from SAND-II calculations.[15] The results are ordered in terms of increasing radiation hardness parameter for NJOY. The spectra labeled "NJOY Fission" and "NJOY 14 MeV" are the corresponding fission and 14 MeV components of Equation 5. The NJOY Fission results are bounded by those of ^{235}U and ^{252}Cf.

Table 4

RADIATION HARDNESS PARAMETER OF SILICON FOR VARIOUS DAMAGE MODELS AND NEUTRON SPECTRA
$[E_{min}, E_{max}]$ = [0.01, 18.0] MeV

DAMAGE MODEL	NEUTRON SPECTRUM											
	Delayed	ACRR bare	Thermo-nuclear	^{238}U Fiss	SPRIII Leak	WSMRFBR Leak	SPRIII Cavity	^{235}U Fiss	NJOY Fiss	^{252}Cf Fiss	37Grp 14MeV	NJOY 14MeV
PKSC	0.565	0.802	0.877	0.948	0.981	0.959	1.017	1.285	1.311	1.316	2.968	2.989
37 group	-1% *	17%	28%	24%	17%	14%	17%	24%	25%	25%	57%	58%
ASTM81	0.578	0.747	0.764	0.833	0.920	0.933	0.955	1.163	1.187	1.195	2.257	2.258
37 group	2%	12%	12%	9%	10%	11%	10%	12%	13%	13%	19%	20%
RSIC DLC-31	0.646	0.762	0.809	0.845	0.930	0.940	0.969	1.142	1.164	1.171	2.486	2.491
37 group	14%	12%	18%	11%	11%	11%	12%	10%	10%	10%	31%	32%
Bendel	0.551	0.678	0.646	0.755	0.835	0.840	0.867	1.037	1.055	1.061	1.620	1.615
37 group	-3%	-0.7%	-6%	-1%	-0.6%	-0.5%	0.1%	0.2%	0%	0%	-14%	-14%
Rogers	0.584	0.757	0.764	0.826	0.917	0.931	0.941	1.151	1.176	1.183	2.250	2.250
37 group	3%	11%	12%	8%	9%	10%	9%	11%	12%	12%	19%	19%
DNA Smith	0.536	0.754	0.777	0.853	0.917	0.914	0.941	1.180	1.204	1.211	2.496	2.514
37 group	-6%	10%	13%	12%	9%	8%	9%	14%	14%	14%	32%	33%
New Messenger	0.450	0.749	0.784	0.855	0.917	0.918	0.932	1.230	1.261	1.269	2.240	2.242
37 group	-21%	14%	14%	12%	9%	9%	8%	18%	19%	19%	18%	19%
Analytic	0.449	0.734	0.783	0.852	0.902	0.901	0.917	1.224	1.256	1.264	2.239	2.240
New Messenger	-21%	7%	14%	12%	7%	7%	6%	18%	19%	19%	18%	19%
Old Messenger	0.435	0.841	0.988	0.969	1.041	1.053	1.047	1.442	1.490	1.501	3.237	3.240
37 group	-24%	23%	44%	27%	24%	25%	21%	39%	41%	42%	71%	72%
Analytic	0.434	0.823	0.986	0.965	1.022	1.033	1.027	1.432	1.481	1.492	3.236	3.240
Old Messenger	-24%	20%	44%	26%	22%	22%	19%	38%	41%	41%	71%	72%
ASTM83-L	0.573	0.736	0.760	0.824	0.907	0.922	0.939	1.149	1.173	1.181	2.260	2.261
261 points	1%	8%	10%	8%	8%	9%	8%	11%	11%	11%	19%	20%
ASTM83-M	0.560	0.726	0.755	0.815	0.894	0.911	0.928	1.135	1.160	1.168	2.259	2.261
260 groups	-2%	6%	10%	7%	6%	8%	7%	10%	10%	10%	19%	20%
SPECTER	0.561	0.688	0.694	0.765	0.840	0.843	0.864	1.038	1.057	1.062	2.020	2.021
101 points	-1%	1%	1%	0.1%	0%	-0.1%	-0.2%	0%	0.3%	0.2%	7%	7%
NJOY 283 grp	0.569	0.683	0.685	0.764	0.840	0.844	0.866	1.035	1.054	1.060	1.892	1.888

* Percentage deviation from NJOY result.
All results normalized to $K_D(E_o)$ = 95.0 MeV-mb.

For comparison purposes the percentage deviation of the various damage models from the NJOY results (normalized to $K_D(E_o)$ = 95 MeV-mb) are indicated beneath the radiation hardness parameters in Table 4.

The SPECTER (100 group) and NJOY (238 group) results agree quite well for all the neutron spectra considered here with a variation of $\pm$ 1 percent in the radiation hardness parameter, except for the 14 MeV spectrum, where there is a maximum variation of 7 percent. Even then the agreement between SPECTER and NJOY is better than with any other damage model calculated.

The ASTM83 kerma data given in Reference 2 are presented in point format as $K_D(E_i)$ vs E_i, $1 \leq i \leq 261$. Linear interpolation between data points would seem to be implied and justified. This linear modeling is denoted ASTM83-L. It is also feasible to interpret the data as in the SAND-II multigroup modeling, matching the point data energies with the SAND-II energy boundaries. That modeling should be in agreement with SAND-II calculated results and is denoted ASTM83-M.

The ASTM83-M radiation hardness parameter results in Table 4, excluding the 14 MeV spectra, indicate a -2 percent to 10 percent variation for the spectra considered when compared to NJOY results. It is noted that the calculated radiation hardness parameters for the ACRR, SPR-III Leakage, WSMR-FBR Leakage, and SPR-III Cavity have values of 0.726, 0.894, 0.911, and 0.928, respectively. These results were obtained using the SAND-II derived spectra[15] and the ASTM83-M kerma. The corresponding SAND-II independently determined radiation hardness parameters[15] have values of 0.726, 0.895, 0.911, and 0.928, respectively. The Integrator results for these four different spectra are identical with SAND-II results except for the SPR-III Leakage spectrum, where the radiation hardness parameter difference is 0.001.

The ASTM83-L model uses linear interpolation between the ASTM83 point kerma data defined on the energy interval [0.01, 18.0] MeV. The ASTM83-L results have 1-2 percent larger radiation hardness parameter values than ASTM83-M, the multigroup model.

The ASTM81 kerma are a 37 group approximation of the ASTM representation. The ASTM81 model radiation hardness parameters are typically 1-2 percent larger than ASTM83-L and 2-13 percent larger than the NJOY 283 group results, excluding the 14 MeV spectra results. The 14 MeV results differ from NJOY by about 20 percent.

Ordering the ASTM models as ASTM83-M, ASTM83-L, and ASTM81, the radiation hardness parameters differ by about 0.01 to 0.016 between models for the same spectrum. This represents a 2-3 percent relative difference due to the group structure and modeling assumptions.

Many of the damage models (except SPECTER) have a deviation greater than 10 percent from the NJOY results for 14 MeV spectra.

These variations between NJOY and other models for the 14 MeV spectra represent an area of potential modeling concern. Comparing the radiation hardness parameter using the 37 group and analytic 14 MeV spectrum (the rightmost two columns of Table 4), the results for the "14 MeV 37 group" and "14 MeV NJOY" analytic spectra differ by less than 1 percent. Thus, the multigroup 14 MeV spectrum approximation is probably not the primary cause of any significant variation in the results. Rather, the disagreements are more likely due to the physics approximations associated with the damage model kerma spectra treatment.

The Bendel and NJOY models show good agreement with a variation of 6 percent to 1 percent, except for the 14 MeV spectra results (-14 percent). The Bendel result for the 14 MeV spectra differs by 39 percent from ASTM83-M. The Bendel kerma reported in Reference 4 had been collapsed to 37 groups from 61 group kerma data.

The ASTM81 and Rogers results are quite consistent, differing from each other by about 1 percent to 2 percent. The Rogers model has a spectral variation of 3 percent to 12 percent compared to NJOY, excluding the 14 MeV spectrum, where the difference is about 19 percent.

The DNA-Smith results are typically 1-3 percent higher than the ASTM81 results and differ from the NJOY results by 8-14 percent, except for the Delayed (-6 percent) and 14 MeV spectra (33 percent).

The Messenger (New and Old) 37 group and analytic expressions agree well with each other, indicating the multigroup approximation used for this displacement kerma does not introduce any serious errors. However, the deviations from NJOY are -21 percent to 19 percent for New Messenger and -24 percent to 72 percent for Old Messenger.

In the radiation hardness parameters reported in Table 4 the energy integration range was $[E_{min}, E_{max}]$ = [0.01, 18.0]. If, instead, we had used the range [1.0E-11, 18.0] MeV, as in Reference 4, the results for the Delayed, ^{235}U, ^{238}U, ^{252}Cf, and 14 MeV spectra would be substantially the same because of the small spectral contribution in that data below 0.01 MeV.

However, the situation is not this simple for the Thermonuclear, ACRR, SPR-III, and WSMR-FBR spectra. In Table 5 we compare the radiation hardness parameters (HP_B/HP_A in Table 5) for selected damage models and spectra on two different energy intervals: A = [0.01, 18.0] MeV and B = [2.5E-8, 18.0] MeV. The ^{238}U, SPR-III Cavity, and ^{235}U spectra have radiation hardness parameter variations of less than 0.1 percent for E_{min} = 0.025 eV and 0.01 MeV. This indicates very little sensitivity to the specific E_{min} value for these spectra. However, the ACRR, Thermonuclear, SPR-III Leakage, and WSMR-FBR Leakage spectra on [2.5E-8, 18.0] MeV result in radiation hardness parameter changes of 36 percent,

Table 5

COMPARISON OF HARDNESS PARAMETERS AND RELATIVE SILICON DAMAGE CONTRIBUTION (R) FOR E_{min} = 10 keV and 0.025 eV

NEUTRON SPECTRUM

DAMAGE MODEL	ACRR	Thermo-nuclear	^{238}U Fiss	SPR-III Leakage	WSMRFBR Leakage	SPR-III Cavity	^{235}U Fiss
S_{AB}-1	0.642	0.881	1.000	0.983	0.970	1.000	1.000
ASTM83-L HP_A	0.736	0.760	0.824	0.907	0.922	0.939	1.149
HP_B	0.472	0.670	0.824	0.891	0.894	0.938	1.148
HP_{B_R}/HP_A	0.641	0.882	1.000	0.982	0.970	0.999	0.999
	1.00	1.00	1.00	1.00	1.00	1.00	1.00
ASTM83-M	0.726	0.755	0.815	0.894	0.911	0.928	1.135
	0.467	0.665	0.815	0.879	0.883	0.927	1.135
	0.643	0.881	1.000	0.983	0.969	0.999	1.000
	1.00	1.00	1.00	1.00	1.00	1.00	1.00
SPECTER	0.688	0.694	0.765	0.840	0.843	0.864	1.038
	0.442	0.613	0.765	0.826	0.817	0.863	1.038
	0.642	0.883	1.000	0.983	0.969	0.999	1.000
	1.00	1.00	1.00	1.00	1.00	1.00	1.00
NJOY	0.683	0.685	0.764	0.840	0.844	0.866	1.035
	0.439	0.605	0.764	0.825	0.818	0.866	1.035
	0.643	0.883	1.000	0.982	0.969	1.000	1.000
	1.00	1.00	1.00	1.00	1.00	1.00	1.00

HP_A calculated on [0.01, 18.0] MeV
HP_B calculated on [0.025 eV, 18.0 MeV]

12 percent, 2 percent, and 3 percent, respectively, in NJOY and SPECTER. These apparent variations could be significant for some applications.

In order to understand the difference in the hardness parameter calculated for two different energy ranges, $[E_{min}, E_{max}]$, we define A = [10 keV, 18.0 MeV] and B = [0.025 eV, 18.0 MeV], and rewrite Equation 2 as

$$HP_x = \frac{\int_x K_D(E)\phi(E)\,dE}{K_D(E_o)\int_x \phi(E)\,dE} \qquad (9)$$

where the range x = A or B. If we define the ratio of the spectral integrals as

$$S_{AB} = \int_B \phi(E)\, dE \;/\; \int_A \phi(E)\, dE \qquad (10)$$

and

$$R = HP_A/HP_B/S_{AB} = \int_A K_D(E)\phi(E)\, dE \;/\; \int_B K_D(E)\phi(E)\, dE \qquad (11)$$

then the quantity (1-R) is a measure of the damage contribution from neutrons below 10 keV.

In Table 5 we summarize the evaluations of HP_A, HP_B, HP_B/HP_A, S_{AB}^{-1}, and R for the ASTM83-Linear, ASTM83-Multigroup, SPECTER, and NJOY models in the ACRR, Thermonuclear, ^{238}U fission, SPR-III Leakage, WSMR-FBR Leakage, SPR-III Cavity, and ^{235}U fission spectra.

As a point of reference, we recall that the calculations on the energy interval [0.01, 18.0] MeV reported in Table 4 reproduce the SAND-II hardness parameter results for the ASTM83-M model and the ACRR, SPR-III Leakage, WSMR-FBR Leakage, and SPR-III Cavity, as one would expect.

Clearly, the hardness parameters in Table 5 can sometimes change dramatically due to the minimum energy, E_{min}, of the energy interval being reduced from 10 keV to thermal (0.025 eV). For the ACRR spectrum and NJOY damage model there is almost a 36 percent reduction effect in the hardness parameter (HP_B/HP_A in Table 5), whereas for ^{238}U, ^{235}U, and the SPR-III Cavity spectra there are no significant changes.

Examining the definition of the hardness parameter in Equation 9, there are two contributing integral factors: the integral in the numerator and denominator. As the energy interval is increased, the flux integral in the denominator will increase, which will tend to reduce the HP. This turns out to be the major effect here.

Similarly, the flux weighted kerma integral in the numerator will increase or remain constant as the energy interval is increased depending on the range of definition of the kerma. For ASTM83 the numerator integral remains constant since K_D is zero outside the energy range [10 keV, 18.0 MeV]. For NJOY and SPECTER, however, the kerma is non-zero below 10 keV, and, thus, the numerator term would be increased somewhat ($\leq$ 0.2 percent) for E_{min} = 0.025 eV.

Taking into account the spectral normalization factors, S_{AB}, the damage contribution due to this energy interval change, R, is essentially negligible, being well below the 1 percent level. Thus,

the main contribution to the reduction of hardness parameter in changing the lower energy bound from 10 keV to 0.025 eV must be due to the denominator normalization integral since the ratio, R, of the flux weighted K_D integrals in the HP numerator (Equation 9) is essentially unity (1.00) for the cases considered here.

Thus, although the hardness parameter can change dramatically for different E_{min}, here the entire effect is due entirely to the spectral normalization integral and does not imply any significant change in the spectral integrated K_D.

It may not always be or seem appropriate to only use a 10 keV lower energy cutoff for all radiation hardness evaluations, especially if there is a large thermal spectral component that is not experimentally filtered out. The radiation hardness parameter changes resulting from including contributions to the kerma and spectra with energies below 10 keV can sometimes be quite large. However, these altered results should be examined carefully to determine the relative contributions of the spectral normalization and the spectral weighted K_D integrals since the spectral normalization integral change could be the dominant effect.

CONCLUSIONS

The radiation hardness parameters in Table 4 (the relative effectiveness of neutrons in the spectrum producing damage in silicon as compared to 1 MeV neutrons) were compared to those obtained with the NJOY calculated $K_D(E)$ on [0.01, 18.0] MeV. Some values in Table 4 differ significantly from the NJOY values. For example:

> RSIC DLC-31 and DNA Smith differ by 18 percent and 13 percent, respectively, from the NJOY result for a reference thermonuclear spectrum. ASTM83 differs by 12 percent for the thermonuclear spectrum and 20 percent at 14 MeV, but otherwise provides agreement in the range of 2 percent to 12 percent. It is noteworthy that for the same spectra the Bendel model differs by -6 percent and -14 percent and agrees extremely well for the other spectra. Additionally, the SPECTER results differ by 1 percent for the thermonuclear spectrum, 7 percent for the 14 MeV, and by only 1 percent for all other spectra.

When used with an operational environment spectrum significant errors in hardness parameter can affect survivability estimates, the estimated range to a specified environment, and the balancing of weapon damage criteria. For some of the representative environments addressed in Table 4, the uncertainties are large enough to be of concern in vulnerability applications.[4]

The usual energy range taken for radiation hardness parameter estimates is [0.01, 18.0] MeV. While this energy range is usually appropriate and yields satisfactory results for many spectra, there are exceptions. The Thermonuclear and ACRR spectra indicate a sensitivity to the value chosen for E_{min}. As shown in Table 5, the choice of E_{min} = 0.025 eV (neutron thermal energy) can lead to significantly different radiation hardness parameter predictions (12 percent to 36 percent) for some spectra while others change hardly at all. However, as shown for the cases examined here, this is a spectral normalization effect and does not represent any significant contribution to damage from neutrons below 10 keV.

An error in the hardness parameter does not necessarily result in a significant error in simulation testing. Simulation fidelity, which is dependent on the ratio of hardness parameters in the operational environment to that for the simulation environment, is addressed in Table 6, where $[E_{min}, E_{max}]$ = [0.01, 18.0] MeV. For each representation of the silicon $K_D(E)$, the ratio of the hardness parameters of Table 4 is given for various simulations. The ratio at the top of each column is to be read as the simulation of "numerator environment" with "denominator facility." For example, column 3 of Table 6 represents the simulation of a Thermonuclear (Th) environment with the Annular Core Research Reactor (ACRR) using the given $K_D(E)$ in establishing the operational and simulation environments. Percentages listed under the ratios represent the deviations from the hardness parameter ratio obtained by the NJOY calculation. If the NJOY calculated $K_D(E)$ is assumed to be correct, this percentage is also the error introduced by using the "wrong" $K_D(E)$. These errors result from differences in the shape of the $K_D(E)$ used and not in their normalization, $K_D(E_o)$. The data in Table 6 show that, except for the extreme case of trying to simulate a 14 MeV environment with a reactor, most damage models produce neutron spectrum fidelity to within about 10 percent of either the NJOY or SPECTER results. The NJOY and SPECTER results, except for the 14 MeV spectra, agree to $\pm$ 1 percent. This conclusion assumes that the $[E_{min}, E_{max}]$ = [0.01, 18.0] MeV is an adequate representation.

There are many other potential sources of uncertainty in neutron damage simulation including uncertainties in dosimetry which are not addressed here. However, errors that may have resulted from the use of different damage functions by users and the facility operators can be evaluated with the data of Table 4. Evaluation of errors in normalization (e. g., use of a different value for $K_D(E_o)$ at 1 MeV) is straightforward.

Table 6

NEUTRON SIMULATION FIDELITY
$[E_{min}, E_{max}] = [0.01, 18.0]$ MeV

DAMAGE MODEL	Th / ^{252}Cf	Th / SPR-L	^{238}U / SPR-L	Th / ACRR	^{235}U / SPR-L	^{235}U / ^{238}U	^{252}Cf / ACRR	14 MeV / ^{252}Cf	14 MeV / SPR-L	14 MeV / ACRR
PKSC	0.66	0.89	0.97	1.09	1.31	1.36	1.64	2.26	3.03	3.70
	3%	9%	7%	9%	7%	0%	6%	26%	35%	34%
ASTM 81	0.64	0.83	0.91	1.02	1.26	1.40	1.60	1.89	2.45	3.02
	-2% *	1%	0%	2%	2%	3%	3%	6%	9%	9%
RSIC	0.69	0.87	0.91	1.06	1.23	1.35	1.54	2.12	2.67	3.26
	6%	9%	0%	6%	-0%	-1%	-0.6%	18%	19%	18%
Bendel	0.61	0.77	0.90	0.95	1.24	1.37	1.57	1.53	1.94	2.39
	0%	-6%	-1%	-5%	0.8%	1%	1%	-15%	-14%	-14%
Rogers	0.65	0.83	0.90	1.01	1.26	1.39	1.56	1.90	2.45	2.97
	0%	1%	-1%	1%	2%	2%	0.6%	6%	9%	7%
DNA-Smith	0.64	0.85	0.93	1.03	1.29	1.38	1.61	2.06	2.72	3.31
	-2%	4%	2%	5%	5%	2%	4%	15%	21%	20%
New Messenger	0.62	0.86	0.93	1.05	1.34	1.44	1.69	1.77	2.44	2.99
	-5%	5%	2%	5%	9%	6%	9%	-1%	8%	7%
Analytic New Messenger	0.62	0.87	0.95	1.07	1.36	1.44	1.72	1.77	2.48	3.05
	-5%	6%	4%	7%	11%	6%	11%	-1%	10%	10%
Old Messenger	0.66	0.95	0.93	1.18	1.39	1.49	1.79	2.16	3.11	3.85
	2%	16%	2%	18%	13%	10%	16%	21%	38%	39%
Analytic Old Messenger	0.66	0.97	0.94	1.20	1.40	1.48	1.81	2.17	3.17	3.93
	2%	18%	3%	20%	14%	9%	17%	21%	41%	42%
ASTM83-L	0.64	0.84	0.91	1.03	1.27	1.39	1.61	1.91	2.49	3.07
	-2%	2%	0%	3%	3%	2%	4%	7%	11%	11%
ASTM83-M	0.65	0.85	0.91	1.04	1.27	1.39	1.61	1.93	2.53	3.11
	0%	4%	0%	4%	3%	2%	4%	8%	12%	12%
SPECTER	0.65	0.83	0.91	1.01	1.24	1.36	1.54	1.90	2.41	2.94
	0%	1%	0%	1%	1%	0%	-0.6%	6%	7%	6%
NJOY	0.65	0.82	0.91	1.00	1.23	1.36	1.55	1.78	2.25	2.76

* Percentage deviation from NJOY result.

ACKNOWLEDGMENTS

The authors wish to express their thanks to Drs. J. G. Kelly (SNL), M. L. Lazo (UNM), D. Muir (LANL), and R. MacFarlane (LANL) for kindly supplying their data to us prior to publication.

REFERENCES

1. "Standard Practice for Characterizing Neutron Energy Fluence Spectra in terms of an Equivalent Monoenergetic Neutron Fluence for Radiation-Hardness Testing of Electronics," Annual Book of ASTM Standards, Vol 12.02, E 722-80, National Standards, American Society for Testing and Materials, Philadelphia, PA, 1981.

2. "Standard Practice for Characterizing Neutron Energy Fluence Spectra in terms of an Equivalent Monoenergetic Neutron Fluence for Radiation-Hardness Testing of Electronics," Annual Book of ASTM Standards, Vol 12.02, E 722-80, National Standards, American Society for Testing and Materials, Philadelphia, PA, 1983.

3. "Standard Practice for Characterizing Neutron Energy Fluence Spectra in terms of an Equivalent Monoenergetic Neutron Fluence for Radiation-Hardness Testing of Electronics," Annual Book of ASTM Standards, Vol 12.02, E 722-85, National Standards, American Society for Testing and Materials, Philadelphia, PA, 1985.

4. P. J. Griffin, R. Zombola, and G. Grange, "The Effect of Uncertainty in the Silicon Displacement Damage Function on Nuclear Environment Predictions," Kaman Sciences Corp. report K-84-102U(R) 1984.

5. W. Bendel, "Displacement and Ionization Fractions of Fast Neutron Kerma in TLDs and Si," IEEE Transactions on Nuclear Science, NS-24, No. 6, pp. 2516-2520 (1970).

6. V. Rogers, L. Harris, D. Steinman, and D. Bryan, "Silicon Ionization and Displacement Kerma for Neutrons from Thermal to 20 MeV," IEEE Transaction on Nuclear Science, NS-22, No. 6, pp. 2326-2329, Errata NS-23, No. 1, pp. 875-876 (1976).

7. G. Messenger, "Displacement Damage in Silicon and Germanium Transitors," IEEE Transactions on Nuclear Science, April 1965.

8. T. Wicklund, "Neutron Fluence and Damage in Silicon for Free Air Over an Earth Surface," Harry Diamond Laboratories report HDL-TR- 1494 (1970).

REFERENCES (CONTINUED)

9. L. G. Greenwood and R. K. Smither, "Specter: Neutron Damage Calculations for Materials Irradiations," Argonne National Laboratory report ANL/FPP/TM-197 (January 1985).

10. Radiation Shielding Information Center (ORNL) Data Package DLC-31 DLP-1/FEWG1, Coupled 37 Neutron, 21 Gamma Ray Group Cross Sections, Contributed by ORNL.

11. E. C. Smith, D. Binder, P. A. Compton, and R. I. Wilbur, "Theoretical and Experimental Determination of the Neutron Energy Deposition in Silicon," IEEE Transactions on Nuclear Science, NS-13, No. 6, pp. 11-17, December 1966.

12. M. Lazo, UNM Nuclear Engineering Department, private communication (1985).

13. D. Muir, Los Alamos National Laboratory, private communication (1986).

14. J. Grundl and C. Eisenhaver, "Fission Rate Measurements for Materials: Neutron Dosimetry in Reactor Materials," Proc. 1st ASTM Euratom Symposium on Radiation Dosimetry, pp. 430-431.

15. J. G. Kelly, Sandia National Laboratory, private communication (1986).

Editor's Note: This paper was unavailable for publication. A summary is included.

A COMPARISON OF TRIGA AND FBR DAMAGE IN 2N2222 TRANSISTORS

James W. Malloy
Raytheon Co.

An independent means of verifying the 1 Mev damage equivalent fluence reported by a reactor facility for a neutron exposure was developed, using 2N2222 transistors as radiation damage monitors. This dosimetry system has been in use for the last 18 months and has proven useful in comparing the dosimetry at the reactors used by Raytheon for TREE testing. Numerous exposures at the University of Lowell and Penn State TRIGA reactors have shown a close correlation between the 1 Mev fluences reported by the facility and those predicted using the 2N2222 data. Limited data available for exposures of the 2N2222 transistors in fast-burst reactors (WSMR and Sandia) showed a significant discrepancy between the reported and predicted 1 Mev fluences. Based on these data, purportedly equivalent fluences reported for exposures in the TRIGA's and FBR's disagree by approximately a factor of 2 at lower fluences and ~1.5 at higher fluences.

SESSION III

APPLICATIONS

A. De La Paz, Chairman
White Sands Missile Range

Editor's Note: This paper was unavailable for publication. A summary is included.

HPRR OPERATING EXPERIENCE AND APPLICATIONS*

E. G. Bailiff, C. S. Sims, and R. E. Swaja
Dosimetry Applications Research Facility
Oak Ridge National Laboratory
Oak Ridge, Tennessee 37831

SUMMARY

The Health Physics Research Reactor (HPRR) is a small, unmoderated fast pulse reactor located at the Oak Ridge National Laboratory (ORNL). The HPRR is the principle research tool of ORNL's Dosimetry Applications Research (DOSAR) Group. The reactor is described, its operating experience is presented, and its major applications are discussed.

Description

The HPRR core is a right circular cylinder (20-cm diameter and 23-cm in height) consisting of 11 nickel-coated enriched uranium (93.14% ^{235}U) fuel plates held together with fuel bolts. The uranium fuel is alloyed with 10% (by weight) molybdenum. The scrammable element is a safety block containing about 10% of the core total of 97 kg of ^{235}U and has a reactivity worth of about 20 dollars. There are three control rods: A ^{235}U mass adjustment rod (worth two dollars), an aluminum regulating rod (worth 15 cents), and a ^{235}U pulse rod (worth 1.10 dollars). The temperature coefficient of reactivity is about -0.31 cents/°C.

The HPRR can be operated at steady-state power levels up to 10 kW and can produce pulses of up to 10^{17} fissions. With this variation of level and mode of operation and with the various shields (e.g., concrete, Lucite) available, the HPRR offers experimenters a wide range of radiation parameters from which to choose. The neutron-to-gamma dose ratio can be varied by a factor of 20 (0.5:1-10:1), the pulse width by a factor of 500 (60μs-30ms), and the neutron dose rate by 15 orders of magnitude (10^{-8}-10^{7} Gy/s). The maximum fluence from a single pulse at an accessible experimental location is about $8(10^{13})$ n/cm^2.

* Research sponsored by Physical and Technological Research Division, RS. Department of Energy, under contract DE-AC05-840R21400 with Martin Marietta Energy Systems, Inc.

Operating Experience

The initial criticality of the HPRR occurred on March 30, 1962. By the end of FY 1985, the HPRR had been operated on 2,909 different days and had achieved criticality about 7,000 times. A total of 1,010 pulses had been done by the end of FY 1985. The average pulse has yielded about 6.3 (10^{16}) fissions and expended 0.57 kWh of energy. The average steady-state operation expended 0.25 kWh of energy. The original core is still in use and has "burned up" a total of about 100 mg of fuel.

Applications

The HPRR is used by dosimeter vendors, government laboratories, nuclear power utilities, the military, and universities as well as by the ORNL staff for a wide variety of applications. For convenience in presentation, these applications have been divided into six categories. These six are discussed below:

Biological Effects Studies. Studies in this category have accounted for about 30% of HPRR operations over the past decade. The majority of these have involved experiments with mice in attempting to correlate low-level absorbed neutron doses with life shortening, tumor formation, and incidence of myeloid leukemia. Other studies have involved neutron-induced chromosome damage, neuron damage, radioprotective drug development, and activation of body elements (e.g., blood sodium and hair sulfur).

Criticality Alarm Testing. From 1979 through January 1986, six different organizations have used the HPRR to help develop criticality alarm systems and to test compliance with performance criteria suggested by the American National Standards Institute (ANSI/ANS-8.3-1979). A total of 71 pulses and 57 steady-state runs have been performed in tests to provide dose rates, fission yields, and radiation fields consistent with those specified in the performance standards.

Dosimetry Intercomparison Studies. Two types of radiation dosimetry intercomparison studies have been periodic events for over a decade.

1. Nuclear accident dosimetry intercomparison study. A total of 22 of these studies has been conducted at the HPRR since 1965. These week-long studies have attracted participants from 62 organizations (20 foreign). Participants have made 1,311 neutron dose measurements and 978 gamma dose measurements during 69 simulated criticality accidents. Overall, 67% of the neutron measurements and 51% of the gamma measurements meet established criteria.

2. Personnel dosimetry intercomparison study. Eleven of these studies have been conducted sine 1974. A total of 105 organizations (36 foreign) has participated in these mail-in studies and made 4,417 neutron dose equivalent measurements and

4,393 gamma dose equivalent measurements. The HPRR has been operated 69 times with a variety of shields to provide dose equivalents in the 0.50-20 mSv range for these studies.

Neutron and Gamma Dosimeter Development. The well-known spectra from HPRR (both bare and with various shields) are used by the ORNL staff and visiting researcheers for dosimeter development. Typically, the visiting researchers include health physicists from nuclear power utilities, dosimeter vendors, Ph.D. candidates from universities, and scientists from government laboratories.

Simulation of Nuclear Weapon Spectra. The HPRR is being increasingly called upon to provide radiation exposure, both in the steady-state mode and in the pulse mode, to simulate nuclear weapon environments. Recent applications in this category include testing of Army personnel battlefield dosimeters, investigation of radiation effects on laser materials of interest to the Strategic Defense Initiative, and irradiation of Japanese artifacts in an attempt to better define radiation doses due to the Hiroshima device.

Training. The HPRR is used in two basic types of training:

1. Nuclear engineering training. About 450 students from seven universities have received nuclear engineering training at the HPRR during the past ten years. Typically, they perform four basic experiments involving approach to criticality, rod calibration, thermal cycling, and pulse operation.

2. Dosimetry training. Since 1982, the HPRR has been used in formal training courses in personnel dosimetry and in criticality accident dosimetry. A total of 130 participants has received detailed instruction in practical aspects of neutron and gamma dosimetry.

Reactor-Pumped Laser Experiments in the Sandia SPR-III Facility*

D. A. McArthur, G. N. Hays, D. R. Neal
P. S. Pickard and J. K. Rice

Sandia National Laboratories
Albuquerque, NM 87185

ABSTRACT

Experiments on the excitation of short-wavelength gas lasers have recently been performed in the central cavity of the Sandia fast burst reactor SPR-III. Small-signal gain coefficients ~ 0.7 %/cm were measured in XeF laser mixtures excited with either the ^{3}He(n,p)T reaction or with fission fragments emitted from the wall of the laser cell. Specialized apparatus helpful in performing these measurements is described. Preliminary experiments included measurement of radiation effects on cell window materials and laser mirrors, and measurement of energy deposition in the laser gas as a function of time for various cell geometries and polyethylene moderator thicknesses. The optical distortion of the laser medium by the energy deposition process was much more severe for fission fragment excitation. Fluorescence spectra were also measured for XeF laser mixtures with an optical multichannel analyzer, and these spectra were consistent with the XeF gain measurements.

1.0 INTRODUCTION

An analytic and experimental program is being carried out at Sandia National Labs to determine the scientific and engineering feasibility of high-power, short-wavelength reactor-pumped lasers. Reactor-pumped lasers offer the potential for extremely compact energy storage, geometrical scaleup of reactor power and energy, a range of laser pulsewidths, and a set of technical challenges very different from conventional laser technologies. The Sandia program includes both reactor design studies, and experiments to investigate the reactor-pumping of candidate laser media having potential for high efficiency.

In this paper we report details of the laser excitation experiments performed in the central cavity of the Sandia fast burst reactor SPR-III. In these experiments, energy and power

*This work performed at Sandia National Laboratories, Albuquerque, NM, supported by the U. S. Department of Energy under contract number DE-AC04-76DP00789.

deposition in the excited laser medium have been measured as a function of laser cell and polyethylene moderator geometry. The gas mixtures were excited either by the $^3He(n,p)T$ reaction or by fission fragments from thin U_3O_8 coatings on the inside of ceramic cylinders. Small-signal gain in XeF laser mixtures has been measured for a limited range of gas compositions. Optical distortions introduced by energy deposition in the laser medium complicated the gain measurements, but a suitable optical system was developed to correct the distortions sufficiently well to make the measurements possible.

The peak optical gain coefficient observed with ^3He excitation was ~ 0.7 %/cm, and was approximately the same with fission fragment excitation. Gain was observed only at 351 nm with ^3He excitation, but was observed also at 333 and 363 nm with fission fragment excitation. Significant differences in the time dependence of the gain were observed for the two modes of excitation. XeF fluorescence spectra observed were consistent with these gain results.

Section 2 of this paper describes previous Sandia work, sections 3 and 4 describe specialized apparatus and preliminary experiments, and section 5 describes the gain results.

2.0 PREVIOUS SANDIA WORK

The first reactor-pumped laser was demonstrated at Sandia National Labs in 1974 by pumping low-temperature CO gas with fission fragments.[1] In 1977 conceptual designs for large reactor-pumped lasers employing specialized nuclear reactor structures were described.[2] These concepts invoked only moderate extensions of current reactor material and control technology. Studies of the room-temperature reactor-pumped CO laser, and cooperative laser experiments with other laboratories were carried out over the next several years.[3,4]

In 1983 the desirability of very large lasers for the SDI program resulted in renewed interest at Sandia in defining the limits of this technology. Since no short-wavelength, efficient laser had been pumped with a reactor, in 1983 a series of experiments was defined on SPR-III to investigate the pumping of the ultraviolet excimer lasers, emphasizing KrF and XeF. The next section describes the apparatus for these experiments.

3.0 LASER EXPERIMENT APPARATUS

Figure 1 shows the overall layout of the reactor-pumped-laser experiment at the SPR Facility. The laser cell was located inside the central cavity of the SPR-III, at the center of the Kiva. The Kiva, a concrete hemisphere of ~ 8.8 m inside diameter with 1.5 m thick walls, provides sufficient shielding that ordinary electronic apparatus can operate without difficulty outside the

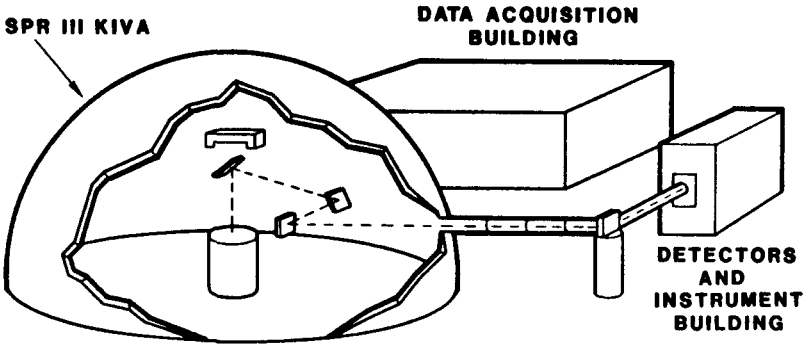

Fig. 1: Overall Arrangement of SPR-III Laser Experiment

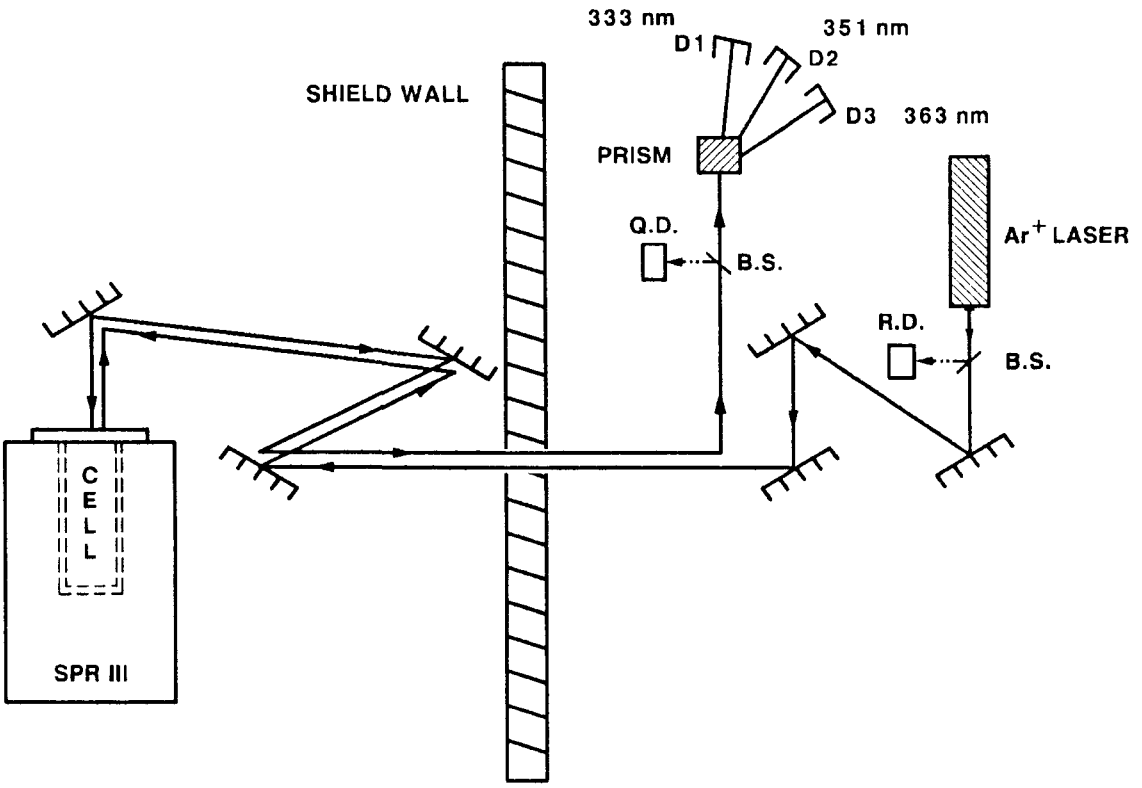

Fig. 2: Schematic of Optical System for Measuring Gain

Kiva. Additional shielding was provided by sheets of 1.3-cm-thick lead and 2.5-cm-thick borated polyethylene mounted between the laser instrumentation trailer and the Kiva. A beam port (10 cm inside diameter) allowed optical communication between the laser cell and the instrumentation trailer. Although personnel were not permitted inside the trailer during an actual SPR-III pulse, work could be carried out in the trailer while the reactor was cooling between bursts and during the wait period preceding each burst.

The trailer (2.4 m by 10.6 m) was fitted with a positive-pressure, filtered air-conditioning system to reduce dust buildup and temperature variations that might affect optical apparatus. A 1.2 m by 3.7 m optical table was installed on air supports inside the end of this trailer closest to the beam port. A probe laser, beam alignment apparatus, and a wavelength-selective detector system were installed on this table (Fig. 2).

The beam path between the trailer and the beam port entrance was enclosed in an insulated temporary building to protect the optical beams against weather, dust, and atmospheric turbulence associated with temperature differences, and to allow convenient alignment of the beams. To eliminate turbulence associated with air flow out of the trailer or into the Kiva, good-quality optical windows were placed at these boundaries.

The gas-handling system was placed close to the cell inside the Kiva to reduce the length of vacuum lines. To minimize personnel exposure to radiation, all valves in this system were remotely operated with compressed air. Thus, gas mixtures could be made, mixed thoroughly, and admitted to the laser cell without requiring personnel entry to the activated Kiva between bursts. After a burst, the contaminated gas from the cell was pumped through a chemical trap to remove fluorine compounds, through the vacuum pump, through an airline filter and finally into the hot exhaust of the Kiva.

Major modifications to the apparatus that involved working close to the irradiated laser cell for long periods of time (e.g. installation of new mirrors, alignment of a new optical system, absolute intensity calibrations) were usually performed early in the work week to minimize personnel dose.

The SPR-III was initially supported by a hydraulic elevator when in position around the laser cell. The polyethylene moderator around the cell caused a large negative experiment worth, so that if the reactor dropped (moving the cell out of the central cavity), a positive reactivity insertion could occur.

To assure reactivity stability and alignment, a frame to support the SPR-III in the raised position (Fig. 3, the SPARLOCK) was developed. Two rigid aluminum spars were inserted through support pockets on the reactor stand after the reactor was raised, and the

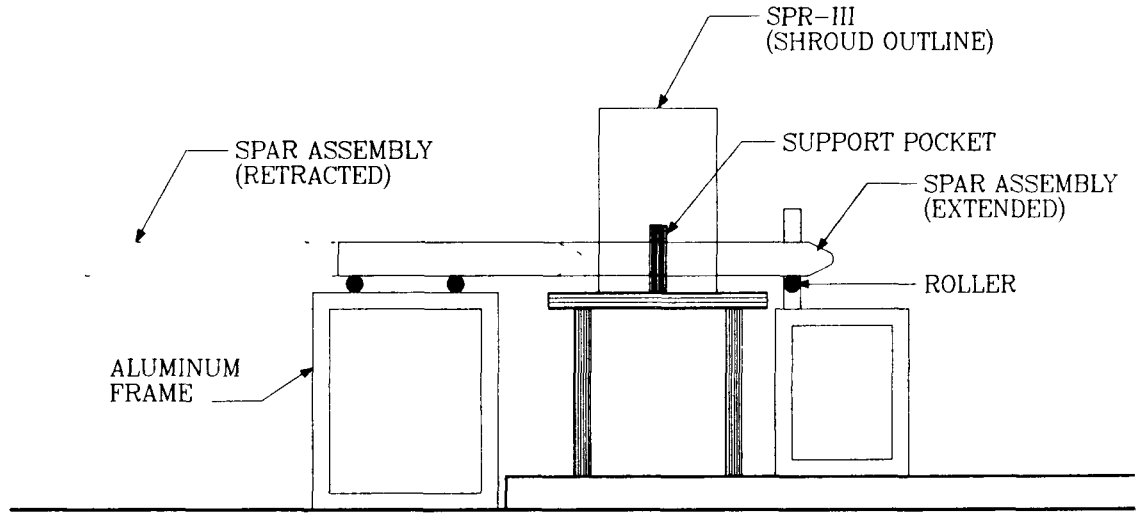

Fig. 3: Positive Support for SPR-III ("SPARLOCK")

reactor was lowered slightly so that the SPR-III rested on these spars whenever it was being operated with a laser experiment in the central cavity. This system completely eliminated any variations in reactivity associated with reactor movement relative to the laser experiment.

4.0 PRELIMINARY EXPERIMENTS

4.1 Effect of Radiation on Optics

Previous work[5] showed the effect of radiation on laser cell optics for several ultraviolet optical materials (7940 fused silica, BaF_2, MgF_2, and sapphire). The permanent absorption induced by fast neutrons and the gamma rays from SPR-III was measured[5] by taking an absorption spectrum both before and after irradiation. The transient absorption was also measured with a probe laser at $\lambda = 257$ nm.

experiments[5] showed that these materials were relatively little affected by radiation for wavelengths 300 nm $< \lambda <$ 700 nm, but large differences in transmission were noted for $\lambda <$ 300 nm. Based on these measurements, 7940 fused silica was chosen to minimize radiation-induced absorption, both transient and long-term.

Detailed measurements were not made of the radiation effects on dielectric coatings, but suppliers were requested not to use

specific coating materials having high cross-sections for neutron absorption (which presumably would result in enhanced radiation damage). Observation of the probe laser beam intensity with an evacuated cell did not show any obvious radiation effect on the reflectivity of the dielectric mirrors used. It should be noted however that long-term exposure to a high-power laser beam in the presence of background radiation and the excited laser gas did produce a region of lower reflectivity on the lower cell mirror, an effect that is not completely understood.

4.2 Energy Deposition Measurements

Gas lasers vary widely in the minimum excitation rate that produces efficient lasing (from ~ 50 w/cm^3 to > 1 Mw/cm^3, depending on laser type, gas pressure, etc.). Existing laboratory reactor facilities can produce excitation rates up to ~ 10 kw/cm^3, for carefully optimized conditions. To characterize a given laser accurately, it is thus very important to know the rate of energy input to the laser gas.

The energy input to the gas was investigated through neutron-transport calculations made for potential laser cell configurations and polyethylene moderator geometries. A two-dimensional discrete ordinates radiation transport code (TWOTRAN) was used to estimate the total energy deposition in the laser gas, E_d. Initial energy deposition measurements agreed approximately with these TWOTRAN calculations; however, the presence of the laser cell increased the reactor pulsewidth by a factor of five to ten (compared to the free field pulsewidth for the same yield).

Therefore, a Monte Carlo code (KENO) was used to estimate both E_d and the neutron generation time l_{gen} (for calculating the width of the energy deposition pulse). Most of the reactor pulsewidth increase was eventually traced to the presence of several grams of enriched uranium in the laser cell combined with polyethylene moderator thickness greater than 1 cm. Reducing the uranium mass in the experiment to ~ 0.5 g reduced the reactor pulsewidth to more normal values and permitted experiments at higher power deposition levels, at the expense of reduced laser cell volume. These results are discussed further in a related paper in this Workshop.[6]

The time dependence of the energy deposition pulse was measured with a cobalt thermal neutron detector wound around the cell inside the polyethylene moderator. This cobalt detector was compared against a ^{235}U detector and found to give a nearly identical pulse shape for situations involving thick polyethylene moderator. Figure 4 shows a typical energy deposition pulse shape ("THERMAL NEUTRON PULSE") as indicated by the cobalt detector.

Although measurement of the energy deposition pulsewidth is relatively straightforward, measurements of E_d are complicated by

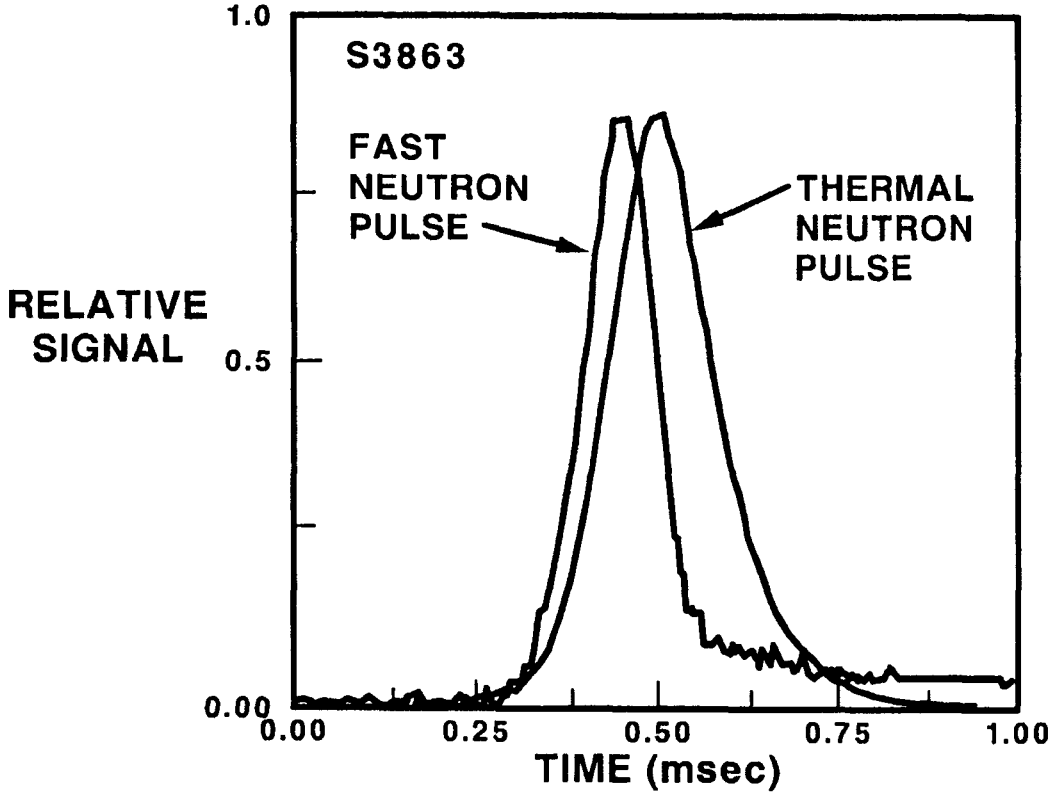

Fig. 4: Delay and Broadening of the Excitation Pulse

the fact that E_d depends both on the amount of energy created in the ^{235}U lining the laser cell, and on the efficiency with which this energy is transported out of the uranium coating into the laser gas. Since the laser gas may be heated nonuniformly by the energy deposition process, which in turn will cause gas motion during the excitation pulse, the stopping power of the laser gas may also be a strong function of time and space during the reactor pulse.

Typical laser mixtures in the experiments reported here have been predominantly He, Ne, or Ar. For noble gases it was assumed that the input energy was converted completely to heat within a fraction of a millisecond. Therefore, the pressure rise in the excited laser gas was measured for each reactor pulse, and the pressure rise related to a total energy input (through the gas heat capacity). Figure 5 shows typical pressure oscillations measured during gain experiments, together with a gas dynamic calculation of the pressure signal to be expected for the complex geometry of the laser cell.

Although the time dependence of the pressure signal appears to be well understood based on the agreement shown in Fig. 5, the

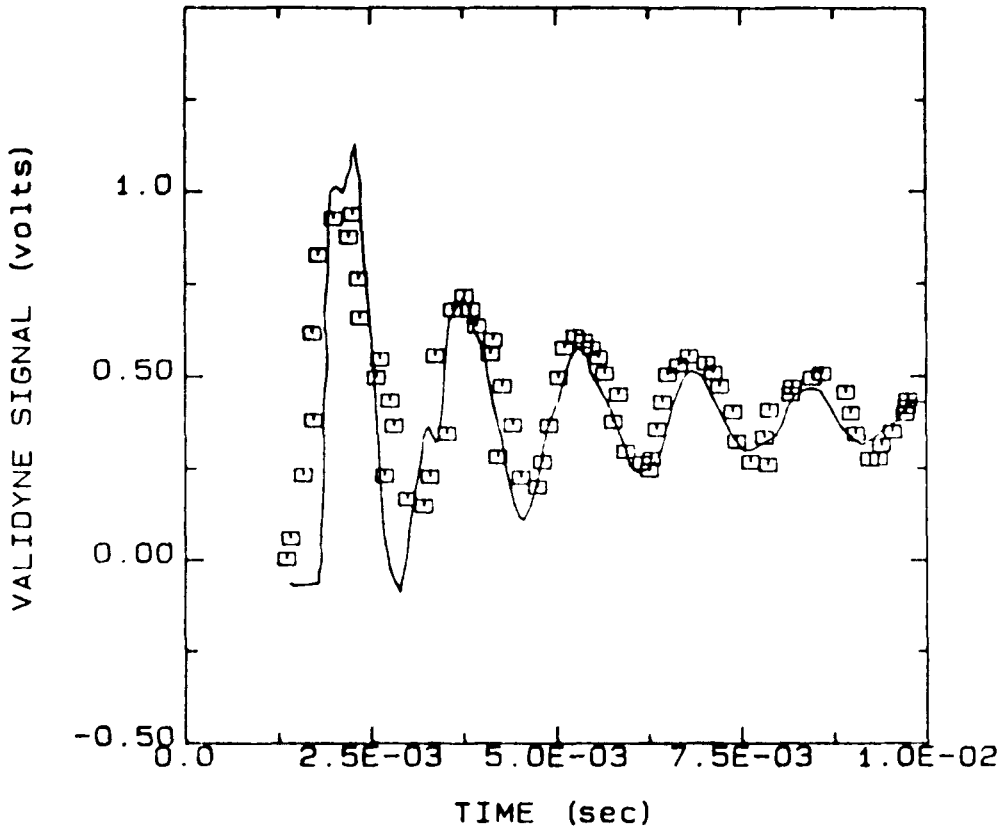

Fig. 5: Measured (squares) and Calculated Pressure Rise in Laser Gas

integrated energy input inferred from these pressure rises was significantly lower than that calculated with neutron transport codes. This discrepancy is not understood at present, but it may be related to the propagation of the pressure pulse from the highly-excited laser region to the pressure transducer, or to the fission fragment energy deposition path length which causes large spatial variations in the gas temperature.

5.0 LASER EXCITATION EXPERIMENTS

5.1 Laser Cell Design

The vertically-oriented cylindrical laser cell (Fig. 6) was suspended from an aluminum frame so that when the SPR-III was raised from its storage pit, the central cavity of the reactor surrounded the cell. The cell consisted of a thin-wall stainless steel cylinder with adjustable mirror/window holders at each end. The mirrors were located a few cm beyond the intensely-excited portion of the laser gas to reduce mirror damage caused by impact of energetic charged particles.

A cobalt thermal neutron detector was wrapped around the stainless steel cell to measure the time dependence of the excitation pulse.

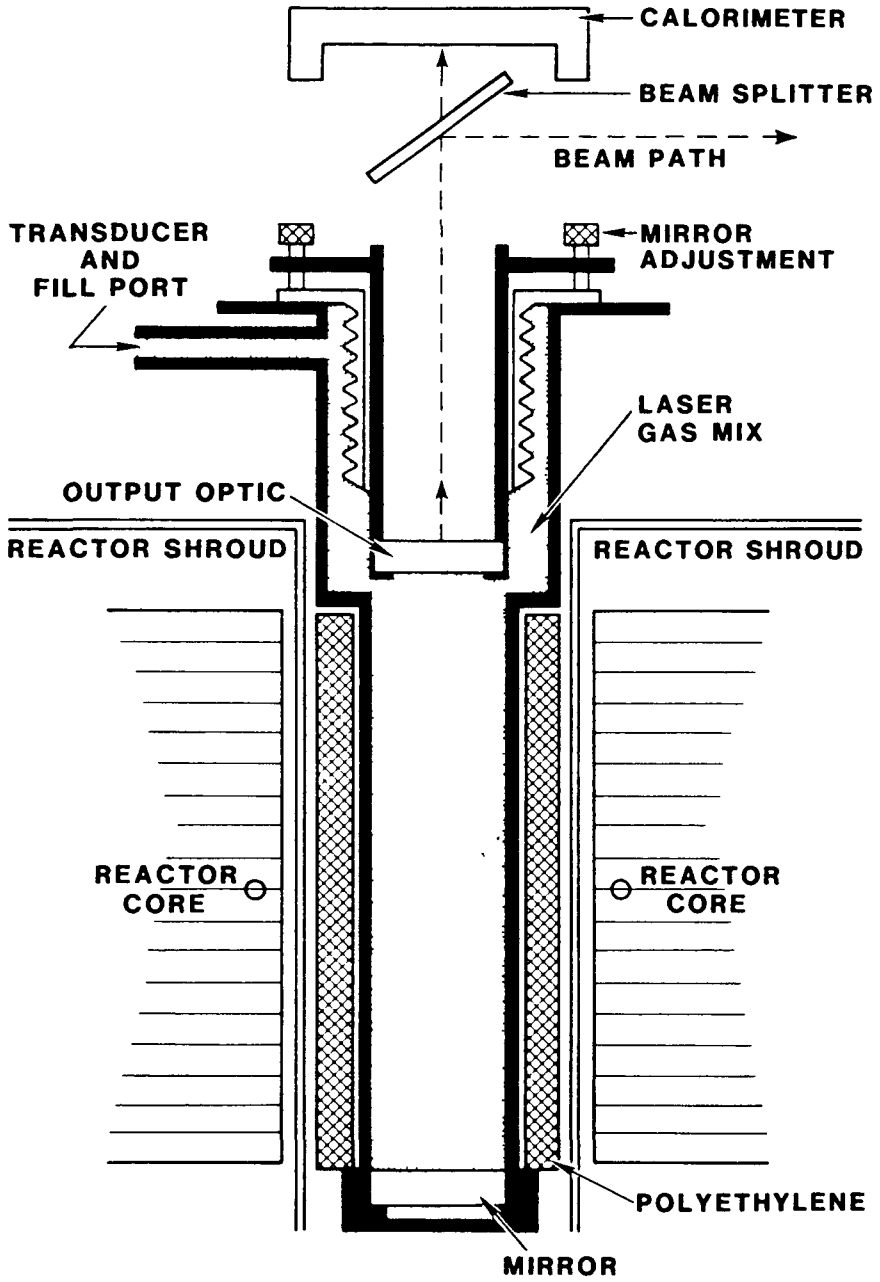

Fig. 6: Cylindrical Laser Cell in SPR-III Central Cavity

An annular polyethylene cylinder 3.2 cm in thickness and having an outer diameter of 9.5 cm surrounded the cell to provide partial moderation of the fast neutrons produced by SPR-III. A thin-wall stainless steel cylinder surrounded the polyethylene to contain it in the unlikely event that reactor cooling failed immediately after a burst and the polyethylene melted.

The gas was excited either by neutron-induced fission of ^{3}He added to the laser gas mixture, or by fission fragments emitted from a

U_3O_8-coated alumina cylinder surrounding the laser gas. The cylinders were 30.5 cm long, with a 1.6 cm inside diameter, a wall thickness of 0.31 cm, and a U_3O_8 coating thickness of ~ 3 μ. They were coated by repeating the following process 20 - 30 times:[7] The inside surface was painted with a uranyl nitrate solution, allowed to dry thoroughly in air, and the cylinder was then fired to high temperature to convert the uranyl nitrate to uranium oxide.

5.2 Optical System Design

The beam from a 5-w argon ion laser located in the instrumentation trailer outside the SPR Kiva (about 15 m from the laser cell) was directed into and back out of the cell through the SPR beam port. Signals were recorded on detectors located in the instrumentation trailer.

The energy deposition in the laser gas varies spatially because of either neutron self-absorption or because of the varying energy deposition along the path of a fission fragment. The resulting variations of temperature and pressure give rise to a density profile in the laser gas which acts as a weak lens, distorting the input laser beam. This effect was noticeable in excitation by ^3He, and was dominant for fission fragment excitation.

By restricting the size of the input laser beam at the cell (to ~ 1 mm diameter), aligning it accurately along the axis of the laser cell, and maximizing the angular field of view of the detector system optics, these effects could be reduced so that meaningful gain signals could be measured. During these experiments, this was best accomplished by using beam splitters to separate the input and output laser beams, and by using beam-expanding and beam-contracting telescopes so that the beam was aligned along the axis of the cell and had the desired diameter.

The return beam from the cell passed through a Pellin-Broca prism to separate it into the 333, 351, and 363 nm components, and each component was directed onto a separate scatter plate viewed by a separate photodiode (the scatter plates were used to eliminate signal variations caused by variations in sensitivity across the face of the photodiode).

5.3 Gain Results with ^3He Excitation

When exciting the laser gas with ^3He, it was necessary to use slow-neutron shielding material (thin Cd sheets) near the laser cell mirror and window locations to reduce transient radiation damage caused by charged particles from the $^3He(n,p)T$ reaction.

Figure 7 shows the gain signal measured at λ = 351 nm using a continuous-wave Ar^+ laser, for ^3He excitation at ~ 5 kw/cm^3 pump

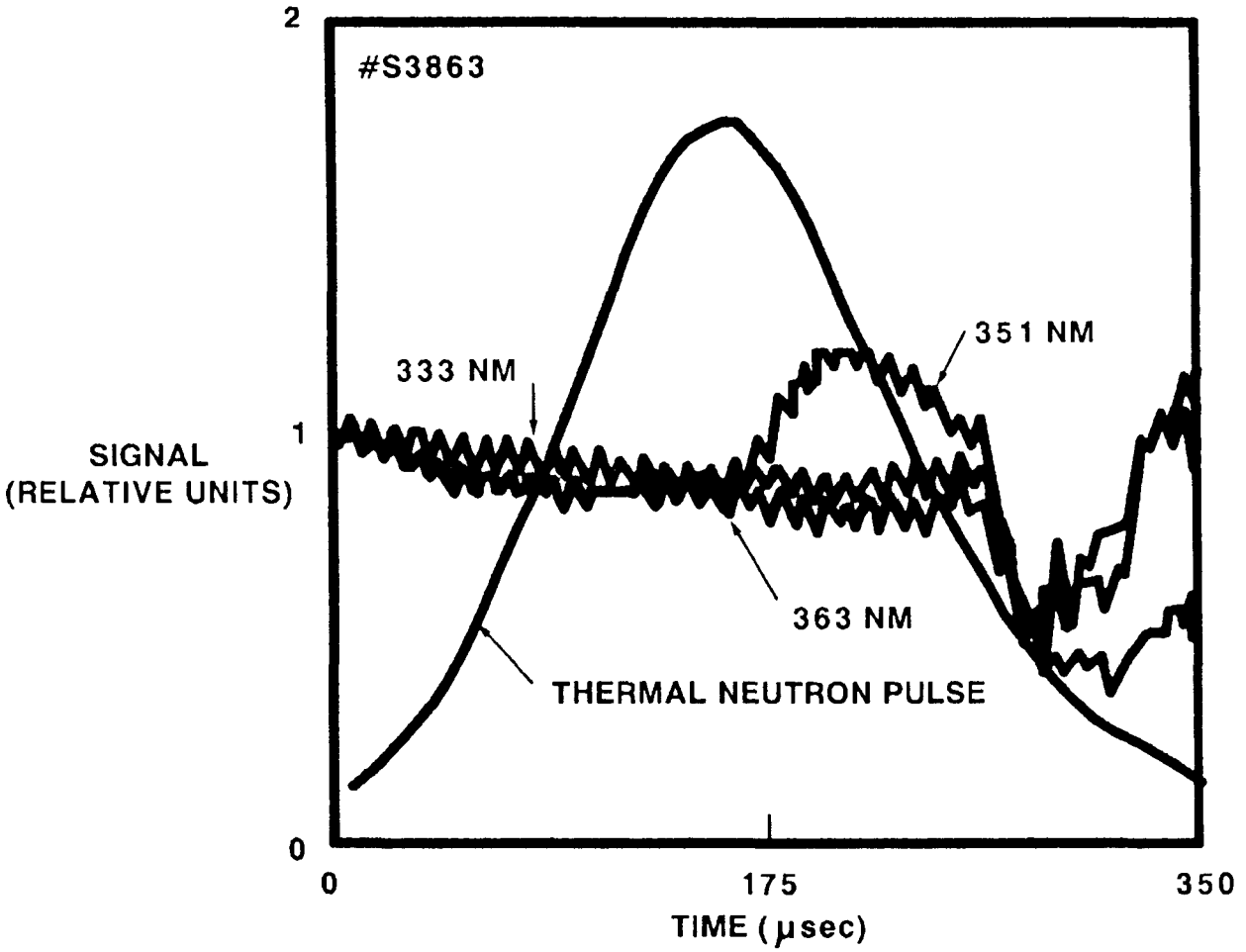

Fig. 7: Typical XeF Gain Signals with ^{3}He Excitation

power. The gas mixture was 1500 Torr of ^{3}He, 20 Torr of Xe, and 2 Torr of NF_3. The ~40 percent signal increase at 351 nm corresponds to ~0.7 percent/cm gain coefficient, which corresponds well with an extrapolation of gain measurements in XeF at the much higher pumping rates obtained with electron beam excitation. Simultaneous measurements with other laser lines at λ = 333 nm and 363 nm show a slight absorption. The approximately constant signal levels at the nearby wavelengths of 333 and 363 nm show that optical distortion of the medium cannot be responsible for the signal increase (or gain) at λ= 351 nm.

The ~ 100 μs delay before the appearance of the gain signal at 351 nm is not understood in detail, but may be associated with some optically-absorbing species which is consumed about midway through the excitation pulse, or with an increase of gas temperature which increases the gain by reducing the population of the weakly-bound lower laser level.

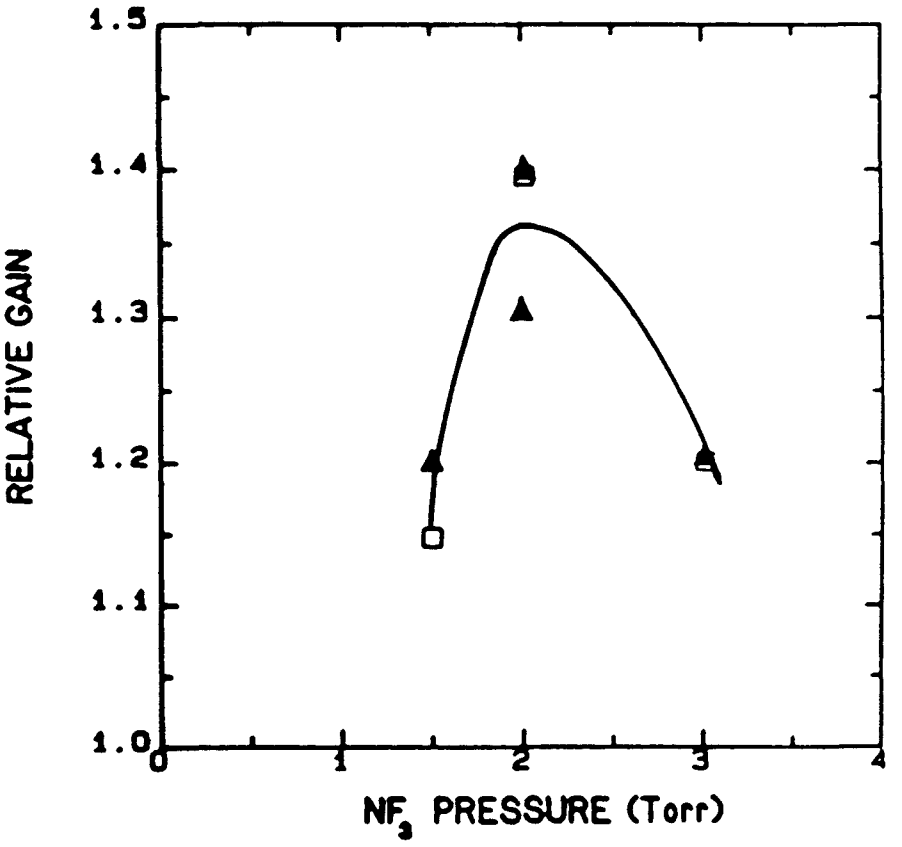

Fig. 8: Dependence of Gain on NF_3 Pressure

The gain signal at 351 nm was also a strong function of the laser gas composition, as shown in Fig. 8 for the NF_3 pressure (at 1500 Torr ^3He and 20 Torr Xe). The gain signal disappeared whenever the Xe or NF_3 constituent of the gas mixture was deleted, and a fairly narrow range of ^3He pressures produced gain.

5.4 Gain Results with Fission Fragment Excitation

The gain signals in XeF laser mixtures are significantly different when fission fragment excitation is used. Figure 9 shows gain signals in a mixture of 900-Torr Ar, 10-Torr Xe, and 3-Torr NF_3 when excited by fission fragments. In particular, gain appears not only on the 351 nm line, but also on the 333 and 363 nm lines of the argon ion laser. The gain also appears early in the excitation pulse, and peaks before the peak of the excitation pulse. The peak gain is comparable to that observed with ^3He excitation.

Similar dependence of gain was observed with Ar and Ne buffer gases.

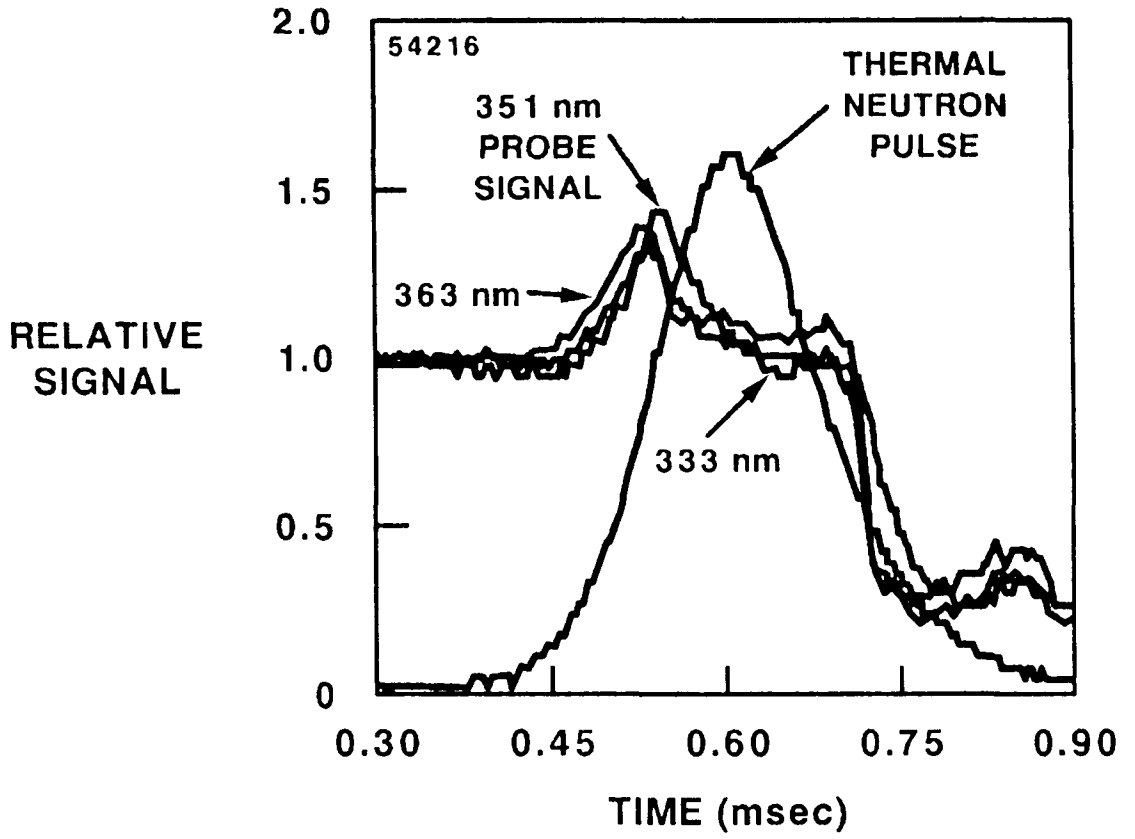

Fig. 9: XeF Gain Signals with Fission Fragment Excitation

5.5 Measurement of XeF Fluorescence Spectra

The observation of gain at 363 nm is surprising in light of previous XeF laser investigations with more conventional excitation; therefore measurements of XeF fluorescence were made with an optical multichannel analyzer (OMA). Figure 10 shows a representative XeF fluorescence spectrum at 900-Torr Ar, 10-Torr Xe, and 3-Torr NF_3, when excited with fission fragments. The violet-degraded sharply-peaked band at 350 nm is the XeF (B to X) band, and the broad, low-intensity band centered near 480 nm is the XeF (C to A) band. The relative intensity of these bands was a strong function of time during the excitation pulse, and the B to X band showed significant intensity at 363 nm.

The OMA showed very low sensitivity to background radiation noise (compared to a photomultiplier), and appears to be a very powerful experimental tool for obtaining data in these situations involving a very low reactor pulse repetition frequency.

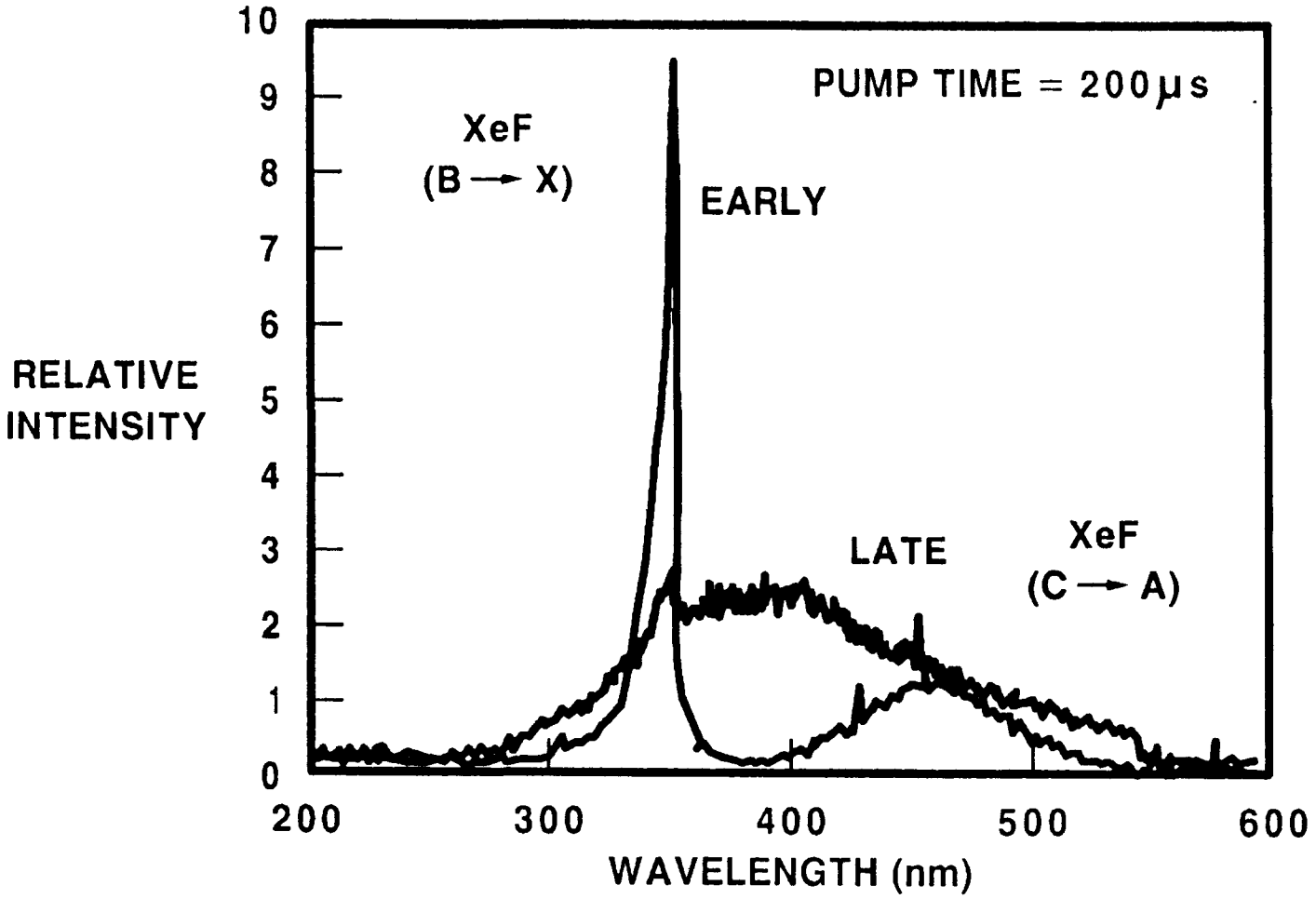

Fig. 10: Early- and Late-Time XeF Fluorescence Spectra (Data are not corrected for the wavelength-dependent response of the detector system)

6.0 CONCLUSIONS

This series of experiments on SPR-III has for the first time demonstrated significant gain in reactor-pumped excimer laser media. They represent an important and encouraging first step toward the development of an efficient, short-wavelength reactor-pumped laser.

The SPR-III facility can also be used effectively to measure gain and fluorescence spectra of reactor-pumped laser media over a range of excitation rates similar to those which might be used in a large reactor-excited laser system. The data provided by these experiments are encouraging for the development of large reactor-excited lasers. Specialized apparatus developed over the past two years has allowed efficient use of time on the heavily-used SPR-III facility.

7.0 ACKNOWLEDGEMENTS

The authors gratefully acknowledge the able technical assistance of D. Plath, J. Wray, R. Cohen and T. Hamilton, and the cooperation of the SPR Operations staff.

8.0 REFERENCES

1. D. A. McArthur and P. B. Tollefsrud, "Observation of laser action in CO gas excited only by fission fragments," Appl. Phys. Lett. 26, 187 (1975).

2. D. A. McArthur, T. R. Schmidt, J. S. Philbin and P. B. Tollefsrud, Concepts for the Construction of Large Reactor-Excited Laser Systems, Sandia Labs Report SAND 76-0584, September 1977 (reprinted November 1983).

3. D. A. McArthur, "Fission Fragment Pumping of CO Gas Mixtures," First Intl. Symposium on Nuclear Induced Plasmas and Nuclear Pumped Lasers, May 23 - 25, 1978, Orsay, France, Les Editions de Physique.

4. M. A. Akerman, G. H. Miley, and D. A. McArthur, "A helium-mercury direct nuclear pumped laser," Appl. Phys. Lett. 30, 409 (1977).

5. P. J. Brannon and R. W. Morris, Nuclear Radiation Induced Absorption in Optical Materials, Sandia National Labs Report SAND84-2437, January 1985.

6. D. M. Minnema, "Nuclear Pumped Laser Kinetics Effects on SPR-III," Fast Burst Reactor Workshop, Sandia National Labs, Albuquerque, NM, April 7 - 9, 1986.

7. D. J. Sasmor, Sandia National Labs, private communication.

HEATING OF ALUMINUM BY SPR-III BURST

Stephen V. Judd
C.S. Draper Laboratory

ABSTRACT

Real time temperature measurements were made on an aluminum cylinder exposed to radiation bursts at SPR-III at neutron levels from 10^{11} cm^{-2} to $4.5x10^{14}$ cm^{-2}. Precision thermistors and high speed A/D converters were used to measure temperature with .0025°C resolution at 20ms intervals following the burst. Temperature data is presented as a function of neutron fluence.

1. Description

The goal of a recent test program at CSDL was to obtain 1ppm diode voltage measurements through neutron bursts at the SPR-III facility. One requirement to obtain meaningful data was to provide an accurately controlled thermal environment. For this purpose, a test fixture was designed using a double oven configuration. The test fixture consisted of an inner aluminum cylinder, which housed the diodes, an insulation layer, a 1/8" aluminum shell, a second insulation layer, and an outside 1/8" aluminum shell. (See figure 1).

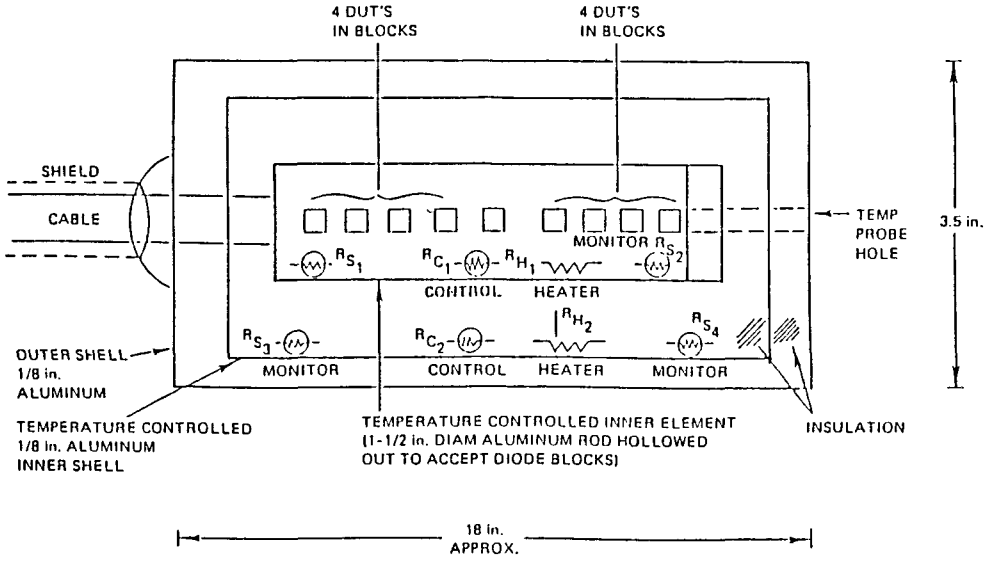

Figure 1 - Temperature controlled diode test fixture.

The diodes were mounted in aluminum blocks which were mounted in the inner cylinder as shown in figure 2. The cylinder was approximately 27 cm long and 4 cm in diameter and had an assembled aluminum filling factor of about .64. Both the inner and outer ovens were thermally insulated and temperature controlled. The resulting thermal time constant of the inner oven was approximately 200 minutes.

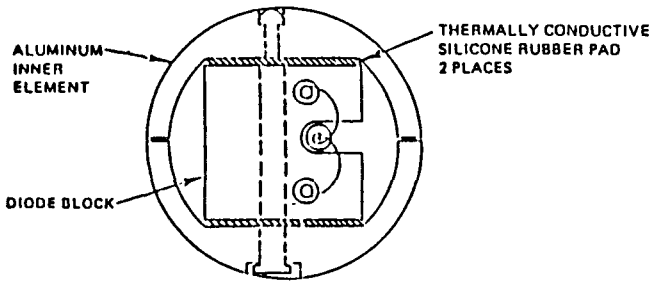

Figure 2 - End view of test fixture showing diode mounting block.

The temperatures were maintained on the two ovens by strip heaters attached to their surfaces. Precision temperature controllers and thermistors were used to regulate the oven temperatures. The inner oven was held at 65°C during the experiment, with a stability of better than ±.01°C/day, the outer oven was kept 5° cooler.

Sensing thermistors were attached to the outer face of the inner cylinder in two places using a thermal epoxy. A precision bridge measurement scheme was used in conjunction with a high speed A/D converter with a resolution equivalent to .0025°C. The resulting thermistor thermal time constant was approximately 1 second.

An external probe was used to calibrate the system both 45 minutes before and 1 hour after each shot. A four wire measurement technique was used in the external probe so that wire resistance did not affect the measurement. The external probe was in turn calibrated using three temperature reference baths: water triple point, gallium, and succhino nitrile. The net absolute temperature accuracy is estimated at better than +.01°C.

Pre to post thermistor shifts were less than .005°C on all but the shots over 10^{14} n/cm². The maximum shift was .024°C at 4.4×10^{14} n/cm² which was small compared to the radiation heating.

Data sampling by the A/D converter started upon receiving the reactor trigger. The data rate was adjusted such that each thermistor was sampled every 20ms from t=0 to t=1 second, every 50ms from t=3 to t=5 seconds, every 500ms from t=5 to t=30 seconds, then every 500ms from t=30 seconds to t=65 minutes. A two second gap after t=1 second resulted from changing the operation mode of the A/D converter.

Both neutron and gamma dosimeters were attached around the outside of the fixture. Sulfur pellets and TLDs were used. A

transfer ratio between doses inside and outside of the fixture was determined in earlier experiments by placing dosimeters in several locations inside and out. The inside dose was roughly 90% that measured on the outside for both 1Mev equivalent neutrons and gamma. Calculated doses are expected to be within 10% to 20% of the actual dose.

2. Experimental Results

Both the gamma dose and neutron fluence were calculated for each shot at each thermistor. The ratio of gamma dose to neutron fluence was found to be roughly linear with a ratio of about 3×10^{-18} rads/neutron cm^{-2} (see figure 3).

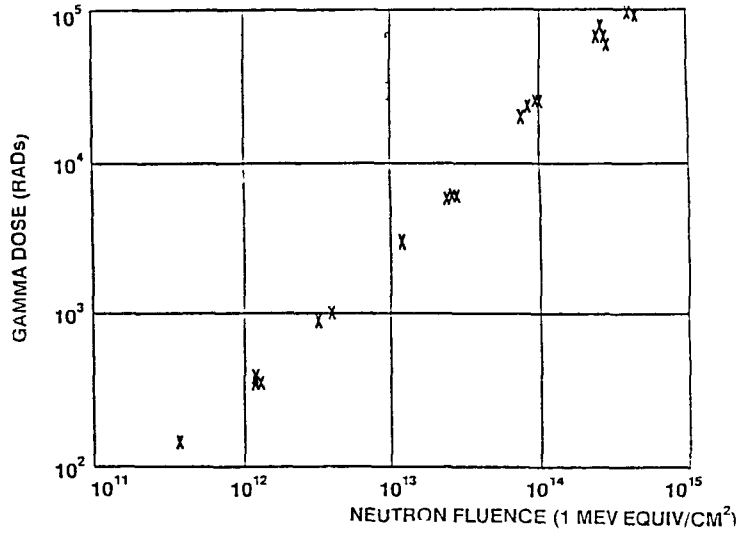

Figure 3 - Measured gamma dose vs. neutron fluence.

A typical temperature time profile is shown in figure 4. The reactor trigger is received at t=0. The temperature typically peaked within about 100ms. It then decayed with a time constant expected for the thermistor for the first couple of seconds. The decay rate then assumed that expected for the inner cylinder. Qualitatively, all of the thermistors indicated a similar behavior. Variations in peaking and decay times were attributed to variations in thermistor mounting and wiring. Gaps in the data are from dead time during which the A/D converter changed modes.

The temperature peak near t=0 was due to heating in the thermistor itself. Heating in the thermistors was expected to be higher than in the aluminum due to the presence of nickel, manganese, and copper within the device.

Following the decay of the initial peak, the slope becomes approximately that expected for the aluminum cylinder. The temperature rise in the aluminum at t=0 was therefore calculated by projecting the y intercept from the t=10 second temperature, based on the thermal time constant for the fixture.

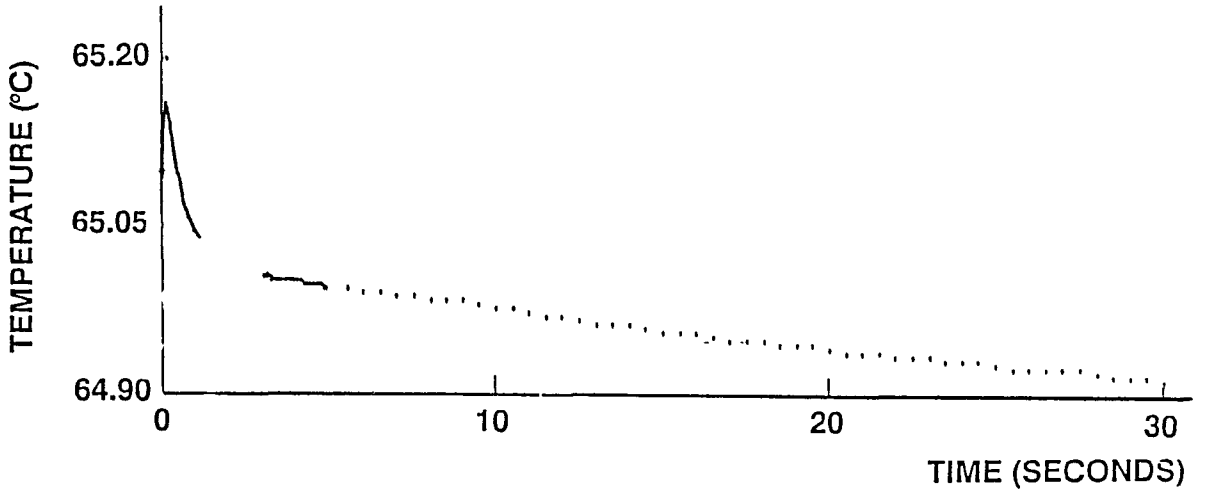

Figure 4 - Typical temperature time profile.

Data was collected from 8 test fixtures in a total of 16 bursts to levels from $1x10^{12}$ to $4.5x10^{14}$ neutrons per cm^2. The temperature peak measured on these shots is plotted in figure 5 as a function of neutron fluence. The temperature rise in the aluminum at t=0 is plotted in figure 6.

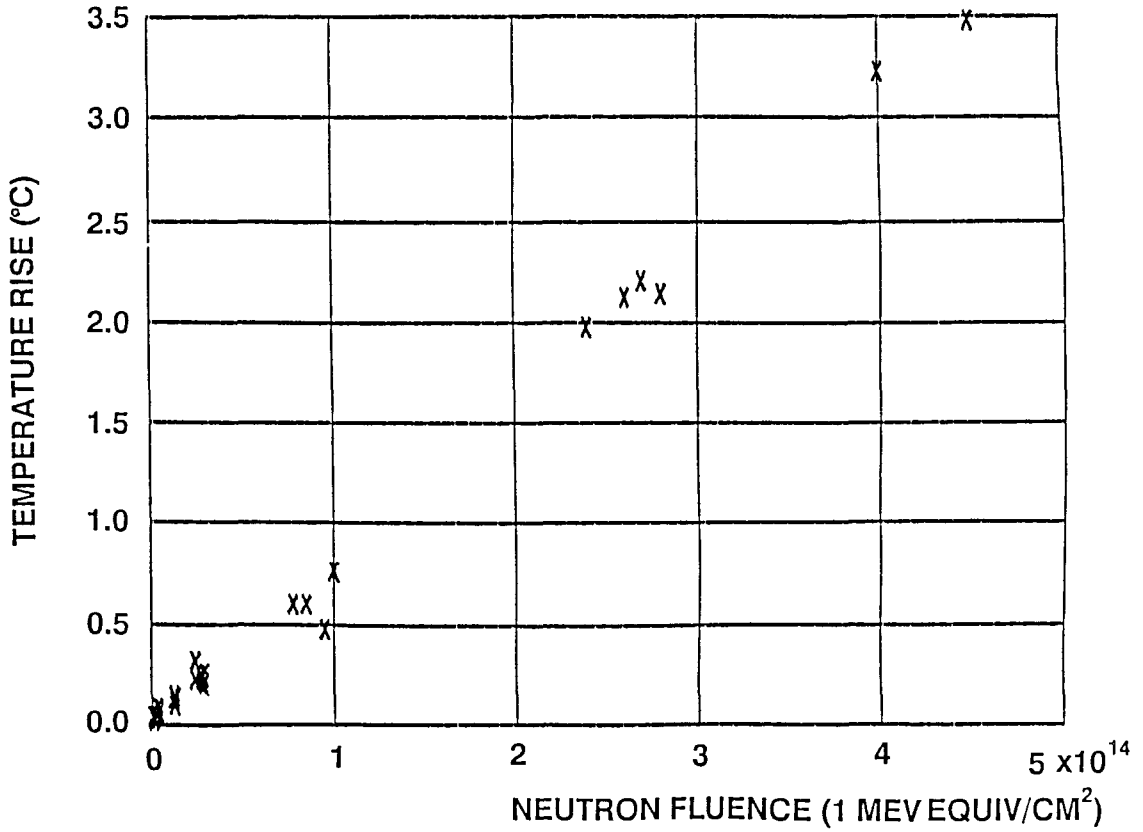

Figure 5 - Peak temperature rise measured following each shot.

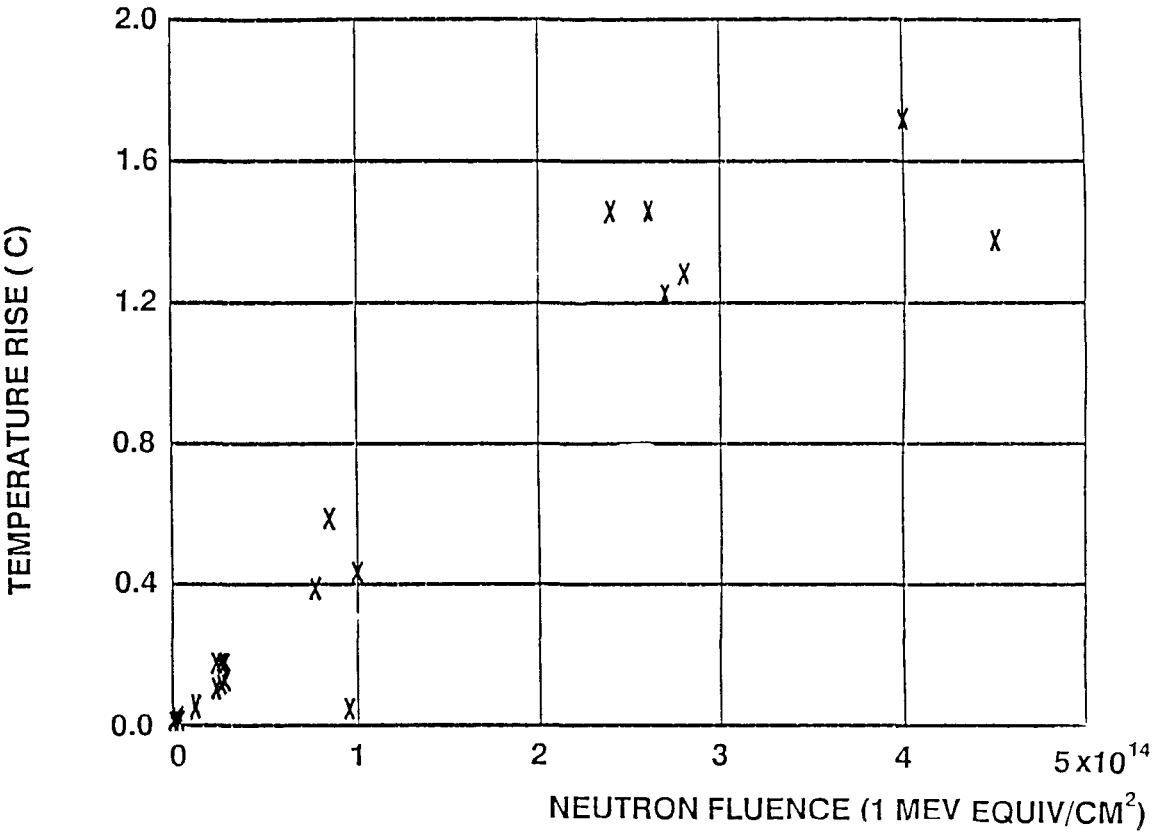

Figure 6 - Temperature rise in the aluminum block at t=0+.

3. Calculations

During the early phases of the experiment planning, the unavailability of temperature data necessitated the development of a quick guess technique for estimating radiation heating in various materials. Based on many assumptions, an analytic solution was found for the energy deposition by neutrons and gamma in a slab geometry. The heating predictions made using this technique were within 20% of the measurements.

The analytic solution was based on the following assumptions: Free field gamma energy deposition in rads is converted directly to heat. A mass absorption coefficient was used, assuming 2 Mev monoenergetic gamma photons, to estimate the energy deposition as a function of distance. The removal cross section for a fission neutron spectrum was used, and it was assumed that all neutrons removed, were captured. It was then assumed that gammas were emitted by the capturing nuclei in 5 energy ranges with known probabilities. Each point in the target was then considered a gamma source. An average mass absorption coefficient, for each energy range, was used to calculate the attenuation and absorption between the source and observation points. The kinetic energy of the neutrons was ignored.

The following discussion outlines the derivation of the solution. A one dimensional geometry is assumed such that material fills the space from x=0 to L. Neutrons are incident from the -x direction. The gamma source strength is estimated by multiplying the derivative of the neutron fluence by the probability and energy of gammas produced in any energy bin at x.

$$S_i(x) = P_i E_i I_{n\circ} e^{-\Sigma_n x}$$

where P_i is the probability of emitting a photon of energy E_i, Σ_n is the neutron removal cross section, and $I_{n\circ}$ is the neutron fluence. At any point, $x_\circ$, the gammas seen from the source at x can be expressed as

$$\Gamma(x, x_\circ) = \tfrac{1}{2} S_i(x)\, e^{-\Sigma_{gi} |x - x_\circ|}$$

Σ_{gi} is the gamma absorption cross section for the i^{th} energy. The ½ appears since only ½ of the photons travel in the direction of the observer. The energy deposited at $x_\circ$ is found by from the derivative of Γ with respect to $x_\circ$. The total energy at $x_\circ$ is then found by summing the contributions from all sources through the target.

$$I = \int_\circ^L dx \, \frac{d}{dx_\circ} \Gamma(x, x_\circ)$$

This expression can be integrated to yield the energy deposited per unit length.

$$I(x_\circ) = \tfrac{1}{2} P_i E_i I_{n\circ} \Sigma_n \Sigma_{gi} \left[\frac{e^{-\Sigma_{gi} x_\circ} - e^{-\Sigma_n x_\circ}}{\Sigma_n - \Sigma_{gi}} + \frac{e^{-\Sigma_n x_\circ} - e^{-\Sigma_n L}\, e^{-\Sigma_{gi}(L - x_\circ)}}{\Sigma_n + \Sigma_{gi}} \right]$$

The energy deposited by the incident gamma flux is then calculated as

$$I_g(x_\circ) = I_{g\circ}\, e^{-\Sigma_g x_\circ}$$

where $I_{g\circ}$ is the incident gamma dose in rads. $I_g(x_\circ)$ is then added to $I(x_\circ)$ to find the total energy deposited.

A simple computer program was written to calculate this expression for various slab thicknesses and materials. Figure 7 shows the predicted temperature rises at the the center of a 1cm thick slab of several materials as a function of neutron fluence. The measured neutron to gamma ratio was used to include the expected gamma dose.

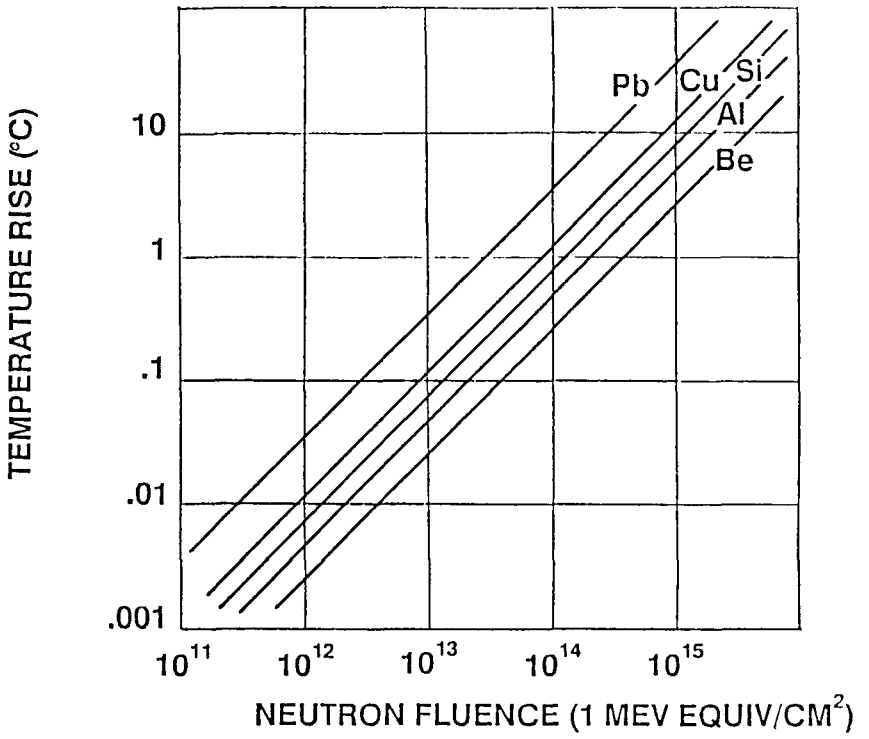

Figure 7 - Predicted heating in a 1cm thick slab from a $1x10^{14}$ n/cm^2 fluence and an expected $3x10^4$ rad gamma dose.

4. Conclusions

The temperature rise in a cylindrical aluminum test fixture was measured at about .55°C per 10^{14} (1 Mev equiv) neutrons/cm^2 and associated gamma in an SPR-III burst. This rise was estimated within 20% using an approximation technique for slab geometries. This agreement may be coincidental. Future experiments are planned to test the predictions for temperature distributions in other geometries and materials.

SESSION IV

DOSIMETRY

J. L. Meason, Chairman
White Sands Missile Range

COMPARISON OF DOSIMETRY RESULTS FROM THE SANDIA SPR-III REACTOR FACILITY

W. Sallee, D. Vehar(*), C. Heimbach(+), J. Meason, T. Luera(*)

Nuclear Effects Laboratory, White Sands Missile Range, NM

ABSTRACT

Due to reported inconsistencies in results from neutron damage studies on electronic piece parts, a series of neutron exposures at the three fast burst reactor facilities which are principally involved in the studies has commenced. The purpose of these exposures is to determine the calibration consistency between the three facilities. Of primary importance in this study is the consistency of neutron fluence data as determined by the principal monitoring system, the sulfur fluence monitor. Results from the first and second exposures in this series indicate that agreement between the three reactor facilities is fair. The results vary by less than 16% between laboratories.

1.0 INTRODUCTION

Historically, three pulse reactor facilities have been used for the majority of the testing of electronic piece-parts to the neutron radiation environment. These reactor facilities are: the White Sands Fast Burst Reactor Facility, the Sandia SPR facility, and the Aberdeen Pulsed Radiation Facility. Some questions have recently arisen concerning the consistency of dosimetry practices between these three facilities (as well as several other facilities used less frequently for this type of testing). In order to determine if these apparent inconsistencies are due to dosimetry calibration errors and to quantify and document the degree of agreement or disagreement between dosimetry results provided by these three facilities, a series of neutron exposures of dosimeters at each of these reactors have been planned. The first and second exposures in this inter-laboratory dosimetry comparison were performed at the Sandia SPR-III reactor on 25 Jul 85 and 18 Feb 86, respectively. In this paper, the dosimetry results of the first exposure will be detailed and a discussion of the experimental arrangement and

---

* Sandia National Laboratory, Albuquerque, NM
+ Aberdeen Pulsed Reactor Facility, Aberdeen Proving Ground, MD

exposure conditions will be presented. And, while the analysis of all the data from the second exposure is not yet complete, the sulfur results are available and will be presented.

2.0 EXPERIMENTAL

The principal dosimeter used to monitor the neutron fluence at each of these facilities is the sulfur pellet (reference 1). Accordingly, the dosimetry sections for each of these facilities provided sulfur pellets to the Sandia Dosimetry Laboratory. The Sandia Dosimetry Laboratory mounted these dosimeters along with nickel foils from White Sands and Sandia on three fixtures for irradiation at 17 inches and 72 inches from the core centerline and in the reactor's glory hole. Figure 1 is a line drawing indicating the relative locations of the fixtures. The dosimeters at 17 inches (4 inches from the core surface) were mounted on a curved aluminum plate. While, the dosimeters in the glory hole were mounted on a cardboard cylinder. The dosimeters at 72 inches were mounted on a flat cardboard plate. Dosimeters from the various laboratories were mounted so as to intermix the sulfur pellets across the face of each of the mounting plates (see figures 2 through 4). Thus, if there was any non-uniformity in the exposure, all the various organizations would have been equally affected. For the 18 Feb 86 exposure, only the 17 inch location was used.

For each exposure, all the dosimeters from the participating laboratories were exposed at one time. On 25 July, a five minute power run was used, while the 18 February exposure was a 301 degree burst operation. In each case the dosimeters were then returned to their respective dosimetry sections for analysis. There the foils were counted using the standard procedures developed by the staff of each organization. All three laboratories utilize standard beta proportional counting techniques which follow ASTM standards E 265-82 and E 181-82 (references 1 and 2). The results were tabulated in terms of the fluence greater than 3 MeV.

In addition to sulfur dosimetry, Sandia and White Sands also provided nickel foils for exposure in order to check gamma ray counting techniques. Both organizations use the threshold foil techniques of ASTM standards E 720 and E 721 (references 3 and 4) to determine the neutron spectra at their respective reactors. These techniques rely heavily on the gamma ray counting. Additionally, nickel can be used in lieu of sulfur to monitor the neutron fluence greater than 3 MeV (reference 5). The nickel foil activities were tabulated in terms of Becquerels (Bq) per gram of 58-Nickel.

3.0 RESULTS AND DISCUSSION

Each laboratory performed an independent evaluation of the fluence greater than 3 MeV for each location based upon their sulfur monitors. For example, for the July 86 exposure, Sandia obtained a value of 7.671 E11 for the 17 inch location, White Sands obtained a value of 7.23 E11 and Aberdeen obtained a value of 7.17 E11. The average of these fluences greater than 3 MeV is 7.36 E11. For the purpose of comparison, this average fluence greater than 3 MeV has been tabulated as a function of exposure location and exposure date. Table 1 gives the results of the comparisons for the sulfur data relative to this average at each location for both exposures. In comparing the results from the July 85 exposure, White Sands and Aberdeen obtained very similar results (differing by only 3% at 72 inches), while Sandia was approximately 7% higher than the other groups at all locations. Based upon estimated error bars of 5 to 7% for sulfur dosimetry, the results are in good agreement even though each laboratory utilized the spectrum average cross section appropriate for their respective reactor's environment. But in February 86, the agreement is not as good with Sandia and White Sands differing by 10%, Sandia and Aberdeen differing by 15%, and Aberdeen and White Sands differing by 5%.

The reason for this marked difference between the results of July 85 and February 86 is at present unexplained. However, Sandia believes that an adjustment to the spectrum average cross section of the SPR-III free field spectrum needs to be made. This would result in a systematic lowering of their stated fluence by approximately 12%. Such a change would result in a substantial improvement in the agreement of the results.

What is not shown in Table 1 is the very good internal consistency of the data for each laboratory. The standard deviation of the mean at each location for each laboratory was no more than 3%, usually much less. This indicates that potential foil placement errors were quite small.

All three organizations utilize the same techniques in calibrating their respective dosimetry systems. Thick foils relative to the average beta energy are employed. White Sands uses a 0.75 inch diameter by 0.25 inch thick sulfur pellet exclusively. Sandia typically uses a 0.25 inch diameter by 0.20 inch thick pellet. Aberdeen typically uses two sizes of dosimeters, 0.25 inch thick by either 0.25 inch or 1.00 inch diameter. Calibration is accomplished according to the procedures in paragraph 8.1.1 of ASTM standard E 265-82, i.e., irradiation with a source of neutrons for which the neutron spectrum is well characterized and for which the total fluence has been accurately determined. Usually, a 252-Cf facility is

Table 1
Comparison of the Sulfur Dosimetry

Location	Average Fluence > 3 MeV	Per Cent Difference Sandia	WSMR	APG
	(neutron/cm^2)	(%)	(%)	(%)
	25 Jul 1985			
Glory Hole	1.39 E13	+ 5.32	- 2.88	- 2.88
17" C-CL	7.36 E11	+ 4.23	- 1.77	- 2.58
72" C-CL	4.08 E10	+ 5.71	- 4.41	- 0.98
	18 Feb 1986			
17" C-CL	2.66 E12	+ 8.53	- 1.50	- 6.77

Table 2
Comparison of the Nickel Activation

Location	Nickel Activation Sandia	WSMR	Per Cent Difference Relative to Sandia's results
	(Bq/gm-Ni-58)		(%)
Glory Hole	7.469 E3	7.340 E3	- 1.73
17" C-CL	3.910 E2	3.741 E2	- 4.32
72" C-CL	2.303 E1	2.026 E1	- 1.20

employed for this purpose because the free field 252-Cf and a fast burst reactor spectra are very similar. Further, because the facilities are used for government testing, the source calibration must be traceable to the National Bureau of Standards. To date, only the NBS 252-Cf facility and the University of Arkansas' SEFOR Calibration Center (also a 252-Cf facility) meet the traceability requirement. Aberdeen's calibration was confirmed by an exposure at the NBS facility in August 1985. The White Sands calibration was last confirmed in the spring of 1983 using the SEFOR Calibration Center. And, Sandia's calibration is based upon data collected at NBS in approximately 1979-1980.

The results of the comparison of nickel counting are tabulated in Table 2. Both Sandia and White Sands follow the standard gamma counting practices outlined in ASTM standard E 181-82. The agreement is obviously very good considering that the estimated calibration error is approximately 4% based upon the information provided by the suppliers of gamma ray calibration sources. Both laboratories use standard gamma ray point sources to obtain the absolute counting efficiencies for each of their gamma ray detectors and for each geometry used. These standard sources were either obtained from the NBS or have certificates of traceability to the NBS.

4.0 CONCLUSIONS

The overall results from the first and second exposures in the inter-laboratory dosimetry comparison indicate fair agreement between the three reactor groups which participated. There is, however, room for improvement and areas of improvement are being actively investigated. The proposed change in the spectrum average cross section for SPR-III data is one such area which will greatly improve agreement between the three laboratories. The importance of obtaining agreement which is as good as possible has lead to an informal arrangement to continue these comparisons on a regular basis for at least the next several years. The next exposure is currently scheduled for the summer of 1986.

The questions concerning dosimetry practices at the three facilities arose from electronic piece part damage studies conducted by various experimenters which have used all three of the fast burst reactor facilities and three TRIGA reactor facilities (references 6 and 7). These damage studies indicate differences in the damage to devices of the same type for the same reported 1 MeV equivalent fluence from the different facilities which are as high as 50% (reference 7). Differences of this magnitude clearly cannot be attributed to inconsistencies

in the sulfur calibrations or counting practices at the three laboratories. This is not to say, however, that inconsistencies do not exist. This inter-laboratory dosimetry study does not address the issues which arise from the application of ASTM standards E 720, E 721 and E 722 (references 3, 4, and 8, respectively) which are used to calculate the 1 MeV Equivalent Damage Fluence in piece parts. Nor does this study address potential errors which may arise from placement of piece parts around the reactors. This study should be viewed as only the first step in addressing this critical issue. Studies of other aspects of this problem are underway.

5.0 REFERENCES

1. Standard Method for Determining Fast-Neutron Flux Density by Radioactivation of Sulfur, E 265-82, Annual Book of ASTM Standards, Volume 12.02, pages 130-134 (1985).

2. Standard General Methods for Detector Calibration and Analysis of Radionuclides, E 181-82, Annual Book of ASTM Standards, Volume 12.02, pages 34-55 (1985).

3. Standard Guide for Selection of a set of Neutron-Activation Foils for Determining Neutron Spectra Used in Radiation-Hardness Testing of Electronics, E 720-80, Annual Book of ASTM Standards, Volume 12.02, pages 449-454.

4. Standard Method for Determining Neutron Energy Spectra with Neutron-Activation Foils for Radiation-Hardness Testing of Electronics, E 721-80, Annual Book of ASTM Standards, Volume 12.02, pages 455-462.

5. Standard Method for Determining Fast-Neutron Flux Density by Radioactivation of Nickel, E 264-82, Annual Book of ASTM Standards, Volume 12.02, pages 125-129 (1985).

6. Private Communication between W. Sallee and B. Ahlport (Northrup Corporation), Spring 1985. (Also see the paper in the proceedings of this conference by B. Ahlport on "Silicon Damage Equivalence at FBR's".)

7. Private Communication between W. Sallee and J. Malloy (Raytheon Company), March 1986.

8. Standard Practice for Characterizing Neutron Energy Fluence Spectra in Terms of an Equivalent Monoenergetic Neutron Fluence for Radiation-Hardness Testing of Electronics, E 722-80, Annual Book of ASTM Standards, Volume 12.02, pages 463-469.

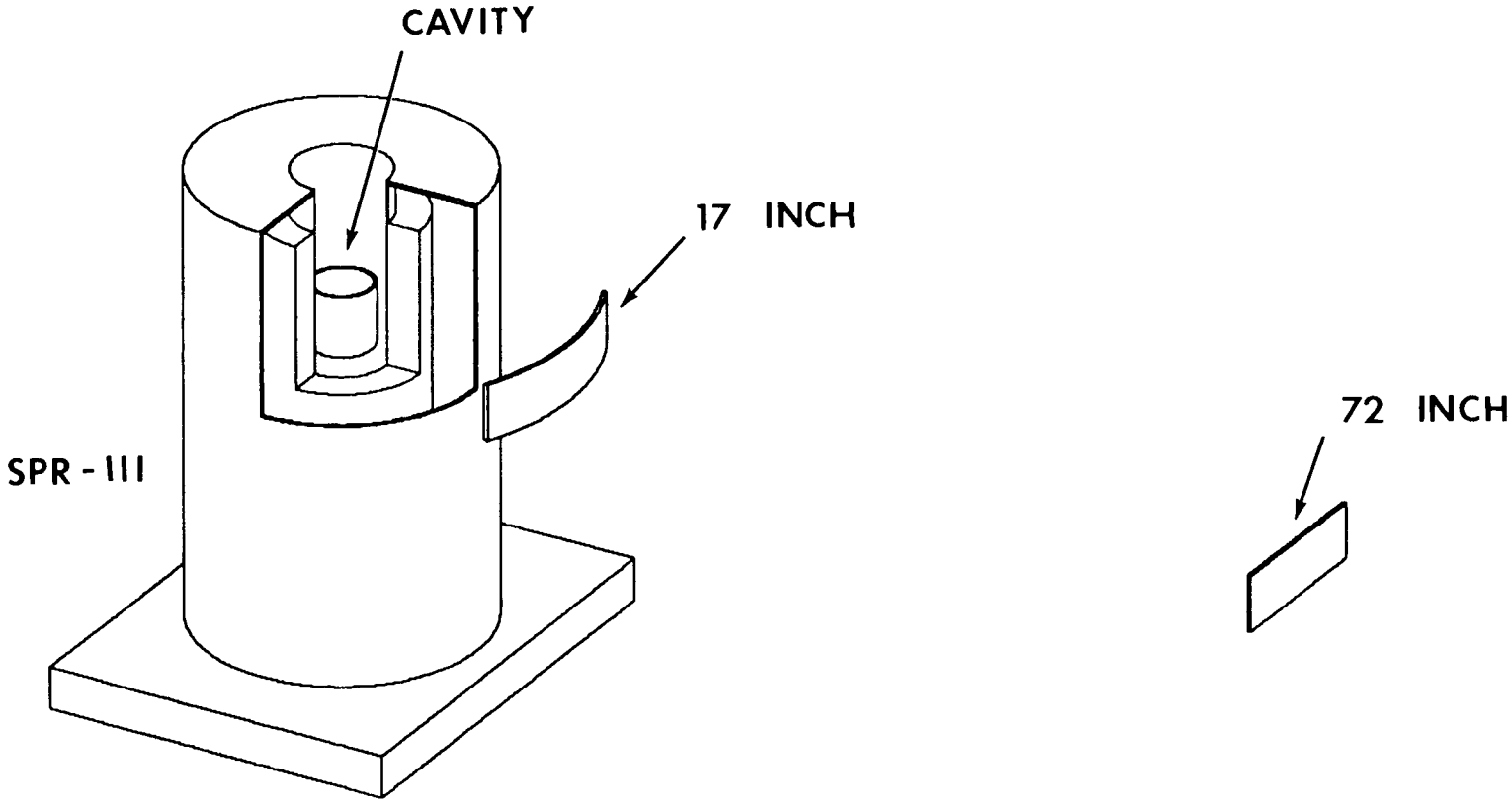

Figure 1. Irradiation Fixture Placement

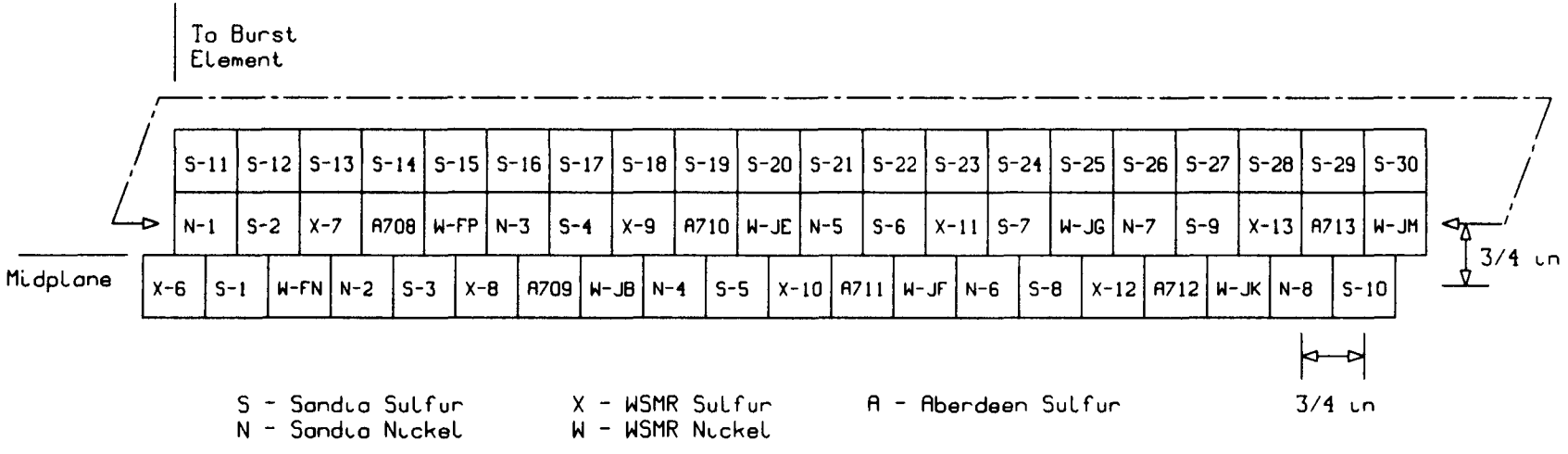

Figure 2. Foil Placement for Cavity Irradiation

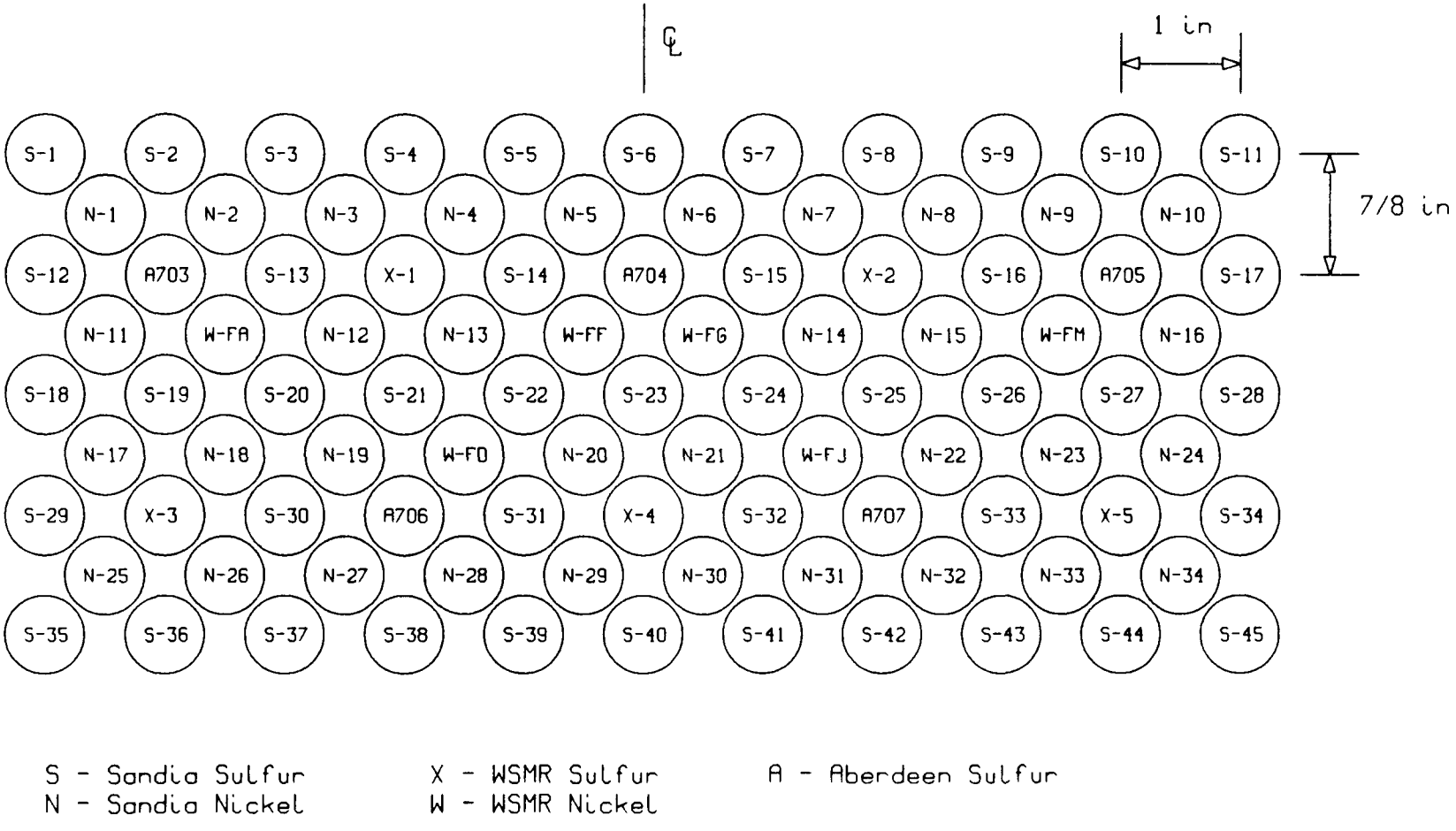

Figure 3. Foil Placement for 17-inch Irradiation

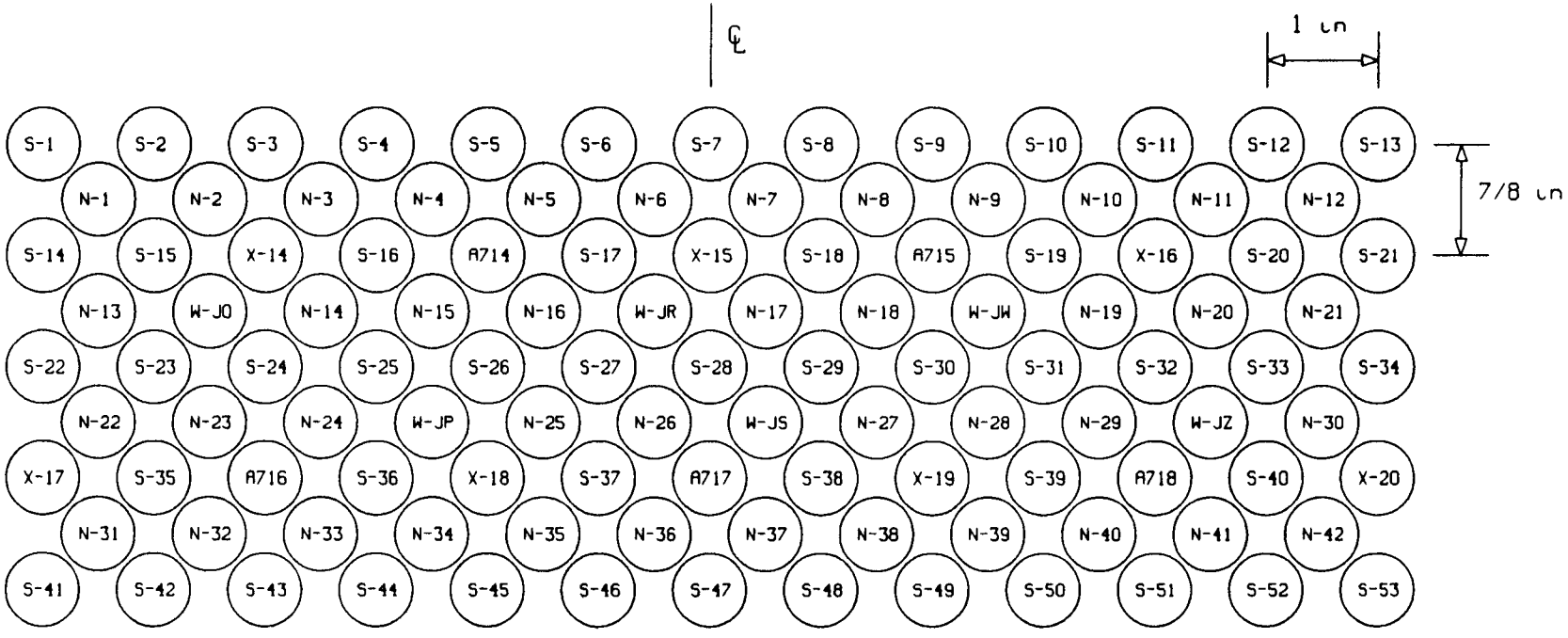

Figure 4. Foil Placement for 76-inch Irradiation

USE OF THE FOIL ACTIVATION METHOD WITH ARBITRARY TRIAL FUNCTIONS TO DETERMINE NEUTRON ENERGY SPECTRA*

John G. Kelly and David W. Vehar

Sandia National Laboratories
P. O. Box 5800
Albuquerque, NM 87185

ABSTRACT

Neutron Spectra have been measured by the foil activation method in thirteen different environments in and around the Sandia Pulsed Reactor (SPR III), the White Sands Missile Range FBR, and the Annular Core Research Reactor (ACRR). The unfolded spectra were obtained by using the SANDII code in a manner which was not dependent on the initial trial. This altered technique is, therefore, better suited for the determination of spectra in environments that are difficult to predict by calculation, and it tends to reveal features that may be biased out by the use of standard trail functions.

1.0 INTRODUCTION

Accurate determination of the responses of materials and electronic devices to neutron irradiation in a variety of environments is becoming increasingly important because of the accelerating interest in nuclear and space radiation effects. Furthermore, devices often must be tested in radiation fields which do not duplicate the environments for which they are intended. For example, components to be used in satellites may be tested at a nuclear reactor. It is imperative therefore, that the radiation spectrum of the test source at the location of the device under test be determined so that models to calculate its response can be confirmed and used to predict responses in the intended environment.

The foil activation method, together with suitable spectrum unfolding codes, have become very effective in determining neutron energy spectra in a wide variety of environments. Some of the unfolding codes still in use are SANDII,[1] STAY'SL,[2] and FERRET.[3] The latter two provide completely determined solutions but require full knowledge not only of the values of the appropriate trial functions, the activities of the foils, and the cross sections for each reaction, but also of the errors and correlation functions of each of the data sets. The SANDII procedure uses only the values of the trial

*This work performed at Sandia National Laboratories which is operated for the U.S. Department of Energy under contract number DE-AC04-76DP00789.

functions, activities, and cross sections. However, in this case the solutions are underdetermined (fewer activity values than flux values in the solution), and the code must iterate on a trial spectrum shape until the calculated activities are within some acceptable standard deviation of the measured values. For the k^{th} iterated spectrum the activity of isotope number i is calculated by equation 1.

$$A_i^K = \lambda \int_E \sigma_i(E)\ \phi^K(E)\ dE \qquad (1)$$

where A_i^K is the activity, σ_i is the reaction cross section of isotope i, and $\phi^K(E)$ is the differential fluence. The decay constant for the reaction product is λ. Since a spectrum that satisfies the activity set within the specified standard deviation is not unique, one can only call it an "appropriate" solution. All of these codes have required a reasonable trial spectrum to start with (as they have been used in the past). This requirement imposes some practical difficulties. Calculated trials can be expensive to obtain, and the models may have to overly simplify features that may be important. Also, trials based on previous measurements may not be appropriate in a new environment.

The objectives for this work were to develop a method of determining acceptable spectra which are less dependent on the shape of the trial function and to investigate how well these spectra are determined by the activity and cross section values by means of foil sets that exhibit adequate sensitivity over a broad energy range.

2.0 THE PROCEDURE

The procedure we have developed for the SANDII code is very simple in principle, but does require careful activity measurements and the application of knowledge about the reaction response functions. Generally the code cannot iterate directly from an arbitrary trial to an acceptable solution, but it will provide very important clues as to how a better trial function can be constructed. One then iterates the code using simple criteria based on physical principles until he is satisfied with the spectral shape and standard deviation. Our experience, with a broad range of environments, is that the reasonable solutions are indeed quite well determined.

The example to be discussed first illustrates the progression from a flat trial spectrum to one which the SANDII code finally accepts as a converged solution without trying to make significant changes in the final trial. The activities obtained from a foil set exposed 17" from the centerline of the Sandia Pulsed Reactor (SPR III) are listed in Table 1. Beside each reaction are listed the filter cover, its thickness, and the activity at the end of the irradiation period. The activity determinations are not discussed in this

Table 1

Foil Activities from the SPR-III 17" Free Field Leakage Spectrum

Reaction	Reaction Name	Cover (atoms/barn)	Activity (dis/sec. nucleus)
$AU^{197}(n,\gamma)Au^{198}$	AU197G	2.587-3 cadmium	1.094-16
$AU^{197}(n,\gamma)Au^{198}$	AU197G	- -	1.275-16
$Mn^{55}(n,\gamma)Mn^{56}$	MN55G	2.587-3 cadmium	3.490-17
$Mg^{24}(n,p)Na^{24}$	MG24P	2.587-3 cadmium	2.067-19
$Fe^{56}(n,p)Mn^{56}$	FE56P	2.587-3 cadmium	9.104-19
$Fe^{54}(n,p)Mn^{54}$	FE54P	2.587-3 cadmium	2.486-20
$AL^{27}(n,p)Mg^{27}$	*AL27P	2.587-3 cadmium	5.159-17
$AL^{27}(n,\alpha)Na^{24}$	AL27A	2.587-3 cadmium	1.034-19
$Ni^{58}(n,p)Co^{58}$	NI58P	2.587-3 cadmium	1.402-19
$Na^{23}(n,\gamma)Na^{24}$	NA23G	2.587-3 cadmium	2.033-19
$Zr^{90}(n,zn)Zr^{89}$	ZR902	2.587-3 cadmium	2.476-21
$S^{32}(n,p)P^{32}$	S32P	- -	4.680-19
$In^{115}(n,\gamma)In^{116}$	*IN115G	- -	5.363-15
$In^{115}(n,n')In^{115}$	*IN115N	- -	1.069-16
$In^{115}(n,\gamma)In^{116}$	*IN115G	2.587-3 cadmium	2.992-15
$In^{115}(n,n')In^{115}$	*IN115N	1.587-3 cadmium	1.076-16
$Ni^{58}(n,p)Co^{58}$	*NI58P	4.705-3 cadmium 0.101 boron	1.400-19
			Activity (fissions/nucleus)
$U^{235}(n,f)F$	U235F	4.705-3 cadmium 0.101 boron	2.326-11
$U^{238}(n,f)F$	U238F	4.705-3 cadmium 0.101 boron	3.406-12
$Pu^{239}(n,f)F$	PU239F	4.705-3 cadmium 0.101 boron	3.085-11
$Np^{237}(n,f)F$	NP237F	4.705-3 cadmium 0.101 boron	1.640-11

*Reactions not used in the unfold procedure.

paper. The reactions marked with an asterisk were not used in the SANDII unfolding process for the reasons that will be discussed below. This set of reactions was chosen because it provides responses over a very broad energy range, and in our experience has demonstrated that reasonable solutions are obtainable in all spectra measured thus far.

The reactions marked by asterisks were left out of the analysis for the following reasons.

1) $AL^{27}(n,p)Mg^{27}$ - In almost all of the spectra measured thus far the calculated activity for spectra compatible with the other activities is 20 to 50% low. For this reason the reaction has usually been left out of the unfolding procedure. The cause of this discrepancy has not yet been identified.

2) $Ni^{58}(n,p)Co^{58}$ inside the boron ball containing the fission foils - The exponential attenuation of the fluence in the boron as applied by the SANDII code is not adequate to account for the measured free field nickel activity to boron ball nickel activity ratios. The ball reduces the induced nickel activity by more than the code calculates.

3) $IN^{115}(n,\gamma)IN^{116}$ - The reaction threshold is at 1 eV and for the foil thicknesses presently available severe self shielding has been observed.

4) $IN^{115}(n,n')IN^{115}$ - The threshold for this reaction is at 1 Mev. The activity always appeared to be higher than the calculated value. Wes Sallee from the White Sands Missile Range[4] has suggested to us that the metastable state in the reaction product can also be produced by γ,γ' reactions. This explanation is supported by the fact that the activity acquired by In in a cadmium cover is often greater than that induced in the bare foil.

Other reactions have been rejected in some of the other spectra measurements, but serious efforts have been made to fit in all reactions for which no satisfactory explanation for disagreement can be found.

The graphs in Figure 1 show some of the stages in the generation of a solution for this SPR III 17" leakage spectrum. Figure 1.a shows the SANDII solution obtained with a flat trial and 22 normal SANDII iterations.

On the graph are marked some of the principle resonances of certain reactions in the foil set. It is obvious that the solution is not physically realistic in many regions because one of these tiny foils cannot alter the fluence by orders of magnitude. Clearly the code attempts to obtain agreement with the measured activities in the fastest way possible - by changing the spectrum where the reaction responses are the highest. In this example the Au foil clearly shows that the trial function fluence should be higher at the Au resonance (5ev) and the Mn and Na foils indicate that the spectrum should be lower at 3×10^{-4}, 1.0×10^{-3}, and 3×10^{-3} Mev. A new trial was constructed that passed in a sensibly smooth manner through the points where the foil set has high response. The SANDII result obtained with this second trial is shown in Figure 1.b. The improvement is dramatic even though only a very simple rule has been followed - draw a trial through SANDII solution values where the response is high. The case 1.b indicates that the trial would be even more successful if it were yet slightly higher at 5ev and lower at 3×10^{-4} Mev.

Further improvements may require a little more experience on the part of the analyst. Sodium, for example, not only responds at thermal energies but also at 3×10^{-3} Mev, 3×10^{-2} Mev, 5×10^{-2} Mev, and higher. SANDII will try to fit the activity by changing the

spectrum in all high response regions even if the error in the trial is only at one location. The two small dips in Figure 1.b at 3 and 5×10^{-2} Mev can be eliminated with a trial having a slightly lower value at 3×10^{-3} Mev. The validity of this maneuver is supported by the fact that the dips induced by the Na are not compatible with the flux level required in that region by the U^{235} and Pu^{239} fission reaction responses. Incorporation of this type of reasoning along with simple smoothing procedures led to the spectrum shown in Figure 1.c. This final result is essentially the same as that obtained with SANDII using a trial calculated with the MORSE Monte Carlo Code by Ray Sartor.[5] This clearly shows that the solution is very insensitive to the initial trial. The standard deviation of measured-to-calculated activities in this result was 0.8%.

The success of the procedure just illustrated is very dependent on a number of factors. First, the cross section set must be accurate. With the set originally supplied with the SANDII code, reasonably smooth solutions did not result from the unfolding procedure, and standard deviations of less than 5% were difficult to obtain. For example, the sulfur and nickel activities obtained with the solution spectrum typically disagreed by 15%. (The sulfur activity indicated the fluence greater than 3 Mev should be 8% higher and the nickel indicated it should be 7% lower.) When the latest cross section set from RSIC[6] was placed in the cross section library, the improvement in solution compatibility and smoothness was dramatic. Now sulfur and nickel measured activities usually agree within 3% with the activities calculated with the final spectrum.

Second, it is very important that all activities be accurately determined. This means care must be taken that the foils are exposed to the same fluence (or can be accurately normalized), and that the counting process provides adequate counting statistics on a number of different, but properly calibrated detectors. A sufficiently compatible set of data provides not only much smoother spectrum results, but also permits the identification of much more subtle spectrum details.

Third, the more reactions there are in the foil set the better for defining the solution spectrum as long as the cross sections are accurate. Clearly, with more reactions to match, the unfolding process is more difficult, and small experimental or counting errors will lead to incompatibilities that no physically reasonable spectrum can quite resolve. Sensitivity studies that have been carried out have shown that very little departure from the solutions found by this procedure are allowed. Furthermore, solutions settle to values with characteristics that are very close to what one would expect in the geometries where the foils were exposed. For example, a spectrum was measured inside a boron and lead liner in the ACRR cavity. There were two expectations for this spectrum. First, the thermal end of the spectrum should be depressed by the boron. Second, the high energy neutrons should be strongly attenuated by inelastic scattering in the lead. The comparison between the ACRR

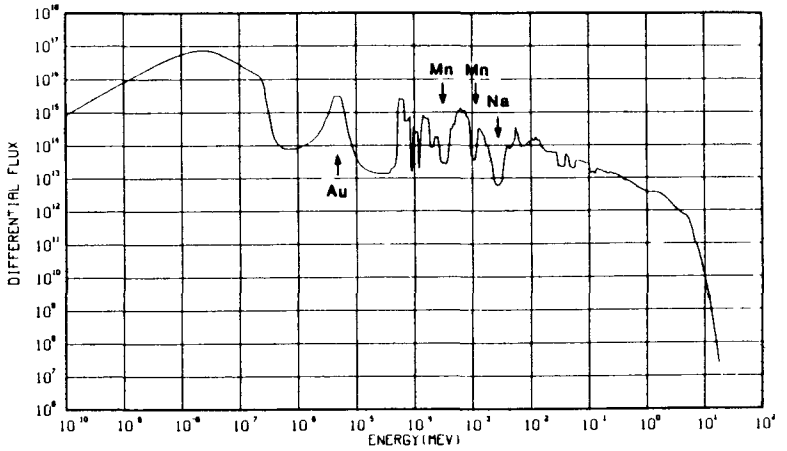

a. First Iteration with Flat Trial

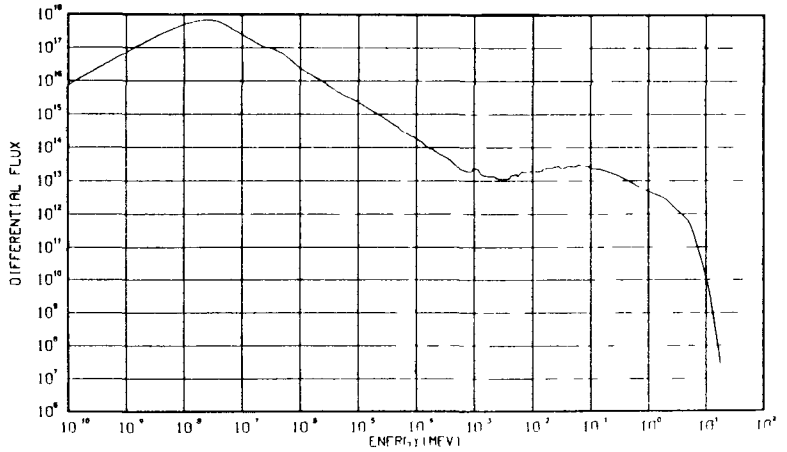

b. Second Outer Iteration

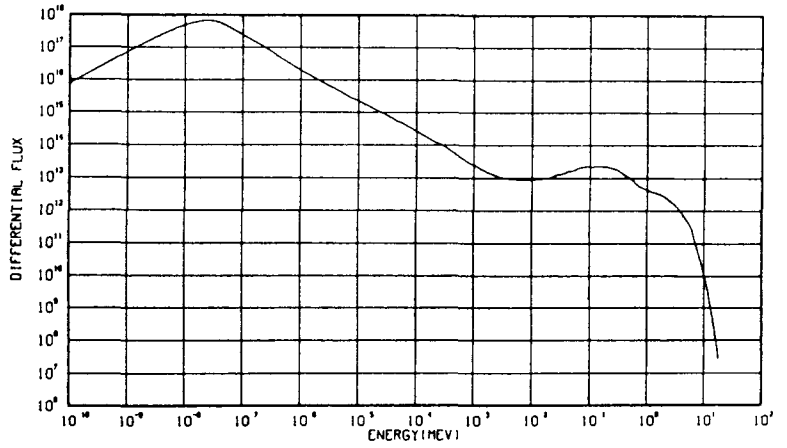

c. Final Iteration

Figure 1. Progression to Final Solution from a Flat Initial Trial

free field spectrum and the PB-B liner spectrum are shown in Figure 2. The curves are normalized at 3 Mev.

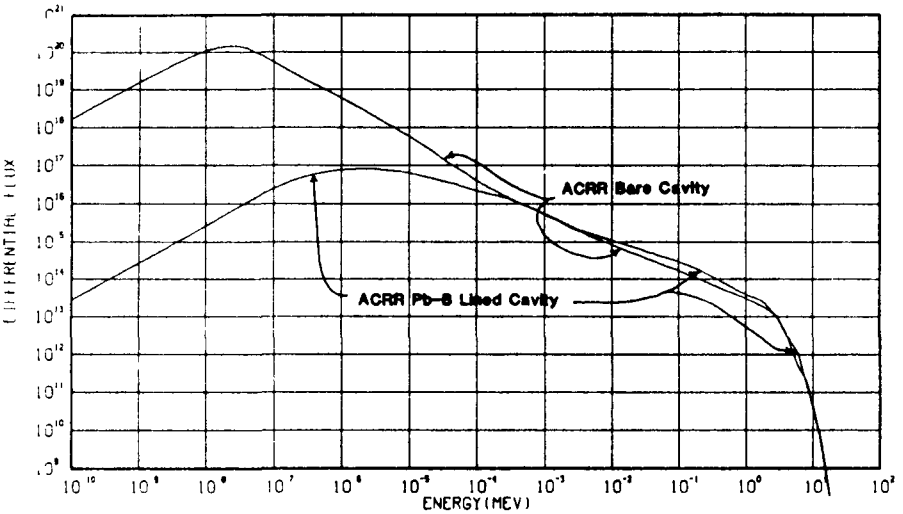

Figure 2. ACRR Cavity Spectra

The attenuation at the thermal end is easily discerned, but on this logarithmic scale and where the curves fall swiftly, the attenuation of the fast neutrons is not so evident. However, if one uses the definition of spectral index (SI) (which is the ratio of the fluence above 10 keV to that above 3 Mev), the difference is more obvious. For the free field case SI=12.1$\pm$0.5 and for the PB-B liner case it is 16.8$\pm$0.5. There is little flexibility in either of these values.

Another case shows how an unbiased approach to trial functions has led to the discovery of a new feature in the SPR III central cavity spectrum which had been calculated to drop away as E at low energies. Figure 3 shows the spectrum generated with such a trial spectrum calculated by WSMR personnel for SPR III in one dimensional cylindrical geometry. Also included is the spectrum arrived at by the present procedures of allowing the activities alone to define the spectrum. To fit the gold foil activity the trial spectrum had to be raised by 8 orders of magnitude at thermal energies. The WSMR calculation did not account for thermal neutrons that could leak in from the top and bottom openings in the cavity.

A fifth example of the unfolded spectra is that obtained from the WSMR Fast Burst reactor. The foil set exposed there and counted at Sandia Laboratories produced the spectrum shown in Figure 4. The 17" leakage spectrum from SPR III is shown in the same figure for comparison since they are both produced in fast burst reactors. The spectra look quite similar, but have significantly different spectral indices. SPR III is softer, with SI=7.6, while the WSMR FBR SI=6.7. The former value compares with the 7.25 previously used at Sandia Laboratories for SPR III, and the latter agrees with the spectral index used by White Sands as their spectral index and measured independently by them. These curves are also normalized at

3 Mev. The differences between the SPR III and the WSMR FBR result from the external reflectors of SPR III and differences in room return radiation.

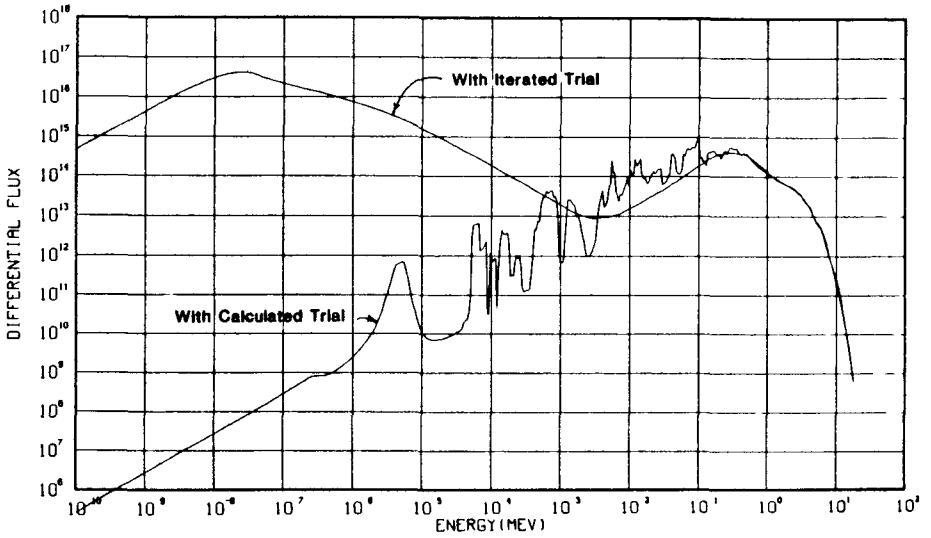

Figure 3. SPR III Cavity Spectra

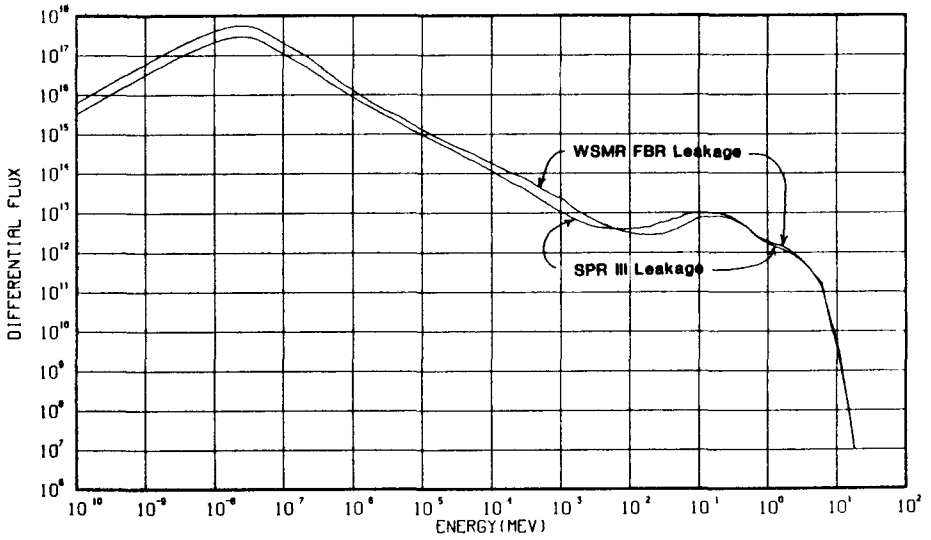

Figure 4. Fast Burst Reactor Leakage Spectra

To provide some data that others may use to test codes and to determine quantities that depend on neutron spectra, tables of the activities and the spectra for the five environments discussed in this section are presented in the appendix.

3.0 RELATIONSHIPS OF SPECTRA WITH SULFUR DOSIMETRY AND SILICON DAMAGE FUNCTIONS

Experimenters testing electronic devices frequently wish to relate the fluence measured with sulfur dosimeters to the displacement

damage induced in silicon devices. This is not in general possible unless the neutron spectrum irradiating the devices is known. To make the proper connections between sulfur dosimetry and silicon damage, some additional quantities must be introduced. The spectrum averaged cross section of sulfur is defined by equation 2.

$$\bar{\sigma} = \frac{\int_0^\infty \phi(E)\sigma_s(E)dE}{\int_t^\infty \phi(E)dE} = \frac{\int_0^\infty \phi(E)\sigma_s(E)dE}{\Phi(E>t\ \text{Mev})} \qquad (2)$$

Here the lower limit t stands for the threshold energy of the reaction (generally taken to be 3 Mev for sulfur). The quantities $\sigma(E)$ and $\phi(E)$ are the $S^{32}(n,p)P^{32}$ reaction cross sections and the neutron differential fluence respectively. The $\Phi(E>3\ \text{Mev})$ is the integral fluence above 3 Mev. From equations 1 and 2 the flux greater then 3 Mev fluence is given by

$$\Phi_s(E>3\ \text{Mev}) = \frac{A_s}{\lambda\bar{\sigma}_s}\ . \qquad (3)$$

One has to know the spectrum and the sulfur cross section to determine $\bar{\sigma}_s$. Using the spectral index one finds the fluence above 10 keV which is important for the determination of damage in silicon.

$$\Phi_s(E>10\ \text{keV}) = SI\cdot\Phi_s(E>3\ \text{Mev}) \qquad (4)$$

The displacement damage in silicon is calculated by use of the definition below.

$$D_{si} = \int_{10\,\text{kev}}^\infty \phi(E)k(E)dE \equiv \Phi(E>10\ \text{kev})\bar{k}_R = \Phi_s(E>3\text{Mev})\cdot Si\cdot\left(\frac{\bar{k}_R}{D_1}\right)D_1 \qquad (5)$$

The k(E) is the damage function vs energy in silicon. For this work we have used the function published in the ASTM standard E722-85.[6] The quantity, D_1, is the average damage caused by 1 Mev neutrons and is taken to be 95 Mev·mb as recommended by the same ASTM standard. Thus if the analyst has determined a spectrum, he can generate all the quantities needed to calculate the damage once the experimenter provides the sulfur pellets to be read from the experiment. The SANDII printout provides the integral fluences $\Phi(E>3$ Mev) and $\Phi(E>10$ kev) so that the SI is determined. The ratio $\bar{k}_R/D_1$ (defined

as the hardness parameter) is calculated by integration of the fluence with the damage function

$$\left(\frac{\bar{k}_R}{D_1} \right) \equiv h_p = \int_E \phi(E)k(E)d(E) \cdot \frac{1}{95 \text{ Mev.mb}} .$$

Then the calculated damage will be

$$D_{si} = \Phi_s(E>3 \text{ Mev}) \cdot SI \cdot h_p \cdot D_1 \qquad (6)$$

Once the spectrum is known, the last 3 factors are fixed, and the damage can be determined when the counting laboratory provides the $\Phi_s(E>3 \text{ Mev})$.

The subscript "s" on the fluence $\Phi(E>3 \text{ Mev})$ has been purposely left in place because there are two important situations in which this number may not agree with the $\Phi(E>3 \text{ Mev})$ provided directly by the SANDII code. First, if the activity, A, does not agree exactly with the activity calculated by SANDII with the solution spectrum, then a normalization error may be introduced by the amount of that disagreement. Usually we assume that the statistical variations in the sulfur pellets account for this disagreement and that the spectrum determined activity will be the correct one on the average. The difference is usually less than 3%. The second source of error in the determination of $\Phi_s(E>3 \text{ Mev})$ is the spectral averaged cross section in the denominator of equation 3. The $\bar{\sigma}_s$ used by the counting laboratory must be the same as that which is calculated from the spectrum provided by the unfolding code. We had noticed in 1985 that the fluence reported by the counting laboratory from sulfur measurements was on the average approximately 10% higher than the SANDII results obtained with the same sulfur activity together with the rest of the foil set. Investigation revealed that the spectrum averaged cross section then in use by the laboratory was 287 mb for the SPR III free field leakage system. This is the same value one calculates with the SANDII solution and the "old" SANDII cross section library. The RSIC cross section library used now yields 320.5 mb. The correction to the counting laboratory fluence reported in the past for this reactor environment based on Eq. 3 is therefore the following.

$$\Phi_n(E>3 \text{ Mev}) = \frac{\bar{\sigma}_o}{\bar{\sigma}_n} \Phi_o(E>3 \text{ Mev})$$

$$= .895\Phi_o(E>3 \text{ Mev})$$

where n and o refer to new and old values respectively.

With this change in reported fluence the Sandia sulfur fluences agree within 5% with those determined by WSMR and Aberdeen Proving Ground personnel measured at SPR III simultaneously and with their own sulfur dosimeters and counting systems. This interlaboratory comparison is reported on more thoroughly by Wes Sallee and C. Heimbach in these proceedings.[4]

Each spectrum of course yields its own $\bar{\sigma}_s$ so that the laboratory must use different constants to determine $\Phi(E>3$ Mev) for each environment. This is why it is dangerous to assume values for $\bar{\sigma}_s$, SI or h_p for environments in which spectra have not been measured. TABLE II lists these three parameters for the five spectra that have been discussed in this paper.

TABLE II

Parameters Derived from the Neutron Spectra

Spectrum Environment	Calculated Spectrum Averaged Sulfur Cross Section ($\bar{\sigma}_s$)	Spectral Index (SI)	Silicon Hardness Parameter (hp)
SPR III Bare Cavity	325.0 mb	8.78	.924
SPR III 17" Leakage	320.5	7.57	.872
WSMR FBR Leakage	316.3	6.65	.916
ACRR Bare Cavity	341.1	12.14	.726
ACRR PB-B Lined	352.2	16.84	.659

4.0 SUMMARY AND CONCLUSIONS

A procedure has been outlined which yields satisfactory neutron energy spectra with the foil activation technique in a manner that is insensitive to the form of the initial trial spectrum. The method is most useful if the foil set has good coverage over all energies of interest, and if the activities are accurately determined. The best reaction cross sections must be used in the analysis. A few of the most important spectra and the parameters derived from them have been discussed. For those experimenters who test silicon devices subject to neutron induced displacement damage, the means to estimate this damage based on the fluence measured with sulfur dosimeters has been reviewed. The variations of these parameters exhibited in TABLE II indicate the risk involved in making damage predictions before satisfactory spectrum measurements have been made. We have made additional spectrum measurements (not included here) in a wider variety of configurations. These geometries include polyethylene filters, cadmium loaded polyethylene walls and within other neutron shielding structures. This extensive

library of spectra has revealed consistent deviations of measured to calculated activities that point to potential errors in the cross section files and to the possibility of identifying additional real structural details in the spectra. Experimenters using these facilities are advised to consult reactor personnel as to the most recently determined parameters for environments that are relevant for their tests.

5.0 ACKNOWLEDGEMENTS

The authors wish to express their appreciation to the operating personnel at the reactor facilities for their patience and very helpful assistance. They also are grateful to C. Holm in the counting laboratory for his accurate activity determinations. T. Luera and G. Cano provided the essential encouragement and advice.

6.0 REFERENCES

1. S. Berg and W. N. McElroy, "A Computer-Automated Iterative Method for Neutron Flux Spectra Determination by Foil Activation," Atomics International, Tech. Rep. No. AFWL-TR-67-41, Sept. 1967.

2. F. G. Perry, "Least Squares Dosimetry Unfolding: The Program STAY'SL," ORNL/TM-6062, ENDF-254, Oak Ridge National Laboratory (1977).

3. F. Schmittroth, "FERRET Data Analysis Code" HEDL-TME 79-10, Hanford Engineering Development Laboratory, Richland, WA (Sept. 1979).

4. W. Sallee, D. Vehar, C. Heimbach, J. Meason, T. F. Luera, "Comparison of Dosimetry Results from the Sandia SPR-III," Fast Burst Reactor Workshop, Albuquerque, NM, April 2-9, 1986.

5. R. F. Sartor, Texas A&M University, November 1985, private communication.

6. American Society for Testing and Materials (ASTM) Standard E722-85.

7.0 APPENDIX

For each of the spectra referred to in the text, two tables are included in this appendix. The first lists the reactions and their activities and the second lists the fluence values at 50 energies.

Table A.1

Foil Activities from the SPR-III Cavity Free Field

Reaction	Cover (atoms/barn)	Activity (dis/sec. nucleus)
AU197G	2.587-3 cadmium	2.170-16
AU197G	- -	2.277-16
MN55G	2.587-3 cadmium	1.504-16
MG24P	2.587-3 cadmium	4.092-18
FE56P	2.587-3 cadmium	1.778-17
FE54P	2.587-3 cadmium	4.481-19
*AL27P	2.587-3 cadmium	1.056-15
AL27A	2.587-3 cadmium	1.972-18
NI58P	2.587-3 cadmium	2.863-18
NA23G	- -	2.207-18
ZR902	2.587-3 cadmium	5.874-20
S32P	- -	9.554-18
*IN115G	- -	1.704-14
*IN115N	- -	2.147-15
*IN115G	2.587-3 cadmium	1.698-14
*IN115N	2.587-3 cadmium	2.185-15
*NI58P	4.705-3 cadmium 0.101 boron	2.465-18
		Activity (fissions/nucleus)
U235F	4.705-3 cadmium 0.101 boron	5.397-10
U238F	4.705-3 cadmium 0.101 boron	7.129-11
PU239F	4.705-3 cadmium 0.101 boron	7.003-10
NP237F	4.705-3 cadmium 0.101 boron	4.052-10

*Reactions not used in the unfolding procedure.

Table A.2

SPR-III BARE CAVITY SPECTRUM

(normalized to $\Phi(E>10^{-2}$ Mev) = 1.00)

E(Mev)	Differential	Integral	E(Mev)	Differential	Integral
1.0-9	9.719	1.001	7.2-4	5.882-2	1.000
2.0-9	1.867+1	"	1.0-3	4.318-2	"
5.0-9	4.131+1	"	2.0-3	2.301-2	"
1.0-8	6.745+1	"	3.0-3	1.963-2	"
2.0-8	8.991+1	"	5.0-3	2.135-2	"
5.0-8	6.739+1	"	7.2-3	2.573-2	"
1.0-7	4.825+1	"	1.0-2	3.415-2	"
2.0-7	3.482+1	1.000	2.0-2	6.645-2	9.995-1
3.0-7	2.992+1	"	3.0-2	9.704-2	9.987-1
5.0.7	2.351+1	"	5.0-2	1.729-1	9.961-1
7.2-7	1.961+1	"	7.2-2	2.747-1	9.913-1
1.0-6	1.667+1	"	1.0-1	4.215-1	9.819-1
2.0-6	1.130+1	"	2.0-1	8.269-1	9.187-1
3.0-6	8.815	"	3.0-1	9.205-1	8.311-1
5.0-6	6.155	"	5.0-1	7.848-1	6.589-1
7.2-6	4.685	"	7 2-1	4.844-1	5.191-1
1.0-5	3.504	"	1.0-0	2.911-1	4.083-1
2.0-5	1.933	"	1.5-0	1.657-1	2.935-1
3.0-5	1.296	"	2.0-0	1.299-1	2.183-1
5.0-5	8.064-1	"	3.0-0	7.878-2	1.139-1
7.2-5	5.761-1	"	4.0-0	3.863-2	5.616-2
1.0-4	4.196-1	"	5.0-0	1.775-2	2.871-2
2.0-4	2.061-1	"	6.0-0	1.106-2	1.426-2
3.0-4	1.411-1	"	8.0-0	1.874-3	2.706-3
5.0-4	8.345-2	"	10.0-0	4.464-4	6.385-4

File #BAR247 Date: 11-13-84 Reactor Shot #3436

Standard Deviation for 15 foils	=	2.99%
Spectral Index	=	8.78
Total Fluence per MJ	=	6.882×10^{13} n/(cm^2·MJ)
Total Energy in Core	=	6.55 MJ
Total Neutrons	=	4.508×10^{14} n/cm^2
Fluence per MJ > 3 Mev	=	7.838×10^{12} n/(cm^2·MJ)

Table A.3

Foil Activities from the SPR-III 17"
Free Field Leakage Spectrum

Reaction Name	Cover (atoms/barn)	Activity (dis/sec. nucleus)
AU197G	2.587-3 cadmium	1.094-16
AU197G	- -	1.275-16
MN55G	2.587-3 cadmium	3.490-17
MG24P	2.587-3 cadmium	2.067-19
FE56P	2.587-3 cadmium	9.104-19
FE54P	2.587-3 cadmium	2.486-20
*AL27P	2.587-3 cadmium	5.159-17
AL27A	2.587-3 cadmium	1.034-19
NI58P	2.587-3 cadmium	1.402-19
NA23G	2.587-3 cadmium	2.033-19
ZR902	2.587-3 cadmium	2.476-21
S32P	- -	4.680-19
*IN115G	- -	5.363-15
*IN115N	- -	1.069-16
*IN115G	2.587-3 cadmium	2.992-15
*IN115N	1.587-3 cadmium	1.076-16
*NI58P	4.705-3 cadmium 0.101 boron	1.400-19
		Activity (fissions/nucleus)
U235F	4.705-3 cadmium 0.101 boron	2.326-11
U238F	4.705-3 cadmium 0.101 boron	3.406-12
PU239F	4.705-3 cadmium 0.101 boron	3.085-11
NP237F	4.705-3 cadmium 0.101 boron	1.640-11

*Reactions not used in the unfolding procedure.

Table A.4

SPR-III 17" LEAKAGE SPECTRUM

(normalized to Φ(E>10 kev) = 1.00)

E(Mev)	Differential	Integral	E(Mev)	Differential	Integral
1.0-9	3.620+3	1.018	7.2-4	1.719	1.005
2.0-9	6.951+3	"	1.0-3	1.238	1.005
5.0-9	1.539+4	"	2.0-3	6.742-1	1.004
1.0-8	2.512+4	"	3.0-3	5.190-1	1.003
2.0-8	3.346+4	"	5.0-3	4.654-1	1.002
5.0-8	2.479+4	1.017	7.2-3	4.487-1	1.001
1.0-7	1.239+4	1.016	1.0-2	4.530-1	1.000
2.0-7	6.198+3	1.015	2.0-2	5.136-1	9.952-1
3.0-7	3.956+3	"	3.0-2	6.582-1	9.892-1
5.0.7	2.156+3	1.014	5.0-2	8.374-1	9.742-1
7.2-7	1.453+3	"	7.2-2	1.080	9.531-1
1.0-6	1.003+3	1.013	1.0-1	1.159	9.218-1
2.0-6	5.082+2	"	2.0-1	1.118	8.081-1
3.0-6	3.430+2	1.012	3.0-1	8.910-1	7.065-1
5.0-6	2.147+2	"	5.0-1	4.995-1	5.696-1
7.2-6	1.452+2	1.011	7.2-1	2.862-1	4.850-1
1.0-5	1.147+2	"	1.0-0	2.149-1	4.140-1
2.0-5	6.028+1	1.010	1.5-0	1.726-1	3.161-1
3.0-5	4.230+1	1.009	2.0-0	1.362-1	2.370-1
5.0-5	2.539+1	"	3.0-0	7.699-2	1.320-1
7.2-5	1.834+1	1.008	4.0-0	4.471-2	7.158-2
1.0-4	1.334+1	"	5.0-0	2.550-2	3.678-2
2.0-4	6.567	1.007	6.0-0	1.475-2	1.658-2
3.0-4	4.684	1.006	8.0-0	2.237-3	3.311-3
5.0-4	2.594	"	10.0-0	5.647-4	7.694-4

File #SLEAK21 Date: 2-18-86 Reactor Shot #4328

Standard Deviation for 15 foils = 0.81%
Spectral Index = 7.58
Total Fluence per MJ = 3.029×10^{12} n/(cm^2·MJ)
Total Energy in Core = 6.66 MJ
Total Neutrons = 2.017×10^{13} n/cm^2
Fluence per MJ > 3 Mev = 3.926×10^{11} n/(cm^2·MJ)

Table A.5

Foil Reactions for WSMR FBR Leakage Spectrum

Reaction	Cover (atoms/barn)		Activity (dis/sec. nucleus)
AU197G	2.587-3 cadmium		6.463-17
AU197G	- -		8.579-17
MN55G	2.587-3 cadmium		2.311-17
NI58P	2.587-3 cadmium		5.906-20
S32P	- -		2.076-19
MG24P	2.587-3 cadmium		7.695-20
FE56P	2.587-3 cadmium		3.921-19
*FE54P	2.587-3 cadmium		1.293-20
NA23G	4.705-3 cadmium		1.057-19
NA23G	- -		4.032-19
*NI115G	2.587-3 cadmium		1.415-15
*NI115N	2.587-3 cadmium		4.543-17
*NI58P	4.705-3 cadmium	0.101 boron	5.620-20
*NI58P	- -		5.981-20
			Activity (fissions/nucleus)
U235F	4.705-3 cadmium	0.101 boron	8.693-12
U238F	4.705-3 cadmium	0.101 boron	1.343-12
PU239F	4.705-3 cadmium	0.101 boron	1.184-11
NP237F	4.705-3 cadmium	0.101 boron	6.467-12

*Reactions not used in the unfolding procedure.

Table A.6

WSMR FBR LEAKAGE SPECTRUM

(normalized to Φ(E>10 kev) = 1.00)

E(Mev)	Differential	Integral	E(Mev)	Differential	Integral
1.0-9	7.816+3	1.032	7.2-4	3.982	1.008
2.0-9	1.501+4	"	1.0-3	3.169	1.007
5.0-9	3.322+4	"	2.0-3	1.298	1.005
1.0-8	5.423+4	"	3.0-3	8.699-1	1.004
2.0-8	7.223+4	"	5.0-3	5.934-1	1.002
5.0-8	5.348+4	1.030	7.2-3	4.709-1	1.001
1.0-7	2.679+4	1.028	1.0-2	4.070-1	1.000
2.0-7	1.336+4	1.026	2.0-2	3.609-1	9.962-1
3.0-7	7.843+3	1.025	3.0-2	3.867-1	9.925-1
5.0.7	4.075+3	1.023	5.0-2	5.269-1	9.835-1
7.2-7	2.466+3	"	7.2-2	7.315-1	9.700-1
1.0-6	1.728+3	1.022	1.0-1	9.778-1	9.462-1
2.0-6	7.778+2	1.021	2.0-1	1.073	8.424-1
3.0-6	5.330+2	1.020	3.0-1	9.046-1	7.423-1
5.0-6	3.564+2	1.019	5.0-1	5.624-1	5.960-1
7.2-6	2.386+2	"	7.2-1	3.060-1	5.026-1
1.0-5	1.736+2	1.018	1.0-0	2.177-1	4.283-1
2.0-5	9.196+1	1.017	1.5-0	1.642-1	3.316-1
3.0-5	6.430+1	1.016	2.0-0	1.321-1	2.564-1
5.0-5	4.407+1	1.015	3.0-0	8.118-2	1.503-1
7.2-5	3.137+1	1.014	4.0-0	4.988-2	8.503-2
1.0-4	2.389+1	1.013	5.0-0	3.058-2	4.497-2
2.0-4	1.314+1	1.012	6.0-0	2.051-2	1.878-2
3.0-4	9.907	1.011	8.0-0	2.004-3	2.904-3
5.0-4	5.728	1.009	10.0-0	4.830-4	6.850-4

File #WHSL25 Date: 8-9-85 Reactor Shot #

Standard Deviation for 13 foils = 2.50%
Spectral Index = 6.65
Total Fluence per MJ = $n/(cm^2 \cdot MJ)$
Total Energy in Core = MJ
Total Neutrons = 7.828×10^{12} n/cm^2
Fluence per MJ > 3 Mev = $n/(cm^2 \cdot MJ)$

Table A.7

Foil Activities for the ACRR Bare Cavity Spectrum

Reaction	Cover (atoms/barn)	Activity (dis/sec. nucleus)
AU297G	- -	3.113-14
AU197G	2.587-3 cadmium	2.799-14
MN55G	2.587-3 cadmium	5 435-15
FE54P	2.587-3 cadmium	9.764-20
FE56P	2.587-3 cadmium	2.888-18
*AL27P	2.587-3 cadmium	1.846-16
AL27A	2.587-3 cadmium	3.832-19
NI58P	2.587-3 cadmium	5.910-19
MG24P	2.587-3 cadmium	7.768-19
ZR902	2.587-3 cadmium	1.682-20
S32P	- -	1.927-18
NA23G	- -	1.058-16
CO59G	2.587-3 cadmium	1.397-18
*FE58G	2.587-3 cadmium	1.582-18
*IN115G	2.587-3 cadmium	6.642-13
*IN115N	2.587-3 cadmium	4.985-16
*IN115G	- -	1.188-12
*IN115N	- -	4.935-16
*CU63G	- -	4.643-18
*NI58P	4.705-3 cadmium 0.101 boron	4.964-19
		Activity (fissions/nucleus)
U235F	4.705-3 cadmium 0.101 boron	1.850-10
U238F	4.705-3 cadmium 0.101 boron	1.741-11
PU239F	4.705-3 cadmium 0.101 boron	2.002-10
NP237F	4.705-3 cadmium 0.101 boron	9.633-11

*Reaction activity not used in the unfolding procedure.

Table A.8

ACRR BARE CAVITY

(normalized to ϕ(E>10 kev) = 1.00)

E(Mev)	Differential	Integral	E(Mev)	Differential	Integral
1.0-9	1.225+5	1.579	7.2-4	5.427+1	1.134
2.0-9	2.352+5	"	1.0-3	3.999+1	1.120
5.0-9	5.206+5	1.578	2.0-3	2.314+1	1.089
1.0-8	8.499+5	1.575	3.0-3	1.624+1	1.070
2.0-8	1.133+6	1.565	5.0-3	1.088+1	1.043
5.0-8	8.396+5	1.533	7.2-3	8.454	1.021
1.0-7	4.194+5	1.503	1.0-2	6.590	1.000
2.0-7	2.097+5	1.473	2.0-2	3.964	9.490-1
3.0-7	1.408+5	1.456	3.0-2	3.022	9.139-1
5.0.7	8.893+4	1.433	5.0-2	2.129	8.625-1
7.2-7	6.339+4	1.416	7.2-2	1.653	8.208-1
1.0-6	4.661+4	1.401	1.0-1	1.340	7.785-1
2.0-6	2.380+4	1.367	2.0-1	7.776-1	6.766-1
3.0-6	1.543+4	1.347	3.0-1	5.698-1	6.090-1
5.0-6	9.239+3	1.323	5.0-1	3.845-1	5.143-1
7.2-6	6.418+3	1.306	7.2-1	2.999-1	4.386-1
1.0-5	4.540+3	1.290	1.0-0	2.348-1	3.625-1
2.0-5	2.058+3	1.260	1.5-0	1.697-1	2.595-1
3.0-5	1.227+3	1.243	2.0-0	1.306-1	1.831-1
5.0-5	6.854+2	1.224	3.0-0	7.525-2	8.024-2
7.2-5	4.682+2	1.212	4.0-0	2.804-2	3.379-2
1.0-4	3.136+2	1.201	5.0-0	8.955-3	1.339-2
2.0-4	1.571+2	1.178	6.0-0	3.779-3	7.235-3
3.0-4	1.038+2	1.165	8.0-0	1.528-3	2.221-3
5.0-4	7.142+1	1.148	10.0-0	3.614-4	5.417-4

File #ACRRCF28 Date: 10-1-84 Reactor Shot #2172

Standard Deviation for 15 foils = 1.95%
Spectral Index = 12.14
Total Fluence per MJ = 2.022×10^{13} n/(cm^2·MJ)
Total Energy in Core = 10.0 MJ
Total Neutrons = 2.022×10^{14} n/cm^2
Fluence per MJ > 3 Mev = 1.027×10^{12} n/(cm^2·MJ)

Table A.9

Foil Activities for NEW PB-B Liner in ACRR Cavity

Reaction	Cover (atoms/barn)	Activity (dis/sec. nucleus)	
AU197G	2.587.3 cadmium	6.431-15	
AU197G	- -	7.299-15	
MN55G	2.587-3 cadmium	8.732-15	
NI58P	2.587-3 cadmium	1.879-18	
*AL27P	2.587-3 cadmium	5.719-16	
AL27A	2.587-3 cadmium	1.028-18	
MG24P	2.587-3 cadmium	2.127-18	
FE54P	2.587-3 cadmium	2.924-19	
FE56P	2.587-3 cadmium	9.563-18	
NA23G	4.705-3 cadmium	2.705-17	low thermal
NA23G	- -	2.729-17	low thermal
S32P	- -	6.208-18	
ZR902	2.587-3 cadmium	3.459-20	
*IN115G	2.587-3 cadmium	1.013-13	
*IN115N	2.587-3 cadmium	1.859-15	low thermal
*IN115G	- -	1.014-13	
*IN115N	- -	1.838-15	
*FE58G	2.587-3 cadmium	2.669-18	
*NI58P	4.705-3 cadmium 0.101 boron	1.631-18	
		Activity (fissions/nucleus)	
U235F	4.705-3 cadmium 0.101 boron	7.398-10	
U238F	4.705-3 cadmium 0.101 boron	6.165-11	
PU239F	4.705-3 cadmium 0.101 boron	7.876-10	
*NP237F	4.705-3 cadmium 0.101 boron	3.288-10	

*Reaction not used in the unfolding analysis.

Table A.10

ACRR PB-B LINED CAVITY SPECTRUM

(normalized to ϕ(E>10 kev) = 1.00)

E(Mev)	Differential	Integral	E(Mev)	Differential	Integral
1.0-9	1.466	1.166	7.2-4	3.930+1	1.106
2.0-9	2.933	"	1.0-3	3.031+1	1.096
5.0-9	7.332	"	2.0-3	1.752+1	1.073
1.0-8	1.466+1	"	3.0-3	1.229+1	1.058
2.0-8	2.933+1	"	5.0-3	9.093	1.037
5.0-8	7.331+1	"	7.2-3	7.251	1.019
1.0-7	1.355+2	"	1.0-2	5.999	1.000
2.0-7	2.280+2	"	2.0-2	4.059	9.508-1
3.0-7	2.803+2	"	3.0-2	3.172	9.140-1
5.0.7	3.450+2	"	5.0-2	2.349	8.586-1
7.2-7	3.882+2	"	7.2-2	1.964	8.108-1
1.0-6	4.182+2	"	1.0-1	1.629	7.601-1
2.0-6	4.468+2	"	2.0-1	9.782-1	6.342-1
3.0-6	4.404+2	1.165	3.0-1	6.611-1	5.521-1
5.0-6	4.010+2	1.164	5.0-1	4.012-1	4.471-1
7.2-6	3.797+2	1.163	7.2-1	2.805-1	3.719-1
1.0-5	3.421+2	1.162	1.0-0	2.077-1	3.028-1
2.0-5	2.599+2	1.159	1.5-0	1.617-1	2.090-1
3.0-5	2.177+2	1.157	2.0-0	1.157-1	1.373-1
5.0-5	1.757+2	1.153	3.0-0	4.670-2	5.939-2
7.2-5	1.417+2	1.150	4.0-0	1.849-2	2.821-2
1.0-4	1.181+2	1.146	5.0-0	9.796-3	1.426-2
2.0-4	8.803+1	1.136	6.0-0	5.782-3	6.448-3
3.0-4	7.332+1	1.128	8.0-0	8.432-4	1.227-3
5.0-4	5.017+1	1.116	10.0-0	2.014-4	2.953-4

File #LBACRR12 Date: 11-4-85 Reactor Shot #2607

Standard Deviation for 16 foils = 3.5%
Spectral Index = 16.84
Total Fluence per MJ = 1.233×10^{13} n/(cm^2·MJ)
Total Energy in Core = 50 MJ
Total Neutrons = 6.166×10^{14} n/cm^2
Fluence per MJ > 3 Mev = 6.280×10^{11} n/(cm^2·MJ)

Radiation Environment for the White Sands Missile Range Fast Burst Reactor in Outdoor Operations

T. M. Flanders
J. L. Meason
M. H. Sparks

Nuclear Effects Laboratory, White Sands Missile Range, N.M.

ABSTRACT

The White Sands Missile Range Fast Burst Reactor (FBR) can be operated outdoors to provide a reasonable simulation of nuclear weapon radiation environments which require air-ground interface interaction components and "sky shine" components. In this operational mode, the FBR can produce measurable radiation environments up to 1 kilometer away. Transport calculations have been performed in order to characterize the FBR produced radiation environment. To complement these calculations, a number of measurements have been carried out with the aim of measuring both spectral characteristics and total dose levels of the radiation environment. This paper will address, in some detail, the transport calculation results and make comparisons to an experimental measurement of the neutron spectrum obtained at a distance of 170 meters from the FBR.

Transport calculation results indicate good agreement with experimental results when the DNA library of cross-sections is used but only limited agreement when the EPR-based library of cross-sections was used. One calculation was performed in which the resulting radiation environment passed through approximately 12 inches of a wood platform. The effects of wood on the resulting neutron spectrum are very apparent.

Finally, neutron environments at 170 meters from the FBR are compared to experimental measurements performed at the Aberdeen Pulse Reactor also at 170 meters from the reactor. Reasonable agreement between the two sets of data are observed, especially when one considers the difference in the physical environments between White Sands and Aberdeen.

INTRODUCTION

Straker and Mynatt (1) considered the effects of the air- ground interface on the neutron environment produced by a fission source. For this work they used the two dimensional transport code DOT. The calculations were compared with dose data from the BREN

experiment (2). It was noted at this time, that the effect of the interface depends strongly on the amount of water present in the ground, with the largest differences appearing in the thermal flux distribution.

In 1967, a seminar-workshop on "The Discrete Ordinates Sn Method for Radiation Transport Calculations" was held at Oak Ridge, Tennessee. Straker et. al. (3) studied the effect of cross section treatment on calculations. It was suggested that few-group calculations should be sensitive to the type of flux weighting used in the collapsing run with ANISN. The weighting spectra studied were an infinite air medium spectrum and a zone-dependent spectrum. The second weighting spectrum accounts for a relatively large spectral change with the spatial parameter. It was found that the calculated thermal flux distribution, using the infinite medium weighted and zone weighted cross sections, agreed within 5% when 22 energy groups were used. Straker's summary concluded that the importance of zone-weighting the cross sections appeared to be small or nonexistent if a proper group structure is used. The proper group structure, in this case, means that consideration is given to the medium which perturbs the basic fission spectrum. The agreement of two dimensional calculations varied by factors of two or three at some ranges, but the causes for disagreement could not be accounted for.

Sandmeier et.al. (4) used the Los Alamos Scientific Laboratory (LASL) discrete ordinates program TWOTRAN-FC (5) to calculate the neutron transport from a 14.1 MeV neutron source in an air over ground geometry. This program provided a substantial improvement over the regular LASL TWOTRAN (6) program in that it was capable of generating a volume distributed first collision source. This method was thought to essentially eliminate ray effects (7). For a source height 100 meters above ground they found that the ground acts as an absorber over the whole range.

Straker (8) had earlier noted that for short ranges the ground acts as a reflector, but at large ranges the ground behaves as an absorber. The difference between the Straker and Sandmeier et. al. work may be due to the source height. For both neutron and photon dose there was essentially no difference between the detector height at 100 meters above the source and infinite air results. For Silicon dose, which emphasizes high energy neutrons and gammas, the effect of the ground was minimal. They verified the small difference, from a calculational standpoint, between infinite air and air over ground as found by Straker.

We have recalculated the environment produced by the FBR when operated at it's new outdoor site. The calculations have been performed to provide spectral information as well as neutron dose data. The spectra produced by some of the very early calculations were also used as the initial guess for unfolding experimental data at 170 meters from the reactor. The resulting unfolded spectrum shows essentially an identical shape to the later

calculations which were made using a different cross section data set.

CALCULATIONAL PROCEDURE

The infinite air calculations were done using the ANISN one dimensional transport code (9). The ANISN calculations used 16 angles. The simulation of the air over ground geometry was effected using the DOT-III code(10). The geometry was a cylindrical coordinate system (R,Z), with the axis of symmetry through the reactor position. The two-dimensional DOT calculations used 48 angles. The spatial grid was of variable mesh size with cells smallest near the source, increasing in size as the distance from the source increased. The Z-axis included a lower zone of ground approximately 30 centimeters deep. A vacuum boundary was used on the bottom. The height of the source position was 5.63 meters above the ground plane, supported by a wooden platform 12 inches thick. The detector positions are represented by the spatial cells centered at 10 cm, 2 meters and 10 meters above the ground plane at radial positions of 1, 10, 170, 600, and 1000 meters.

Two cross section libraries were used during the course of the calculations. The early ANISN and DOT-III runs used the EPR library obtained from Oak Ridge (11). The 100n-21g library was collapsed to 34 neutron groups using ANISN. As the calculations progressed, it was suspected that this cross section library was producing questionable results. A comparison for identical geometrical configurations using the DNA Few Group Coupled Neutron-Gamma Cross Section Library (12) and the EPR-based library was made. The sources for these comparison calculations were a 14 MeV source and the standard FBR source. The DNA library appeared to give results more consistent with other calculations and with experiments. The older 34 group EPR based library produced much higher group fluences in the energy region from about 10 keV to 800 keV.

The cross section library used for the most recent calculation was the DNA Few Group Coupled Neutron-Gamma Cross Section Library. This structure has 37 neutron groups and 21 gamma groups. The group structure is presented in Table 1. The air density for all calculations was taken to be 4.96 E-5 atoms/b-cm. The ground was assumed to contain less than 5% water.

Harvey (13,14) has done extensive calculations and measurements of the neutron leakage spectrum of the the FBR. Therefore, it was not necessary to include the explicit details of the FBR in the modeling process. The source, when treated in this manner, takes the form of a distributed source located within some volume element. The leakage spectrum utilized in this work is for the

FBR located in its' old outdoor experimental site, which is situated on a concrete pad (15). The source spectrum was regrouped to fit the DNA cross section energy grid (16,17). In order to minimize ray effects, the first collision source code GRTUNCL (18) was used. Ray effects occur in two dimensional geometries when point or isolated sources are present in a weakly scattering medium. GRTUNCL determines the uncollided fluence and first collision scattering source moment distribution throughout the calculational geometry.

EXPERIMENTAL

The neutron spectral shape has also been determined by experimental methods at 7 and 170 meters. A total of 36 individual activation detectors were placed on styrofoam boards and mounted 5 feet above ground 170 meters from the reactor position. The reactor was operated at 4 kilowatts for 5 hours. In a separate experiment, 17 foils were placed 7 meters from the reactor position. The reactor power output was 29 kW-hrs.

The activation foil data was unfolded using SAND-II. The trial spectra for the unfolding runs were based on early transport runs done at the University of Arkansas. These runs utilized a 34 group cross section structure which was derived from the EPR cross section library. The transport calculations utilizing the 34 group cross sections and the experimental determinations of the spectral shapes predate the 37 group transport calculations by about 2 years.

RESULTS

The results of the calculation are presented in Tables 2 and 3. Table 2 shows the differential fluences for two positions 2 meters above ground level for groups 9 through 37. These groups correspond to energies from 10 MeV to thermal. For the leakage spectrum of the FBR, source neutrons having energies outside this range account for approximately 0.1% of the total fluence.

The detectors at radial ranges of 1 and 10 meters show similar spectral shape with the exception of the detector at 10 cm above ground level and 1 meter ground range from the core surface. The increased moderation of this spectrum is due to the fact that this detector must look at the source position through several inches of wood. Figure 1 clearly shows the effect of the wooden support ramp on the spectrum at the detector position 10 cm above the ground. Further investigation of the neutron field at very close ground ranges may be necessary due to the complexity of the environment in the immediate vicinity of the FBR.

The fluence distributions at the more distant detectors show the expected moderating effects of air. As the penetration depth increases, the characteristic peaks due to oxygen and nitrogen at about 2.3 MeV and 4.8 MeV become more prominent. Table 3 summarizes the data obtained from the DOT-III calculation utilizing the DNA Few Group Cross Sections.

The data for the detector position at 170 meters, 2 meters above ground, may be compared to the experimental data of Harris (19). In his work, Harris determined the neutron spectrum 170 meters away from the FBR in its' outdoor experimental configuration. The spectrum was determined by unfolding activation foil data. The SAND-II code (20) was selected as the unfolding routine and the trial spectrum was calculated at the University of Arkansas (21). It is important to note that the trial spectrum used for unfolding was somewhat different from the current calculations and a different cross section data base (11,12) was used in calculating the trial spectra.

The spectral index (fluence > 10 keV divided by fluence > 3 MeV) obtained by Harris for the 170 meter position was 28.6. The present DOT-III calculation yields a spectral index of 29.5. This is excellent agreement between the two techniques. Figure 2 shows the two spectral shapes to be nearly identical. The comparison of integral quantities is dependent on a normalization factor which relates the number of leakage source neutrons to the power level of the reactor. Harvey (23) has reported the neutron output of the FBR at 12 and 20 inches from the core surface. However, these measurements were made with the reactor inside the exposure cell where there may be some wall return effect. Harvey pointed out that the transport calculations seemed to overestimate the effect of the wall return neutrons. In particular, he pointed out that as the distance between the point of interest and the core surface decreased, the spectral parameters (based on transport calculations) became harder. The experimental data showed that, within experimental error, the spectral index remained essentially the same. It is noted that the same experimental data at 12 inches and at 20 inches form the core surface would lead to different normalization values. In particular, the more distant measurement leads to a higher value, as if wall return neutrons were also contributing to the "source" neutron population.

Thus, one must be cautious about interpreting the agreement between integral quantities of experimentally and theoretically calculated data. A normalization of about 1.15 E17 source neutrons per kilo-watt hour has been used for the experimental configuration. Keeping in mind the above considerations, the present transport calculation gives the total fluence greater than 10 keV as 5.18 E-10 neutrons/cm^2-source. The experimentally determined value is 4.65 E-10 neutrons/cm^2-source. This represents good agreement considering the uncertainties involved in normalizing the two methods.

Kazi et. al. (24,25) have reported data for measurements made at 170 meters at The Army Pulse Reactor Facility. Figure 3 shows the experimental measurements at each facility to have similar spectral shapes. This represents remarkable qualitative agreement when one takes into account the distinctly different experimental techniques involved. The APRD data was based on a NE-213 unfolded spectrum above about 800 keV and on Boron-Triflouride data for the epithermal range. The total number of neutrons in the spectrum was 8.70 E-10 Neutrons/Source Neutron. The fluence greater than 3 MeV was 1.87 E-11 Neutrons/Source Neutron. Folding the Rindi dose function with the reported spectrum, the neutron dose is 7.97 E-19 Rad/Source Neutron. This represents very good agreement with the WSMR determined value of about 8.17 E-19 Rad/Source Neutron.

REFERENCES

1) Straker, E. A. and F. R. Mynatt, Calculations of the Effect of the Air-Ground Interface on the Transport of Fission Neutrons Through the Atmosphere, ORNL-TM-1819 (1967).

2) Haywood, F. F., J. A. Auxier, and E. T. Loy, An Experimental Investigation of the Spatial Distribution of Dose in an Air Over Ground Geometry, CEX 62.14 (1964).

3) Straker, E. A., N. M. Greene, and R. J. Rodgers, Calculations of Neutron Transport in the Atmosphere and the Effects of Input Cross-Sections, ORNL-RSIC-19.

4) Sandmeier, H.A., K. D. Lathrop, F. W. Brinkley, G. E. Hanson, and J. E. Cambell, Two Dimensional Coupled Neutron-Gamma Sn Transport from a 14.1 MeV neutron Source in Air Over Ground Geometry using the LASL TWOTRAN-FC Program, Review of Calculations of of Radiation Transport In Air, ORNL-RSIC-33 (1972).

5) TWOTRAN-FC is a modification of the LASL TWOTRAN code utilizing a first collision source routine.

6) Lathrop, K. D., and F. W. Brinkley, Theory and Use of the General Geometry TWOTRAN Program, USAEC Report LA-4432, Los Alamos Scientific Laboratory (1973).

7) Lathrop, K. D., Remedies for Ray Effects, Nucl. Sci. Eng., 45, 255, (1971).

8) Straker, E. A., Time-Dependent Neutron and Secondary Gamma Ray Transport in Infinite Air and in Air Over Ground Geometries, ORNL-TM-2781 (1970).

9) Engle, W. W. Jr., A Users Manual for ANISN, A One-Dimensional Discrete Ordinate Transport Code with Anisotropic Scattering, USAEC Report K-1693, Union Carbide Corporation, (1967).

10) Rhoades, W. A., and F. R. Mynatt, The DOT-III Two Dimensional Discrete Ordinates Transport Code, Report ORNL-TM 4280, Oak Ridge National Laboratory (1973).

11) Ford, W. E., R. T. Santoro, R. W. Roussin, and D. M. Plaster, Modification Number One to the Coupled 100n-21g Cross Sections for EPR Calculations, ORNL-TM-5249 (1976).

12) Bartine, D. E., J. R. Knight, J. V. Pace III, and R. W. Roussin, Production and Testing of the DNA Few Group Coupled Neutron-Gamma Cross-Section Library, ORNL/TM-4840 (1977).

13) Wright, H. L., J. L. Meason, M. L. Wolf, and J. T. Harvey, IEEE NS-23, No. 6, 2007 (1976).

14) Harvey, J. T., J. L. Meason, and H. L. Wright, Unfolding of Neutron Spectra from Godiva Type Critical Assemblies, ORNL-RSIC 40, 177 (1976).

15) Harvey, J. T., Unpublished work, University of Arkansas.

16) Flanders, T. M., 30 Day Report for Contract No. DAAD 07-80-K 0263, 25 December 1980.

17) Flanders, T. M., 30 Day Report for Contract No. DAAD 07-80-K 0263, 25 February, 1980.

18) Rhoades, W. A., and F. R. Mynatt, Input Instructions for the GRTUNCL Routine, ORNL-TM-4280 (1973).

19) Harris, D. C., Free Field Radiation Environment From Fission Sources, Ph.D. Thesis, University of Arkansas (1980).

20) McElroy, W. N., S. Bert, T. Crockett, and R. G. Hawkins, SAND-II, A Computer Automated Iterative Method for Neutron Flux Determination by Foil Activation, AFWL-TR-41, Vol I-IV, (1967).

21) Flanders, T. M., Neutron Spectra Produced by a Fast Pulse Assembly in Free Field and Perturbed Environments, Ph.D. Thesis, University of Arkansas (1980).

22) Rindi, A., An Analytical Expression for the Neutron Flux-to-Absorbed Dose Conversion Factor, Health Physics, 33, 264, (1977).

23) Harvey, J. T., Neutron Spectra Associated with a Fast Pulse Assembly, Ph. D. Thesis, University of Arkansas (1977).

24) Kazi, A. H., C. R. Heimbach, R. C. Harrison, L. Schanzler, and F. W. Bucholtz, Measurements of the Free Field Radiation Environment at the APRD Reactor, TECOM Project 2-DDO-430-APR 027, Test Agency Report No. APG-MT-5297.

25) Kazi, A. H., C. R. Heimbach, R. C. Harrison, Neutron and Gamma Radiation Measurements and Calculations Up to 1.1 Kilometers From a Fission Source, APG-MT-5490.

Table 1

DNA ENERGY GROUP STRUCTURE

Group	Upper Energy (ev)		Group	Upper Energy (ev)	
1	1.96	E+7	21	1.11	E+6
2	1.69	7	22	5.50	5
3	1.49	7	23	1.58	5
4	1.42	7	24	1.11	5
5	1.38	7	25	5.25	4
6	1.28	7	26	2.48	4
7	1.22	7	27	2.19	4
8	1.11	7	28	1.03	4
9	1.00	7	29	3.35	3
10	9.05	6	30	1.23	3
11	8.19	6	31	5.83	2
12	7.41	6	32	1.01	2
13	6.38	6	33	2.90	1
14	4.97	6	34	1.07	1
15	4.72	6	35	3.06	0
16	4.07	6	36	1.13	0
17	3.01	6	37	4.14	-1
18	2.39	6	38	1.00	-5
19	2.31	6			
20	1.83	6			

TABLE 2
DOT-III Calculated Spectra - FBR Source
(Neutrons/cm^2-MeV-Source)

Group	Ground Range 170 M H = 2.0 M	Ground Range 1000 M H = 2.0 M
9	1.32 E-13	5.15 E-17
10	2.58 -13	1.28 -16
11	4.29 -13	1.60 -16
12	9.31 -13	5.45 -16
13	2.27 -12	1.34 -15
14	4.47 -12	4.65 -15
15	4.16 -12	1.83 -15
16	8.10 -12	1.93 -15
17	2.18 -11	8.66 -15
18	3.23 -11	1.89 -14
19	3.39 -11	1.36 -14
20	6.47 -11	2.13 -14
21	1.73 -10	6.81 -14
22	3.44 -10	1.18 -13
23	7.57 -10	2.53 -13
24	9.98 -10	3.60 -13
25	1.71 - 9	6.42 -13
26	2.61 - 9	9.91 -13
27	3.39 - 9	1.37 -12
28	7.53 - 9	3.26 -12
29	1.99 - 8	9.03 -12
30	4.62 - 8	2.21 -11
31	1.30 - 7	6.62 -11
32	5.83 - 7	3.14 -10
33	1.72 - 6	9.70 -10
34	4.68 - 6	2.71 - 9
35	1.34 - 6	8.07 - 9
36	3.18 - 5	1.95 - 8
37	2.28 - 4	1.33 - 7

TABLE 3
DOT-III Calculation FBR Source

	1 m	10 m	170 m	1000 m
Fluence > 10 keV				
h = 0.10 m	1.33 E- 7	1.13 E- 7	5.47 E-10	1.89 E-13
2.0 m	8.19 - 7	1.25 - 7	5.18 -10	1.91 -13
10.0 m	4.19 - 7	9.66 - 8	5.46 -10	1.97 -13
Fluence > 1 MeV				
h = 0.10 m	4.15 - 8	4.64 - 8	1.26 -10	4.27 -14
2.0 m	3.85 - 7	5.12 - 8	1.15 -10	4.34 -14
10.0 m	1.98 - 7	4.14 - 8	1.21 -10	4.40 -14
Fluence > 3 MeV				
h = 0.10 m	8.70 - 9	9.75 - 9	1.91 -11	7.38 -15
2.0 m	8.91 - 8	1.07 - 8	1.75 -11	7.25 -15
10.0 m	4.61 - 8	9.05 - 9	1.82 -11	7.38 -15
KERMA				
h = 0.10 m	2.35 -16	2.31 -16	8.31 -19	2.90 -22
2.0 m	1.82 -15	2.55 -16	8.01 -19	2.92 -22
10.0 m	9.35 -16	2.03 -16	8.03 -19	2.97 -22
1 MeV Equivalent Fluence (Equivalent 1 MeV Neutrons/cm^2-Source)				
h = 0.10 m	1.04 E- 7	1.01 E- 7	3.87 E-10	1.39 E-13
2.0 m	7.88 - 7	1.11 - 7	3.58 -10	1.40 -13
10.0 m	4.05 - 7	8.84 - 8	3.73 -10	1.42 -13

TABLE 4

Comparison of Calculations and
Experimental Data at 170 Meters

	ANISN	DOT-III/UA	DOT-III/DNA	SAND
Fluence > 10 keV	1.02 E- 9	1.01 E- 9	5.18 E-10	4.65 E-10
> 1 MeV	1.58 -10	1.29 -10	1.15 -10	1.08 -10
> 3 MeV	2.69 -11	2.35 -11	1.75 -11	1.62 -10
Spectral Index	37.8	43	29.6	28.6
KERMA			8.01 -19	
Henderson Dose	1.15 -18	1.03 -18	9.74 -19	
Rindi Dose (22)	1.60 -18	1.51 -18	9.86 -19	8.17 -19

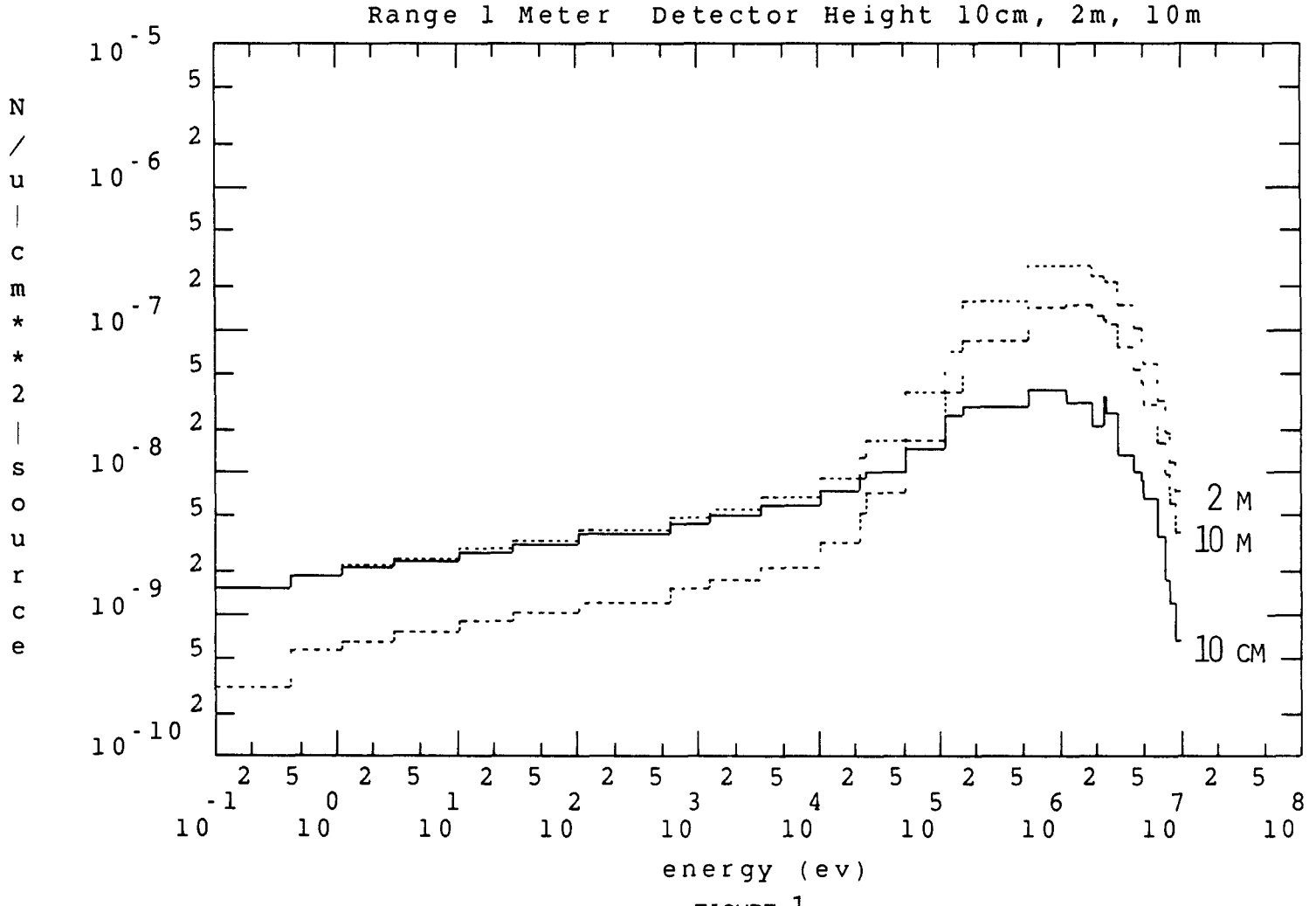
Range 1 Meter Detector Height 10cm, 2m, 10m
N/u—cm**2—source
10^-5
10^-6
10^-7
10^-8
10^-9
10^-10
5
2
2 M
10 M
10 CM
10^-1
10^0
10^1
10^2
10^3
10^4
10^5
10^6
10^7
10^8
energy (ev)

FIGURE 1

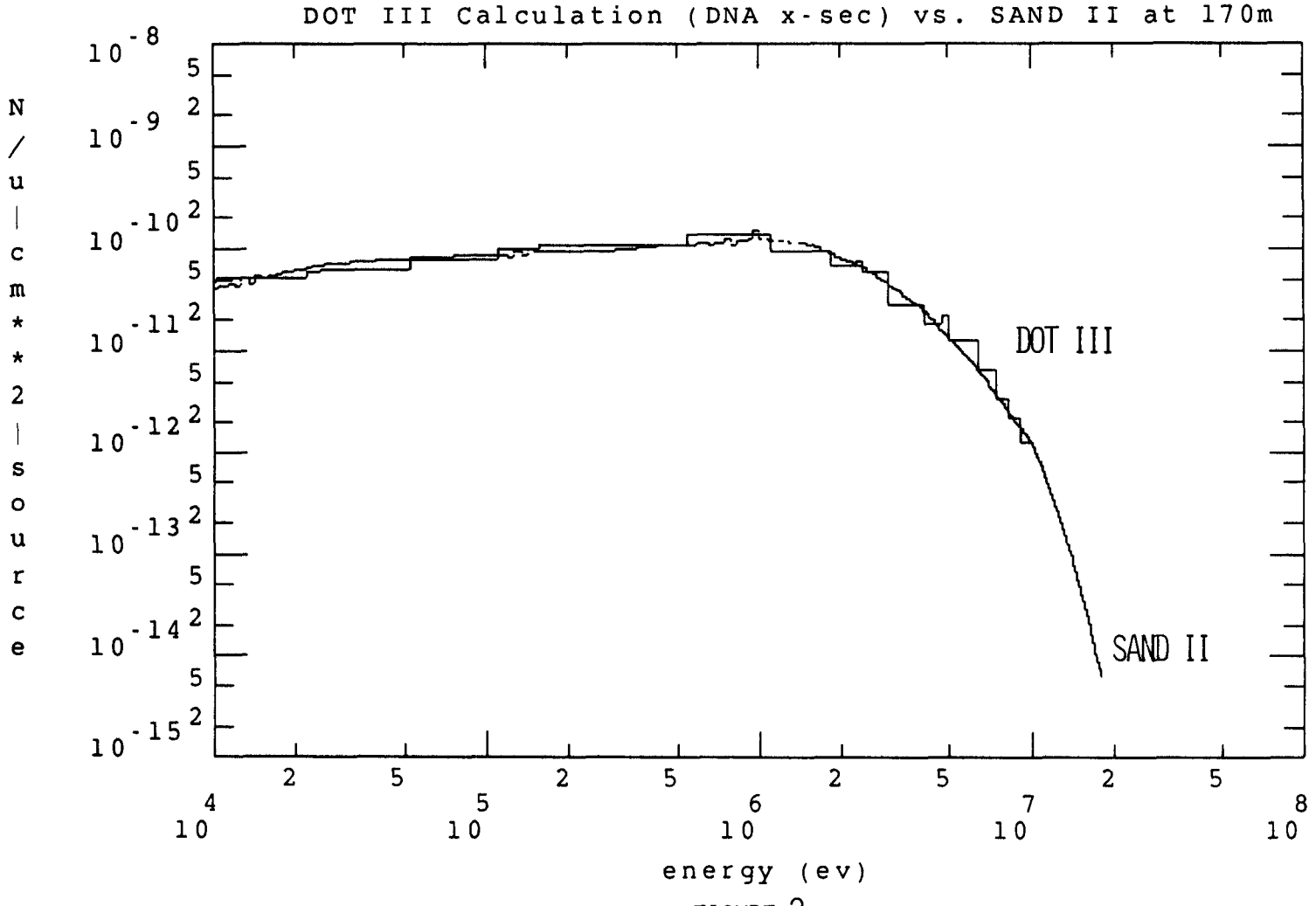
DOT III Calculation (DNA x-sec) vs. SAND II at 170m
N/u/cm**2/source
10-8
10-9
10-10
10-11
10-12
10-13
10-14
10-15
DOT III
SAND II
2 5 2 5 2 5 2 5
10^4 10^5 10^6 10^7 10^8
energy (ev)

FIGURE 2

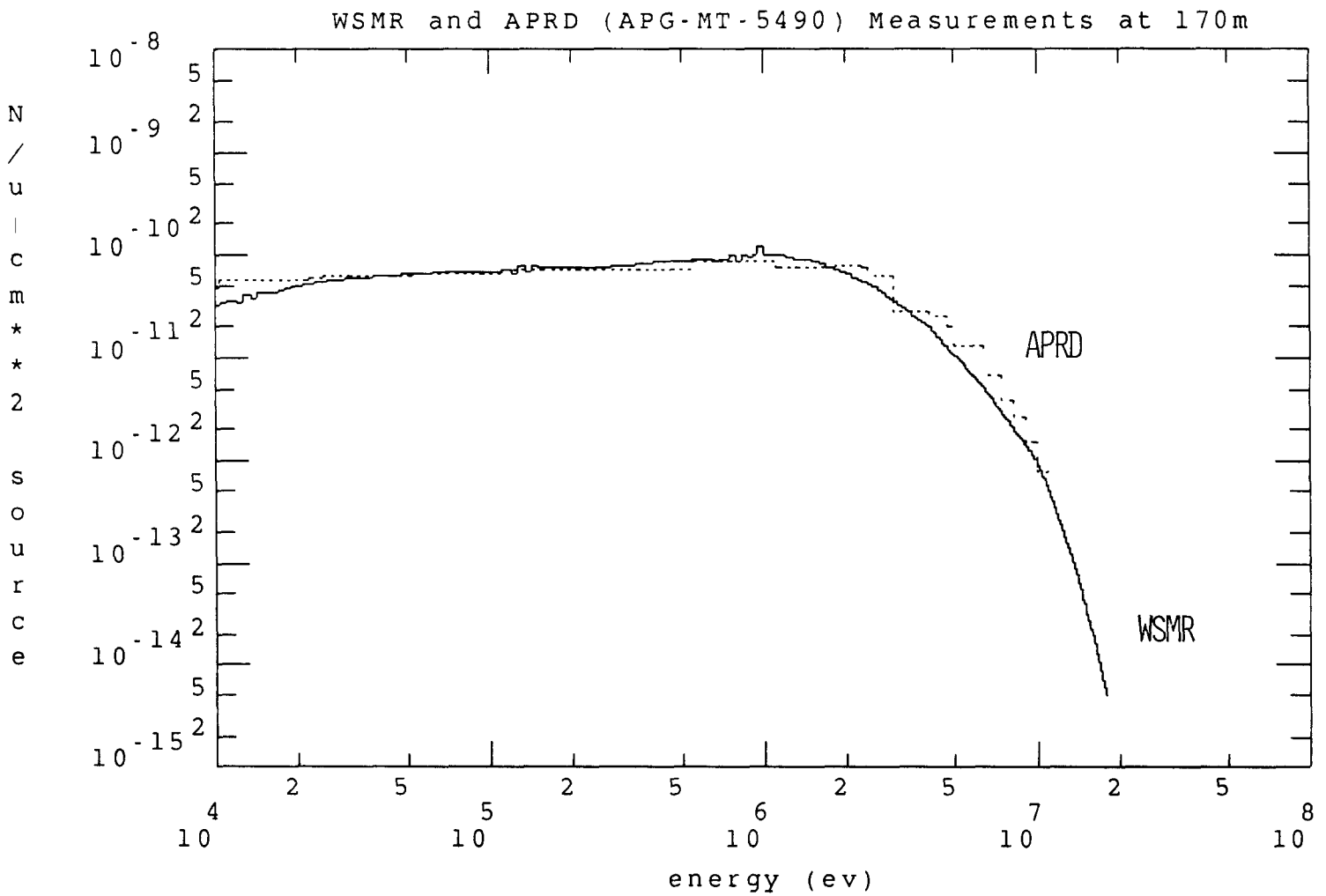
WSMR and APRD (APG-MT-5490) Measurements at 170m
N / u - cm**2 source
energy (ev)
APRD
WSMR

FIGURE 3

Editor's Note: This paper was unavailable for publication. A summary is included.

PIN DIODES FOR MEASUREMENT OF THE GAMMA DOSE RATE PRODUCED BY THE FAST BURST REACTOR OPERATING IN THE GAMMA ENHANCEMENT MODE

J. L. Meason and E. H. Hayth
Nuclear Effects Laboratory
White Sands Missile Range
New Mexico

BACKGROUND: The Fast Burst Reactor (FBR) is operated in the gamma enhancement mode to produce long pulses of gamma radiation for special test requirements. In this particular mode of operation, varying thickness of cadmium and dysprosium loaded polyethylene are used to enhance the gamma radiation environment of the FBR. In principle, the polyethylene thermalizes the fast neutron component of the FBR, the thermal and epithermal neutrons are captured by the cadmium and dysprosium which, in turn, results in a strong capture gamma ray environment.

The enhanced gamma environment is used for selected nuclear survivability tests. In addition to the total ionizing dose (measured by thermoluminescent detectors), the gamma dose rate and rate profile is of prime importance. In fact, the peak gamma dose rate is most often the desired quantity. PIN diodes have proven a very useful method for measuring the instantaneous dose rates from the FBR gamma enhanced mode of operation. This presentation will describe results nd characteristics of these diodes for making such measurements along with calibration methods and long term stability of the diode calibration.

FBR CONFIGURATION FOR GAMMA ENHANCEMENT: Only two of many gamma enhancement shield configurations will be described in this presentation. These configurations represent those of most common usage. Figures 1 and 2 provide the schematic diagram of those configurations. Figure 1 is representative of a test environment produced over the top of the FBR while Figure 2 is representative of the test environment produced to the side of the FBR. Dose rates range upward to 1.5E8 rads(Si)/sec for both configurations.

PIN DIODES AND DATA ACQUISITION SET-UP: Diodes that have been found suitable for measuring gamma dose rates are Quantrad 125 and 250 and Texas Instruments 8015A and 8121A. These diodes have demonstrated linearity between 5E5 and 1E8 rads(Si)/sec. The data acquisition set-up and software used in the data acquisition has been reported elsewhere (1). Typical data output from the PIN diode data acquisition system is shown in Figure 3.

TOTAL DOSE CORRELATION WITH TLD DATA: Diodes are calibrated relative to TLD's. TLD's are calibrated in a cobalt-60 environment using National Bureal of Standards calibrated ion chambers. PIN diodes are calibrated in the FBR enhanced gamma environment. Extensive studies have been performed between PIN diode data and TLD data (2). A typical correlation plot is shown in Figure 4. An additional discussion on the correlation studies will be given in this presentation.

REFERENCES

1. Test Methodology Report, Gamma Dosimetry Improvement and Modernization Program, TECOM Project 7-CO-PB1-WS1-001, 19 Apr 1985.

2. Gamma Dose Rate Measurements at the Nuclear Effects Laboratory Fast Burst Reactor, Dosimetry Technical Report Number 86-1, E. H. Hayth, October 1985.

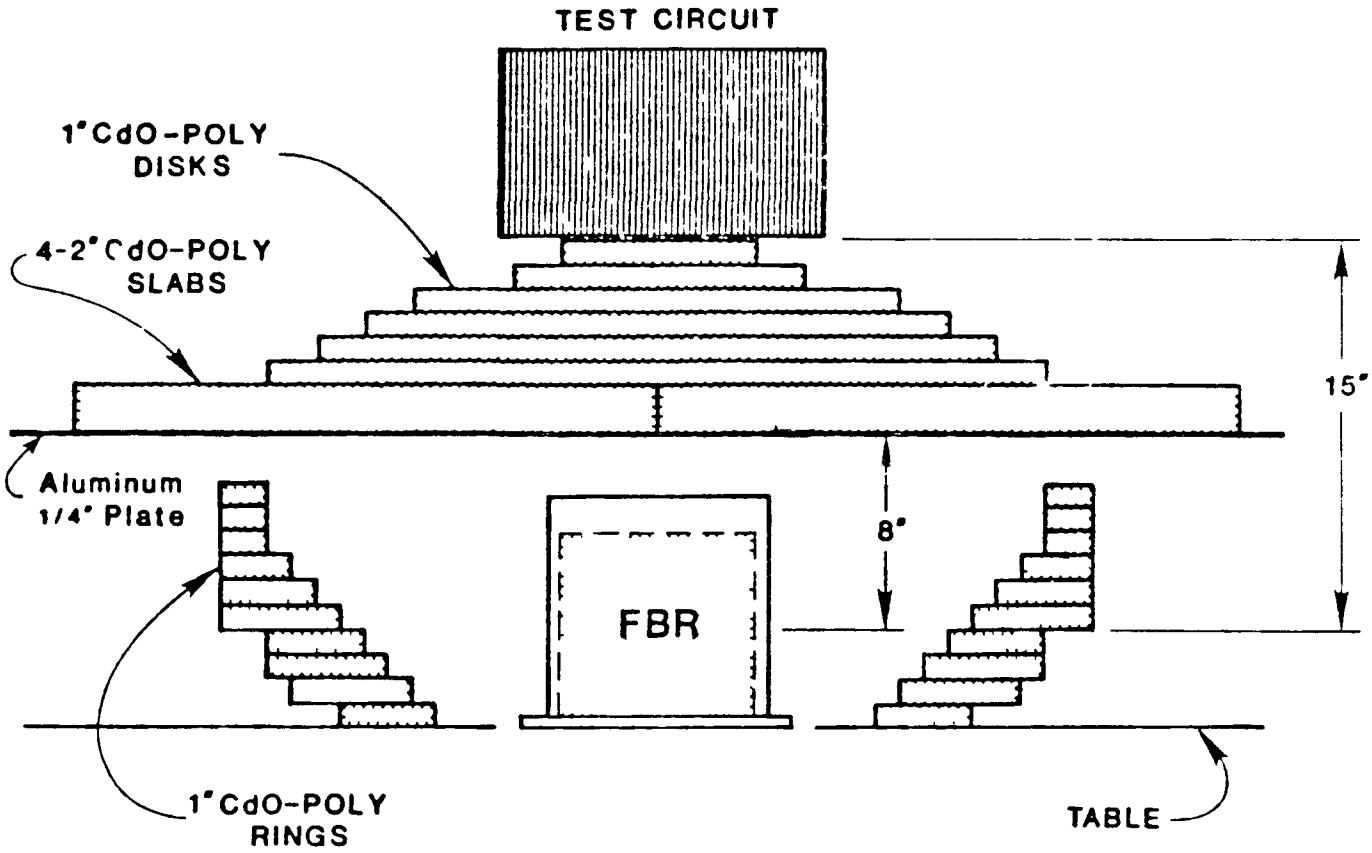

FULL CdO POLY SHIELD CONFIGURATION

OPERATION NUMBERS FOR THIS CONFIGURATION

9932	9953	9957
9933	9954	9958
9950	9955	9959
9952	9956	9961

FIGURE 1. SCHEMATIC OF CONFIGURATION TWO

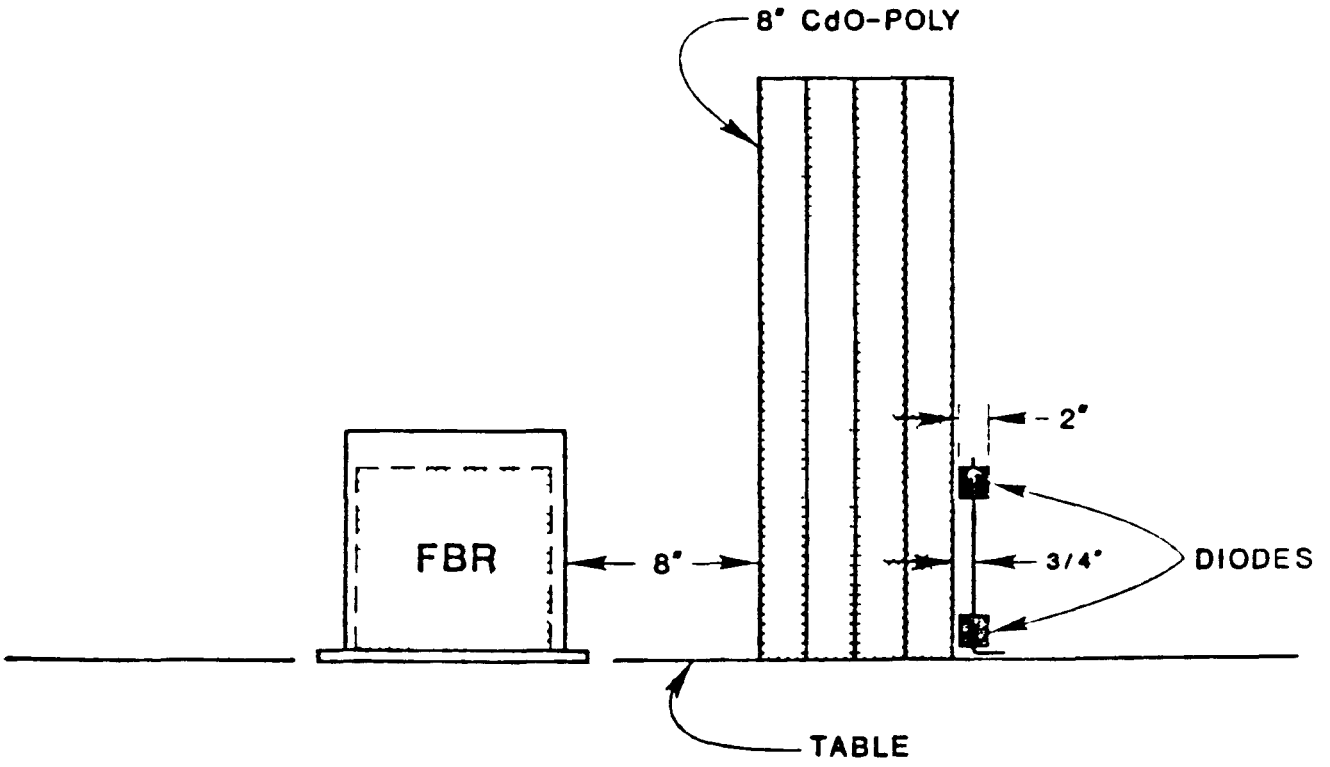

For FBR operations 10319 through 10320 one CD POLY bar was removed and the shield was placed 7 1/2" from the core surface.

FIGURE 2. SCHEMATIC OF CONFIGURATION FIVE

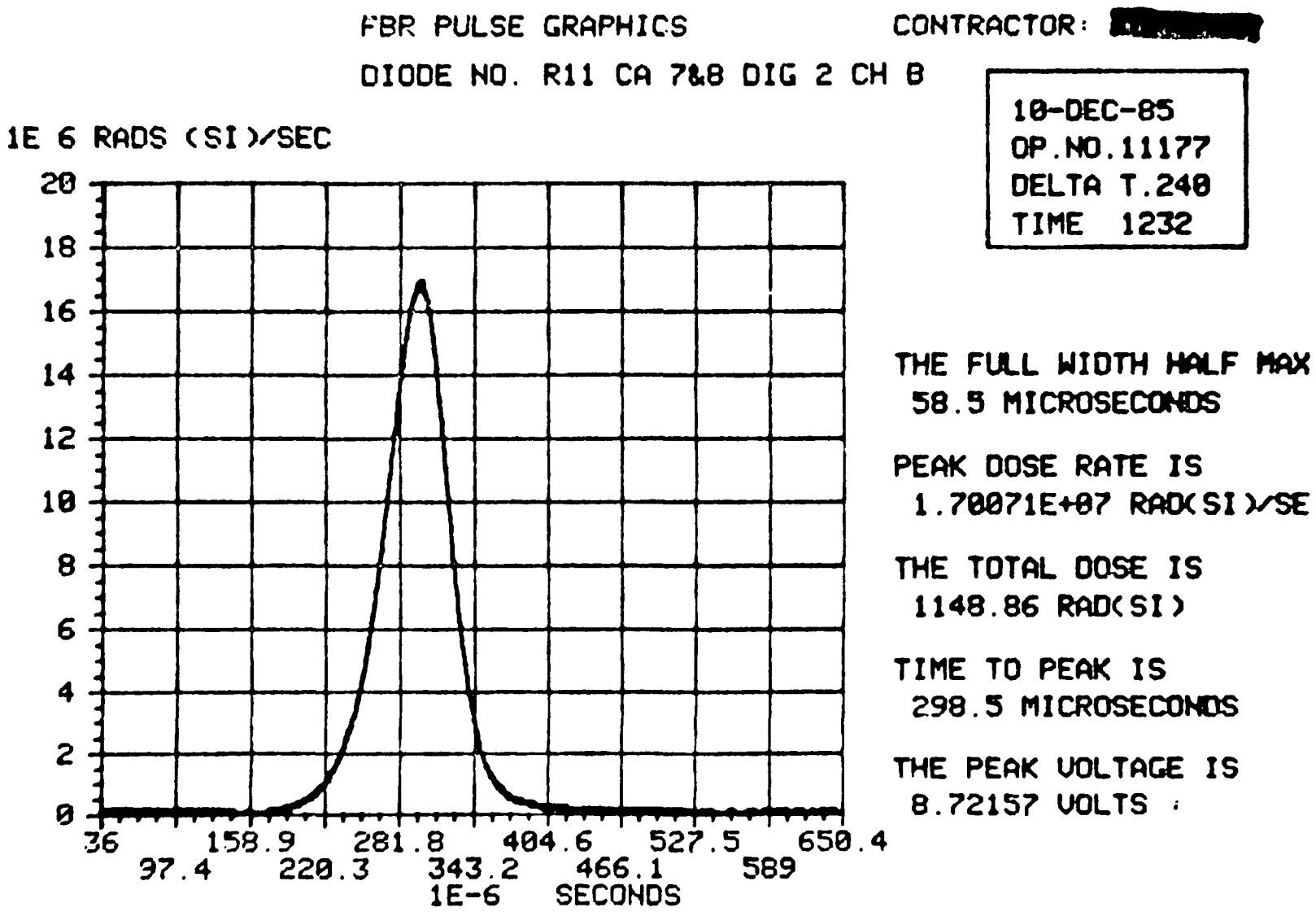
FBR PULSE GRAPHICS
CONTRACTOR: [redacted]
DIODE NO. R11 CA 7&8 DIG 2 CH B
10-DEC-85
OP.NO.11177
DELTA T.240
TIME 1232
1E 6 RADS (SI)/SEC
20
18
16
14
12
10
8
6
4
2
0
36
97.4
158.9
220.3
281.8
343.2
404.6
466.1
527.5
589
650.4
1E-6 SECONDS
THE FULL WIDTH HALF MAX
58.5 MICROSECONDS
PEAK DOSE RATE IS
1.70071E+07 RAD(SI)/SE
THE TOTAL DOSE IS
1148.86 RAD(SI)
TIME TO PEAK IS
298.5 MICROSECONDS
THE PEAK VOLTAGE IS
8.72157 VOLTS

FIGURE 3

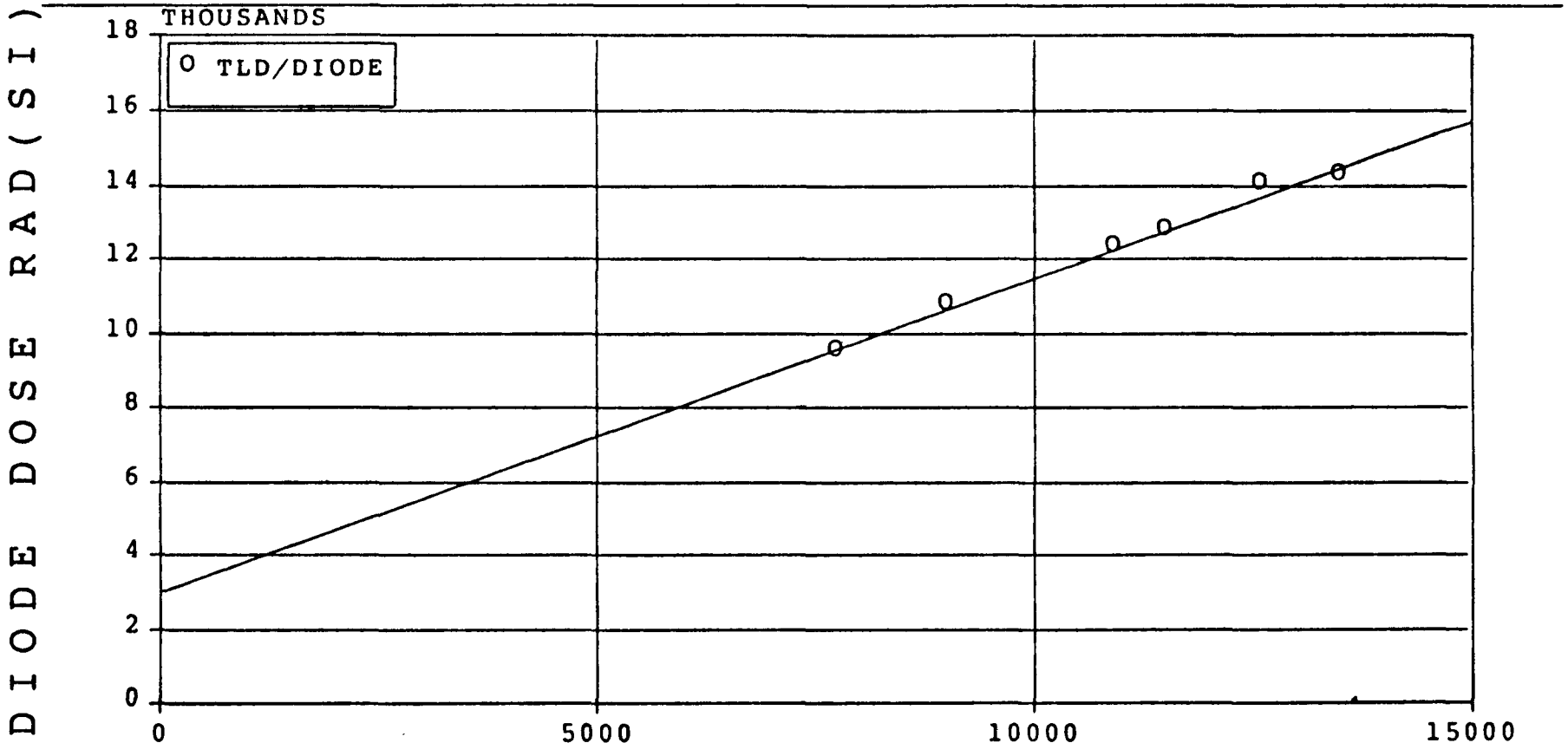
GAMMA DOSIMETRY DECEMBER 1984
FBR OP 10617-19-20-21-26-28 DIODE Q125-T
DIODE DOSE RAD(SI)
THOUSANDS
18
16
14
12
10
8
6
4
2
0
O TLD/DIODE
0
5000
10000
15000
TLD CAF2 DOSE RAD(SI)

FIGURE 4

SESSION V

OPERATIONS AND MAINTENANCE

J. A. Reuscher, Chairman
Sandia National Laboratories

SANDIA PULSE REACTOR PERSONNEL DOSE REDUCTION PROGRAM*

Jeffrey S. Philbin
Sandia National Laboratories
P. O. Box 5800
Albuquerque, NM 87185

ABSTRACT

A personnel dose reduction and facility modernization program has resulted in a new appearance and new methods of operation at the Sandia Pulse Reactor (SPR) Facility. By making improvements in many diverse areas--the facility, facility support systems, the reactor stand, and administrative policies--a significant reduction (60%) in the overall personnel dose has been achieved. New support systems include a remotely controlled, chain-driven experiment retrieval device and a movable, 1.75-inch thick, lead shadow shield. The shadow shield attenuates the radiation field by factors of 10 or higher at normal positions occupied by personnel performing the tasks.

1.0 INTRODUCTION

In 1982 Sandia National Laboratories initiated the Dose Reduction/ Facility Modernization Program at its Sandia Pulse Reactor (SPR) Facility. The Dose Reduction Program (as it became known) identified and implemented changes to the facility, the reactor, and administrative procedures that were necessary for reducing personnel dose and increasing experiment throughput. These changes fell into five major categories:

1) Modifications to the reactor building,
2) Modifications to the SPR-III reactor stand,
3) Procurement of a remotely controlled forklift,
4) Design, fabrication and use of a personnel maintenance shield, and
5) Administrative changes.

The SPR Facility consists of an instrumentation building, a control building and a dome-shaped reactor building (or Kiva). Two bare, fast burst reactors, SPR-II and SPR-III, are operated from the elevator stand at the center of the Kiva on an interchangeable basis. Funding for the Program was identified in January 1982. A project team was formed in February 1982 to study the dose issue at SPR and make recommendations. All major construction items were

*This work was supported by the U. S. Department Of Energy under contract number DE-AC04-76DP00789.

completed by September 1983. Fine-tuning of the modifications (primarily on the reactor stand) continued, however, for another 6-12 months to improve repeatability of performance. The capital cost of the Dose Reduction Program was $871K.

2.0 BACKGROUND

SPR-III, a 258-kg fully enriched, all-metal, externally reflected reactor, is routinely operated for experimenters who wish to use the 6.5-inch diameter by 14.5-inch high internal cavity or leakage neutrons adjacent to the core. SPR-III can be removed from its operating position in the center of the Kiva by forklift and replaced by SPR-II. SPR-II is a 106-kg fully enriched Godiva-type reactor, for experimenters requiring narrower pulses or higher dose rates than those achievable by SPR-III. SPR-II has been operational since 1967 and SPR-III since 1975. Maintenance requirements have increased over the years as a result of wear and the hostile thermal stress and radiation environments. Additionally, utilization of the reactors increased substantially in the late 1970's and remains at a high level (723 operations in 1985). As a consequence, there was a gradual increase in the doses received by operations personnel in operation and maintenance activities during the late 70's and early 80's. The highest annual whole body exposure for the SPR staff was 20 man-rem. Usually, a few individual doses each year would be in the 3.5 to 5-rem range. In 1979, for example, Sandia accounted for 2 of the 13 exposures greater than 4 Rem among all DOE contractors. These facts were the focus of discussions between Sandia management and DOE/AL in Spring, 1981. Recommendations eventually led to the formation of a Dose Reduction Project team in February 1982 to study the issues and implement plans to reduce personnel doses.

The goal of the program was to reduce the total radiation exposure of personnel in the operation and maintenance of the reactor by 33 percent.

3.0 KIVA MODIFICATIONS

The modifications to the Kiva were extensive. These included:

1) Replacement of the existing flooring with boron-loaded concrete.
2) Installation of chain-driven, remotely controlled experiment retrieval device (ERD).
3) Installation of a positive indexing feature at the top of the reactor lift stroke.
4) Modernization of the nitrogen cooling system.
5) Installation of an adjustable maintenance platform for elevation of the reactor above the normal operating position.
6) Installation of 220 volt power to the reactor stand for a new pulse element drive system.

Some of these changes are shown in the photograph, Figure 1.

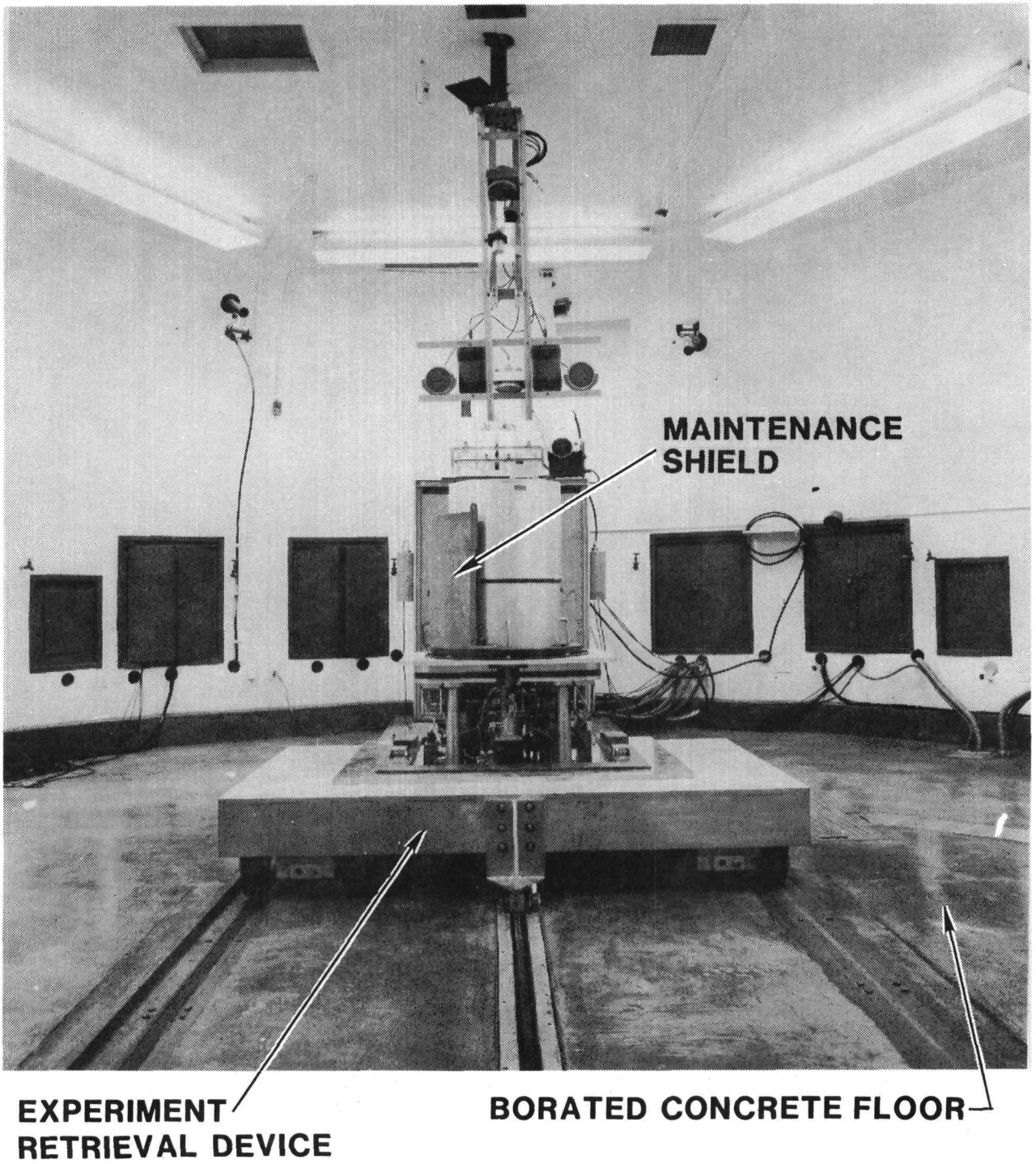

Figure 1. KIVA Modification

4.0 REACTOR STAND MODIFICATIONS

The modifications to the reactor stand were also extensive. Every system was examined and changes were made in those systems and components that most frequently required maintenance. This resulted in the following major changes and several minor ones:

1) Installation of a forklift-actuated release mechanism to automatically uncouple the reactor from its elevator stand.
2) Addition of a lead shielding layer in the aluminum table plate of the reactor.
3) Simplified control element, burst element, and safety block packages for easier installation and maintenance.
4) Improved coolant distribution.
5) Improved accessibility and adjustment of fasteners, limit switches, and instrumentation devices.

5.0 MAINTENANCE OPERATIONS AND THE MAINTENANCE SHIELD

Members of the Health Physics staff at the SPR facility collected data on personnel doses to determine which job functions resulted in the highest doses. The job functions were divided into three general categories that typify personnel exposures at SPR. These categories were: reactor maintenance, reactor changeouts (replacing one of the SPR reactors with another), and normal operations (mostly experiment setup and recovery).

This informal study was conducted over a 5.5 month period from the end of Aug. 1981 to the middle of Feb. 1982. No statistical analysis of the data was attempted nor was any correction made to correlate the frequency of job functions over this test period with observed frequencies of those same job functions over longer periods of time. All measurements were made using pocket dosimeters rather than TLD badges for simplicity and convenience. Furthermore, the dosimeters provide output in Roentgens rather than rem. The official dose values in man-rem were slightly lower than the values reported. The results for the test period are given in Table 1.

Table 1. SPR Personnel Exposures by Job Function, Aug. 1981 to Feb. 1982 -- Roentgen (% of total)

REACTOR MAINTENANCE	REACTOR CHANGEOUT	REACTOR OPERATIONS	TOTAL
11.9 (64.5%)	2.5 (13.5%)	4.1 (22%)	18.5 (100%)

Reactor maintenance operations dominate the dose as expected since these operations are carried out in closest proximity to the reactor. This information supported the decision to expedite the design and construction of a 1.75-inch thick lead shield having an annular shape with a 110°sweep. The movable shield can be rotated around the periphery of the reactor by the person performing the maintenance. See Figure 2.

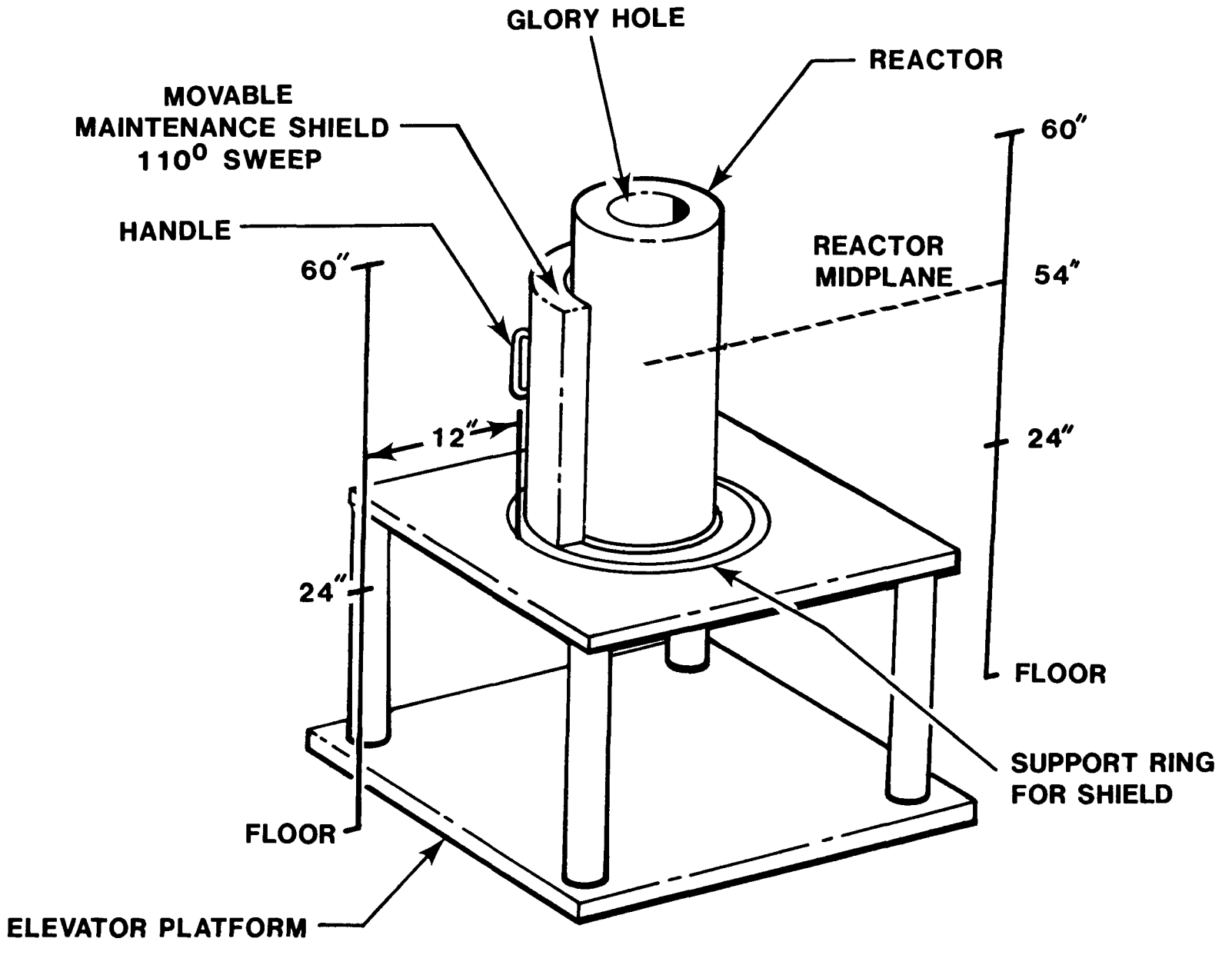

Figure 2. Maintenance Shield Experiment

During the course of some maintenance operations, such as changing thermocouples, it is necessary to work around the edge or above the shield, hence exposing the head. Head-to-whole body dose ratios of 2 were deduced from gamma-field measurements and noting the relative positions of the head and body during lower stand maintenance on the bare reactors. These ratios may increase as body doses are sharply reduced with efficient use of the shield. The lower whole body doses may lead to a false sense of protection in this case thereby increasing the importance of monitoring the head doses separately. It was this realization that led to the practice (at SPR) of monitoring both eye dose and whole body dose. TLD doses both with and without the maintenance shield are given in Table 2. The highest elevation (60") is slightly above the shield and is representative of dose to the eyes. The maintenance shield reduces whole body dose on some maintenance operations by a factor of 10 or more.

Table 2. TLD Measurements With And Without The Maintence Shield
Total Exposure Time = 16 Hrs

Elevation (inches)	Location 1 Unshielded (R)	Location 2 Shielded (R)	Reduction Factor
24	9.04	0.72	12.6
50	34.6	1.03	33.6
60	34.6	7.32	4.7

6.0 ACTIVATION STUDIES

Activation studies were conducted to assess the relative background that could be expected from existing and proposed shield materials for the reactor building floor modification. Individual samples of neutron and gamma shield materials were irradiated at SPR (fast spectrum) to obtain activation signatures at 1 hr and 1 day following irradiation. The background dose from these materials on a "per gram" basis, see Table 3, is one way to rank the materials, although this ranking does not take into account the relative thickness or cost required to use this material as shield.

Table 3. A Ranking Of Test Materials In Order Of Increasing Specific Activation By Fast Neutrons

Rank	Material
1	Graphite
2	Boron-loaded (5%) Poly
3	Hemlock Wood
4	Plywood
5	Gypsum
6	Silicon-based, Boron-loaded (2%) Neutron Shield
7	Lead
8	Aluminum

Activation gamma sources were calculated using the Gammon Activation Library to assess the combined shielding and activation characteristics of the existing and proposed floor designs. The distributed gamma sources were then used in a radiation transport code to calculate the gamma flux and gamma dose rate in the reactor room as functions of irradiation time and time after shutdown. After careful consideration of all criteria (including cost) the design selected was three inches of boron-frit-loaded concrete (2.0 w/o boron) over the existing base concrete floor. Based on calculated results, the borated concrete would probably rank between 6 and 7 on the above chart.

7.0 ADMINISTRATIVE CHANGES

The following administrative changes were instituted to aid in the dose reduction:

1) Steady-state power operations are scheduled near the end of a week to permit decay of radiation levels over the weekend.

2) SPR-II was placed in semiretirement and is used only when necessary.

3) Auxiliary equipment not directly related to operating the reactor was removed from the Kiva to reduce the room background radiation.

4) A new light-weight portable stand is available so experiments can be set up outside the Kiva and carried inside for final positioning. We have also encouraged the use of quick disconnect cabling, standardized interchangeable experiment packages, and prepackaged dosimetry cards in order to minimize setup and retrieval times within the Kiva.

5) The SPR-III mockup is used to test maintenance procedures prior to performing the work on the reactor.

6) Additional maintenance assistance is being drawn from support groups and from the Annular Core Research Reactor operations staff.

8.0 RESULTS

Eye dose and whole body doses for the operations staff at SPR from 1982 through 1985 are shown in Figures 3 and 4. The bar charts show the accumulation by quarter. Figure 5 shows the operational activity at SPR over the same time period. A higher number of operations would typically indicate higher radiation levels and a higher number of maintenance operations. The 1985 whole body and eye exposures are both ~40% of their 1982 levels, a reduction of about 60%.

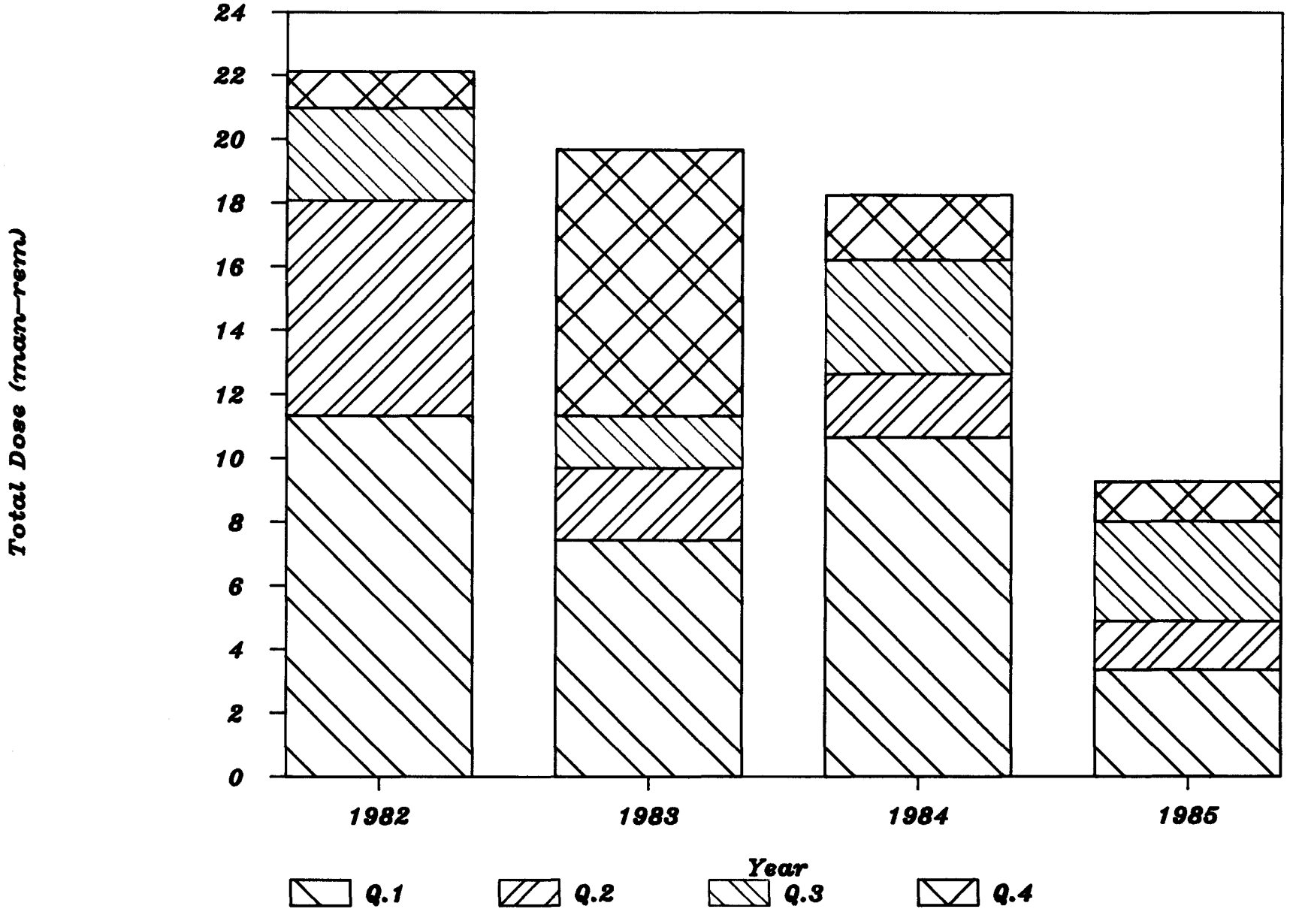

Figure 3. *Eye Dose History for SPR Staff*

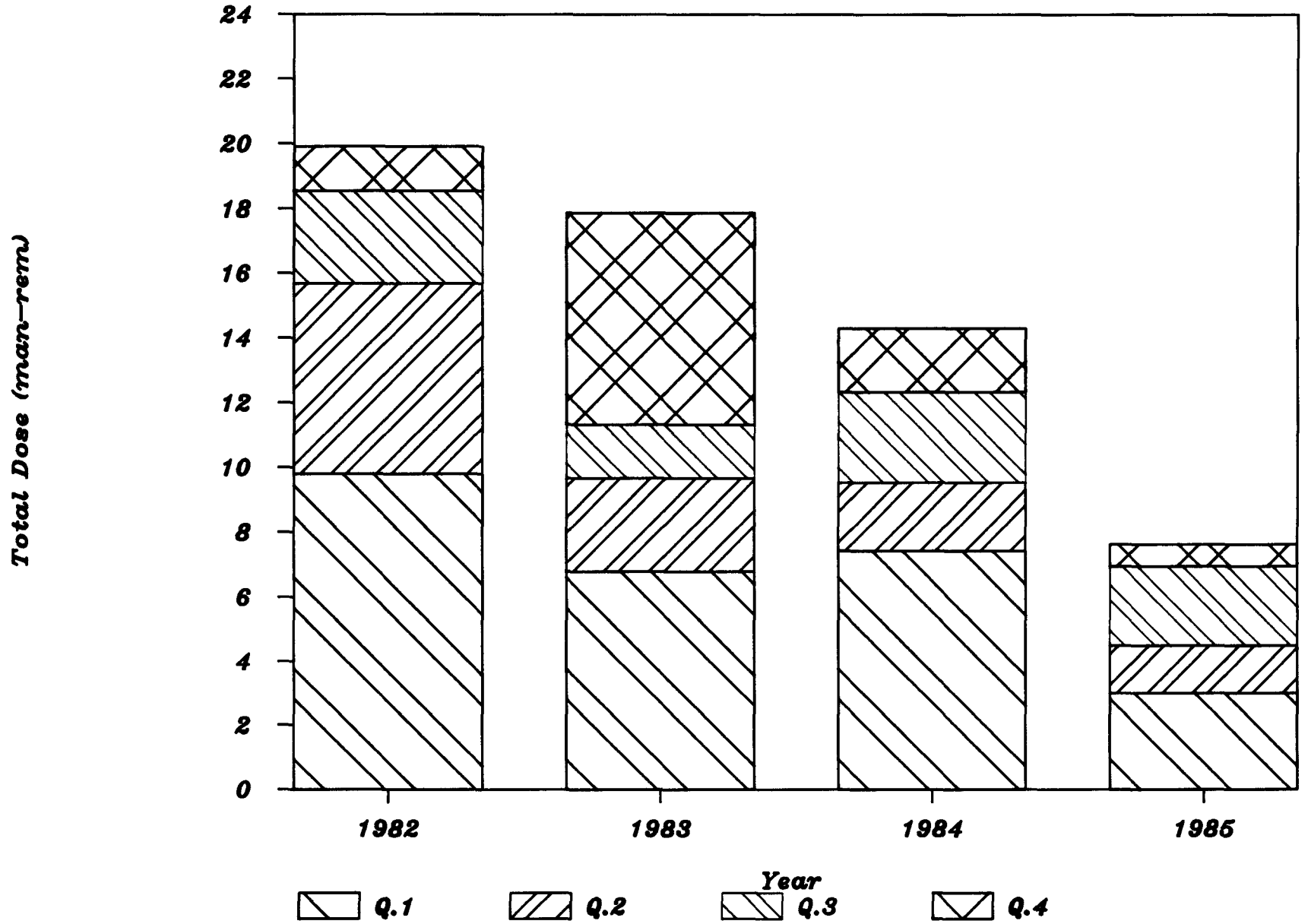

Figure 4. *Whole Body Dose History for SPR Staff*

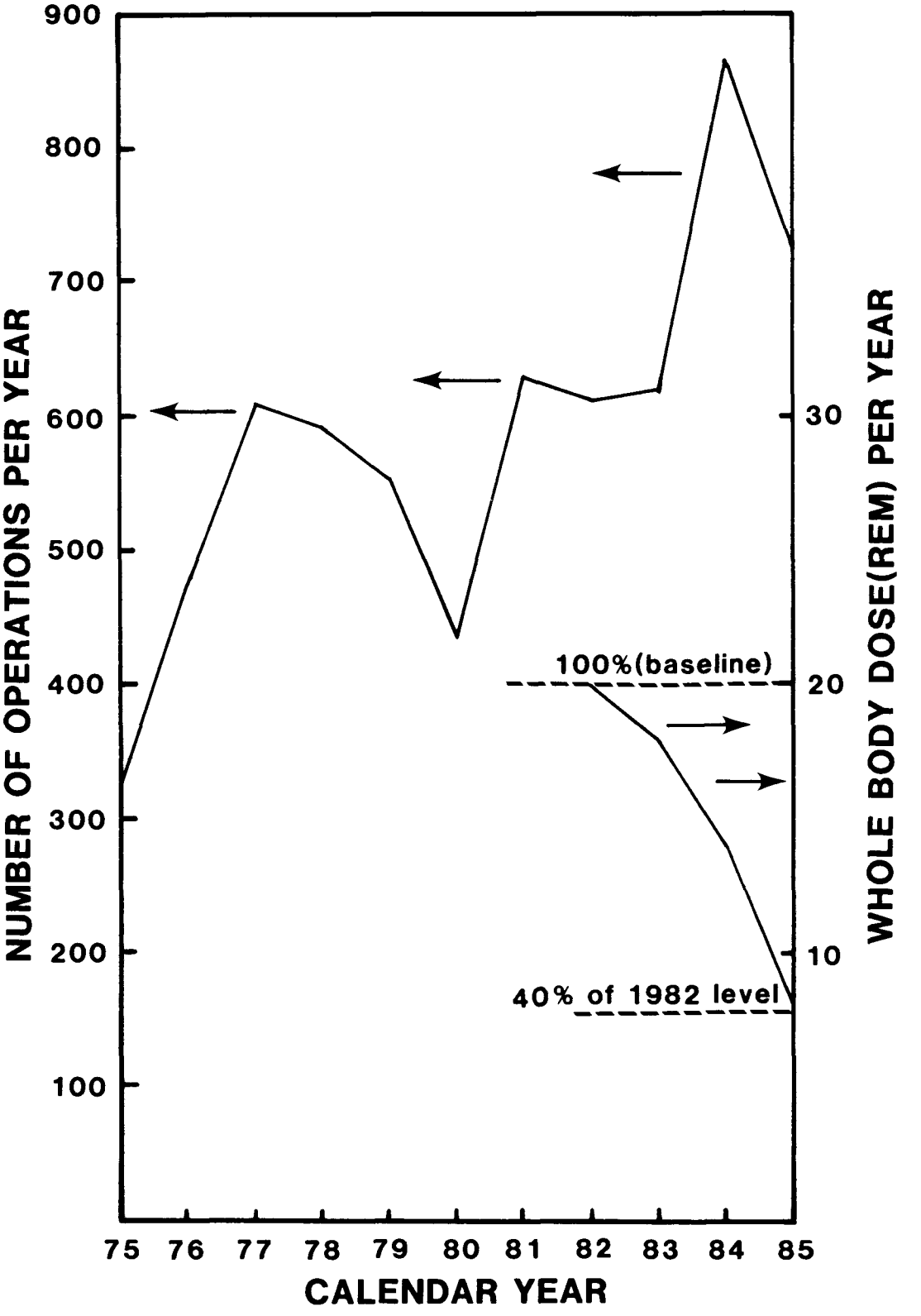

Figure 5. Operation Activity and Dose History

9.0 COST OF DOSE REDUCTION EQUIPMENT AND MODIFICATIONS

The cost of new equipment and modifications is given in Table 4.

Table 4. Cost Of New Equipment And Modifications Associated With The Dose Reduction Program

Item Description	Cost($K)
Maintenance Shield	6
Remote Fork Lift With Crane And Accessories	35
Rebuild Reactor Stand (plus spare parts, mockup)	400
Building Mods and Construction (includes A&E fee)	430
Total	871

10.0 SUMMARY

By making improvements in many diverse areas--the facility support systems, the reactor stand, and administrative policies--a significant reduction (60%) has been achieved in the overall personnel dose at the SPR facility since 1982. The reduction on specific maintenance operations has been quite substantial (factors of 10 or higher) with the use of a movable, 1.75-inch thick lead personnel shield. The capital cost of the Dose Reduction Program was $871K.

11.0 ACKNOWLEDGMENTS

Dose history information presented in this paper was compiled by Richard Stump of Sandia's Health Physics Organization, 3312. SPR operations data was supplied by Donald Berry of the Reactor Applications Division, 6451. Mr. Stump and Mr. Berry also made significant design contributions to the Dose Reduction Project. Other individuals who contributed to the success of the Dose Reduction Project as designers or reviewers include: T. F. Luera, S. Domingues, B. F. Estes, T. M. Debey, D. Minnema (all 6451); M. F. Aker, C. W. Tucker, D. W. Vehar, R. Stinebaugh (6452); and I. Hamilton (retired).

A REMOTE MAINTENANCE ROBOT SYSTEM FOR A PULSED NUCLEAR REACTOR*

S. Thunborg
Sandia National Laboratories
Intelligent Machine Systems Division
Albuquerque, New Mexico 87185

ABSTRACT

This paper presents a remote maintenance robot system for use in a hazardous environment. The system consists of turntable, robot and hoist subsystems which operate under the control of a supervisory computer to perform coordinated programmed maintenance operations on a pulsed nuclear reactor. The system is operational and the oral presentation will include a videotape of the system in operation.

1.0 INTRODUCTION

Sandia National Laboratories currently maintains a fast-burst nuclear reactor as a laboratory tool to study how various materials, components, and systems respond to nuclear radiation. Sandia Pulse Reactor III (SPR III) produces bursts of neutrons and associated gamma radiation that reach power levels of 118,000 MW and last only fractions of a second. If the reactor and its room are allowed to cool down for several days after a burst, the residual radiation becomes low enough to allow hands-on maintenance on the reactor by operating personnel. However, such maintenance does result in occupational radiation exposure (ORE) for some operating personnel. Allowing the reactor to cool down also results in a loss of operating time increasing test costs.

Guidelines recently established for ORE specify that exposure should be "As Low As Reasonably Allowable" (ALARA). In conformance with these guidelines, Sandia has developed a Remote Maintenance Robot (RMR) System for use in the SPR III facility. The RMR should reduce occupational radiation exposure by a factor of four and decrease reactor downtime.

Other goals include developing a technology base for a more advanced pulse reactor and for the nuclear fuel cycle programs of the Department of Energy (DOE) and the Nuclear Regulatory Commission (NRC).

2.0 SYSTEM TASKS

SPR III is shown in Figure 1. The reactor is 72-inches high and 32-inches wide by 25-inches deep. The reactor core consists of eighteen 11.7-inch diameter cylindrical rings of bare, enriched uranium fuel. These are fastened into two parts of nine rings each.

*Work supported by the U. S. Department of Energy at Sandia National Laboratories under Contract DE-AC04-76DP00789.

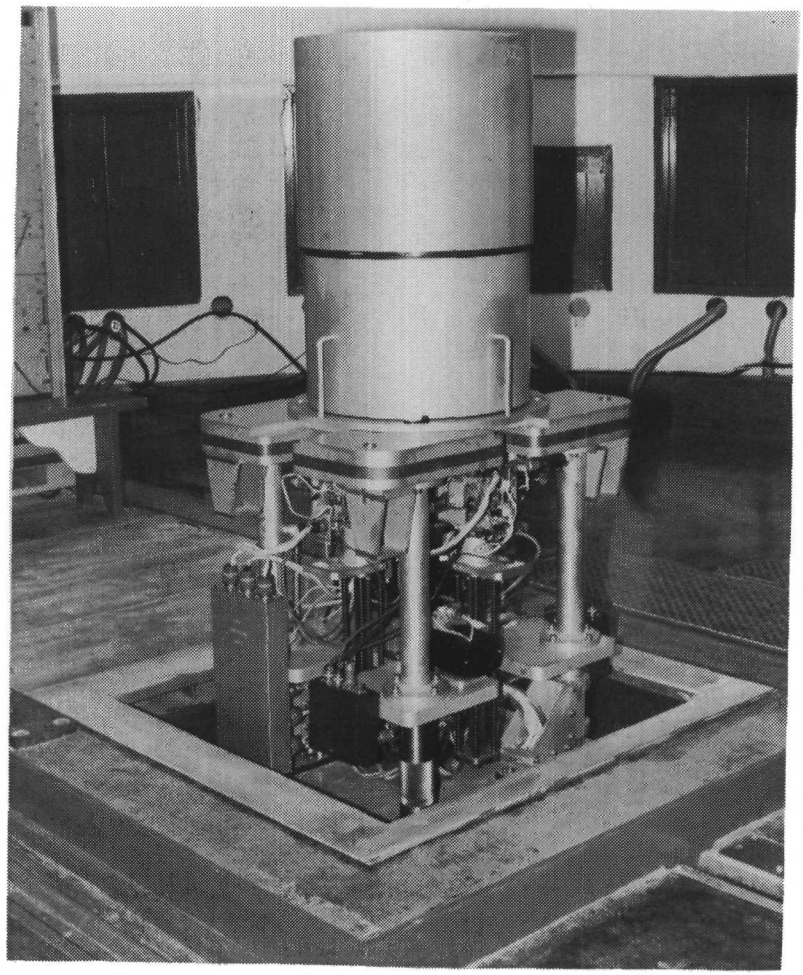

Figure 1. SPR III

The rings are enclosed in a cooling shroud containing a 6.5-inch diameter cavity that extends into the core. This cavity is the primary experiment cavity. Four control elements reflect neutrons back into the uranium rings to establish criticality. One of the elements, the burst element, is closed last and extremely fast to trigger the nuclear burst. The control elements contain electric motors, potentiometers, switches, etc., that require routine maintenance as a consequence of the radiation environment. Figure 2 depicts a typical control element.

The fuel rings contain small thermocouples that also must be frequently replaced because of thermal shock. The uranium fuel rings are subject to microcracks after long use and a periodic inspection is required. The following tasks were established for the RMR system.

2.1 Initial Tasks

- The removal and replacement of shroud
- The removal and replacement of the control element drive assemblies (3 ea)

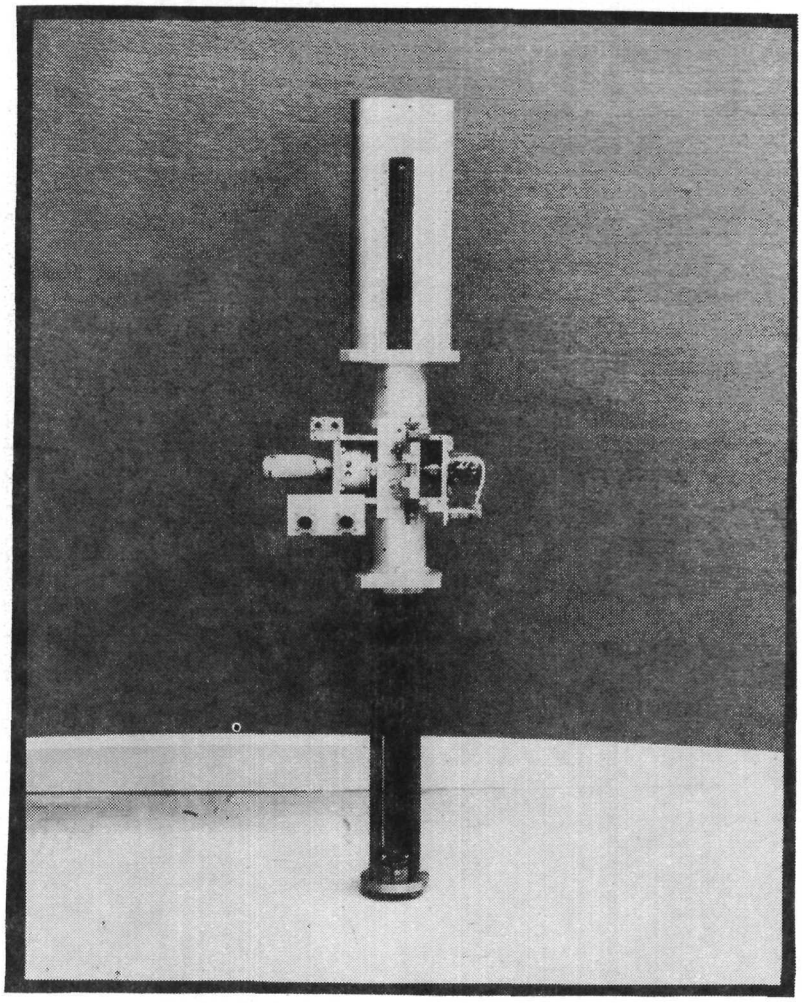

Figure 2. Control Element

- The removal and replacement of the burst element drive assembly (70 lb)
- Adjustment of the control element-limit switch
- Replacement of the fuel-ring thermocouples

2.2 Future Tasks

- Removal and replacement of upper fuel-ring assembly (400 lb)
- Removal and replacement of the lower-fuel ring assembly (400 lb)

All tasks in the initial category have been demonstrated; development on the other tasks is planned.

An additional task for the system is to handle unplanned events through a computer-supervised, error-recovery process or by manually operating all system components in a teleoperator mode. More flexibility for unplanned events is provided by an automatic or manual tool-changing capability for the robot.

3.0 OVERALL SYSTEM DESCRIPTION

The RMR has five major subsystems:

- A chain-driven cart that delivers the system into the reactor room
- A programmable turntable that orients the manipulator to any of the reactor's four sides
- A robotic manipulator that performs dextrous operations
- A programmable overhead hoist that handles reactor components weighing up to 400 lbs.
- A supervisory control console for system operations

Figure 3 is a schematic of the turntable, hoist, and robot systems in position around the SPR III reactor. Once the system is in position at the reactor, it performs the required tasks in a preprogrammed, closed-loop fashion. The operator is there only in a supervisory capacity.

4.0 CART SUBSYSTEM

The chain-driven cart system that transports the RMR system to the reactor is an already-existing system that also transports experiments to the reactor. The cart runs on rails permanently installed in the reactor room; Figure 4 shows it in its storage location outside the reactor room.

5.0 TURNTABLE SUBSYSTEM

When mounted on the cart, the turntable provides mobility for the system. The reactor's control elements are located on all four sides of the reactor, and the turntable, with its 300° of rotation, allows the robot access to all sides.

The SPR III reactor is mounted on a hydraulic elevator that allows the reactor to be stored in a well below ground when not in use or raised up into the reactor room for experiments or maintenance. During maintenance, the RMR is positioned over the well and the reactor is raised up through the center of the turntable. The turntable system contains four air-operated support bars that are positioned under the reactor. The reactor is then lowered on these support bars thereby providing a more rigid support for robotic operations than is available with the reactor's hydraulic lift system.

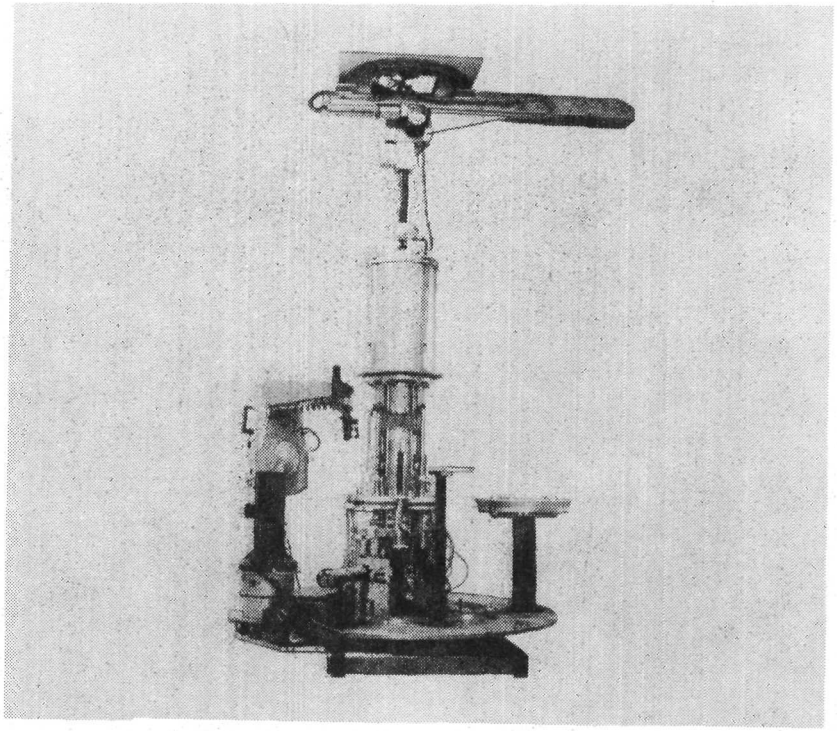

Figure 3. System Drawing

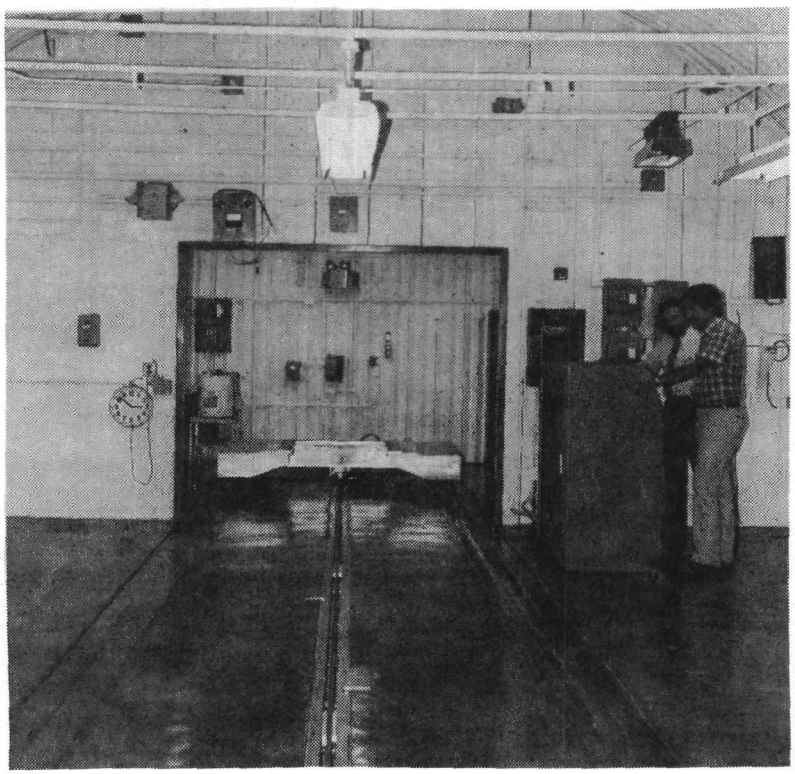

Figure 4. Cart

The following are some basic features of the turntable system:

- Stepper motor drive with radiation-hardened, resolver-position indicators
- Forty-nine-inch-OD ball bearing on which the robot system rotates
- An air supply across the rotating bearing's interface with the rotating mounting plate to supply the robot end effector with air
- Air driven system that moves the reactor support bars
- Safety features that monitor the position of the support bars and the condition of the air-supply pressure
- To change robot end effectors, a tool-changer rack with acknowledge switches
- Remotely operated zoom-lens. TV camera with pan and tilt features
- Audio system that allows the operator to listen to the operations
- Storage stand, with acknowledge switches, for reactor components

6.0 ROBOT SUBSYSTEM

Initial studies revealed that access to the required areas in the reactor was maximized with a revolute-joint-type of robot; we selected the Puma 560 robot with 6 degrees of freedom.

Geometric locations for maintenance operations to be performed by the robot are in the robot memory but they are in relation to a given point on the reactor. At the start of each maintenance operation, the location of this point in relation to the robot coordinate system may not be known to the accuracy required. The positioning and holding capability of the SPR elevator system is less than that required for robotic operations. A touch-off procedure whereby the robot "feels" 6 points on the reactor to determine the XYZ axis of the reactor has been developed. This procedure requires the use of a force sensor on the robot. The force sensor controls the robot through a logic branching program in conjunction with the Val II REACT command to determine when contact has been made with the reactor. The computer program then reads the robot's position encoders and uses the information to calculate the reactor's location relative to the robot. The sensor also measures the torque applied to the reactor's control-element bolts and helps mate electrical connectors.

The force sensor is also an important safety check during maintenance. Since it is continuously monitored by the supervisory computer, if unusual or unexpected forces are detected, the system stops programmed operation and waits for the operator to intervene.

The Puma 560 has brakes to maintain position during a power failure on the first 3 joints, i.e., Joints 1, 2, and 3. However, it does not have brakes on Joints 4, 5, and 6. A power failure resulting in gravity movement of the robot while the robot is engaged with the nuclear reactor could have potentially dangerous results. Consequently, a brake system for Joints 4, 5, and 6 was designed, tested, and installed on the RMR system robot. These brakes were tied in electrically with the Joint 1, 2, and 3 brakes and a power failure activates all brakes simultaneously.

To facilitate teaching of the robot a program has been developed using the force sensor to allow the robot to be hand led to given features on the reactor and the location of reactor features committed to robot memory. Sensor driven control of the robot is accomplished by using the force sensor output and the Val II ALTER command. In essence, the robot maintains zero force on the force sensor by moving in the direction of any applied force.

The robot's tasks are usually performed in a preprogrammed, closed-loop fashion. However, the operator can manually control the system in the event of an unexpected situation.

Multifunction end effectors have been designed for each task so a tool change during routine operations is not required. However, the ability to change end effectors for special situations has been provided.

7.0 HOIST SUBSYSTEM

Maintenance operations on the reactor require handling up to 400 lbs (Fuel Ring Assembly) which is well beyond the capabilities of a reasonably sized robot system. Consequently, a 3 degree of freedom programmable hoist system was designed to operate in conjunction with the robot (Figure 5). It is a polar coordinate system that is radiation hardened since it is permanently in the reactor room and is subject to the reactor burst.

Two application requirements result in several unique features for the hoist system. The first is a requirement for a low head room system as a result of the low ceiling height in the reactor room. The second is a requirement to monitor push and pull forces during a vertical lift.

Both these requirements were met through the use of a semirigid vertical mast lift system. The mast is a flat 11-foot-long stainless steel spring 0.010-inches thick and 5.5-inches wide and formed to be an open sided cylinder 2 inches in diameter and 11-feet long. When being retracted the cylindrical mast is flattened out and rolled up on storage drums thereby minimizing overhead clearance problems.

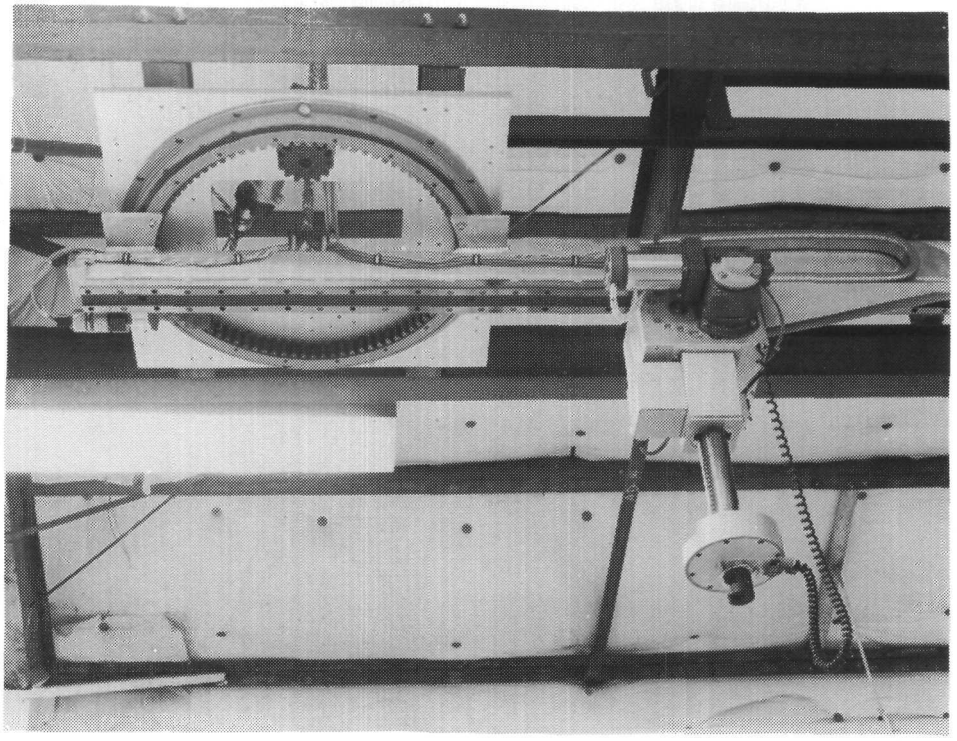

Figure 5. Hoist

The rigid mast allows the use of a 2-axis force sensor on the end of the mast. The force sensor is monitored at all times by the supervisory computer and, if unusual forces are detected, the system stops and waits for the operator to intervene.

Locations for programmed operation are taught to the hoist controller through a teach program provided the operator. Since the hoist hook accommodates a 3/8-inch tolerance when engaging, it does not require a "touch-off" procedure to determine the precise location of the hoist to the reactor.

Routine hoist system tasks are performed in a programmed, closed-loop fashion in conjunction with the robot.

The operator can manually control the system by using a pendant located at the system control console.

Some basic features of the hoist subsystem are as follows:

- o 400-lb lift capacity
- o 5-ft radius operating area
- o 11-ft vertical reach
- o Stepper motor drive with radiation-hardened resolver position feedback (3 axis)

- Gear ratios

θ drive	191/1
R drive	5/1
Z drive	60/1

- Worm gear drive on Z axis to prevent load release at power failure

8.0 SUPERVISORY CONTROL SUBSYSTEM

A master controller and two slave controllers provide overall control of the system. The master controller is the LSI-11 microcomputer; one slave is the Unimate robot controller, and the other slave is the motor controller for the hoist and turntable. The master controller communicates with the operator, establishes the sequence of tasks required for a particular operation, continuously monitors the force sensors, checks for error conditions, responds to emergency interrupt conditions, and establishes the protocol for recovering from errors.

For programmed operation, the master controller software is broken into two levels. The first level consists of the Supervisory Program written in Macro-11 assembly language. The second level consists of several Pascal programs that control specific operations of the robot, the hoist, and the turntable and which communicate directly with their respective slave controllers.

The Supervisory Program has two modes of operation: the program and manual. The program mode executes programmed sequences of tasks. The manual mode is used to provide the operator with manual control of the robot, hoist, and turntable. Most of the time the system is operated in the program mode to perform the automatic maintenance tasks with the operator in a supervisory function only. Programmed operations for a typical system task require up to 30 minutes to complete. The manual mode is available if the operator desires to perform an operation that is not part of the programmed menu or if an error occurs in the program mode.

A control hierarchy schematic of the control system is shown in Figure 6. The operations control console is shown in Figure 7.

A key feature of the supervisory control system is its error recovery capability. Considering the hazardous environment and the complexity of the tasks, provisions for error recovery that do not require human entry to the hazardous environment must be made. When there is an indication of error, the supervisory program halts operations and notifies the operator to move the system robot or hoist manually to a safe position. It then gives the operator three choices, i.e.,

- Abort
- Continue with present subtask
- Redo last subtask

REMOTE MAINTENANCE ROBOT CONTROL HIERARCHY

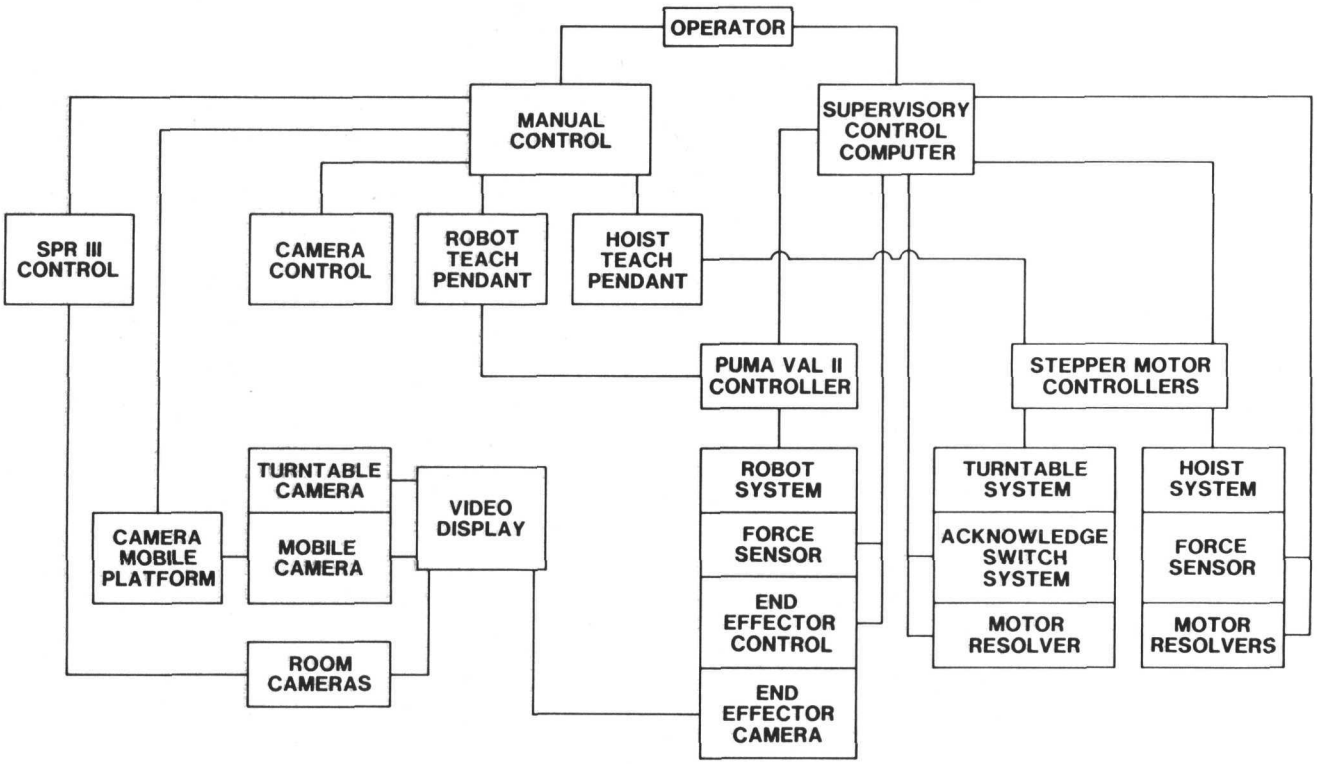

Figure 6. Control Hierarchy Schematic

Figure 7. Control Console

Selecting either of the latter two options commands the supervisory program to resume operations and complete the subtask specified. The supervisory program has a starting point location in memory for each subtask and if a selection is made to continue or redo a subtask the supervisory program automatically moves the robot or hoist from the safe position manually selected by the operator to the subtask starting point. From there the supervisory program continues the subtask in a routine manner.

Following are some of the key features of the system:

- o Supervisory Controller
  - Allows operator interaction at appropriate times
- o Programmed and manual modes
  - Allows operator control, if necessary
- o Continuous force monitoring
  - Excessive forces immediately halt all motion
  - Force thresholds are task dependent
- o Operator intervention
  - Operator can stop motion in emergency situations
- o Battery backup computer memory
  - System can determine when power up follows an abnormal power loss
- o Error recovery
  - Operator manually moves components to safe, neutral positions before proceeding
  - Operator may choose method for recovery
- o Status confirmation
  - Confirms status of the system's acknowledgement switches
- o Multiple TV monitoring of all operations
  - Turntable camera
  - Reactor room cameras (stationary)
  - Reactor room camera (on mobile cart)
  - Camera end effector for robot

More complete details on the operation of the control system have been presented in a paper by M. Moya, et al, "Sensor-driven, Fault-tolerant Control of a Maintenance Robot."

9.0 CURRENT STATUS

At the time of fabrication of the SPR III, a duplicate reactor was fabricated using aluminum fuel rings instead of uranium fuel rings. This unit is used to test all proposed changes or additions to the reactor and to confirm experiment hardware compatibility before actual installation or use on the radioactive SPR III. All Initial Tasks specified herein have been successfully and repeatedly performed using the aluminum ring mock-up reactor.

A training area for the RMR system is being installed at a nonradioactive location adjacent to the reactor room. Using the actual RMR system and the SPR mock-up the reactor operators can become familiar with the equipment and gain confidence in all maintenance operations before their actual use in a radioactive area. Development of the fuel ring removal tasks specified previously will be accomplished in the training area by the reactor operators. Initial operations in a radioactive environment are currently scheduled for the spring of 1986.

10.0 CONCLUSION

The RMR program has demonstrated the feasibility of a robotics system to perform the relatively complex tasks associated with routine reactor maintenance. The RMR was designed specifically for use with the SPR III reactor, however, the technology developed such as sensor driven control, computer hierarchy, error recovery, etc., could have widespread application in the development of other remote maintenance or inspection systems in hazardous environments.

SENSOR-DRIVEN, FAULT-TOLERANT CONTROL OF A MAINTENANCE ROBOT*

Mary M. Moya - William M. Davidson
Sandia National Laboratories
Intelligent Machine Systems Division
Albuquerque, New Mexico 87185

ABSTRACT

A robot system has been designed to do routine maintenance tasks on the Sandia Pulsed Reactor (SPR). The use of this Remote Maintenance Robot (RMR) is expected to significantly reduce the occupational radiation exposure of the reactor operators. Reactor safety was a key issue in the design of the robot maintenance system. Using sensors to detect error conditions and intelligent control to recover from the errors, the RMR is capable of responding to error conditions without creating a hazard. This paper describes the design and implementation of a sensor-driven, fault-tolerant control for the RMR. Recovery from errors is not automatic; it does rely on operator assistance. However, a key feature of the error recovery procedure is that the operator is allowed to reenter the programmed operation after the error has been corrected. The recovery procedure guarantees that the moving components of the system will not collide with the reactor during recovery.

1.0 INTRODUCTION

Using robots to do tasks in a hazardous environment can remove human workers from that environment and can significantly reduce human exposure to the hazard. As a result, robots can be particularly useful for maintaining nuclear reactors, since the environment around the reactor is radioactive and potentially dangerous to human operators. Sandia National Laboratories owns and operates a pulsed nuclear reactor, which applies a calibrated burst of radiation to microelectronic components to test them for radiation hardness. This reactor is called the Sandia Pulsed Reactor (SPR). The SPR is maintained by human operators. Before beginning a maintenance task, these operators allow the radiation in the reactor room to decay for several days after a burst before entering the reactor room. To reduce the exposure of the operators to the radioactive environment, Sandia established a project to develop a robotic maintenance system for the SPR. The Intelligent Machine Systems Division at Sandia has designed and constructed a Remote Maintenance Robot (RMR) for this purpose. The RMR is scheduled to be installed and to begin operation in the reactor room in the spring of 1986.

The key to a successful design for the RMR system was making it work safely and reliably and making it easy to use. In designing equipment to work on and around a nuclear reactor, safety and

---

*Work supported by the U. S. Department of Energy at Sandia National Laboratories under Contract DE-AC04-76DP00789.

reliability were extremely important considerations. It was also important to incorporate an effective operator/machine interface, because if the operator finds the system difficult to use, he may choose to ignore it in favor of executing the maintenance task himself, regardless of the radioactivity. These considerations were given high priority in the design of the system, and they led to the following set of specific system design goals:

1) The RMR system shall be easy for the operator to learn and to use. It shall be menu-driven and interactive. The RMR shall minimize the amount of remote manipulation that the operator has to do. Once the operator starts the programmed operation, the system shall operate autonomously without further directions or guidance from the operator unless an error occurs. It shall provide for operator intervention at any time and facilitate a return to the programmed operation when the operator chooses to do so.

2) The RMR system shall operate in the safest possible manner. It shall be sensor-driven so that it can detect error conditions and potentially dangerous situations should they occur. When something goes wrong, it shall stop immediately and allow the operator the opportunity to correct the error before proceeding. Under no circumstances shall any component of the system contact the reactor in an uncontrolled manner.

3) The RMR system shall provide the capability to recover from error conditions and return to the programmed operation. Specifically, the system shall begin to pick up programmed operations where it left off rather than starting at the beginning.

4) Even if an unrecoverable error occurs, the operator shall be able to withdraw the RMR system from the reactor room. Errors shall not handicap the system so much that human operators have to be sent into the reactor room to retrieve the RMR.

Therefore, the control system for the RMR was designed to incorporate the aforementioned features. The purpose of this project was not to do research in the area of robot control, nor was it intended to develop any new robot technology. Instead, the project was intended to demonstrate a real application of sensor-driven control. The objective was to incorporate commercially-available sensors into a commercially-available robot system and to create a general control structure which would make them operate and respond as a single system and which would make the system capable of intelligently responding to error conditions. The technical challenge came in designing the system control to react safely, reliably, and in real time.

2.0 GENERAL SYSTEM DESCRIPTION

Following are concise descriptions of the SPR and the RMR systems. More detailed descriptions of both systems are contained in reference 1.

The SPR consists of a set of uranium rings and a set of four reflector plates. To start a critical reaction, the reflector plates are driven vertically so that they are adjacent to the uranium rings and can reflect neutrons back into the uranium. The assembly that contains the reflector plate, the mechanical drive gear, the drive motor, and the associated wiring and connectors is called the drive assembly. The drive assembly also contains limit switches that regulate the upper and lower limits of motion of the reflector plate. There are four drive assemblies, one on each side of the reactor, and each can be completely removed from the reactor for repair and maintenance. During operation, the reactor is covered with a large, cylindrical shroud, which moderates the neutrons. The reactor and its shroud are shown in the center of Figure 1.

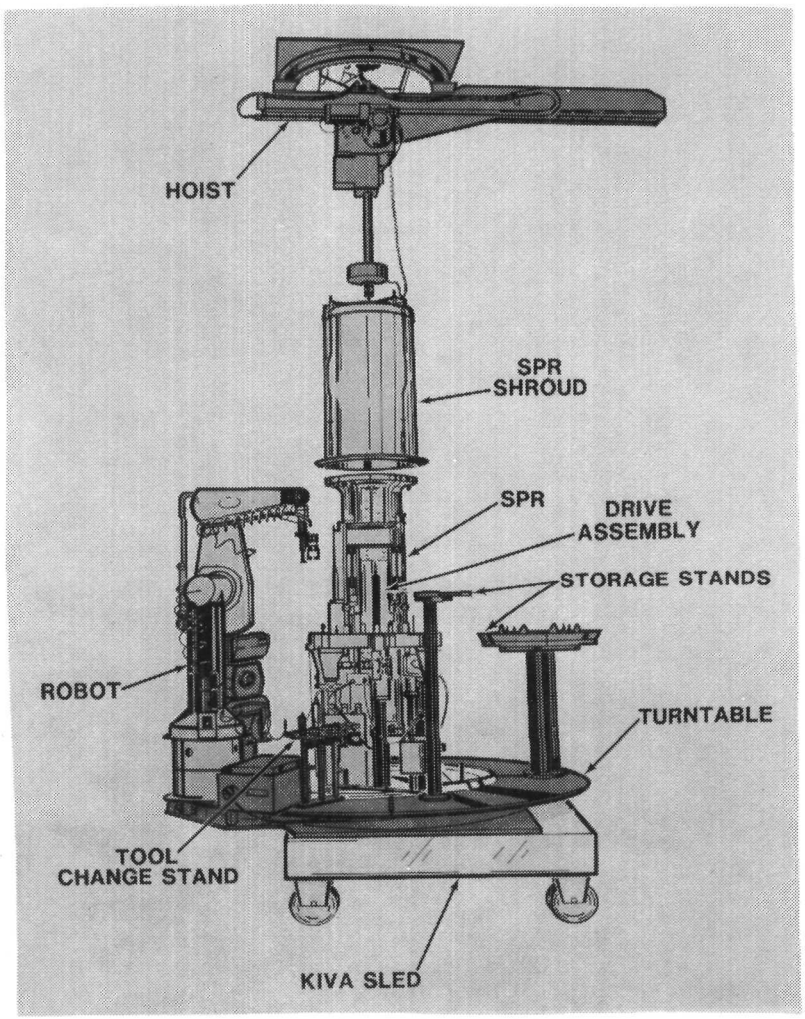

Figure 1. Remote Maintenance Robot (RMR) System

The reactor usually operates in the burst mode, which means that a tremendous amount of energy and radiation are generated in a short time. Consequently, there are several components on the drive assemblies that are subject to failure and that need to be replaced periodically. The RMR system has been programmed to repair and maintain the drive assemblies on all four sides of the reactor. The RMR system will remove the reactor shroud, remove the drive assembly in need of repair, and place it on a stand so that it can be taken out of the reactor room. In addition, the RMR system can replace the drive assembly and the shroud and adjust the locations of the limit switches.

Figure 1 shows the components of the RMR system surrounding the SPR. A programmable turntable can move around the reactor to all its four sides. The turntable is mounted on top of a remotely operated sled, which runs on a track extending out of the reactor room. The SPR is mounted on hydraulic supports, which can raise and lower the reactor out of and into its storage pit located in the floor. During maintenance operations, the sled is positioned over the storage pit. The reactor is then raised up from its storage pit through the center of the sled and turntable. On completion of maintenance operations, the reactor is lowered into its pit and the sled is wheeled out of the reactor room. The other major components of the RMR include the programmable six-degree-of-freedom robot arm and the programmable three-degree-of-freedom hoist. The robot arm and several storage stands are mounted on top of the turntable. The storage stands are used to store the reactor shroud, a drive assembly from the reactor, and various lifting adapters used in the maintenance operations. The hoist is attached to the ceiling of the reactor room, and it remains in the reactor room at all times. The RMR is controlled from a system control console, which is located outside the reactor room.

During a maintenance operation, the robot arm does tasks such as mating connectors and fastening and unfastening bolts. The robot arm cannot, however, lift more than five pounds. Thus, the programmable hoist is available to lift and maneuver the heavier reactor components, which include the shroud and drive assemblies. The robot arm has a six-degree-of-freedom force sensor mounted between its last link and its end effector. The arm force sensor can resolve applied forces into three components along orthogonal axes and can resolve applied moments into three components about those axes. The hoist has a one-degree-of-freedom force sensor mounted between the end of its extension tube and its end effector. The hoist force sensor detects forces applied along the vertical axis only. Additional components in the system include a variety of verification switches and limit switches located on the storage stands and on the moving components of the system.

Figure 2 shows that the robot arm and the hoist are each controlled from a dedicated slave controller. The overall control for the system is provided by the supervisory computer, which communicates with each of the slave controllers over a serial data link. In addition, the force sensors located on the hoist and on the robot arm interrupt the supervisory computer every sixtieth of a second to

provide new force information. The supervisory computer also has constant access to the states of all the verification and limit switches. This sensory information makes the system capable of working autonomously without sacrificing safety and reliability. A description of how this sensory information is used in the system control is given in the next section.

3.0 SYSTEM CONTROL

The control of the RMR system has been designed to have an intelligent operator interface and to provide a high degree of safety and reliability. The system is easy to use because the intelligent software control makes the separate components in the system function as a single unit. In addition, the supervisory computer is menu-driven and interactive. Its operation is semiautonomous; that is, once the operator sets up the system and initializes the programmed operation, the system will operate without further directions or guidance from the operator, unless an error occurs. The supervisory computer can also respond to inputs in real time without delay. Thus, the operator can intervene at any time. Under most circumstances, regardless of when the operator intervened, it is possible to return to the programmed mode of operation.

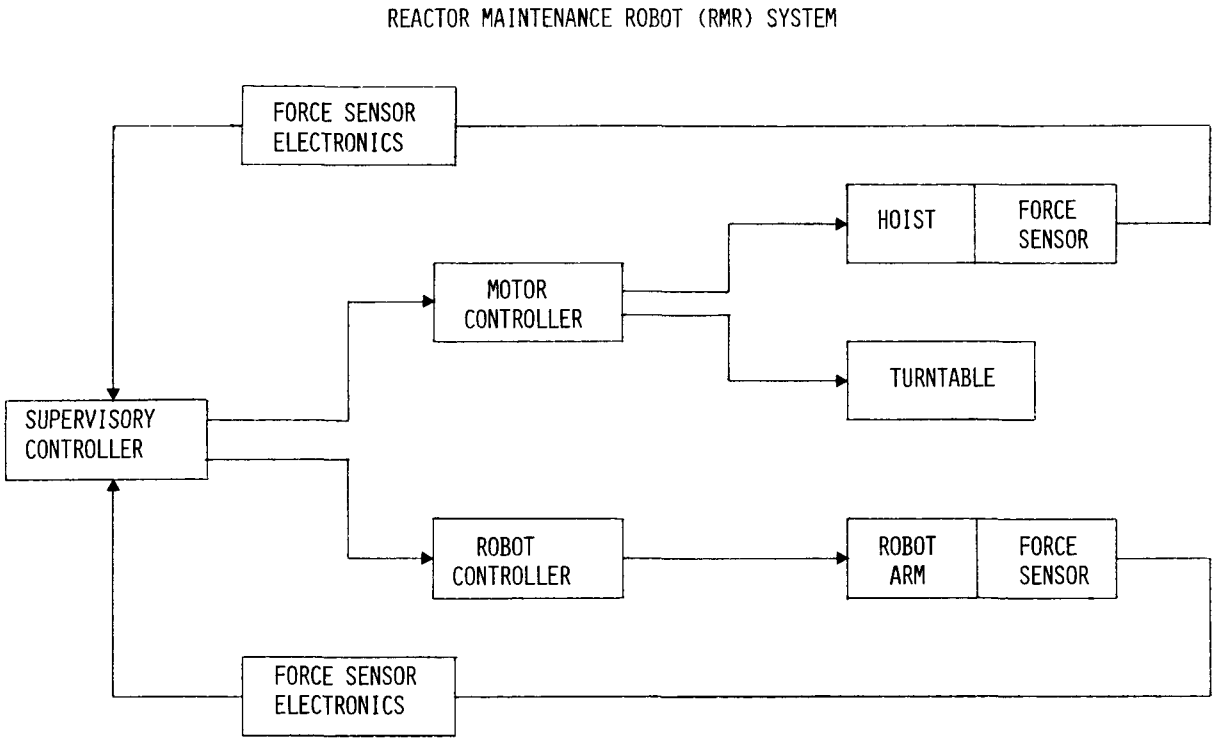

Figure 2. Control Structure for RMR System

The RMR system must operate with a high degree of reliability and safety. To accomplish this, it must be tolerant to error conditions. It uses one of two strategies for handling errors. The first strategy is to anticipate error conditions and make special accommodations for them. This strategy will be described in more detail in the following paragraphs. The second strategy is designed to cope with unexpected error conditions that cannot be anticipated. The strategy involves not trying to prevent an error, but letting it occur, and then monitoring for such error conditions and facilitating the recovery from the error. As will be demonstrated in the discussion to follow, both these strategies rely on the availability of sensory data. Therefore, the control is necessarily a sensor-driven control.

3.1. Anticipating and Accommodating Error Conditions

One way of dealing with potential errors is to anticipate when and where they might occur and adjust for those in one of two ways: either, to build appropriate tolerances into the system or to program conditions into the system that accommodate the errors. This concept of error anticipation and accommodation is incorporated into the following strategies for avoiding errors.

3.1.1. Mechanical Tolerances - One potential source of errors, particularly in the operation of the hoist, is in the positioning and precise placement of objects. To accommodate these errors in the hoist, mechanical guides were built into the system. The hoist end effector and lifting adapters were designed so that positioning could be within plus or minus 3/8-inch. Thus, the system has mechanical tolerances built in that are large enough to cope with the anticipated errors in the system.

3.1.2. Sensory Verification and Task Modification - The positioning and precise placement of objects can also be a significant problem in the operation of the robot arm. Usually, the operations of the robot arm require such precise positioning that mechanical guides are not helpful. Examples of this include the mating of a 19-pin connector and the placement of a wrench on a bolt head. The problem is compounded by the slight repositioning of the reactor each time it is lowered into its pit and raised again. One way of anticipating such error conditions is to use the sensory capability of the system to check for potential errors, and then based on the outputs of the sensors, modify the operation to accommodate them. Two methods were developed to correct the errors introduced into the system by the repositioning of the reactor. The first is called "touch-off", and is a method for recalibrating all the previously learned positions that the system has stored in its memory. The second method is a spiral search, which uses force feedback information to search for the position of a connector.

3.1.2.1. Touch-Off - When the robot arm is initially taught all the positions that it needs to assume during the operation, it is not taught these positions in an absolute sense, but in a relative sense. That is, all the points are taught relative to some index point on the reactor. Therefore, when the reactor moves relative to the robot, it is not necessary to reteach every point in the

operation, it is only necessary for the robot to learn the one index point on the reactor. All the other points are already known relative to the index point. The process by which the robot learns where the index point is located is called "touch-off",[3] and it is a process that interactively uses the force sensor to detect the position of the reactor in three-dimensional space. The touch-off process is similar to the procedure that a blind person uses to find the location and orientation of a table. The blind person feels around until he locates the plane of the table, and then he feels for the edges of the table to establish where the corner is. The robot uses its force sensor to "feel" for the planar surface of the reactor. It slowly moves downward until it detects the contact force from the reactor surface. It then records this position. It executes this procedure three different times in three different locations to give three data points, from which it can establish the plane surface of the reactor. The robot arm then moves to each side of the reactor and slowly moves perpendicular to each side until its force sensor detects a contact force with the edge of the reactor. It also records the location of these points on the reactor. Using the six data points that it collects by sensing points on the reactor surface, it can determine the plane of the reactor top, a line along one of the reactor sides, and the location of the corner point of the reactor. The reactor corner point is then used as the new index point. Each time the RMR system begins a new operation, it executes the touch-off procedure. Thus, the system has used the robot arm and its force sensor to learn where the corner of the reactor is located. This procedure is a good example of how the system anticipates position errors in the operation of the robot and uses its sensory information to modify the task and compensate for the errors.

3.1.2.2. Spiral Search - Using the touch-off procedure at the beginning of every operation significantly improves the ability of the robot arm to locate objects in space precisely. However, there is still one operation that could not be done using dead reckoning alone. That operation is the mating of two 19-pin connectors. Mating the two connectors requires precise positioning to align the pins correctly. To accomplish this, the robot uses dead reckoning as a first guess to try to mate the two connectors. Sometimes this first guess works, and the connectors mate right away. Other times, the connectors are displaced by a small amount, and they will not push together. The computer anticipates this possibility and is constantly monitoring the force sensor to detect high forces indicating this condition. If an abnormal force occurs, it will stop the robot from trying to push the two connectors together and begin executing a spiral search in small increments. After each increment, it stops and again tries to push the connectors together. It continues searching until it detects the force reading that indicates that the two connectors have mated. This procedure, then, is an example of one in which the RMR system expects an error condition and uses its force sensor to search for the correct position.

Both techniques discussed above demonstrate ways in which the RMR system uses sensors to anticipate potential error conditions and to modify the operation to accommodate them. The techniques rely not

only on the availability of sensory data, but also on the predictable nature of the errors that are avoided. However, there are some errors that cannot be predicted. Methods for dealing with unpredictable errors are described in the next section.

3.2. Coping with Unexpected Error Conditions

In dealing with an unpredictable error, even though it is possible to monitor for its occurrence, the system will have no idea what caused the error and, therefore, will not be able to make accommodations to avoid or to correct the error. When an unpredictable error occurs, the objective of the system should be to minimize the effect of the error on the operation of the system and to correct it or get around it if possible. Since the system does not know the cause of the error, it can only accomplish this error recovery with the assistance of the operator. The procedure that the RMR system uses to cope with the unexpected error condition is as follows. The system must first detect the existence of the error condition. Once the error is detected, the RMR stops all movement of the robot arm, the hoist, and the turntable. It then turns control over to the operator either to correct the error or to complete that part of the task in the manual mode. Finally, the operator returns control to the computer which will recover from the error mode and complete the task in the programmed mode. The mechanisms implemented in the RMR control for error detection and error recovery are discussed in the following sections.

3.2.1. Error Detection - There are three ways in which the RMR system can be made aware of an abnormal error condition: 1) sensory monitoring, 2) hard-wired interrupts, or 3) operator supervision. The RMR control makes use of its sensory inputs to monitor for error conditions. Each time an operation is executed, the control checks the appropriate verification switch to confirm that the operation was completed as expected. The RMR system also continuously monitors the force sensors on both the hoist and the robot arm. It compares these force readings against preprogrammed force thresholds, which change as the task changes. If the force threshold is exceeded, then an error condition is assumed to exist. If any of these sensors gives an unexpected value, then the supervisory computer will notify the operator of the error condition and prepare for manual operation and error recovery.

The RMR system has several hard-wired interrupt lines, which indicate different specific error conditions. These interrupt lines are connected to various switches such as the pressure switch in the nitrogen line, which supplies pressure to operate the gripper functions. If the pressure falls below 60 psi, an interrupt is triggered. If any of these interrupts is triggered, then the system will warn the operator and stop all motion of the system. A couple of the interrupts are also connected to buttons, which the operator can use to intervene and stop all movement in the system.

Finally, since the sensors and interrupts will not be able to recognize every possible error condition, the system relies on operator supervision to detect error conditions that the system

would otherwise miss. The operator can intervene at any time by pressing any of the buttons that generate an emergency interrupt to the supervisory computer.

If any of the aforementioned error conditions occur, the system immediately stops all motion in the system and turns control over to the operator. The system is designed so that if the operator can correct the error condition, then it will always be possible to recover from the error and return to programmed operation.

3.2.2. Error Recovery - Error recovery begins after the error has been detected and after the operator has corrected the underlying error that caused the problem in the first place. Error recovery includes the procedures that have been developed to allow the operator to return control of the system to the programmed mode and have it restart the task again at the point specified by the operator. The error recovery described in this paper is operator-assisted; it is not automatic.

The key problems in designing the error recovery procedure are the following. It is difficult to design the system to stop at any point in the operation and start again at any other point. An added complication is that the operator is allowed to move the system components to any location in the manual mode to correct the error. Thus, the system has to cope with moving the system components from an arbitrary location to the exact location required to begin the operation. To accomplish this automatically without operator assistance, it would be necessary for the system control to include a three-dimensional model of the robot and reactor "world." The control would also have to implement path planning to avoid collisions in the process of moving the components from one arbitrary point to another.

Instead of programming a complicated world model and a path planner, we added a couple of restrictions to the system control to make the job of error recovery much more straightforward. The restrictions that were added were the following: first, during error recovery, programmed operation can restart only at the beginning or ending of a predefined subtask; and second, the error recovery procedure must be assisted by the operator who manually guides the system components to safe positions to avoid collisions.

The first restriction requires that reactor maintenance tasks be broken down into specific subtasks. The subtasks are strategically chosen to be as elemental as possible so that if operation stops in the middle of a subtask, the operator does not have to do a significant amount of work in the manual mode to get back to a position where he can reenter the programmed mode. Thus, a typical subtask consists of an approach, an action, and a withdrawal. If the system is stopped during the approach, before the action is completed, then the subtask must be redone after the system has been returned to the programmed mode. If the system is stopped after the action is completed, during the withdrawal, then the subtask may be skipped and the programmed mode should start again at the beginning of the next subtask. If the system is stopped right in the middle

of the action (for example, just as the hoist is engaging a device to be picked up), then the operator has the choice about whether to proceed forward or back up. That is, in moving the components to correct the error and restart the system, the operator will have to decide whether it is easier to finish engaging the device in the manual mode or whether it is easier to back off and leave the device where it was. The operator's decision at this point will then determine whether the current subtask needs to be repeated or skipped. Therefore, the selection of the subtasks within a task will determine how easily the operator-assisted error recovery will proceed. If the subtasks were chosen to be too large, then the operator would have to do several complicated maneuvers before backing up or proceeding to a point where programmed operation could continue.

In the error recovery procedure, the operator may choose to redo the previous subtask or skip to the next subtask. However, the computer cannot start either of these tasks given arbitrary initial positions of the robot arm and turntable. This is the reason for the second restriction that was added to the error recovery procedure. This restriction guarantees that the robot and the hoist will safely return to positions from which either the previous or next subtask can be started. The procedure consists of the following. First, the computer instructs the operator to move the system components to "safe" positions using the manual mode. A "safe" position for the hoist or the robot is defined as one in which the component is out and away from the reactor and can move freely. Then the operator returns control of the system to the supervisory computer. The computer automatically moves the components of the system from their safe positions to points called the "neutral" points. A "neutral" point is defined for each component for each pair of subtasks. The subtask is designed so that it may start operation from the neutral point without colliding with any other objects. Thus, after the error recovery procedure, either the current subtask or the next subtask may begin execution from the neutral point.

In summary, the error detection and recovery procedure begins as soon as the error is detected. The motion in the system is immediately terminated. Control of the system is turned over to the operator, the operator uses the manual mode to attempt to correct the error and to place the hoist and the robot in safe locations, and the operator authorizes the computer to return to the programmed mode of control. The computer then moves the robot and hoist from the safe positions to the neutral positions where they are ready to redo the current task or proceed with the next task. The computer then gives the operator a menu of options. The operator may choose to repeat the current subtask, skip to the next subtask, or abort the operation.

4.0 IMPLEMENTATION OF CONTROL MECHANISMS ON AN LSI-11/73 MINICOMPUTER

The ideal environment for the control mechanisms previously described would be a multi-tasking system that contains real-time support. Thus, the first choice for the kernal and programming

language was Micro-Power Pascal. This package contains both a Pascal compiler with built-in real-time support and a small custom configurable real-time, multi-tasking kernal. Real-time support is important to allow easy interface with the several sensors in the system and to manage the data from the sensors. Multi-tasking is desirable so the large task of control can be broken into several small, well-defined tasks. This package was also attractive because the robot arm and hoist control programs which were developed independently of the control program were written in Pascal. Unfortunately, because of an approaching deadline and limited manpower, there was not enough time to learn a new operating environment and its idiosyncrasies and to modify the robot arm and hoist control programs for the different compiler and run-time environment. Because of familiarity with RT-11 and some expertise with its internals, a choice was made to write the supervisory program to run under RT-11 and to interface with the existing robot arm and hoist control programs.

4.1. Problems Using RT-11

Even with the expertise with RT-11, there still were a few obstacles to overcome.

- Upon delivery, RT-11 is a single user, single-tasking operating system. Multi-tasking is available but the system calls are awkward to use.

- There are four distinct tasks that make up the control system: the control portion of the supervisory program, the interrupt service routine portion of the supervisory program, the hoist control program, and the robot arm control programs. The task that contains the interrupt service routines has to be resident in memory at all times to respond to interrupts. A method to allow any of the remaining three tasks to run at any time had to be developed.

- The control system had to share a limited amount of memory. Regardless of the amount of installed memory available, RT-11 basically limits the amount of memory it can use to 56K bytes. If all controller programs were loaded simultaneously, the total amount of memory required (not including the operating system or the supervisory program) would be over 256K bytes.

- The supervisory program needed to give commands to and receive error status from the controller programs. Also, the controller programs needed the ability to store parameters that could be retained through controller program swaps and power failures to allow easy recovery.

- The robot arm and hoist control programs were initially developed on stand-alone computers to run independently. Because of limited manpower, these programs had to be used with few or no alterations.

4.2. Solutions

The problem with RT-11's difficult multi-tasking feature was overcome by not using it at all. Since the task management was minimal, the management was included in the supervisory program. As each part of an operation needs to be done, the supervisory program starts the appropriate controller program. If an error occurs, the supervisory program's priority is raised and allowed to run to handle the exception. A communication mechanism was developed to allow commands to be passed to the controller programs and task completion status information to be returned back to the supervisory program. To store parameters for the controller programs, an abstract data type was created for both programs. This data structure was included with the interrupt service routine module so as to be available at any time, regardless if the controller program had been swapped out. CMOS memory with battery backup was used to retain information through a power failure.

The memory limit obstacle was defeated with a swapping routine built into the supervisory program. Since part of the supervisory program is required to remain in memory at all times to respond to interrupts, a swapping routine was added to it to load any of the remaining tasks when needed. The problem could have been solved with overlays. This solution would have required combining all of the tasks into one program and then analyzing it to determine an overlay strategy. However, this would have required considerable modification of the controller programs. With the swapper routine resident in the supervisory program, the controller programs required no changes to get them to swap in and out.

5.0 SUMMARY

The RMR system provides the reactor operators with a tool for doing routine maintenance on the reactor. The control system for the RMR relies on sensory information to gain updated knowledge of its environment. It uses its sensors to anticipate and prevent possible errors, and if an unexpected error occurs, it relies on its sensors and on the human supervisor to detect the error condition. Once the error has been corrected, the RMR control can safely recover from the error and return to the programmed mode of operation.

With these features, the system is much more tolerant to error conditions. Consequently, the design goals have been achieved: the system is easy to learn and to use, it is safe to use on the reactor, and it is more reliable because even if an unexpected error occurs, it is possible to restart the programmed operation.

REFERENCES

[1] S. Thunborg, "A Remote Maintenance Robot System for a Pulsed Nuclear Reactor," submitted to IEEE International Conference on Robotics and Automation, San Francisco, CA, April 1986.

[2] M. H. Lee, N. W. Hardy, and D. P. Barnes, "Research into Automatic Error Recovery," Proceedings of UK Robotics Research, Institution of Mechanical Engineers, Mechanical Engineering Publications, Ltd., London, UK, 4-5 December 1984.

[3] P. S. Hamilton and G. P. Starr, "Touch-off: A Method to Determine the Position of an Object by Means of a Sensor-driven Robot," Sandia National Laboratories, SAND84-2562, January 1985.

FAST BURST REACTOR WORKSHOP
BANQUET PRESENTATION

J. A. Grundl
National Bureau of Standards

PURSUING PUBLIC AND PROFESSIONAL PERCEPTION OF NUCLEAR ENERGY WITH THE SMITHSONIAN LADY GODIVA REPLICA AND DEMONSTRATION/DISPLAY

James A. Grundl
National Bureau of Standards
Gaithersburg, Maryland 20899

ABSTRACT

Reading outline of presentation given at the Fast Burst Reactor Workshop Banquet. The visual accompaniment is not included.

1.0 INTRODUCTION

Two noteworthy events have nicely coincided at this meeting: the official recognition of Lady Godiva as an ANS Nuclear Historic Landmark and the rescue of the Smithsonian Lady Godiva Replica from an unbecoming end. The Godiva Replica is now on its way to the National Atomic Museum here in Albuquerque where, with luck and hard work, it will become the centerpiece of a demonstration/display designed to show nuclear energy in all of its — I should say facets, but I will say — glory.

It is my purpose this evening to outline the unique characteristics of Lady Godiva for such a museum display under the title "Pursuing Public and Professional Perception of Nuclear Energy with the Smithsonian Lady Godiva Replica and Demonstration/Display."

2.0 LADY GODIVA AND THE PERCEPTION OF NUCLEAR ENERGY

2.1 Aston's Mass Spectrometer at the University of Chicago

A beautifully crafted instrument: important for the advancement of our knowledge of the nature of matter. As a potential display piece, however, it is visually encumbered and operationally complicated: sources, slits, electric and magnetic fields etc.

Nuclear isotopes: their significance is subtle and without obvious impact in the real world.

2.2 Lady Godiva: A Unique Artifact of Science

The Device that first brought the fast-neutron fission chain and all of its varied behavior into the laboratory

A milestone of science!

- (No physicist would agree that Godiva was in the same league with Aston's mass spectrometer, but physicists are not the whole world even if they have done as much as anyone to remake it.) I mean milestones of science as perceived by the public.

- In this sense, I would suggest that the neutron fission chain, as a natural phenomenon uncovered by science, has become embedded in the public mind – where it is known as nuclear energy – more deeply than any other achievement of physical science since relativity at the turn of the century.

  (You are looking at a bronze sculpture of Einstein, the only monument on the grounds of the National Science Foundation in Washington.)

Lady Godiva is a laboratory device which can exhibit the fascinating behavior of the neutron fission chain with visual elegance and classic simplicity. It is also rich with historic significance.

- It doesn't look like the usual gadget of science: levers, lights and gauges on the outside, nuts, bolts and connections on the inside. No artificial environment is involved – no vacuum, inert atmosphere, screens or shields. It is nothing but 110 pounds of uranium metal setting out in the world like the rest of us.

The rest of us is the public: the curious, the concerned, and even the professionals of nuclear technology.

- What, and how, do they think about nuclear energy? This question is necessary if a Godiva display is to be more than a tinker toy with sound.

2.3 The Question of Public and Professional Perception of Nuclear Energy

There is a broth of opinion regarding public perception of nuclear energy – what it is, and how to deal with it.
Let me call out two examples:

- Reston Symposium in 1981: a highbrow, multi-discipline meeting sponsored by a perplexed federal agency called FEMA, the Federal Emergency Management Agency. These are the people who are there in a disaster – the good guys. The Nuclear Regulatory Commission had just dumped on this unsuspecting agency one of their leading headaches: radiation control in an emergency.

  – The one participating journalist called the Symposium a 3-day mystery story.
  – As the lucky one asked to organize a controversial Session on Public Information and Training, I had to brave the negative views of some, including an important past mentor at Los Alamos, regarding the wisdom of combining nuclear power and nuclear attack emergencies in the same gathering. Yet it was a natural connection for FEMA, and also for the National Council on Radiation Protection which sponsored the meeting.

- NRC and the nuclear power industry: a too-common approach is "We're OK, you're OK!"

  - You can see results of this approach at the NRC Document Room in Washington. In a bulging file, a letter from a 3rd grade school teacher near Harrisburg, Pa. reveals in the hasty handwriting her anger and frustration during the TMI radiation scare. "What should I tell the children?" she asks. "After all, a meltdown is forever."

A Godiva display – precisely because it can embrace so much of what nuclear energy is, and how it got that way – needs a consistent viewpoint and purpose.

2.4 Notions of Public Perception Among Lady Godiva Replicators

The view of public perception that guided the Godiva replicators remains valid, I believe. They have held up in my experience. From organizing Open Houses at Los Alamos, to working tough crowds at two New Mexico State Fairs, on through to Ralph Nader at a radiation effects Symposium at NIH, and especially the Reston Symposium which was a comedy of cross talk, not much has changed.

Here are the perceptions which motivated the developers of the Godiva display, unvarnished and without any of the qualifications which might be necessary to defend them:

In the Public Mind,

- o Nuclear energy is a creation of science – remote and incomprehensible

- o Nuclear radiation is unnatural
  (like tofu and papaya juice, or for those who must be serious, like leprosy or poison gas)

- o Nuclear energy is never really disassociated from nuclear weapons
  (recall connection of weapons fallout and reactor containment failure)

- o Taking chances is judged largely by familiarity.

The belief that Lady Godiva offers unmatched capabilities to engage an audience and widen its perceptions of nuclear energy stands or falls on the validity of the third item – that the peaceful and violent facets of nuclear energy are embedded together in the public mind – and deeply so.

Resisting this fact of life by making technical distinctions only invites suspicion. (What would any of us think of someone who harped on the difference between the flame of a candle and the flames of a forest fire?)

2.5 The Neutron Fission Chain: Complete Embodiment of Nuclear Energy

Whatever public perception has become, in fact, I believe it is too late to change it. It can only be enlarged upon. I would submit that the game, now, is perspective and engagement. And one attractive way to play the engagement game is to use the neutron fission chain itself. And I do mean a game: something with inherent fascination and interest. Certainly not a soft pitch for nuclear energy — I used to talk that way.

The neutron fission chain is a tangible and comprehensive focus for exhibiting all of the elegance and ambiguities of nuclear energy. It is simple in fact and it is simple to imagine — just right for the casual viewer. Yet, it has underlying subtleties which can challenge the more curious and will even hold the attention of sophisticated professionals.

3.0 THE LADY GODIVA REPLICA AND DEMONSTRATION/DISPLAY

3.1 The Foucault Pendulum at the Smithsonian

There was, and is another elegant and subtle device of science at the Smithsonian: The Foucault Pendulum. It never fails to draw a crowd by its simple visual attraction coupled with its challenge to our perception of a whirling earth. People watch it like a campfire while trying to explain it to their companions.

It is not nearly as easy to explain as the neutron fission chain in Lady Godiva, which sat in grand isolation right around the corner from the giant pendulum. The difference was that the fascinating realities of Godiva could not be displayed or demonstrated at the Smithsonian.

I would note with some hope in this regard that the National Atomic Museum here in Albuquerque labels itself as "Free, Factual and Fascinating." Just the ticket for a revival of the Godiva Demonstration/Display.

3.2 Nuclear Radiation from the Replica's Natural Uranium Sphere

The realities of Godiva begin with the nuclear radiations from its natural uranium sphere: Alpha particles come out a finger's length before being absorbed in air; beta particles come out about an arm's length, and the gamma rays reach the viewer. He is engaged. Can he be fascinated?

Perhaps, because the Godiva sphere also emits about 1000 neutrons every second from spontaneous fission in natural uranium. [This is many more, by the way, than come the from the uranium-235 of the real Lady Godiva, a fact that can be exploited in a good display narrative.]

Thus, even in the replica the neutron fission chain exists, and not trivially either. One spontaneous fission in six born in the natural uranium sphere leads to a short neutron fission chain. Most are only 2 or 3 fissions long, but once every second there is a chain that is 6 fissions long.

If the burst reactor professionals in the audience are not impressed by this nascent show of nuclear energy in the Godiva museum piece, let me tell you, or remind you, that in the real Godiva at delayed or prompt critical, 60% of the neutron fission chains are fewer than 4 fissions long!

3.3 Refined Image of the Neutron Fission Chain

Of course, it is the fully developed fission chain and the prodigious energy generation associated with it that must be the focus of a Godiva display.

In simple natural steps the Lady Godiva demonstration/display represents

- --the curious features of the neutron fission chain when it is not self-sustaining (e.g. Godiva is devoid of neutrons 99% of the time when average chains are 100 fissions long)
- --the peaceful behavior at delayed critical when the neutron fission chain is self-sustaining and controllable -- the boon of nuclear power
- --the violent multiplication of a single neutron fission chain which ended a great war and changed the face of world politics.

Here is a short segment of the narration that accompanied the original demonstration of delayed critical:

> "The simple act of bringing 107 pounds of uranium-235 to a near-spherical shape allows myriads of short neutron-fission-chains to form within the material, each one lasting but an instant. The mere existence of this configuration of uranium spawns these chains which together yield about ten thousand fissions per second. These brief flashes of nuclear energy would continue indefinitely.
>
> To multiply this trifling production of energy, one need only add 3 more pounds of uranium-235 to the sphere. Now the neutron-fission-chains may increase in length and number until after a few minutes the heat generated expands the uranium metal sufficiently to prevent further chain growth. The delicate neutronic balance achieved, called "delayed critical", would occur with the reactor generating about two hundred watts of heat energy (equivalent to two common light bulbs). If left entirely alone, Godiva would still be generating one hundred watts of energy 4000 years later, and in that time would have depleted less than 1% of the available nuclear energy in the uranium."

3.4 Abundance of Anecdotal History

Every good museum display should have stories behind it. The lore of Godiva is extensive. Just one story this evening:

The idea of building Godiva at all in 1950 was a matter of some reluctance because of its sensitivity to its surroundings. The subsequent proposal, however, to take the device into the prompt critical realm, where there are no mechanical methods of shutdown, was not everyone's notion of the way to go with an already sensitive reactor. (Richard Feynman had earlier called such investigations "tickling the dragon's tail.")

In addition, the theoretician of neutron fission chain behavior at the time did not feel there was that much to be learned. One man, the leader of the Critical Assemblies Group, Hugh Paxton, with the intuition of the experimentalist, took the responsibility of saying let's have a look anyway.

The difference of opinion regarding the building of Godiva in the first place showed similar predilections. Edward Teller, the famous theoretical physicist, was against it in spite of his reputation for aggressive innovation; Hans Bethe, on the other hand, a sober laboratory physicist of many talents, thought it was a worthwhile project.

3.5 Display Options

Casual vs in-depth presentations; history and tales vs neutron fission chain behavior and nuclear technology

The elegance, the realities, and the historic background of Lady Godiva combine well for another purpose. Museum visitors come with broad interests and available time. They may be off-the-street clock watchers looking for a gee whiz diversion, or they may be specialized groups, students, or professionals, brimming with time and curiosity.
Whatever, I believe the Lady from the kivas of Pajarito Canyon can satisfy them all. I am sure she can do so if, as originally intended, alternative, well-thought-out visuals and narration become a part of the exhibit.

I have mentioned that the gamma rays and the neutrons in the replica are real. Thus, even the casual viewer has something to think about. And every viewer is invited to think of the inevitability of having to deal with nuclear energy when they hear the clack of the simulated neutron counter representing the flash of a prompt neutron fission chain — a given of nature.

For others who have time to be intrigued there are matters like prompt burst delay to be taken up. A remarkable story goes with this arresting behavior of the device.

It was known when the Godiva prompt burst program began that fission chain lengths fluctuated wildly near critical. However, the significance of these fluctuations for Godiva when a delayed neutron source is absent was underestimated. It was a surprise at the time, and it is a wonder still, to assemble Godiva to prompt critical and then wait for nature to play an extraordinary game of chance for as long as a few seconds before hearing the crack of a single neutron fission chain that lasts less than 1 thousandth of a second. This single chain, beginning with one neutron-induced fission, develops a peak energy generation rate greater than the electrical power consumed in any one of the United States except New York or California.

For professionals of technology, like you here at this meeting, there is much else to tell about basic reactor physics measurements, and about the irradiation of mice, monkeys and two burros, of silicon and sidewinders, and of a burst that never happened because a customer casually retracted his sample by remote control when the burst rod went in. And of course, there is the burst that ended Godiva's useful life, also because something moved. What moved was an experiment held together with duct tape, the modern fastener of choice for physicists in a hurry. It is worth remembering that even in 1957 the switchboard at Los Alamos was jammed when the accident was announced. The calls included one from the San Francisco Examiner asking, "How big was the mushroom cloud?"

Let me wind down, now, by reminding you that Lady Godiva of Coventry was a crusader for tax reduction in the 11th century and today is a namesake for fashionable chocolates. A broad career! My purpose this evening has been to show that the opportunities for exhibiting the Lady of nuclear energy are equally wide open. At the same time, I believe the display challenge for this brand new "ANS Nuclear Historic Landmark" remains what it was in the beginning: to pursue public and professional perception of nuclear energy by telling a good story.

At heart, perhaps, I'm just an old-fashioned sideshow hustler.

4.0 Images

As such, one is sometimes in places like this:
(Slide: Open House at Pajarito Site in Los Alamos)

One really likes to see this:
(Slide: Children gathered around Pinocchio, the neutron fission chain simulator also destined for the National Atomic Museum)

And sometimes one catches people like this:
(Slide: Sen. Humphrey at Pinocchio)

It really all started with Tennyson, of course:

Lady Godiva

Then she rode forth, clothed on with chastity.
The deep air listened round her as she rode,
And all the low wind hardly breathed for fear.
The little wide-mouthed heads upon the spout
Had cunning eyes to see; the barking cur
Made her cheeks flame; her palfreys foot-fall shot
Light horrors thro' her pulse. . .

DISTRIBUTION:

DOE TIC-4500 (UC-80: 115 copies)

B. Ahlport
Northrop Corp.
Org. 3020/N3
2301 West 20th Street
Hawthorne, CA 90250

E. G. Bailiff
Oak Ridge National Laboratories
Route 3
Clinton, TN 37716

S. K. Bhattacharyya
Argonne National Laboratory
9700 South Cass Avenue
Argonne, IL 60439

H. M. Busey
SAIC/OMA/HQ
5007 Benton Avenue
Bethesda, MD 20814

A. De La Paz
U.S. Army, WSMR
White Sands Missile Range, NM
88002

C. E. Dickerman
Argonne National Laboratory
9700 South Cass Avenue
Argonne, IL 60439

E. J. Dowdy
Los Alamos National Laboratory
P. O. Box 1663
Group Q-2, MS-J562
Los Alamos, NM 87545

H. G. Dubyoski
Aberdeen Proving Ground
Army Pulsed Reactor Facility
Maryland, 21005

M. Dunlap
Rockwell International
3370 Miraloma Avenue, GB74
Anaheim, CA 92803

K. Elliott
USDOE/AL
P.O. Box 5400
Albuquerque, NM 87185

M. Flanders
U.S. Army WSMR
White Sands Missile Range, NM
88002

E. A. Flores
Nuclear Effects, Fast Burst
Reactor, WSMR
Bldg. 21225, NE-NH
White Sands Missile Range, NM
88002

N. F. Frost
Lockheed Missiles and Space Co.
P.O. Box 3504
Sunnyvale, CA 94088-3504

D. Garrison
Northrop
Org. 3312/N3
2301 West 120th Street
Hawthorne, CA 90250

L. Greene
Rockwell International
3370 Mira Loma Avenue
HB11
Anaheim, CA 92803

J. Grundl
National Bureau of Standards
Gaithersburg, MD 20899

J. Hassberger
Lawrence Livermore National
Laboratory
P.O. Box 808, L-389
Livermore, CA 94550

E. H. Hayth
White Sands Missile Range, TE-N
2250 Hixon Drive
Las Cruces, NM 88005

C. Heimbach
Aberdeen Proving Ground
Combat Systems Test Activity
Bldg. 860
Aberdeen Proving Ground, MD 21005-
5059

L. B. Holland
Oak Ridge National Laboratory
107 Carnegie Drive
Oak Ridge, TN 37830

M. Hoover
Inhalation Toxicology Research Inst.
Lovelace Biomedical & Environmental
Research Institute, Inc.
P.O. Box 5890
Albuquerque, NM 87185

S. Judd
Charles Stark
555 Technology Square, MS 11
Cambridge, MA 02139

C. E. Lee
Jack Tills & Associates, Inc.
209 Eubank NE
Albuquerque, NM 87123

W. G. Lussie
INEL
P.O. Box 1625
Idaho Falls, ID 83415

Richard E. Malenfant
U.S. Department of Energy
DP-22/GTN
Washington, DC 20545

J. W. Malloy
Raytheon Co.
M/S 1K5
528 Boston Post Road
Sudbury, MA 01776

J. Meason
White Sands Missile Range
P.O. Box 477
White Sands Missile Range, NM 88002

G. Moody
White Sands Missile Range
P.O. Box 477
White Sands Missile Range, NM 88002

A. P. Olson
Argonne National Laboratory
9700 South Cass Avenue
Argonne, IL 60439

R. T. Perry
Texas A&M University
Nuclear Engineering Dept.
College Station, TX 77843

E. A. Plassmann
Los Alamos National Laboratory
Group Q2, MS/J562
P.O. Box 1663
Los Alamos, NM 87544

J. A. Reuscher
Nuclear Science Center
Texas A&M University
College Station, TX 77843-3575

G. J. Russell
Los Alamos National Laboratory
Group P-9, MS/H807
Physics Division
Los Alamos, NM 87545

D. R. Sachs
Rockwell International
Critical Mass Laboratory
P.O. Box 464
Golden, CO 80402-0464

W. W. Sallee
White Sands Missile Range
1515 Dorothy Circle
Las Cruces, NM 88001

R. Sartor
1907 Buena Vista SE, #14
Albuquerque, NM 87106

B. E. Simpkins
Science & Engineering Associates
2500 Louisiana NE, Suite 610
Albuquerque, NM 87110

M. H. Sparks
WSMR, TE-NO
White Sands Missile Range, NM 88002

T. F. Wimett
Los Alamos National Laboratory
P.O. Box 1663
Group Q-2, MS-J562
Los Alamos, NM 87545

D. Woodall, Manager
Physica Organization
EG&G Idaho, Inc.
P. O. Box 1625
Idaho Falls, ID 83415

H. Yockey
Aberdeen Proving Ground
Combat Systems Test Activity
Aberdeen Proving Ground, MD 21005

R. M. Jefferson
13136 Montgomery Blvd., NE
Albuquerque, NM

T. A. Parish
Texas A&M University
College Station, TX 77843

C. S. Sims
Oak Ridge National Laboratories
Route 3
Clinton, TN 37716

P. E. Fehlau
Los Alamos National Laboratory
P.O. Box 1663
Los Alamos, NM 87545

Ger Kroesing
S&T Advisory Group of the
Federal Chancellery
BADSTR 9
FRG 8000 Munich 70

Maximo Lazo
University of New Mexico
Chemical & Nuclear Engineering Dept.
Albuquerque, NM 87131

Sandia Distribution:
1111 H. J. Stein
1128 J. Rice
1128 D. R. Neal
1128 G. N. Hays
1144 L. R. Dawson
1230 J. E. Powell
1232 W. Beezhold
1233 L. M. Choate
2116 W. J. Barnard
2120 W. R. Dawes, Jr.
2126 J. E. Gover (2)
2144 P. V. Dressendorfer
2150 E. D. Graham, Jr.
2157 R. F. Rieden
2320 J. H. Renken
2321 L. D. Posey
2321 W. G. Perkins
3312 R. L. Schwing
3312 R. B. Stump
6228 M. M. Moya
6228 S. Thunborg
6228 W. M. Davidson
6400 D. J. McCloskey
6421 G. A. Harms
6421 D. A. McArthur
6421 P. S. Pickard
6416 J. S. Philbin
6450 T. R. Schmidt
6451 T. F. Luera (25)
6451 D. T. Berry
6451 R. S. Domingues
6451 B. F. Estes
6451 D. Griggs
6451 C. D. Harmon
6451 V. E. James
6451 D. M. Minnema
6452 J. W. Bryson
6452 B. B. Conklin
6452 R. A. Rubio
6452 D. W. Vehar
6454 G. L. Cano
6454 C. V. Holm
6454 J. G. Kelly
6511 P. J. McDaniel
7252 D. W. Bushmire
7842 M. F. Aker
3141 S. A. Landenberger (5)
3151 W. L. Garner (3)
8024 P. W. Dean

☆ U S GOVERNMENT PRINTING OFFICE 1987—773-049/41038